

# Polyanionic cathode materials for sodium-ion batteries

Zur Erlangung des akademischen Grades eines

DOKTORS DER NATURWISSENSCHAFTEN

(Dr. rer. nat.)

der KIT-Fakultät für Chemie und Biowissenschaften

des Karlsruher Instituts für Technologie (KIT)

genehmigte

DISSERTATION

von

Herr Huang Zhang

KIT-Dekan: Prof. Dr. Reinhard Fischer

Referent: Prof. Dr. Stefano Passerini

Korreferent: Prof. Dr. Helmut Ehrenberg

Tag der mündlichen Prüfung: 13 Dezember 2018



**To my family**

*“A journey of a thousand miles begins with a single step.”*  
*(Lao-Tzu)*

## Acknowledgments

First of all, I would like to thank my advisor, Prof. Stefano Passerini, for giving me the chance to explore in sodium-ion batteries. I am grateful that he challenged me to meet his high scientific and communication standards, for his flexibility in allowing me to pursue what I found interesting, and for trusting me to solve problems with an independent approach. I really appreciate the enjoyable environment to work in Electrochemistry I group.

I am also very grateful to Prof. Helmut Ehrenberg for being the second examiner of my thesis, especially for his fruitful discussion.

I would like to thank Dr. Daniel Buchholz and Dr. Ivana Hasa with whom I was working in the sodium-ion battery research field. I am really grateful to their help on my work. Dr. Alberto Varzi, Dr. Sangsik Jeong, Dr. Diogo Vieira Carvalho, Lucas Lodovico, and Jakob Asenbauer are also acknowledged. Without their support this thesis would not be possible. I would like to express my gratitude to Dr. Dominic Bresser for his critical review and correction on the thesis. Francesco Liberale from Polytechnic University of Milan is also acknowledged for his critical discussion on the thesis. For sure, I would like to thank all my colleagues at HIU as well as the administrative and technical staff for their help and support.

I would like to thank Dr. Thomas Diemant and Prof. R. Jürgen Behm from Institute of Surface Chemistry and Catalysis, Dr. Dorin Geiger and Prof. Ute Kaiser from Electron Microscopy Group of Materials Science in University of Ulm for their supports and discussion.

I would like to thank Prof. Jan Fransaer and Xuan Zhang from KU Leuven, Prof. Yunlong Xu from East China University of Science and Technology and Dr. Dong Liu from University of Texas at Arlington for their continuous encouragements during my study abroad.

Special thanks to the growing Chinese group in HIU. Thanks to Bingsheng Qin, Xinwei Dou, Yanjiao Ma, Yuan Ma, Dr. Xinpei Gao, Dr. Shan Fang, Xu Liu, Jin Han, Yun Xu, Fanglin Wu, Jinyu Wu and Huihua Li whom not only worked with me side by side, but also enriched the daily life.

Finally, I thank my family for their support which enabled me to accomplish my studies.



## Abstract

Batteries, and more specifically lithium-ion batteries, have been one of the greatest successes in the field of energy storage of the last century. In view of the increasingly growing energy storage demands, however, battery technologies must be diversified with respect to their specific requirements in distinct applications. For the stationary storage, sodium-ion battery represents the most appealing alternative to lithium-ion battery, owing to the abundance and low cost of foreseen raw materials, driving the energy storage to high-scale and low cost. Although several materials have been explored, further progresses toward high performance cathode materials are still needed. Polyanionic compounds, which have already shown their successful implementation in lithium-ion batteries, represent a promising class of cathode materials also for sodium-ion batteries, providing several advantages including high thermal stabilities, improved oxidative stability at high voltages and flat voltage response.

This thesis mainly focuses on the design strategy, synthesis, characterization, and investigation of phosphate-based polyanionic cathodes for SIBs, as well as their implementations in practical electrochemical cells to achieve safe, low-cost, environmental friendly and high performance SIBs.

Sodium vanadium phosphate,  $\text{Na}_3\text{V}_2(\text{PO}_4)_3$ , has been identified as one of the most promising polyanionic cathode materials, showing attractive specific energy density and structural stability upon cycling. However, one of the main drawbacks is represented by the poor electric conductivity and high kinetic barrier for Na diffusion resulting in unsatisfactory electrochemical performance. In this regard, within the thesis framework, a strategy combining nitrogen-doped carbon coating of the active material has been developed. A systematic investigation of the carbon coating effect on the structural and electrochemical properties have been analyzed. The results demonstrate that the nature of the carbon-nitrogen defective species and carbon matrices has different impacts on the structure and electrochemical performance. By properly adjusting these two parameters,  $\text{Na}_3\text{V}_2(\text{PO}_4)_3/\text{C}$  composites have been synthesized exhibiting superior long-term cyclability and rate capability due to reduced electrode polarizations resulting from the enhanced electronic/ionic conductivities and facilitated charge transfer at the electrode-electrolyte interface.

Beside the improvements of known materials to enable their practical use, the research performed within this thesis also involves the development of novel materials characterized by high operating voltage in order to boost the energy. New high voltage phosphate-based cathodes for SIBs have been designed, by optimizing the synthesis parameters and by investigating the structural and morphological properties combined with the study of the sodium storage mechanism. A new

mixed phosphate polyanionic compound, i.e.  $\text{Na}_4\text{Ni}_3(\text{PO}_4)_2(\text{P}_2\text{O}_7)$ , has been proposed. For the first time, the electrochemical activity of the  $\text{Ni}^{2+/3+}$  redox couple has been reported within the mixed polyanionic framework during sodium intercalation. The developed material exhibits a working potential as high as 4.8 V, resulting in a theoretical energy density of about  $600 \text{ Wh kg}^{-1}$  in sodium cell configuration. Furthermore, it is also demonstrated that the vanadium redox couple ( $\text{V}^{3+/4+}$ ) has a higher potential when using more electronegative polyanionic groups such as  $\text{N}(\text{PO}_3)_3$ . The synthesized  $\text{Na}_3\text{V}(\text{PO}_3)_3\text{N}$  material delivered a potential of 4.0 V, which is higher than the one exhibited by  $\text{Na}_3\text{V}_2(\text{PO}_4)_3$ . Both *in situ* and *ex situ* X-ray diffraction techniques were used to unfold the sodium mobility in the structure. Such explorations expanded the group of suitable material to be used as cathodes in SIBs, paving the way for the discovery of new Na-based high potential cathode materials.

In line with the low cost and environmental friendly philosophy of SIBs, efforts were devoted to the design of full cell prototypes, including the use of polyanionic electrode materials both in non-aqueous and aqueous electrolytic media. A symmetric  $\text{Na}_2\text{VTi}(\text{PO}_4)_3//\text{Na}_2\text{VTi}(\text{PO}_4)_3$  and an asymmetric  $\text{NaTi}_2(\text{PO}_4)_3//\text{Na}_3\text{V}_2(\text{PO}_4)_3$  cell prototypes were investigated. In conventional organic electrolyte, these two configurations exhibit attractive power capability and cycling stability. In addition, the  $\text{NaTi}_2(\text{PO}_4)_3//\text{Na}_3\text{V}_2(\text{PO}_4)_3$  cell offers a remarkable high efficiency at high power rates with long cycle life which are suitable characteristic for application in grid-scale energy storage. To further reduce the cost and improve the safety, these prototypes were also investigated in aqueous electrolyte solutions. Indeed, the use of concentrated aqueous electrolyte of “water-in-salt” or aqueous/nonaqueous hybrid electrolytes stabilize the structure of polyanionic materials by forming a resistive but protective interphase, responsible of the stable cycling performance and good rate capability. These results provide important insight for the development of low cost SIBs for large-scale energy storage application characterized by excellent electrochemical performance.

The research conducted within the thesis framework clearly demonstrates that polyanionic phosphate compounds are promising and appealing candidates for application as cathode materials in SIBs. The design and optimization of the structural properties of the proposed materials in combination with the investigation of the structural-function correlation in sodium cells led to the identification of novel high voltage cathode materials with superior electrochemical performance. In addition, the investigated possibility of replacing the commonly employed organic electrolyte with aqueous ones by using polyanionic materials as electrodes defines new safer, lower cost, longer cycle life energy storage technologies for large-scale stationary applications.



## Kurzzusammenfassung

Natrium-Ionen Batterien (NIBn) können potentiell aus günstigen und einfach verfügbaren Rohmaterialien hergestellt werden, und sind deshalb eine aussichtsreiche Alternative gegenüber LIBn, für preiswerte stationäre Energiespeicher. Polyanionische Verbindungen, die bereits erfolgreich in Lithium-Ionen-Batterien eingesetzt wurden, stellen wegen ihrer hohen thermischen und elektrochemischen Stabilität, und ihrer flachen Spannungsantwort eine vielversprechende Klasse von Kathodenmaterialien für Natriumionenbatterien dar.

Diese Dissertation konzentriert sich hauptsächlich auf die Entwicklung, Synthese, Charakterisierung und Untersuchung von polyanionischen Kathoden auf Phosphatbasis für sichere, kostengünstige, umweltfreundliche und hochleistungsfähige NIBn.

Natriumvanadiumphosphat,  $\text{Na}_3\text{V}_2(\text{PO}_4)_3$ , wurde aufgrund der hohen spezifischen Energie und der strukturellen Stabilität, als eines der vielversprechendsten polyanionischen Kathodenmaterialien identifiziert. Allerdings führen die schlechte elektrische Leitfähigkeit und kinetisch gehinderte Na-Diffusion zu einer unbefriedigenden elektrochemischen Leistung. Im Rahmen dieser Dissertation wurden Strategien entwickelt, das Aktivmaterial mit einer stickstoffdotierte Kohlenstoffbeschichtung zu kombinieren. Der Effekt der Kohlenstoffbeschichtung auf strukturelle und elektrochemische Eigenschaften wurde systematisch analysiert. Die Ergebnisse zeigen, dass die Struktur der Kohlenstoff-Stickstoff Defekte und der Kohlenstoffmatrix bestimmend ist für die elektrochemischen Eigenschaften. Durch Einstellung dieser beiden Parameter wurden  $\text{Na}_3\text{V}_2(\text{PO}_4)_3/\text{C}$ -Komposite synthetisiert, die aufgrund einer verbesserten elektronischen/ionischen Leitfähigkeiten und eines erleichterten Ladungstransfers an der Elektroden-Elektrolyt-Grenzfläche eine reduzierter Elektrodenpolarisation und, dadurch eine verbesserte Zyklisierbarkeit und Ratenfähigkeit aufweisen.

Neben den Verbesserungen bekannter Materialien wurden in der vorliegenden Arbeit neuartige Materialien mit hoher Betriebsspannung, und somit gesteigerter Energiedichte, entwickelt. Für die Entwicklung von phosphat-basierten Hochvolt-Kathoden für NIBn wurden Syntheseparameter optimiert und strukturelle und morphologische Eigenschaften sowie der Natriumspeichermechanismus untersucht.  $\text{Na}_4\text{Ni}_3(\text{PO}_4)_2(\text{P}_2\text{O}_7)$  wurde als neue polyanionische Phosphatverbindung vorgeschlagen. Erstmals wurde die elektrochemische Aktivität des  $\text{Ni}^{2+/3+}$  - Redoxpaars innerhalb des gemischten polyanionischen Gerüsts während der Natriuminterkalation beschrieben. Das entwickelte Material weist ein Arbeitspotential von bis zu

4.8 V auf, was zu einer theoretischen Energiedichte von etwa 600 Wh kg<sup>-1</sup> in Natriumzellenkonfiguration führt. Darüber hinaus wird gezeigt, dass die Verwendung von elektronegativeren polyanionischen Gruppen wie N(PO<sub>3</sub>)<sub>3</sub> das Potential des Vanadium-Redoxpaars (V<sup>3+/4+</sup>) erhöht. So liefert das synthetisierte Na<sub>3</sub>V(PO<sub>3</sub>)<sub>3</sub>N ein Potenzial von 4.0 V, also höher als das von Na<sub>3</sub>V<sub>2</sub>(PO<sub>4</sub>)<sub>3</sub>. Die Natriummobilität in der Struktur wurde sowohl durch In-situ als auch ex-situ Röntgenbeugungstechniken untersucht. Durch diese Untersuchungen wurde die Gruppe geeigneter Materialien, die als Kathoden in NIBs verwendet werden können erweitert, und der Weg für die Entdeckung neuer Na-basierter Kathodenmaterialien mit hohem Arbeitspotential geebnet.

Es wurden Vollzellenprototypen zu entwickelt, die polyanionischen Elektrodenmaterialien sowohl mit nicht-wässrigen als auch mit wässrigen Elektrolytlösungen kombinieren. Dabei wurde ein symmetrischer Na<sub>2</sub>VTi(PO<sub>4</sub>)<sub>3</sub>//Na<sub>2</sub>VTi(PO<sub>4</sub>)<sub>3</sub> - und ein asymmetrischer NaTi<sub>2</sub>(PO<sub>4</sub>)<sub>3</sub>//Na<sub>3</sub>V<sub>2</sub>(PO<sub>4</sub>)<sub>3</sub>- Zellprototyp untersucht. In herkömmlichen organischen Elektrolyten zeigen beide Konfigurationen eine gute Ratenfähigkeit bei hoher Zyklenstabilität. Darüber hinaus bieten NaTi<sub>2</sub>(PO<sub>4</sub>)<sub>3</sub>//Na<sub>3</sub>V<sub>2</sub>(PO<sub>4</sub>)<sub>3</sub>-Zellen eine bemerkenswert hohe Energieeffizienz, insbesondere bei hoher Leistung, und eine lange Lebensdauer, und sind daher für stationäre Anwendung geeignet. Zur weiteren Kostensenkung und zur Erhöhung der Sicherheit, wurden außerdem Prototypen mit wässrigen Elektrolytlösungen untersucht. Dabei führt die Verwendung von konzentrierten wässrigen Elektrolyten, sogenannten "Wasser-in-Salz" Elektrolyten, oder die Verwendung von wässrigen/nichtwässrigen Hybridelektrolyten zur Stabilisierung der Struktur von polyanionischen Phosphatverbindungen. Die Stabilisierung wird durch die Bildung einer widerstandsfähigen und schützenden Grenzschicht erreicht, die für die gute Zyklierbarkeit und Ratenfähigkeit verantwortlich ist. Diese Ergebnisse liefern wichtige Erkenntnisse für die Entwicklung von kostengünstigen und leistungsfähigen NIBn für großtechnische Energiespeicheranwendungen.

Die im Rahmen dieser Arbeit durchgeführte Forschung zeigt deutlich, dass polyanionische Phosphatverbindungen vielversprechende Kandidaten für die Anwendung als Kathodenmaterialien in NIBn sind. Das Design und die Optimierung struktureller Eigenschaften der Materialien führten zur Identifizierung von neuen Hochvolt-Kathodenmaterialien mit überlegener elektrochemischer Leistung. Darüber hinaus bietet sich bei diesen Materialien die Möglichkeit, durch die Verwendung von wässrigen Elektrolyten anstelle der üblicherweise organischen Elektrolyte, neue, sicherere und kostengünstigere Energiespeichertechnologien mit längerer Zyklen Lebensdauer für große stationäre Anwendungen zu entwickeln.

# Table of Contents

Acknowledgments .....	I
Abstract.....	III
Kurzzusammenfassung .....	V
Table of Contents.....	VII
<b>1 Introduction.....</b>	<b>1</b>
1.1 Background and Motivation .....	1
1.2 Rechargeable Alkali-ion Batteries.....	2
1.2.1 Working Mechanisms: “rocking-chair” .....	2
1.2.2 Sodium-ion Batteries.....	3
1.3 Materials for Sodium-ion Batteries.....	4
1.3.1 Materials Considerations.....	4
1.3.2 Anode Materials.....	5
1.3.3 Electrolytes .....	6
1.3.4 Cathode Materials.....	7
1.4 Polyanionic Cathodes for Sodium-ion Batteries.....	10
1.4.1 Single Polyanion Group .....	10
1.4.2 Mixed Polyanion Groups .....	10
1.4.3 Phosphate Polyanions.....	10
1.5 Limits of Polyanionic Cathodes for Sodium-ion Batteries.....	11
1.5.1 Electronic Conductivity .....	11
1.5.2 Specific Capacity .....	12
1.5.3 Working Voltage .....	12
1.5.4 Structural Stability.....	12
1.5.5 Strategies for the Materials Optimization .....	12
1.5.6 Strategies for the Materials Design.....	13
1.6 Synthesis Method and Characterization Techniques.....	15
1.6.1 Synthesis Method: Solid State Synthesis.....	15
1.6.2 Materials Characterization .....	15
1.6.3 Electrochemical Characterization of Electrodes.....	18
1.6.4 Ex situ and in situ Analysis Techniques for Electrode Materials .....	19
1.7 Thesis Overview .....	19
<b>2 Sodium Vanadium Phosphates as Cathodes in Sodium-ion Batteries.....</b>	<b>21</b>

2.1	Structure and Electrochemical Properties of Nitrogen-doped Carbon Coated $\text{Na}_3\text{V}_2(\text{PO}_4)_3$ Cathode .....	22
2.1.1	Intorduction.....	22
2.1.2	Experimental Methods .....	23
2.1.3	Results and Discussion .....	24
2.1.4	Conclusions.....	35
2.2	Effect of Nitrogen-doped Carbon Matrix Dimensions on the Electrochemical Properties of $\text{Na}_3\text{V}_2(\text{PO}_4)_3$ Cathode .....	37
2.2.1	Introduction.....	37
2.2.2	Experimental Methods .....	38
2.2.3	Results and Discussion .....	39
2.2.4	Conclusions.....	50
3	High-voltage Cathodes with Phosphate Frameworks for Sodium-ion Batteries .....	51
3.1	Mechanism Investigation of Ni Redox in Mixed-polyanionic Framework $\text{Na}_4\text{Ni}_3(\text{PO}_4)_2(\text{P}_2\text{O}_7)$ .....	52
3.1.1	Introduction.....	52
3.1.2	Experimental Methods .....	53
3.1.3	Results and Discussion .....	55
3.1.4	Conclusions.....	66
3.2	Nitridophosphate $\text{Na}_3\text{V}(\text{PO}_3)_3\text{N}$ as a Zero-strain and Safe High Voltage Cathode Material.....	67
3.2.1	Introduction.....	67
3.2.2	Experimental Methods .....	68
3.2.3	Results and Discussion .....	69
3.2.4	Conclusions.....	76
4	Polyanionic Electrode Based Nonaqueous and Aqueous Sodium-ion Batteries.....	77
4.1	Symmetric Sodium-ion Battery: $\text{Na}_2\text{VTi}(\text{PO}_4)_3//\text{Na}_2\text{VTi}(\text{PO}_4)_3$ .....	78
4.1.1	Introduction.....	78
4.1.2	Experimental Methods .....	79
4.1.3	Results and Discussion .....	81
4.1.4	Conclusions.....	92
4.2	Sodium-ion Battery: $\text{NaTi}_2(\text{PO}_4)_3//\text{Na}_3\text{V}_2(\text{PO}_4)_3$ .....	93
4.2.1	Introduction.....	93
4.2.2	Experimental Methods .....	94
4.2.3	Results and Discussion .....	96
4.2.4	Conclusions.....	110

5	Summary and Outlook .....	113
6	Appendix.....	115
6.1	Abbreviations .....	115
6.2	List of Figures.....	116
6.3	List of Tables .....	121
6.4	Appendix 1 contains the supporting information for Chapter 2.....	122
6.5	Appendix 2 contains the supporting information for Chapter 3. ....	125
	Bibliography .....	129
	List of Publications.....	139



# Chapter 1

## Introduction

### 1.1 Background and Motivation

Global concerns over climate change and constraints of fossil fuels as primary power source have led to the exploration of green and sustainable energy sources, such as solar, wind, geothermal and tidal power.<sup>[1]</sup> Nevertheless, the implant of these technologies into grid requires the integration of efficient energy storage systems. Rechargeable batteries with cost-effective and environmentally friendly features represent the most promising strategy to efficiently store energy.<sup>[2]</sup>

Lithium-ion batteries (LIBs) are one of the greatest successes for electrochemical energy storage applications of the past century. They are light, compact and offer outstanding energy and power density performance. For this reason, LIBs are dominating the market for portable electronics, hybrid and electric vehicles (EV) application.<sup>[3, 4]</sup> However, in view of the increasingly growing field of electric mobility an increasingly growing demand of lithium has been observed with a consequent increase of the lithium price and rising concerns about the future availability of lithium supply. In fact, the major lithium sources are concentrated in brine deposits located in South America and in the Greenbushes mine in Australia. Moreover, the lithium market is dominated by few companies such as Albemarle (ALB US), owing Rockwood Lithium, SQM (SQM US), FMC (FMC US) and Chengdu Tianqi (China), which control around 50% of the total amount of lithium supply.<sup>[5]</sup> In this context, considering the associated potential risks of an economical and geopolitical dependency of lithium supply countries and industries, the consequent uncertainties on the lithium price and the lesson learned from the economic dependency from oil and fossil fuels states the search for alternative battery chemistries appears mandatory.

Sodium represents the most appealing alternative to lithium. Firstly studied during the 80s alongside with LIBs, sodium-ion batteries (SIBs) were sidelined due to the more promising features of LIBs especially in terms of energy density.<sup>[6, 7]</sup> The recent renewed interest in SIBs has been mainly driven by the low cost of the raw materials due to their greater abundance (4<sup>th</sup> most abundant element in the Earth's crust) and uniform distribution, resulting in a lower economic and geopolitical impact.<sup>[8-10]</sup> In their most common configurations, both technologies operate through the "rocking chair mechanism" involving the reversible shuttle of alkali ions between two

host electrodes through an electrolyte medium conducting the alkali ions. Being characterized by a rather similar working principle, the development of SIBs may strongly benefit from the great advances achieved in the field of LIBs within the last 30 years. Indeed, in very few years promising results and an accelerated knowledge has been achieved compared to the LIBs technology and a rather facile implementation of SIBs production in industrial LIBs manufacturers is foreseen. Moreover, the use of sodium-based electrolyte systems and the implementation of aluminum as current collector at the anode side instead of the more expensive copper, represent further cost advantages with respect to LIBs.<sup>[11]</sup> However, due to the larger ionic radius of sodium and its higher redox potential, SIBs possess an intrinsically lower energy density compared to LIBs.<sup>[12]</sup> Nonetheless, these issues can be (partially) addressed via the development of proper electrode materials, allowing for energy density values comparable to the current lithium-ion technology. Continual improvements in power, energy density and safety are required to keep up with the changes in technology.

## 1.2 Rechargeable Alkali-ion Batteries

### 1.2.1 Working Mechanisms: “rocking-chair”

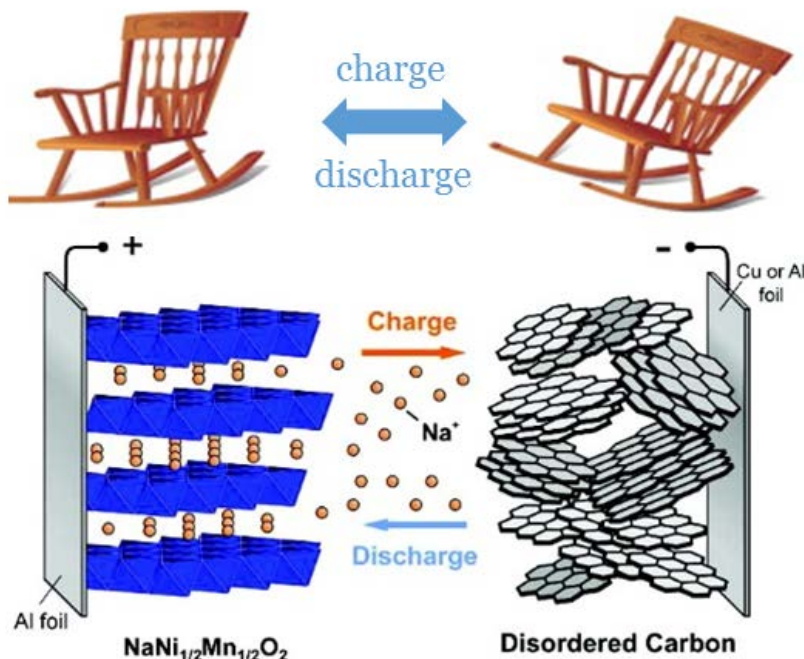


**Figure 1-1.** Schematics of “rocking-chair” mechanism and sodium-ion batteries. Adapted from reference<sup>[13]</sup>.



Batteries are electrochemical devices, which operate by converting chemical energy into electrical energy. A battery consists of one or more electrochemical cells mainly containing a positive electrode (cathode), a negative electrode (anode), a separator and an electrolyte media (ion conductor). During battery operation, the electron migration through an electronic conductor (electrodes) is accompanied by the ion migration through an ionic conductor (electrolyte) in the opposite direction, ensuring the preservation of electro neutrality.<sup>[4]</sup> Based on the reversibility of the chemical reactions, batteries can be classified into primary and secondary batteries. Primary batteries are designed to be used only once, as the occurring reactions are not (fully) reversible. Secondary batteries, also known as rechargeable batteries, can be recharged after having been discharged and the application of an electric current reverses the chemical reactions occurring upon discharge. The term “alkali-ion battery” refers to a family of alkali-ion chemistries, for which the alkali ions act as the charge carrier. A rechargeable alkali-ion battery, also referred to as rocking-chair or swing battery (see **Figure 1-1**), is a specific type of a rechargeable battery for which the alkali-ion, e.g. Li, Na, K, etc., moves from the negative electrode to the positive electrode upon discharge and back upon charge.

### 1.2.2 Sodium-ion Batteries

“Rocking-chair” sodium-ion batteries, as the name indicates already, employ sodium ions as charge carrier, which can reversibly move between the cathode and anode in the ion conductive electrolyte. The battery components and the electrical storage mechanism are very similar to the lithium-ion technology. However, there are some obvious differences between the two systems. Na<sup>+</sup> ions ionic radii (1.02 Å) is larger than the one of Li<sup>+</sup> ions (0.76 Å), affecting the phase stability, transport properties, and interphase formation. Sodium is also heavier than lithium (23 g mol<sup>-1</sup> compared to 6.9 g mol<sup>-1</sup>) and has a higher standard electrode potential (-2.71 V vs. SHE as compared to -3.02 V for lithium); thus, SIBs will be characterized in principle by a lower specific energy density when compared to LIBs.<sup>[5]</sup> Nonetheless, due to the massively growing demand for energy storage systems, SIBs provide an attractive alternative because of the wide availability and accessibility of sodium. Recently, the breakthrough in material science has led to the design of promising materials for application in SIBs, characterized by improved electrochemical performance and cycle life. Despite the great achievement so far reached, it is worth to consider that SIBs are still at an early stage of research and development, thus further improvements in energy density, safety and cost are required before a successful commercialization of large scale SIBs.

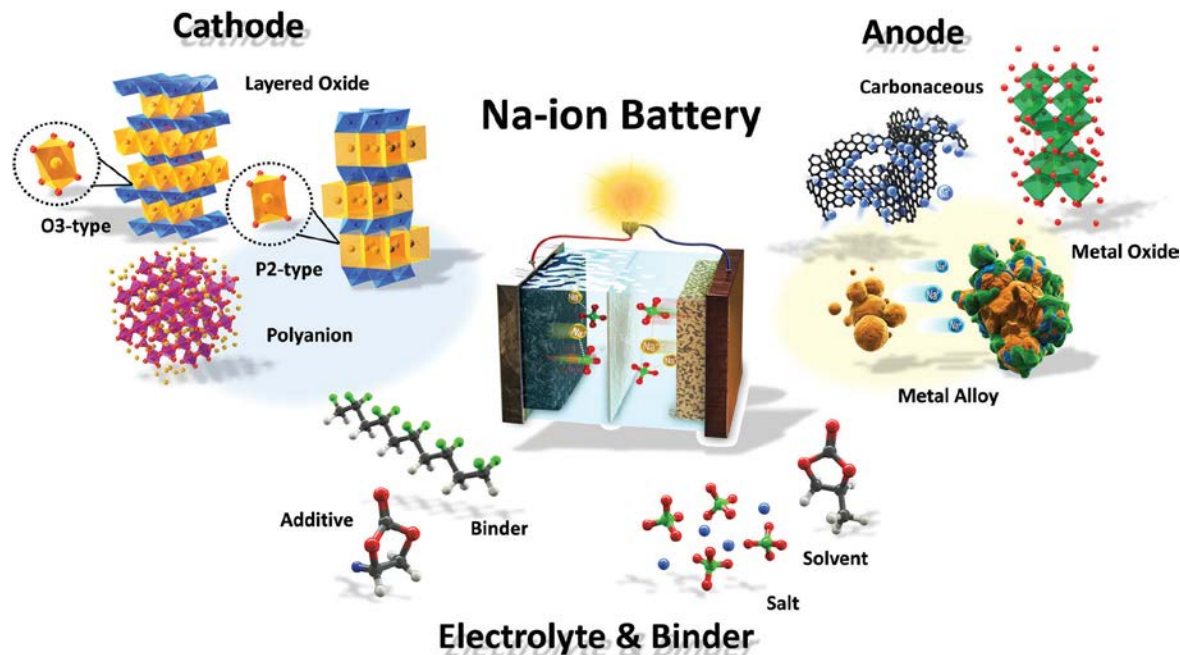


**Figure 1-2.** The illustration of electrode and electrolyte materials in sodium-ion battery system. Adapted from reference<sup>[14]</sup>.

### 1.3 Materials for Sodium-ion Batteries

Materials play a crucial role in the development of high-performance battery systems. **Figure 1-2** illustrates the several representative candidate materials such as cathode and anode materials, electrolytes, separators, and binders that have been identified so far as the most promising choices. The performance and safety of rechargeable batteries depend strongly on the employed materials. An ideal battery system should fulfill performance, cost and safety requirements for every final dedicated application. All of these parameters are strongly dependent and affected by the nature of the employed electrode materials and electrolyte media.

#### 1.3.1 Materials Considerations

The energy density of alkali ion batteries is strongly dependent by the average working voltage and the delivered specific capacity. Thus, in an effort to boost energy density, a rational design of electrode materials involves an optimization of the above mentioned parameters. In ideal conditions, the electromotive force (EMF) is given by the chemical potential difference between the cathode and the anode, which from a physical point of view, is translated into the difference of the electrochemical potential of the electrodes, given by the position of the Fermi level, between the anode and the cathode.<sup>[15]</sup> The working voltage of an alkali-ion cell is generally limited by the

electrochemical stability window of the electrolyte, which is determined by the difference in energy between the highest occupied molecular orbital (HOMO) and the lowest unoccupied molecular orbital (LUMO) of the electrolyte. Both electrodes should be selected taking into account that negative electrodes having a Fermi level higher than the LUMO of the electrolyte will favor electrolyte reduction, while the selection of positive electrodes with a Fermi level lower in energy than the HOMO will lead to electrolyte oxidation.<sup>[4, 16, 17]</sup>

Another crucial parameter to take into account is the cost-effectiveness of the developed battery prototypes. It has been reported that even if the cost of Na-precursors is lower respect to the ones employed in LIBs, the foreseen economic advantage is still not sufficient to compensate for the lower energy density of SIBs when compared to LIBs.<sup>[18, 19]</sup> A boosted energy density alongside with an improved cycle life is highly desired for the next generation rechargeable batteries characterized by low cost. The latter one is certainly strongly affected by the raw materials employed as well as the synthesis methodology adopted, which are two crucial parameters to be taken into account when developing the next generation SIBs materials.

### 1.3.2 Anode Materials

Up to now, various anode materials have been reported, which can be divided into three main groups based on the reaction mechanism involving sodium ions. Insertion-type compounds (carbon-based materials,<sup>[20]</sup> titanium-based materials),<sup>[21]</sup> de-/alloying materials (Sn, Sb, Ge),<sup>[22]</sup> and conversion-type compounds like transition metal oxides (or sulfides, phosphides, nitrides).<sup>[23]</sup> In addition, pure sodium metal also shows promising performance as anode commonly employed in room temperature Na-S, Na-O<sub>2</sub> batteries. However, sodium forms dendrites even more vigorously than lithium and it generally become unstable towards thermal runaway during cycling. Moreover, the increase in temperature during cell operation may lead to the melting of metallic sodium and cause a violent reaction. Consequently, the use of metallic sodium as an anode material would be a poor choice as it implies severe safety concerns.<sup>[24]</sup>

The ideal anode material should exhibit a low de-/sodiation voltage to allow for a large cell voltage, which can be translated in high energy density. On the other hand, it should be considered that too low working potentials might result in a pronounced cathodic (reductive) electrolyte decomposition and consequent instability of the solid/electrolyte interphase (SEI) in addition to the safety issues related to metal plating and dendrite growth.<sup>[25]</sup> The specific capacity of the anode is another critical parameter. Generally, the determining factors are represented by the available “space” (structural sites) to accommodate sodium ions, the ability to change the valence state (at least for insertion- and conversion-type compounds) and the reversibility of the de-/sodiation

reaction. A significant breakthrough of the energy density of sodium-ion cells may be achieved by employing beyond-insertion anode materials.<sup>[5]</sup>

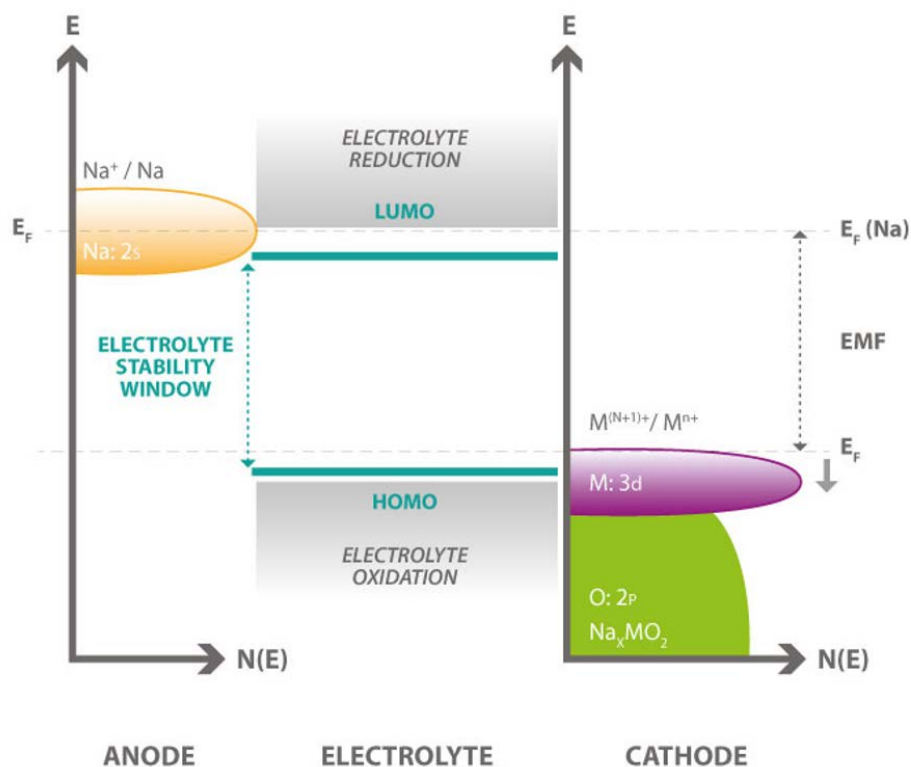


**Figure 1-3.** Schematic energy level diagram for a sodium-ion battery, illustrating the origin of the EMF (electromotive force). The Fermi level of the Na metal anode is reported above the LUMO of the electrolyte indicating reduction of the electrolyte and SEI formation. During deintercalation of sodium at the cathode, the Fermi level will shift down as indicated by the grey arrow. Adapted from reference<sup>[5]</sup>.

### 1.3.3 Electrolytes

Electrolytes used for batteries should provide a high ionic conductivity, while being electronically insulating, so that the ions (e.g.,  $\text{Na}^+$ ) can “easily” shuttle from the anode to the cathode and vice versa, while preventing a significant self-discharge. During cell operation, the electrolyte should sustain all Faradaic processes occurring at the electrodes. This means that the electrolyte should exhibit a wide electrochemical stability window, so that there won’t be any substantial electrolyte degradation within the range of the working potentials of both cathode and anode. Besides, the electrolyte should not react with any other cell component, such as the separator, current collectors and cell packaging materials. Moreover, the applicable electrolytes should be of low

toxicity and cost, meaning that the elements are ideally abundant and the synthesis processes are easily scalable and facile. Based on these considerations, the electrolytes of interest for sodium-ion batteries can be classified into 1) aqueous systems consisting of sodium salts in water, 2) non-aqueous electrolytes consisting of sodium salts dissolved in organic solvents, e.g., 1M NaPF<sub>6</sub> in propylene carbonate (PC), 3) ionic liquid-based electrolytes consisting of an organic salt (R<sup>+</sup>X<sup>-</sup>) doped with a fraction of the sodium salt equivalent (Na<sup>+</sup>X<sup>-</sup>), 4) solid electrolytes including solid polymer electrolytes and ceramic electrolytes, and 5) hybrid electrolytes containing both liquid and solid components.

### 1.3.4 Cathode Materials

Given that cathode materials are the key component which substantially determine the final energy density and cost of a battery, in the past few years, tremendous efforts have been devoted to explore suitable positive electrode materials with high reversible capacity, fast Na ion insertion/extraction, and good cycling stability. Currently, most of the materials so far investigated are essentially lithium analogues, which can be classified into two main categories, i.e. layered oxides and polyanionic compounds. Prussian blue and organic materials have also been examined as cathode materials for SIBs.

#### 1.3.4.1 Layered transition-metal oxides

Sodium-based transition metal layered oxides with general formula Na<sub>x</sub>MO<sub>2</sub> consist of alternately stacking of edge sharing MO<sub>6</sub> octahedral layers and Na ions layers. According to Delmas et al. [7], layered materials can be further categorized into two main groups: P2 or O3 type according to the Na<sup>+</sup> environment and the number of transition metal layers in the repeating unit cell. The symbols “P” and “O” represent a prismatic or octahedral coordination environment of the Na ions, respectively, and the “2” or “3” suggests the number of transition metal layers with different kinds of O stacking in a single unit cell.<sup>[26]</sup>

Among the cathode candidates, single transition metal layered oxides Na<sub>x</sub>MO<sub>2</sub> (M = V, Cr, Mn, Fe, Co, Ni) have been studied, although the initial investigations resulted in poor specific capacity and low retention.<sup>[27-29]</sup> It has been reported that a proper selection of transition metals within the layered structure is a very promising strategy to obtain structurally and electrochemically improved P2-type phases for application in Na cells.<sup>[30-32]</sup> Combining different transition metals leads to the obtainment of advanced materials with tunable and desirable properties reflected on the cycling behavior, such as a high working voltage and solid solution like smooth voltage profile. A great number of materials have been published including NaNi<sub>1/3</sub>Mn<sub>1/3</sub>Co<sub>1/3</sub>O<sub>2</sub>,

$\text{NaNi}_{1/3}\text{Fe}_{1/3}\text{Mn}_{1/3}\text{O}_2$ ,  $\text{Na}_x\text{Fe}_{1/2}\text{Mn}_{1/2}\text{O}_2$ ,  $\text{Na}_{0.5}\text{Ni}_{0.23}\text{Fe}_{0.13}\text{Mn}_{0.63}\text{O}_2$ ,  $\text{Na}_{2/3}\text{Mn}_{1/3}\text{Fe}_{1/3}\text{Co}_{1/3}\text{O}_2$ ,  $\text{Na}_{2/3}\text{Ni}_{1/2}\text{Mn}_{1/2}\text{O}_2$  and  $\text{Na}_{0.6}\text{Ni}_{0.22}\text{Al}_{0.11}\text{Mn}_{0.66}\text{O}_2$ .<sup>[30, 32-37]</sup> Among them manganese and iron based compounds appeared to be of particular interest due to the high abundance and low cost of the raw material.

Extensive research on this class of compounds have led to the obtainment of very promising cathode materials, nevertheless many issues affecting the overall electrochemical performances need to be addressed. Indeed, the electrochemical behavior of layered oxides, in terms of long term cycling stability and energy density, is generally strongly affected by multiple phase transitions and voltage decay upon cycling. In addition, another issue associated with the use of layered oxides is their structural instability when exposed to air and especially to moisture.

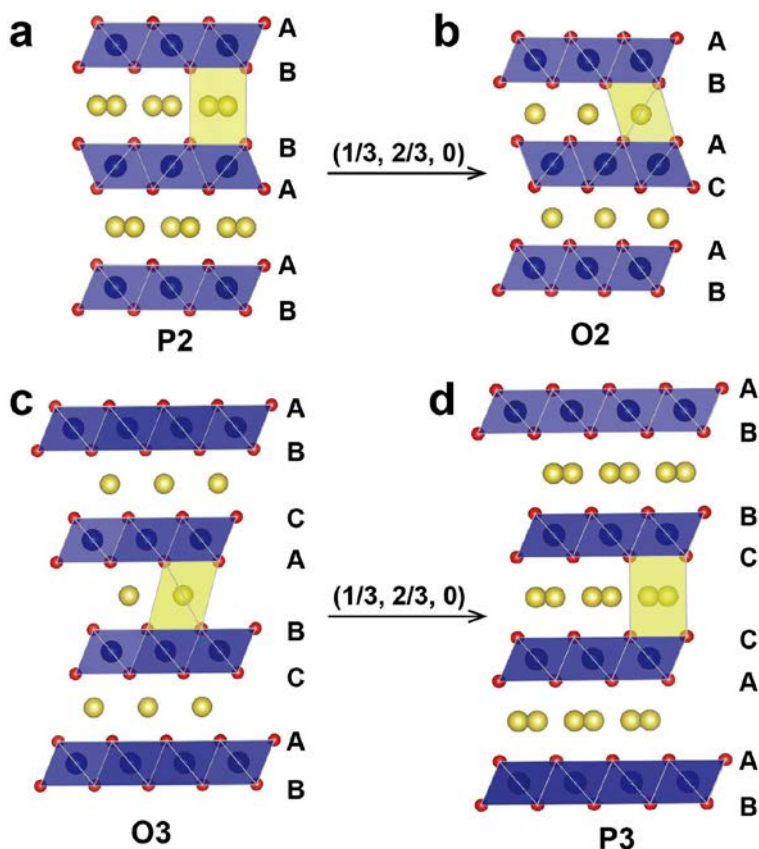


**Figure 1-4.** A schematic illustration of the crystal structures for layered Na-containing oxides ( $\text{Na}_x\text{MO}_2$ ) for a) P2-type, b) O2-type, c) O3-type, and d) P3-type stacking. The blue and yellow balls represent the transition metal and  $\text{Na}^+$  ions in the O-type frameworks, respectively. Adapted from reference<sup>[26]</sup>.

### 1.3.4.2 Metal hexacyanoferrates

Prussian blue (PB) and its analogs (PBAs,  $A_2M[Fe(CN)_6]$ ,  $M = Fe, Co, Mn, Ni, Cu$ , etc.) are a large family of transition-metal hexacyanoferrates with an open framework structure, abundant redox-active sites, and strong structural stability.<sup>[38]</sup> Particularly, due to their large ionic channels and interstices in the lattice, PBs are one of the few host materials that can accommodate larger alkali cations, such as  $Na^+$  and  $K^+$  ions, for a fast and efficient reversible insertion reactions. Benefiting from this structural feature, PB compounds have been intensively investigated as a new alternative and low-cost Na-insertion cathode during the past five years.

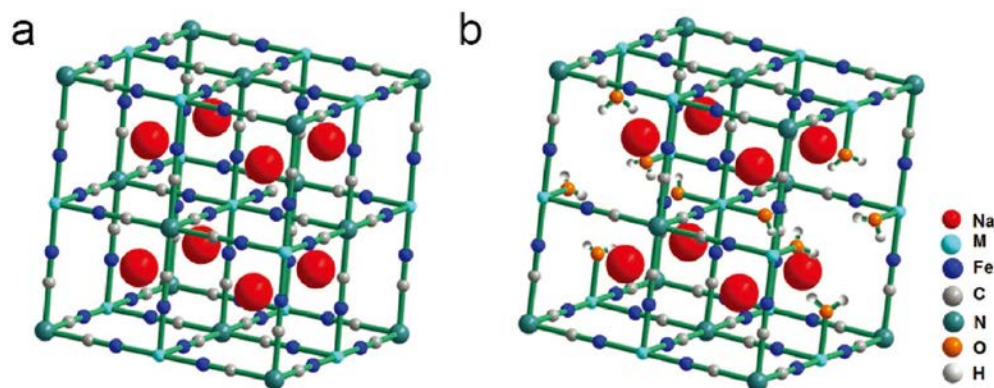


**Figure 1-5.** The schematic crystal structures of Prussian blue frameworks: a) an intact  $Na_2M_{II}[Fe_{II}(CN)_6]$  framework, b) a defective  $NaM_{II}[Fe_{II}(CN)_6]_{0.75}\square_{0.25}$  framework with 25%  $Fe(CN)_6$  vacancies existing in each unit cell. Adapted from reference<sup>[38]</sup>.

### 1.3.4.3 Polyanionic compounds

By definition, polyanion-type electrode materials are a type of compounds that contain a series of tetrahedral anionic units  $(XO_4)^{n-}$  or their derivatives  $(X_mO_{3m+1})^{n-}$  ( $X = S, P, Si, As, Mo, \text{ or } W$ ) connected with strong covalent-bonded  $MO_x$  polyhedra ( $M$  represents a transition metal).<sup>[39]</sup> In most of the polyanion-type compounds, the polyanionic unit not only allows for fast ion conduction within the open framework, but also stabilizes the operative redox potentials of the comprised transition metals. Such a special connection results in a high structural stability also upon sodium ion insertion and extraction. Compared to layered oxides the strong X-O bonding in polyanion-type compounds can introduce ionicity in M-O bonding and the weaker ionic bonding in M-O increases the distance between its antibonding orbitals vis-à-vis the  $A/A^+$  redox couple, leading to a higher redox potential. This is called the “inductive effect” in polyanion-type electrode materials. Furthermore, the strong X-O covalent bonds greatly improve the stability of O in the

lattice, thus increasing the safety of such materials, which make them very appealing for application in rechargeable batteries.

## 1.4 Polyanionic Cathodes for Sodium-ion Batteries

### 1.4.1 Single Polyanion Group

Single polyanionic frameworks, consisting of only one kind of polyanionic groups, such as  $(\text{SO}_4)^{2-}$ ,  $(\text{PO}_4)^{3-}$ ,  $(\text{P}_2\text{O}_7)^{4-}$ , and  $(\text{SiO}_4)^{4-}$ , have been widely investigated as electrode active materials in SIBs. In fact, a rather “simple” structure,  $\text{A}_x\text{M}(\text{XO}_4)$ , has shown promising performance in batteries.<sup>[40]</sup> More complex structures, including different polyanionic groups and different transition metal redox centers generally allow for tuning and further optimization of the electrochemical properties.

### 1.4.2 Mixed Polyanion Groups

Along with the development of single polyanionic compounds, the mixed polyanion concept comes from the idea of tuning the redox couples in NASICON structured materials by anionic substitution, which was firstly introduced by Goodenough et al. in 1998.<sup>[41]</sup> More recently theoretical studies predicted that the combination of  $\text{YO}_3^{2 \text{ or } 3-}$  and  $\text{XO}_4^{3 \text{ or } 4-}$  ( $\text{Y} = \text{C}, \text{B}$ ;  $\text{X} = \text{Si}, \text{As}, \text{P}$ ) could give a series of new  $\text{A}_x\text{M}(\text{YO}_3)(\text{XO}_4)$  compounds ( $\text{A} = \text{Li}, \text{Na}$ ;  $\text{M} = \text{a redox transition metal}$ ; and  $x = 0-3$ ) suitable for use as cathode materials.<sup>[42]</sup> The existence of a continuous, wide compositional domain in a mixed-polyanion system will significantly enrich material design strategies and contribute to the development of new cathode materials for SIBs.

### 1.4.3 Phosphate Polyanions

Phosphate framework-based materials have attracted increasing attention due to their excellent electrochemical performance and versatile structure. Accordingly, they are considered as promising Na storage electrodes – not least based on the following considerations: (i) Phosphate frameworks have high structural stability due to the very stable P-O bond, thus ensuring long-term cycling and enhanced safety content; the thermal properties of phosphate materials are linked directly to the stability of the phosphate-metal bonds, which greatly reduce the likelihood of oxygen release from the structure; (ii) the 3D framework possesses many (and rather large) interstitial sites, hence leading to lower volumetric expansion during Na ion insertion/extraction, which benefits the structural stability; (iii) phosphate or other substituent groups exhibit an



inductive effect on the redox couple, thus enabling higher redox potential values vs. Na/Na<sup>+</sup>. Phosphate framework materials exhibit a very versatile and adjustable structure reflected in a variety of electrochemical responses. Examples include phosphates, pyrophosphates, mixed anions, and materials with various redox centers (Fe, V, Mn, Ni, Co, et al.). Up to now, diverse phosphate-based polyanionic frameworks can be realized by (i) edge/corner sharing coordination of simple PO<sub>4</sub><sup>3-</sup> units, (ii) multiple PO<sub>4</sub><sup>3-</sup> units forming metaphosphates and pyrophosphates, (iii) the combination of mixed polyanions (e.g., PO<sub>4</sub>-P<sub>2</sub>O<sub>7</sub>) and (iv) the combination of PO<sub>4</sub><sup>3-</sup> units with other anions (e.g., F<sup>-</sup>, OH<sup>-</sup>, N<sup>3-</sup>). However, the olivine-type structured NaMPO<sub>4</sub>, as the analogue of LiMPO<sub>4</sub>, is not thermodynamically stable and crystallizes in the maricite phase when prepared by solid-state synthesis procedure. As one of the most typical representatives of phosphate-based polyanionic compounds, pyrophosphate-structured compounds like Na<sub>2</sub>MP<sub>2</sub>O<sub>7</sub> and NASICON-structured Na<sub>x</sub>M<sub>2</sub>(PO<sub>4</sub>)<sub>3</sub> (M = a transition metal) represent the most investigated compounds for application in SIBs.

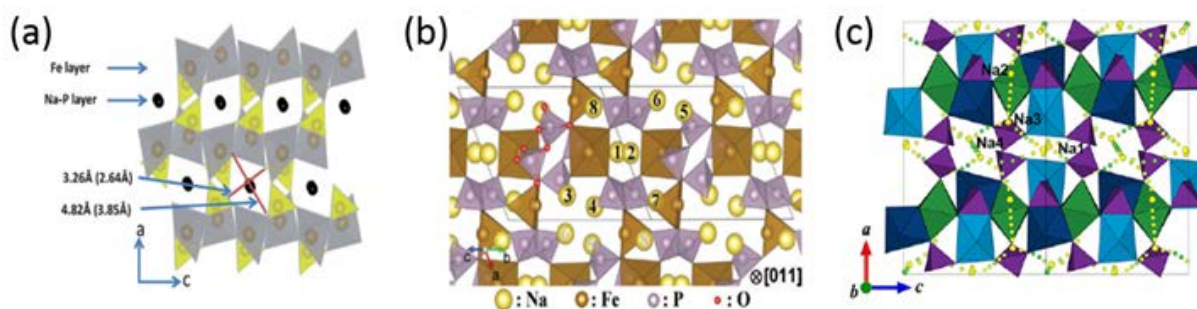


**Figure 1-6.** Crystal structure of (a) NaFePO<sub>4</sub> and (b) Na<sub>2</sub>FeP<sub>2</sub>O<sub>7</sub>, c) Na<sub>4</sub>Fe<sub>3</sub>(PO<sub>4</sub>)<sub>2</sub>(P<sub>2</sub>O<sub>7</sub>). Adapted from references<sup>[43-45]</sup>.

## 1.5 Limits of Polyanionic Cathodes for Sodium-ion Batteries

### 1.5.1 Electronic Conductivity

Despite the several advantages above mentioned, one of the main disadvantages of polyanionic compounds is represented by their poor electronic conductivity, which limit and hinders their practical application. Indeed, the low conductivity significantly affects the reversible capacity and rate capability. Among the widely studied polyanionic compounds for application in SIBs, the most promising materials are certainly represented by vanadium-based phosphates and fluorophosphates due to their relatively high theoretical energy density conferred by the relatively high working voltage and the satisfactory theoretical specific capacity. However, the theoretical

capacity can hardly be achieved due to the poor electronic conductivity of the pristine compounds. Moreover, the sluggish kinetics resulting from poor electron conduction and Na diffusion generally reduce the rate capability and cycling stability. Hence, an improvement of the electronic conductivity of would significantly affect the overall performance of the polyanionic cathodes.

### 1.5.2 Specific Capacity

Generally, the determining factors for the theoretical capacity are the available spaces to accommodate ions, the ability to change the valence state of the redox couple involved in the de-sodiation process and the degree of reversibility of the underlying reactions. A significant breakthrough in the energy density of sodium-ion cells may be achieved by employing high capacity electrode materials for both cathodes and anodes. Accordingly, the exploration of high specific capacity polyanionic cathode represents an important direction for the realization of high energy density SIBs. The specific capacity referred as the ability of store ions can be tuned by making the mass (or volume) of the active materials per exchanged electron as small as possible, resulting in maximized gravimetric and volumetric capacity.

### 1.5.3 Working Voltage

The working potential of the cathode plays a significant role for the improvement of the cell voltage. Currently, cathode materials show specific capacities of 120–200 mA h g<sup>-1</sup> and operating potentials of 2.6–3.5 V (much lower than the oxidation potential of electrolytes, >4.0 V). In order to boost the energy density of SIBs, cathode materials with higher working voltage are required.

### 1.5.4 Structural Stability

Although polyanionic compounds are characterized by an improved structural stability compared to layered oxides, further improvement is desired for the achievement of long lasting SIBs. When a battery is charged, the ion concentration in the cathode decreases (de-sodiation) and the vacancy concentration increases. At very low sodium content, the cathode's crystal structure may become no longer thermodynamically stable, thus leading to unfavorable phase transitions or cathode degradation. For this reasons a rational design of the structural parameters of cathode materials is fundamental for the obtainment of long cycle life cathode materials.

### 1.5.5 Strategies for the Materials Optimization

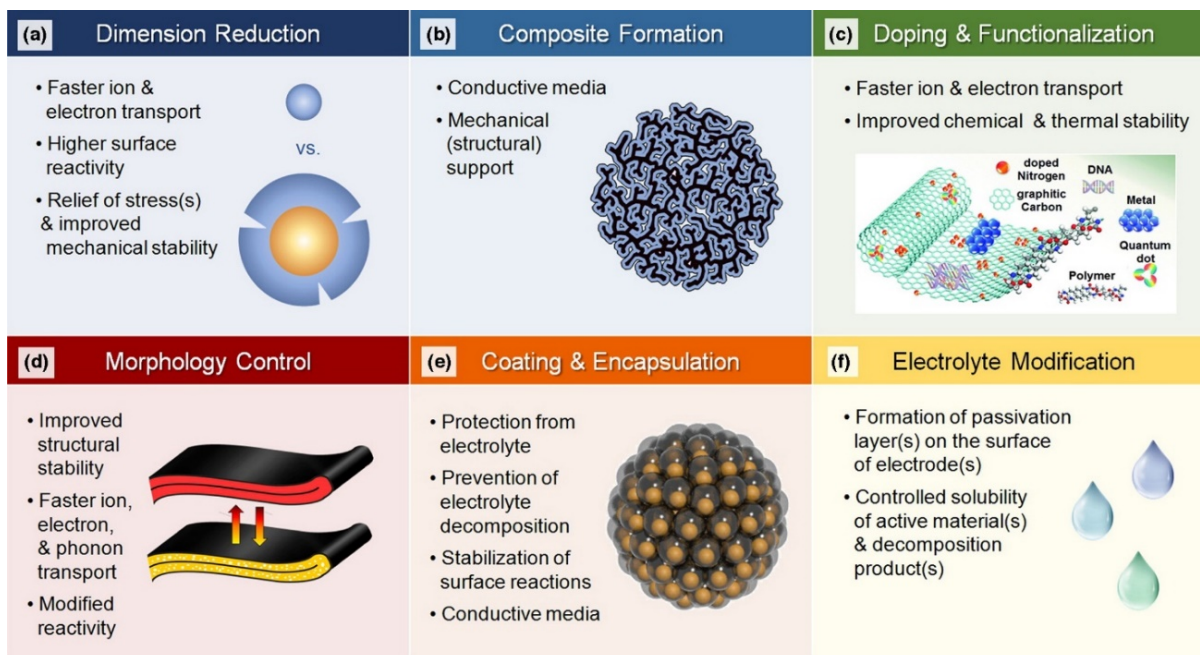


**Figure 1-7.** General strategies for performance enhancement and their rationale. Adapted from reference<sup>[46]</sup>.

Based on the above mentioned considerations, the optimization of existing cathode materials as well as the exploration of new materials is a fundamental ongoing process in search of the next generation high performance cathode materials. Despite the several advantages presented by polyanionic compounds, several issues still need to be addressed before their commercialization as cathode materials for application in SIBs. Materials' optimization and design provide the strategies for performance improvements in terms of structural stability, cycling stability and electrochemical performance in terms of energy density. To meet the cycling stability and rate capability requirements, carbon coatings and particle size and morphology control through specific synthesis conditions have shown promising results toward performance improvements by reducing the  $\text{Na}^+$  diffusion length and facilitating the electron conduction. As indicated in **Figure 1-7**, there are several strategies for the performance enhancement of polyanionic cathodes. In addition of the improvement of the active material, the optimization of the electrolyte system has a great impact on the electrochemical performance, e.g., by forming suitable passivation layers on the electrode surface and limiting the solubility of the active material upon cycling.

### 1.5.6 Strategies for the Materials Design

To design new polyanionic frameworks, enabling high energy density SIBs, an enhancement of the provided capacity and increase of the operational potential is essential. The theoretical

capacity of the materials for the sodium storage is related to the specific amount of charges involved in electrochemical reaction. A multi-electron redox process with the insertion/extraction of more than one sodium ion per transition metal ion is preferred, especially as heavy inactive counter cations (P, S, Si, Wo, etc.) decrease the specific capacity and energy. By using lighter polyanionic units with the same transition metal redox center, the specific capacity may be highly improved. For example, borates contain the lightest polyanionic units ( $\text{BO}_3$ ) and, thus, have a higher theoretical capacity ( $\sim 200 \text{ mA h g}^{-1}$ ) than  $\text{LiFePO}_4$  ( $\sim 170 \text{ mA h g}^{-1}$ ). The theoretically specific capacity ( $Q_{\text{th}}$ ) of the electrode materials can be calculated according to the following equation, known as Faraday's law (1-1):

$$Q_{\text{th}}(\text{mA h g}^{-1}) = \frac{n \cdot F}{3.6 \cdot M} \quad (1-1)$$

where  $n$  is the number of electrons involved in the electrochemical reaction;  $F$  is the Faraday constant ( $96485 \text{ C/mol}$ ) and  $M$  is the molecular weight of the compound.

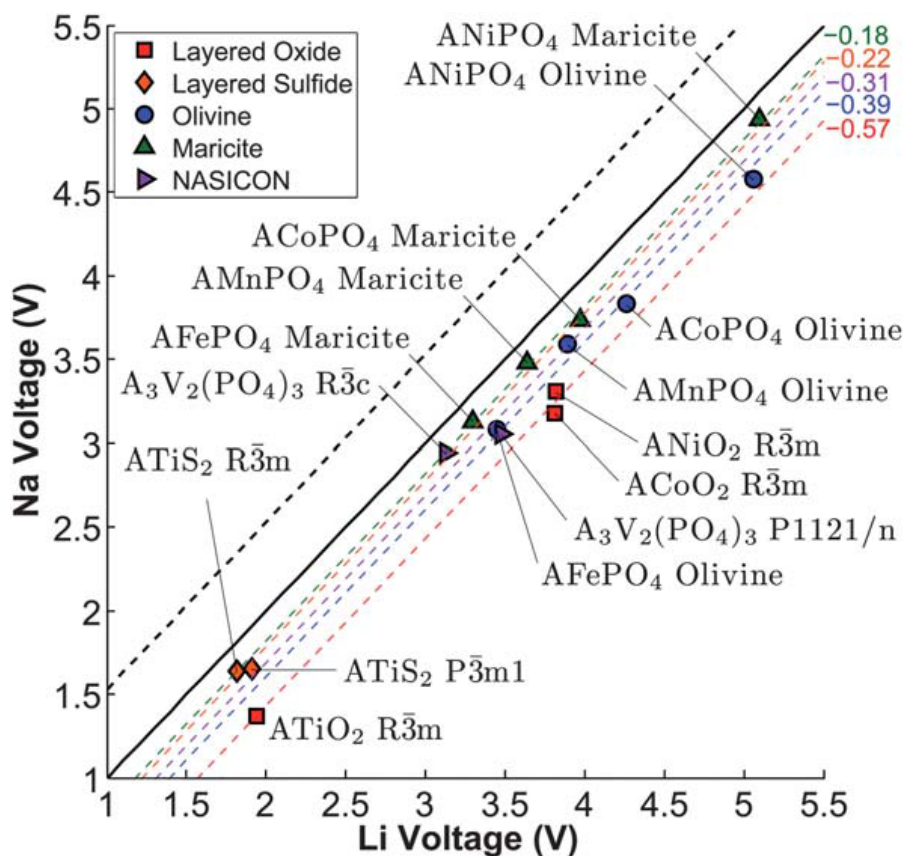


**Figure 1-8.** Calculated Na voltage vs. Li voltage for different structures. Adapted from reference<sup>[47]</sup>.

To achieve a high cell voltage, a high-voltage cathode is required. There are two general approaches for the material design in this case. The first one consist in the choice of a high potential transition metals as the redox center. As shown in **Figure 1-8**, the working voltage depends on the A/A<sup>+</sup> redox couple of the redox active (transition) metal. The second one involves some considerations on the aforementioned inductive effect, which further increases the operational potential. The inductive effect comes into play when another atom X is introduced to form M-O-X bonds. If X has a higher electronegativity than M, the covalency between M-O will be lowered, which will lead to higher potential. According to Pauling's electronegativity values, SO<sub>4</sub>-based compounds would theoretically offer the highest possible redox potential in isostructural polyanionic frameworks.

## 1.6 Synthesis Method and Characterization Techniques

### 1.6.1 Synthesis Method: Solid State Synthesis

The most common synthesis route for cathode materials is the solid state approach. In this method, the precursors' powders are mixed and intimately ground to guarantee a very-fine homogenized final powder. The step is conducted either by hands in a mortar or by mechanical milling. Following a high-temperature treatment is conducted to enable the reactions between the mixed precursors to finally form a thermodynamically stable ceramic (quenching strategies may be applied at the end of the thermal treatment to ensure freezing of the final thermodynamic phase). The feasibility of the solid-state approach for the obtainment of polyanionic cathodes strongly depends on the specific anion chemistry and stability of the final products. In general, due to the strength of the P-O bond, the phosphate-based polyanions can be easily synthesized by solid state method. It is worth mentioning that the obtainment of the crystal structure does not always reflect in the obtainment of electrochemical active materials. Indeed, as an example, direct high-temperature synthesis generally produces olivine-type NaFePO<sub>4</sub> but usually leads to the formation of the thermodynamically favored maricite phase, which exhibits poor electrochemical activity because of its one-dimensional edge-sharing FeO<sub>6</sub> octahedrons, which hinders Na-ions migration (see **Figure 1-6**). In this thesis work, all the materials investigated have been synthesized via solid-state method.

### 1.6.2 Materials Characterization

#### *1.6.2.1 X-ray powder diffraction*

X-ray powder diffraction (XRD) is an analytical technique used for the determination of the structural properties of crystalline materials. The development of this technique as well as the introduction of the Rietveld method, which uses a least squares approach to refine a theoretical diffraction spectrum until it matches the experimental one, allow for an accurate determination of the structural information of the investigated compound. For known compounds, primary reference XRD patterns are available from the Joint Committee on Powder Diffraction Standards (JCPDS) to qualitatively verify the successful synthesis of the materials. For new materials, the Rietveld method is generally used to refine the crystal parameters such as atomic positions and sites, occupancy, lattice parameters, crystallite size, preferred orientation or the ratio of different phases, etc.

#### *1.6.2.2 X-ray photoelectron spectroscopy*

X-ray photoelectron spectroscopy (XPS) is a surface-sensitive, quantitative spectroscopic technique which can measure the elemental composition, chemical state and electronic state of the elements with a sampling depth ranging from 1 to 10 nm. XPS spectra are obtained by irradiating a material with an X-ray beam, while simultaneously measuring the kinetic energy and number of electrons that escape from the material studied. Carbon materials exhibit full  $sp^2$  or  $sp^3$  hybridization or a combination in its typical structure. However, it also may be hybridized by O, S, N heteroatoms in different ratios. XPS is one of the most efficient techniques for studying the elemental compositions and in particular for the distribution and bonding of heteroatom dopants in carbon materials.

#### *1.6.2.3 Raman spectroscopy*

Raman spectroscopy is one of the vibrational spectroscopic techniques used to provide information on molecular vibrations and crystal structures. This technique uses a laser light source to irradiate a sample, which upon contact with the sample generates an infinitesimal amount of Raman scattered light, which is detected as a Raman spectrum. The characteristic fingerprint patterns in a Raman spectrum can be used to identify the chemical nature and structure of Raman-active substances, including polymorphs, and to evaluate local crystallinity, orientation and stress. Here, Raman was used to identify graphite, and disorder in graphitic-carbon materials, including carbon-containing composites.

#### *1.6.2.4 Thermogravimetric analysis*

Thermogravimetric analysis (TGA) is a method of thermal analysis in which the loss of mass of a sample is measured over time as the temperature changes. This measurement provides

information about physical phenomena, as well as chemical phenomena including chemisorptions, thermal decomposition, and solid-gas reactions (e.g., oxidation or reduction). In general, TGA is commonly used to evaluate the thermal stability and to detect the oxidative mass losses of a material.

#### *1.6.2.5 Electron microscopy*

An electron microscope is a microscope that uses an accelerated electron beam as a source to characterize the morphology of materials. As the wavelength of an electron can be up to 100,000 times shorter than that of visible light photons, electron microscopes have a higher resolving power than light microscopes and can reveal the structure of smaller objects. Scanning electron microscopy (SEM) produces images by probing the specimen with a focused electron beam that is scanned across the specimen in a raster pattern. Secondary electrons from inelastic scattering provide information on the morphology and particle size of the sample. The characteristic X-rays collected is used to further semi-quantitatively determine the elemental compositions – commonly referred to as energy-dispersive X-ray spectroscopy (EDX). A transmission electron microscope (TEM) applies higher accelerating voltages for the electron beam to study the specimen. Transmitted electrons go through the specimen and thus additionally provide information about the structure which is magnified by the objective lens system of the microscope to create an image.

#### *1.6.2.6 Nitrogen absorption and desorption*

Surface area and porosity are two important physical properties of electrode materials that impact the electrochemical performance in the cell. Gas absorption/desorption analysis is commonly used for surface area and porosity measurements. This involves exposing solid materials to gases or vapors at a variety of conditions and evaluating either the weight uptake or the sample volume. Analysis of these data provides information regarding the physical characteristics of the solid including: skeletal density, porosity, total pore volume, and pore size distribution. The Brunauer, Emmett and Teller (BET) technique is the most common method for determining the surface area of powders and porous materials. Nitrogen is usually used as the gas to be adsorbed, as it is widely available in highly pure state and interacts with most of the solids. The surface area of the solid is evaluated from the measured monolayer capacity and knowledge of the cross-sectional area of the molecule being used as a probe. For the case of nitrogen, the cross-sectional area is taken as 16.2 Å<sup>2</sup>/molecule.

### 1.6.3 Electrochemical Characterization of Electrodes

#### 1.6.3.1 Cell configurations

To electrochemically characterize the cathode materials herein synthesized, composite electrode films are used. These are generally made using a doctor-blade or dry-rolling method and tested in two- or three-electrode electrochemical cells. The detailed structures of a typical coin cell and T-cell, as used in this thesis, are presented in **Figure 1-9**.

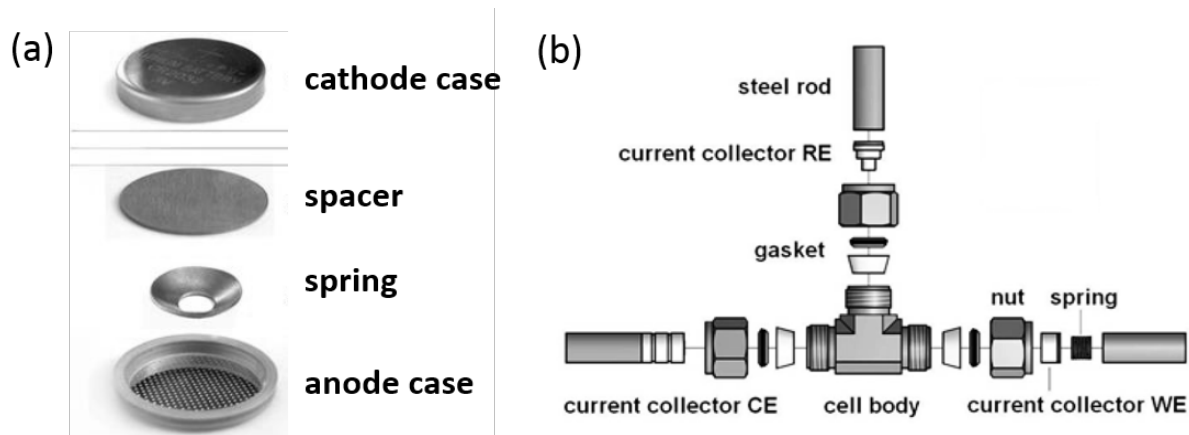


**Figure 1-9.** (a) Coin cell structures and (b) T-cell structures.

#### 1.6.3.2 Cyclic voltammetry

Cyclic voltammetry (CV) is a controlled potential dynamic technique in which a linear potential sweep is applied between the working and reference electrode in an electrochemical cell and the evolving current between the working and the counter electrode is measured. Commonly, the current is plotted versus the applied voltage to give the cyclic voltammogram trace, which reflects the redox processes occurring at the working electrode.

#### 1.6.3.3 Chronoamperometry

Chronoamperometry is a standard electrochemical technique to test the performance and cycling stability of electrodes in half- and full-cell configuration. A controlled current is applied to the cell while the potential response in dependence of the time is recorded. In a three electrode cell the constant current is applied between the counter electrode and the working electrode while the potential is measured by the reference electrode. Once a certain fixed potential (cut-off voltage) is reached, the applied current is inverted inducing the occurrence of the reversed electrochemical process. Generally, batteries are charged and discharged at a constant referred as C-rate and calculated based on the theoretical capacity of the electrode(s). Indeed, the capacity of a battery



is generally rated as 1C, which means that a fully charged battery rated at 1Ah should provide 1A in one hour.

#### 1.6.3.4 Electrochemical impedance spectroscopy

Electrochemical Impedance Spectroscopy (EIS) is a technique to measure the dielectric properties of a medium as a function of frequency. It is usually determined by applying an AC potential to an electrochemical cell and then measuring the evolving current, or vice versa. The impedance at a given frequency is related to processes occurring at timescales of the inverse frequency (e.g.,  $f=10$  Hz,  $t=0.1$  s). In a battery, EIS has been demonstrated to be a useful tool for the study of the charge transfer and transport processes, as well as for the characterization of cell materials and components – for instance, to determine the electronic or ionic conductivity.

### 1.6.4 Ex situ and in situ Analysis Techniques for Electrode Materials

The *ex situ* analysis of cycled electrodes is a powerful method to provide insights into the structural and morphological evolution of the active material and electrode after cycling, by enabling an in depth understanding of the battery failure mechanisms and the materials degradation processes upon cycling. However, despite the meaningful information that *ex-situ* analysis can deliver, it is worth mentioning that the reliability of the obtained results strongly depends on the experimental conditions, such as the electrode washing procedure and the potential contaminations occurring during sample preparation and analysis.

Over the years, several state-of-the-art *in situ* and *operando* analysis techniques have been developed to understand how the electrochemical processes affect the individual battery components under real operating conditions.<sup>[48]</sup> *In situ* surface- and bulk- techniques have been widely applied to identify the material' structural and morphological evolutions through the development of customized electrochemical cells for different radiation sources. *In situ* X-ray-based analysis, for instance, provides significant insights into the structural changes correlated to the observed electrochemical processes. In this technique, an electrochemical cell is cycled while diffraction patterns of the electrode active material are simultaneously collected for varying states of charge and discharge. Thus, real-time changes of the lattice parameters and crystalline structure during electrochemical cycling are observed during operation.

## 1.7 Thesis Overview

This thesis focuses on the development and study of phosphate-based polyanionic compounds as cathode materials for SIB application. Several strategies are considered to address the limits of

these materials. In the following sections, the synthesis, structure and electrochemical performance of various electrode materials – together with the investigation of suitable electrolyte systems – is provided. An improved understanding of the structure-function correlation of these materials is given. In addition, their electrochemical optimization and, more generally, potential strategies for the design of future sodium-ion batteries are described.

Specifically, Chapter 2 presents the synthesis method and the structural and electrochemical investigation of NASICON-structured sodium vanadium phosphate materials as sodium-ion cathodes. Downsizing and functional carbon coating strategies are adopted to improve their performance. A nitrogen-doped carbon coating has shown particular improvement and its effect on the structure and electrochemical performance are reported.

Chapter 3 describes the approach to synthesize new polyanionic cathodes with a high operating voltage. The use of the Ni redox activity in mixed polyanionic structures and the combination of highly electronegative polyanionic groups, such as  $(\text{PO}_3)_3\text{N}$ , are explored with the target to increase the working potential. The resulting structure-performance relations during sodium insertion/extraction are discussed.

Chapter 4 demonstrates the investigation of full sodium-ion batteries based on NASICON electrodes in non-aqueous and aqueous electrolyte systems. The  $\text{Na}_2\text{VTi}(\text{PO}_4)_3//\text{Na}_2\text{VTi}(\text{PO}_4)_3$  and  $\text{NaTi}_2(\text{PO}_4)_3//\text{Na}_3\text{V}_2(\text{PO}_4)_3$  configurations are fabricated in lab-scale prototypes.

Chapter 5 concludes the thesis.

# Chapter 2

## Sodium Vanadium Phosphates as Cathodes in Sodium-ion Batteries

The results in this chapter are partially published in the following publications:

1. **Zhang, H.;** Hasa, I.; Buchholz, D.; Qin, B.; Passerini, S., Effects of Nitrogen Doping on the Structure and Performance of Carbon Coated  $\text{Na}_3\text{V}_2(\text{PO}_4)_3$  Cathodes for Sodium-ion Batteries. *Carbon* 2017, 124, 334-341.
2. **Zhang, H.;** Hasa, I.; Qin, B.; Diemant, T.; Buchholz, D.; Behm, R. J.; Passerini, S., Excellent Cycling Stability and Superior Rate Capability of  $\text{Na}_3\text{V}_2(\text{PO}_4)_3$  Cathodes Enabled by Nitrogen-Doped Carbon Interpenetration for Sodium-ion Batteries. *ChemElectroChem* 2017, 4 (5), 1256-1263.

## 2.1 Structure and Electrochemical Properties of Nitrogen-doped Carbon Coated $\text{Na}_3\text{V}_2(\text{PO}_4)_3$ Cathode

### 2.1.1 Introduction

In the process of exploring an ideal cathode for sodium-ion batteries, much interest centers on polyanionic compounds. The NASICON structured  $\text{Na}_3\text{V}_2(\text{PO}_4)_3$  (NVP) shows a theoretical specific energy of 400 Wh/kg (117.6 mAh/g and 3.4 V vs.  $\text{Na}^+/\text{Na}$  with  $\text{V}^{3+}/\text{V}^{4+}$  redox couple) and superior thermal stability which make it as a promising candidate cathode.<sup>[40, 49]</sup> However, owing to the insulating nature of the material as well as the large ionic radius of  $\text{Na}^+$  and significant kinetic barrier to  $\text{Na}^+$  transport, a limit for durability and rate-capability has been proved as an intrinsic barrier for the production in large-scale.<sup>[50]</sup> One approach to overcoming this is to alter the inherent conductivity by lattice doping. Practically, Mg,<sup>[51]</sup> Cr,<sup>[52]</sup> Mn,<sup>[53]</sup> and B<sup>[54]</sup> dopants have been proved to be beneficial to the electrochemical performance, leading to lower internal resistance and favorable electrode-electrolyte interface. Moreover, carbon has been widely explored as conductivity contributor and templates as well.<sup>[55-57]</sup> Among these, the NVP particles embedded in hierarchical carbon frameworks exhibit superior rate capability and cycling performance, attributed to the conductive carbon skeletons and nanoconfined NVP particles.<sup>[58-61]</sup> This provision of efficient electron and ion transport is a critical issue in advancing the NVP materials as practical cathodes for sodium-ion batteries.

As an important group of carbon derivatives, nitrogen-doped carbon with lattice defects and surface functionalities shows extraordinary interfacial properties with the electrolyte which has already been demonstrated for electro-catalysts and supercapacitor electrodes.<sup>[62-64]</sup> Furthermore, it can also be an intriguing coating material for electronically insulating electrodes materials in batteries. For example, Hu et al. utilized N-containing ionic liquids as precursors to synthesize the N-C coated  $\text{Li}_4\text{Ti}_5\text{O}_{12}$  materials which exhibited superior rate capability and excellent cycling performance in lithium-ion batteries. Both the experimental and theoretical investigations demonstrated that the N-doped carbon coating can strongly improve the interfacial stability and electric conductivity, which is extremely beneficial for the electrochemical performance.<sup>[65, 66]</sup> Accordingly, the N-doped carbon has already been used to improve the performance of NVP materials and, indeed, the N-doped carbon from pyrolyzing the N-contained polymer or biomolecules was found to efficiently improve the stability and reversibility of NVP cathodes.<sup>[67-69]</sup> However, the impact of the N-doping on the structure of carbon layer as well as the electrochemical properties of NVP electrodes is still not fully understood.

In this work, we propose a simple approach to control the preparation of N-doped carbon coated NVP materials with various nitrogen contents. Furthermore, we demonstrate how the structural and electrochemical properties of N-doped carbon coated NVP materials are affected by the presence of N in the carbon layer.

## 2.1.2 Experimental Methods

### 2.1.2.1 Materials synthesis

Stoichiometric amounts of  $\text{CH}_3\text{COONa}\cdot 3\text{H}_2\text{O}$  (VWR,  $\geq 99\%$ ),  $\text{VO}(\text{C}_5\text{H}_7\text{O}_2)_2$  (Acros Organics,  $\geq 99\%$ ),  $\text{NH}_4\text{H}_2\text{PO}_4$  (Alfa Aesar,  $\geq 99\%$ ),  $\text{C}_6\text{H}_8\text{O}_7\cdot \text{H}_2\text{O}$  (Alfa Aesar,  $\geq 99\%$ ), and  $\text{C}_3\text{H}_6\text{N}_6$  (Sigma Aldrich,  $\geq 99\%$ ) were ball-milled in acetone for 8 h and ground after drying at ambient temperature to obtain the precursors. The final products were obtained by pre-heating the precursors at  $300\text{ }^\circ\text{C}$  for 4 h and final sintering at  $800\text{ }^\circ\text{C}$  for 8 h under Ar atmosphere in a tube furnace. For the purpose of comparison, NVP/ONC, NVP/6.7NC and NVP/10.8NC with different nitrogen content (0%, 6.7%, and 10.8%) were prepared by controlling the amount of added melamine precursor (weight ratio of melamine to citric acid is 0:3 for NVP/ONC, 1:3 for NVP/6.7NC and 2:3 for NVP/10.8NC).

### 2.1.2.2 Materials characterization

X-ray diffraction analysis was performed in Bragg-Brentano geometry using a Bruker D8 Advance diffractometer (Bruker, Germany). All diffractograms were recorded with  $\text{Cu K}\alpha$  radiation ( $\lambda = 0.154\text{ nm}$ ) in the  $2\theta$  range of  $10^\circ - 70^\circ$  with a step size of  $0.01^\circ$  and step time of 0.5 s. Morphological characterization was conducted on ZEISS 1550VP Field Emission SEM (Carl Zeiss, Germany). Thermal gravimetric analysis (TGA) was determined by a thermogravimetric analyzer (TGA-209F, Netzsch, Germany). Raman spectra were collected using a Renishaw 2000 system (Renishaw, United Kingdom) with a He-Ne laser (633 nm) and charge-coupled device detector. Spectra were collected using the extended scanning mode from  $880$  to  $1964\text{ cm}^{-1}$  and 10 s accumulation time, with the single scan over the desired range taking 1 min to collect. XPS measurements were performed using a PHI 5800 Multi Technique ESCA system (Physical Electronic, USA). The spectra were acquired using monochromatic  $\text{Al K}\alpha$  ( $1486.6\text{ eV}$ ) radiation. The  $\text{C}1\text{s}$  line with a binding energy of  $284.8\text{ eV}$  was used as reference.

### 2.1.2.3 Electrochemical measurements

The electrochemical tests were performed using Swagelok-type cells assembled in an argon-filled glove box with  $\text{H}_2\text{O}$  and  $\text{O}_2$  contents lower than 1 ppm. Sodium half-cells were assembled by using

glass fiber (Whatman) as separators, 1M NaPF<sub>6</sub> (Alfa Aesar, 99%) in propylene carbonate (PC) with 2 wt.% fluoroethylene carbonate (FEC) (BASF, Battery Grade) as electrolyte and sodium metal (99.8%, Acros Organics) as both counter and reference electrodes. The working electrodes were prepared by doctor-blade casting a slurry with 80 wt.% of active material, 10 wt.% of carbon black (Super C65, IMERYS) and 10 wt.% of polyvinylidene fluoride (6020 Solef, Solvay Group) in N-methyl-2-pyrrolidone (anhydrous, Sigma-Aldrich) on Al foil as current collector. After drying, electrodes with a diameter of 12 mm were punched, pressed and dried at 120 °C under high vacuum. The average active material mass loading is ~3.0 mg cm<sup>-2</sup>. A Maccor 4000 Battery system (Maccor, USA) was used for the galvanostatic charge/discharge test. Cyclic voltammetry was performed on a multichannel potentiostat/galvanostat (VMP2, Biologic Science Instruments, France). Symmetric cells with two identical NVP electrodes were configured in two cathode-cells for the impedance investigation. The AC impedance spectra were obtained at discharged state (1.0 V vs. Na<sup>+</sup>/Na) after a potentiostatic step for 30 min at 1.0 V with an AC oscillation of 10 mV amplitude over the frequencies from 1 MHz to 10 mHz using a multichannel potentiostat/galvanostat (VMP3, Biologic Science Instruments, France). All measurements were performed in climatic chambers at 20 ± 1 °C.

### 2.1.3 Results and Discussion

In order to investigate the effect of nitrogen on the structure and morphology of the prepared NVP/C materials, pristine carbon coated NVP and N-doped carbon coated NVP with various nitrogen contents were synthesized under the same conditions. The XRD patterns of prepared NVP materials with various N-doped carbon coatings are presented in **Figure 2-1a** compared with pristine NVP/C. As shown, the NVP/0NC, NVP/6.7NC and NVP/10.8NC composites can be indexed to a rhombohedral NASICON structure (JCPDS No. 01-078-7289) with space group of *R-3c*, which is consistent with previous reports.<sup>[70]</sup> It is noteworthy that impurity phases are present in the NVP/N-C sample (a weight ratio of melamine to citric acid 3:3), indicating that the overdose of melamine in the precursors adversely affects the crystallization of NVP and introduces the growth of impurities (see **Figure 2-1b**).

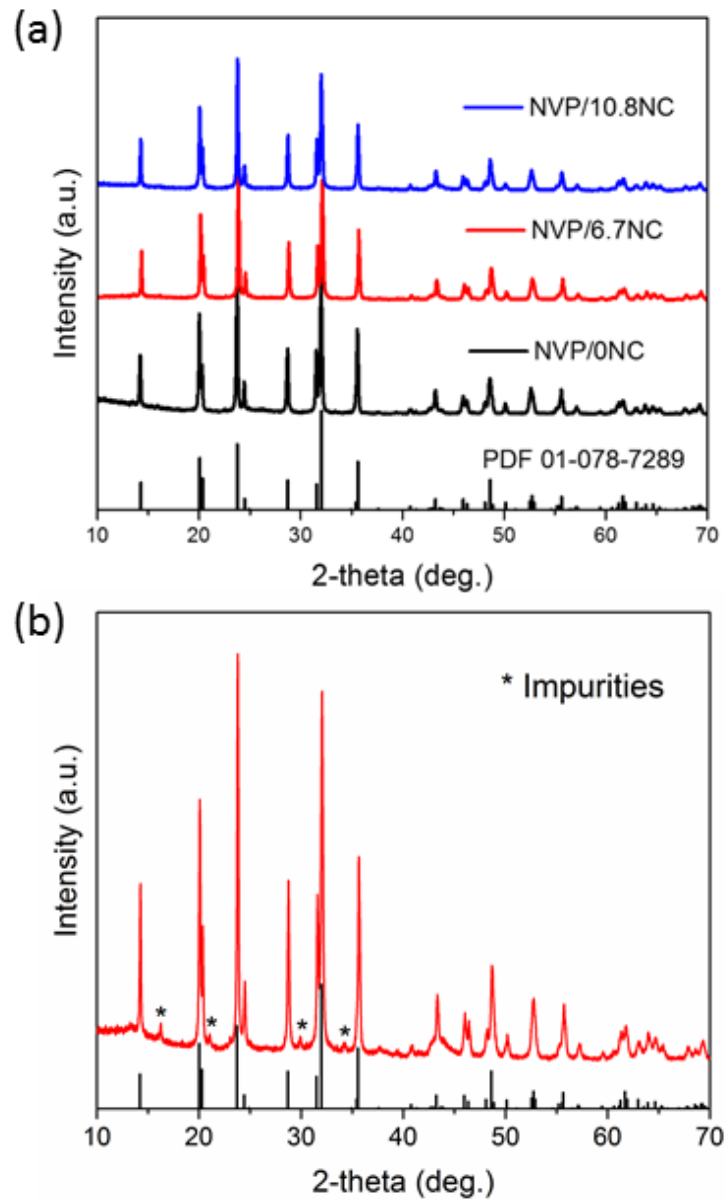


**Figure 2-1.** XRD patterns of (a) NVP/0NC, NVP/6.7NC and NVP/10.8NC composites and (b) NVP/NC composite (with an exceed melamine in weight ratio of melamine to citric acid 3:3).

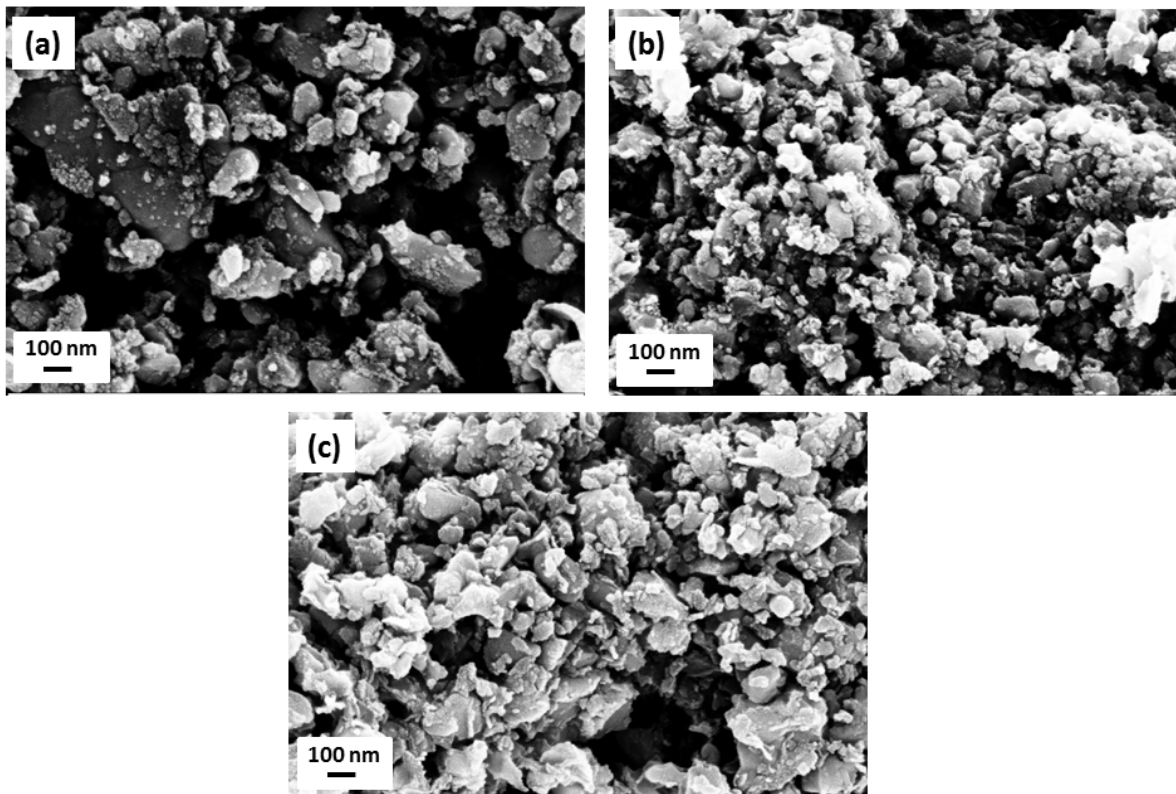


**Figure 2-2.** SEM images of (a) NVP/0NC, (b) NVP/6.7NC and (c) NVP/10.8NC.

The morphologies of prepared NVP/C powders were investigated by scanning electron microscopy (SEM). As shown in **Figure 2-2**, all pristine carbon and N-doped carbon coated NVP materials are composed of particles with irregular morphology. In addition, it is apparent that the introduction of melamine into the precursors reduces the particle size and leads to a more uniform morphology. To detect the carbon contents of these materials, thermogravimetric analysis (TGA) was performed (see **Figure 2-3**). The carbon contents are 6.4 wt.%, 5.2 wt.%, and 3.4 wt.% for NVP/0NC, NVP/6.7NC, and NVP/10.8NC, respectively. Apparently, the carbon content is reduced when more melamine is added, which can be attributed to the pyrolysis of melamine leading to the loss of carbon.



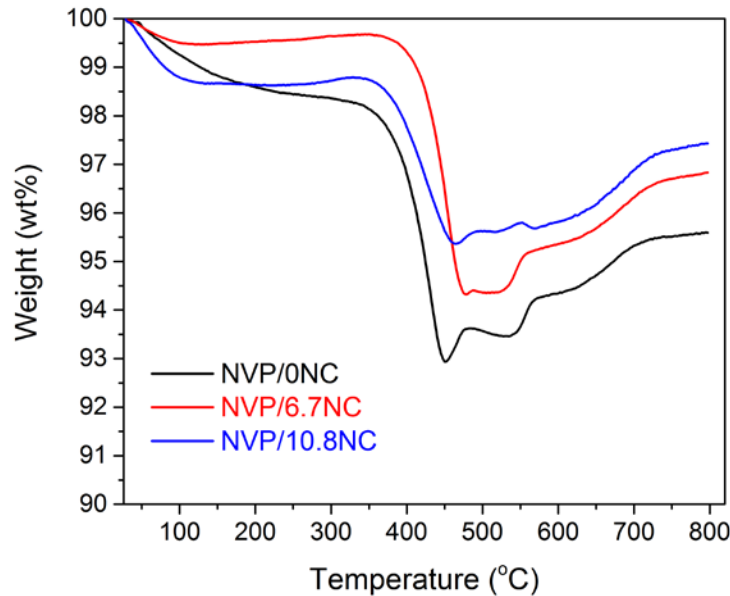


**Figure 2-3.** TGA curves of NVP/NC composite.

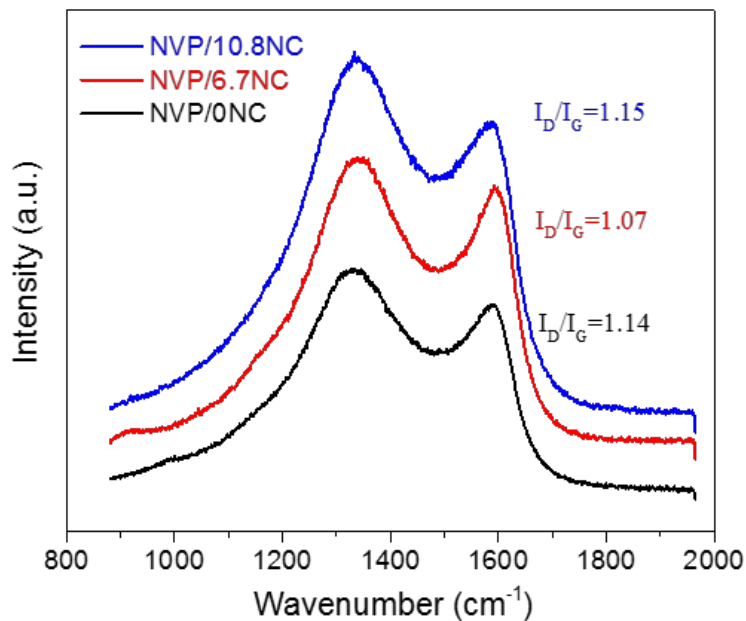


**Figure 2-4.** Raman spectra (a), normalized XPS C1s spectra (b) and high-resolution N1s spectra (c, d) for various NVP composites.

Raman spectroscopy is an efficient technique to detect the complete structural information for carbon materials.<sup>[71]</sup> The Raman spectra of NVP/0NC, NVP/6.7NC and NVP/10.8NC composites are displayed in **Figure 2-4**. All spectra present a D-band at 1357 cm<sup>-1</sup> and a G-band at 1593 cm<sup>-1</sup>, which are characteristic for carbon materials and are associated with defects and graphitic

carbon, respectively.<sup>[72]</sup> The  $I_D/I_G$  ratio is used as one parameter to evaluate the disorder of carbon materials. The value for pristine NVP/C is 1.14 and, interestingly, decreases to 1.07 for N doped NVP/6.7NC, which indicates that the appropriate amount of N-doping can improve the graphitization degree of carbon and, in consequence, enhance the electronic conductivity. However, with higher N- contents doped into the carbon lattice, the  $I_D/I_G$  ratio increases to 1.15 which is higher than those in NVP/ONC and NVP/6.7NC. This can be explained via the extrinsic defects on the surface of carbon.

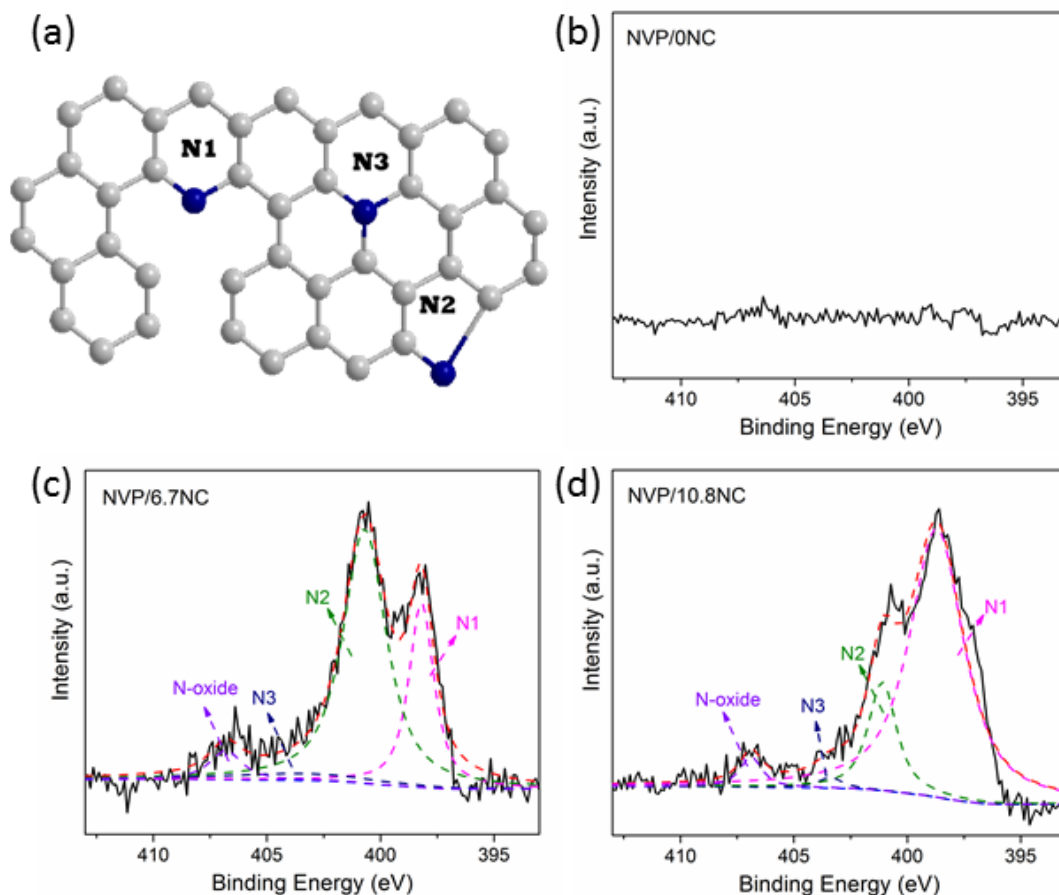


**Figure 2-5.** Normalized XPS C1s spectra (b) and high-resolution N1s spectra (c, d) for various NVP composites.

XPS measurements were used to confirm the coexistence of different chemical states of N in the carbon layer. No N is detected in the pristine NVP/C composite (**Figure 2-5b**). Moreover, the high-resolution N 1s spectra in **Figure 2-5c,d** can be fitted by four peaks which can be identified as chemisorbed nitrogen oxides (N-Ox) at 406.8 eV, quaternary nitrogen at 404.4 eV, pyrrolic nitrogen at 401.1 eV and pyridinic nitrogen at 398.7 eV, respectively.<sup>[67, 73]</sup> The ratios of different

N types in various NVP materials are shown in **Table 2-1**. Notably, the pyrrolic nitrogen (N2) is dominant in NVP/6.7NC. However, for NVP/10.8NC for which an increasing amount of melamine is used in the synthesis, both, the pyrrolic nitrogen and quaternary nitrogen contents, are reduced to relatively low values. In contrast, the pyridinic nitrogen is increased which corresponds to a higher amount of defects in NVP/10.8NC material and is consistent with Raman results. In consequence the higher the amount of melamine in the synthesis the higher is also the content of N doped into the carbon layer, as evidenced by the N/C- ratio which is increasing from 6.7% to 10.8% for NVP/6.7NC and NVP/10.8NC, respectively. These results indicate that the synthesis method proposed herein, is effective to control the amount of defects as well as nitrogen in the carbon layer, which is essential for materials design and optimization.

**Table 2-1.** Content of different N species in N-doped carbon coated NVP/6.7NC and NVP/10.8NC composites.

	NVP/6.7NC	NVP/10.8NC
<b>Pyridinic N1</b>	26.5%	78.6%
<b>Pyrrolic N2</b>	62.6%	16.5%
<b>Quaternary N3</b>	5.6%	1.4%
<b>N-oxide</b>	5.3%	3.5%
<b>N/C atomic ratio</b>	6.7%	10.8%

The electrochemical performance of NVP/ONC, NVP/6.7NC and NVP/10.8NC was systematically investigated in a three electrode Swagelok-type half-cell. **Figure 2-6a,b,c** show the initial charge/discharge curves of various NVP electrodes at 0.1 C, 0.5 C, 1 C, 5 C, 10 C, and 20 C (1 C=110 mA g<sup>-1</sup>) in the potential range of 2.5-4.2 V (vs. Na<sup>+</sup>/Na). As shown in **Figure 2-6a**, the initial discharge capacities of NVP/ONC at 0.1 C, 0.5 C, 1 C, 5 C, 10 C and 20 C are 109 mAh g<sup>-1</sup>, 107 mAh g<sup>-1</sup>, 106 mAh g<sup>-1</sup>, 103 mAh g<sup>-1</sup>, 99 mAh g<sup>-1</sup>, and 90 mAh g<sup>-1</sup>, respectively, while the NVP/6.7NC and NVP/10.8NC deliver 113 mAh g<sup>-1</sup> and 101 mAh g<sup>-1</sup>, 111 mAh g<sup>-1</sup> and 95 mAh g<sup>-1</sup>, 110 mAh g<sup>-1</sup> and 93 mAh g<sup>-1</sup>, 105 mAh g<sup>-1</sup> and 86 mAh g<sup>-1</sup>, 99 mAh g<sup>-1</sup> and 81 mAh g<sup>-1</sup>, 86 mAh g<sup>-1</sup> and 74 mAh g<sup>-1</sup> at each C-rate correspondingly. The improved capacity at low current density of the NVP/6.7NC material compared to the other samples is due to the smaller particle size and high electric conductivity associated with the graphitic carbon coating, which has also been identified from the Raman analysis. However, when cycled at a current density as high as 20 C, the delivered capacities of NVP/6.7NC (86 mAh g<sup>-1</sup>) and NVP/10.8NC (74 mAh g<sup>-1</sup>) are lower than that of NVP/ONC (90 mAh g<sup>-1</sup>). This can be attributed to the graphitic carbon coating and high amount

of extrinsic defects existed between the electrode and electrolyte which may block the Na diffusion and lead to reduced specific capacity at high current rates.<sup>[74-76]</sup> Nevertheless, the Coulombic efficiency of first cycle for NVP/10.8NC at 20 C is 97.4%, higher than NVP/0NC and NVP/6.7NC of 95.0% and 96.3%, which is critical to achieving stable cycling performance. The rate capabilities of the undoped and N-doped carbon coated NVP electrodes are displayed in **Figure 2-6d**. It is evident that the NVP/10.8NC delivers lower capacity than the undoped and moderate doped ones, nevertheless, all materials show good reversibility.

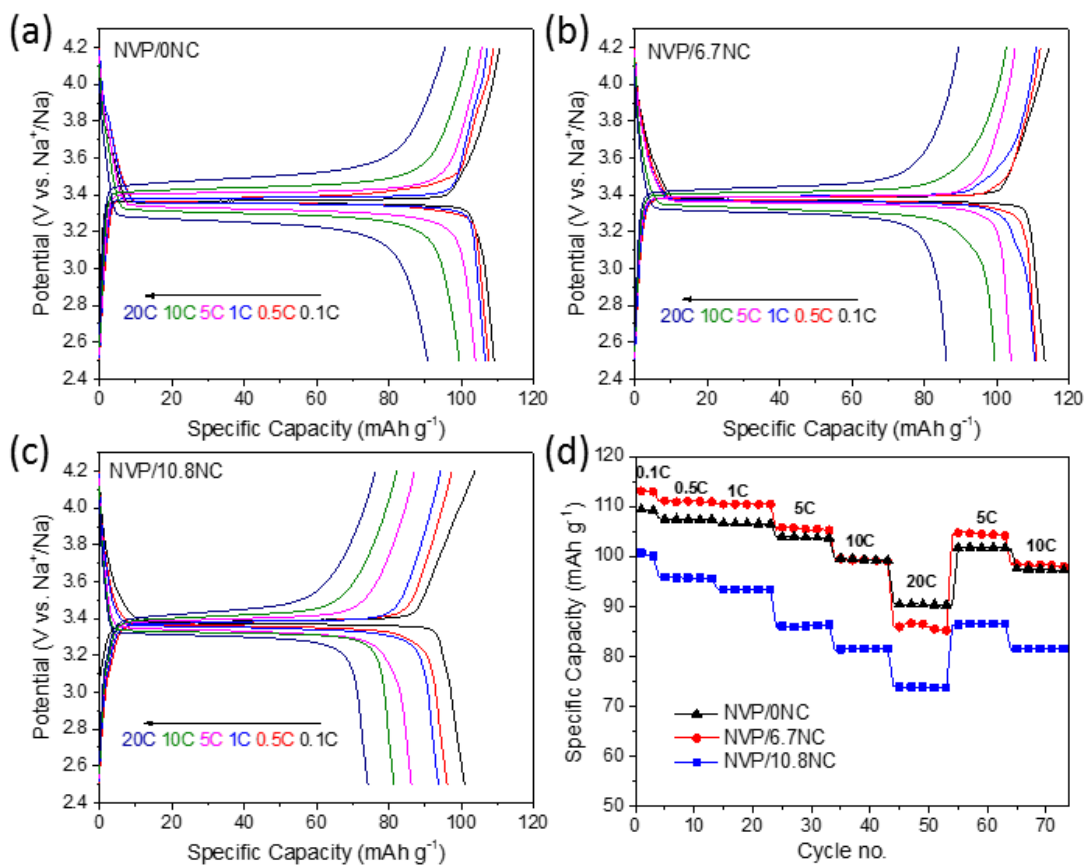


**Figure 2-6.** Initial charge/discharge curves of (a) NVP/0NC, (b) NVP/6.7NC and (c) NVP/10.8NC electrodes in the potential range of 2.5-4.2 V (vs. Na<sup>+</sup>/Na) recorded during a C-rate capability tests. (d) Specific discharge capacity vs. cycle number for the cycling at various current rates.

However, the NVP/10.8NC electrode exhibits the best cycling stability as shown in **Figure 2-7**. At 20 C, the NVP/10.8NC delivers a stable discharge capacity of 71 mAh g<sup>-1</sup> after 1000 cycles which corresponds to high capacity retention of 96% with respect to the initial capacity (74 mAh g<sup>-1</sup>). In contrast, the capacity retention of NVP/6.7NC is moderate (91%), and the one of NVP/0NC is

inferior (86%). To better understand the effect of N-doped carbon coating on the high rate performance of NVP cathode in sodium ion batteries, the voltage efficiencies at various C-rates, *i.e.* the voltage difference at 50% state-of-charge (SOC) and 50% depth-of-discharge (DOD) from the charge-discharge profiles, were calculated and the results are shown in **Figure 2-8**. At low C-rate, the voltage efficiencies of NVP/0NC, NVP/6.7NC and NVP/10.8NC electrodes are 17 mV, 19 mV and 19 mV at 0.1 C, 36 mV, 23 mV and 31 mV at 0.5 C, and 34 mV, 33 mV and 38 mV at 1 C, respectively, showing no obvious improvement with the N-doping modification in the carbon layers of NVP/C composites. However, when the C-rate increases to a higher value, the pristine NVP/0NC material exhibits a severer increase on the voltage efficiency than those of NVP/6.7NC and NVP/10.8NC. For example, the voltage efficiency of NVP/C increases to 252 mV at 20 C, however, the values of NVP/6.7NC and NVP/10.8NC electrodes are only 147 mV and 143 mV, respectively, showing strongly decreased polarization at high rate. This reflects that the N-doped carbon coating facilitates the charge transfer at the electrode/electrolyte interface, which is resulting in lower interfacial resistance. Therefore, the modification with rationally N-doped carbon coating improves the capacity of NVP materials to some extent. Furthermore, with increasing N doping content a lower discharge capacity at the same C-rate is obtained while the cycling stability is gradually enhanced. These results are in agreement with the previous structural analysis.

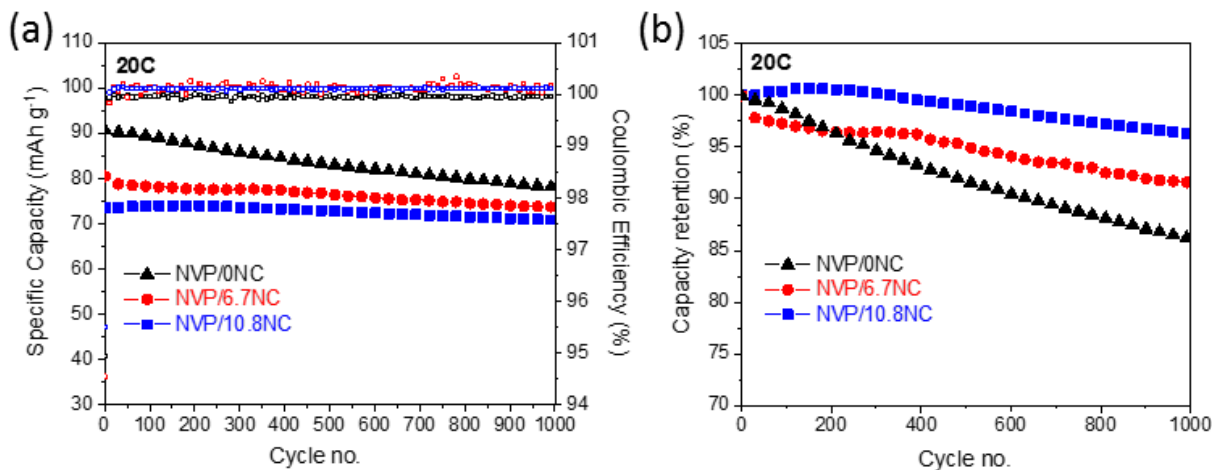


**Figure 2-7.** (a) Long-term cycling performance and (b) capacity retention vs. cycling number of NVP/0NC, NVP/6.7NC and NVP/10.8NC at 20 C.

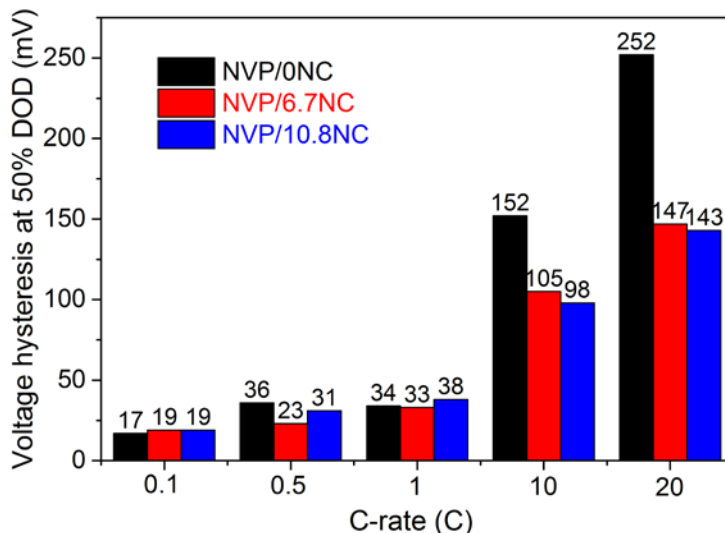


**Figure 2-8.** Voltage hysteresis at 50% depth-of-discharge (DOD) from the charge-discharge profiles of NVP/0NC, NVP/6.7NC and NVP/10.8NC at various C-rates.

To further understand the effects of N-doped carbon on the electrochemical performance of NVP electrodes, cyclic voltammetry (CV) was performed. The cyclic voltammograms were obtained in a three-electrode half-cell between 2.5-4.2 V (vs. Na<sup>+</sup>/Na) at scan rates of 0.1 mV s<sup>-1</sup>, 0.5 mV s<sup>-1</sup>, 1.0 mV s<sup>-1</sup>, 5.0 mV s<sup>-1</sup>, 10.0 mV s<sup>-1</sup> and are shown in **Appendix Figure S2-1**. For all electrodes present a symmetric peak couple at around 3.4 V vs. Na<sup>+</sup>/Na is detected which is due to the redox reaction of V<sup>3+/4+</sup>.<sup>[77, 78]</sup> The CV profiles of NVP/0NC, NVP/6.7NC and NVP/10.8NC electrodes are displayed in **Figure 2-9a** at a fixed scan rate of 0.5 mV s<sup>-1</sup>. The anodic and cathodic peak of NVP/6.7NC and NVP/10.8NC are separated by 0.17 V and 0.23 V which is much lower than that of undoped NVP/C composite. Moreover, the peaks of the N-doped carbon coated NVP composites are more symmetric and sharper than that of NVP/C which is demonstrating the improved redox kinetics from the enhanced conductivity of the composites and is consistent with the charge/discharge profiles.<sup>[79]</sup> The CV results enable the calculation of the apparent diffusion coefficients ( $DI_{Na^+}$ ) at the different peak positions via the simplified Randles-Sevcik Equation (2-1)<sup>[80]</sup>:

$$i_p = k n^{\frac{3}{2}} A D^{1/2} C_{Na^+} \nu^{\frac{1}{2}} \quad (2-1)$$

where  $i_p$  is the peak current (A),  $k$  is a constant value of  $2.69 \times 10^5 \text{ C mol}^{-1} \text{ V}^{-1/2}$ ,  $n$  is the charge-transfer number of the electrochemical reaction,  $A$  is the contact area between the electrode and electrolyte (the geometric area of 1.13 cm<sup>2</sup> for the disc electrode was used),  $C_{Na^+}$  is the concentration of Na<sup>+</sup> in electrode materials ( $3.47 \times 10^{-3} \text{ mol cm}^{-3}$  for NVP)<sup>[80]</sup>,  $\nu$  is the scan rate (V

s<sup>-1</sup>). The calculated results are listed in **Table 2-2**. Obviously, the  $D_{Na^+}$  of NVP/6.7NC material is slightly higher than those of NVP/0NC and NVP/10.8NC, but still in the same order of magnitude, reflecting the fact that the N-carbon coating has no significant improvement on the ionic diffusion in the bulk materials.

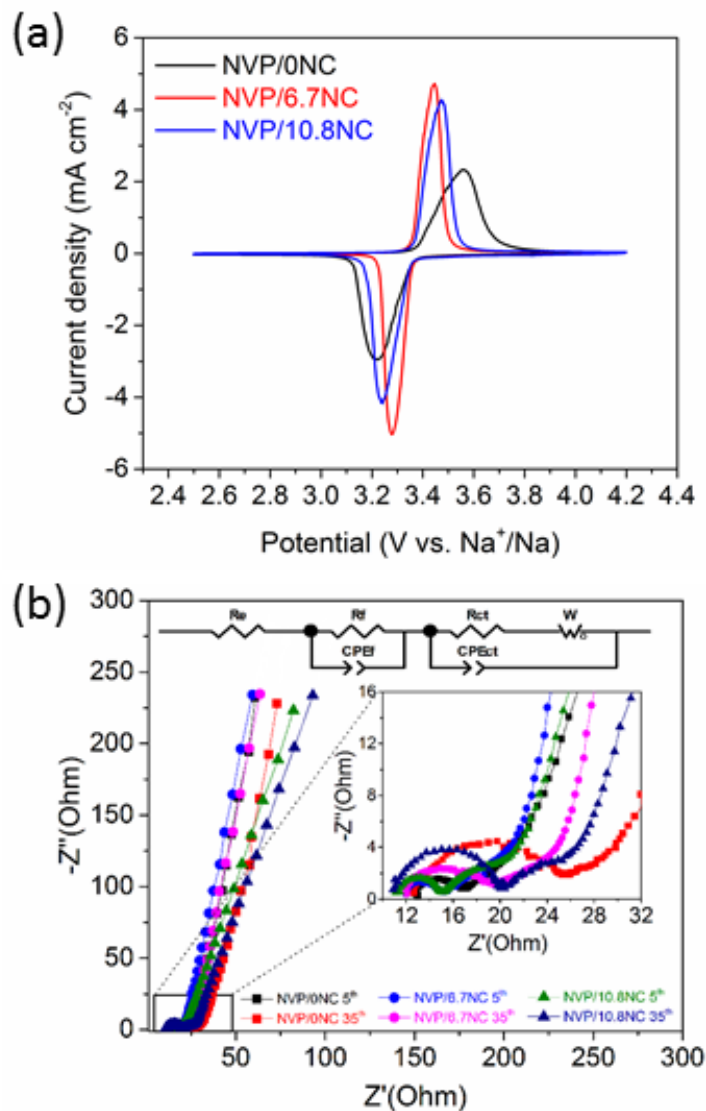


**Figure 2-9.** (a) CV curves at 0.5 mV s<sup>-1</sup> in three-electrode half-cell and (b) Impedance spectra obtained in symmetric cells of NVP/0NC, NVP/6.7NC and NVP/10.8NC electrodes at fully discharged state (1.0 V) in the 5th and 35th cycle (inset: magnified high frequency region and equivalent circuit).

**Table 2-2.** Diffusion coefficients of  $\text{Na}^+$  ( $D_{cv\text{Na}^+}$ ,  $\text{cm}^2 \text{s}^{-1}$ ) calculated from CV curves, and  $R_f$  ( $\Omega$ ),  $R_{ct}$  ( $\Omega$ ),  $\text{Na}^+$  diffusion coefficients ( $D_{EIS\text{Na}^+}$ ,  $\text{cm}^2 \text{s}^{-1}$ ) in symmetric cells calculated from EIS measurements.

	CV		EIS				
	Cathodic $D_{cv\text{Na}^+}$	Anodic $D_{cv\text{Na}^+}$	$R_f$ , 5th	$R_f$ , 35th	$R_{ct}$ , 5th	$R_{ct}$ , 35th	$D_{EIS\text{Na}^+}$
<b>NVP/ONC</b>	$2.3 \times 10^{-12}$	$1.5 \times 10^{-12}$	4.8	9.9	22.4	49.3	$4.6 \times 10^{-13}$
<b>NVP/6.7NC</b>	$5.2 \times 10^{-12}$	$5.6 \times 10^{-12}$	2.6	5.9	12.0	16.1	$8.2 \times 10^{-13}$
<b>NVP/10.8NC</b>	$2.9 \times 10^{-12}$	$2.6 \times 10^{-12}$	5.9	8.0	11.1	11.2	$3.4 \times 10^{-13}$

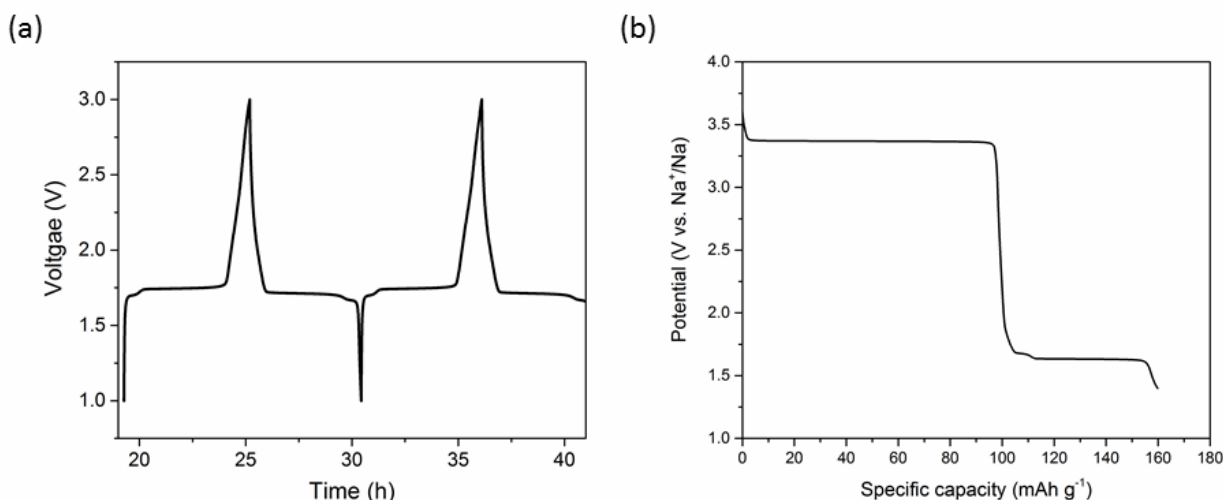


**Figure 2-10.** (a) Typical charge-discharge profiles of NVP symmetric cell at 0.1 C ( $11 \text{ mA g}^{-1}$ ) in the 1.0-3.0 V voltage range. (b) Discharge curves at 0.1 C ( $11 \text{ mA g}^{-1}$ ) of NVP electrode in 1.4-3.6 V (vs.  $\text{Na}^+/\text{Na}$ ) potential range.

Electrochemical impedance spectroscopy (EIS) was applied to investigate the charge transfer resistance and ionic diffusion behavior of prepared NVP cathodes. Symmetric two electrode cells with NVP as both cathode and anode were assembled for the impedance measurement to avoid the impact of the Na-metal electrode.<sup>[81, 82]</sup> The symmetric NVP cell was cycled at 0.1C between 3.0-1.0V. Further information about the typical voltage profile of the symmetric NVP cell at 0.1C between 3.0-1.0V as well as the electrochemical behavior between 3.6 V-1.4 V (vs.  $\text{Na}/\text{Na}^+$ ) in half cell can be found in **Figure 2-10** but also have been reported in literature.<sup>[49]</sup> The impedance spectra were collected at the discharged state (1.0 V) of the 5<sup>th</sup> and 35<sup>th</sup> cycles. The amplified spectra at high frequency region are shown as inset in **Figure 2-9b** together with equivalent circuit inset. The spectra were fitted using ZView software (version 3.3f, Scibner Associates Inc.)



according to the equivalent circuit. Therein, the  $R_e$  is the bulk resistance of the cell.  $R_f$  and  $CPE_f$  are the solid-electrolyte interface film resistance and film capacitance. The  $R_{ct}$  and  $CPE_{ct}$  refer to the charge transfer resistance and double-layer capacitance in series with the Warburg impedance  $W$ , respectively. The overall interfacial resistance of  $R_{ct}$  can reflect the polarization behavior in charge-discharge profiles. The diffusion coefficient ( $D_{Na^+}$ ) of the NVP in the symmetric cells can be calculated by Equation (2-2)<sup>[83]</sup>:

$$D_{Na^+} = \frac{R^2 T^2}{2A^2 n^4 F^4 C_{Na^+}^2 \sigma^2} \quad (2-2)$$

where  $R$  is the gas constant (8.314 J mol<sup>-1</sup> K<sup>-1</sup>),  $T$  is the absolute temperature in Kelvin (298.15 K),  $A$ ,  $C_{Na^+}$  and  $n$  are the contact area, concentration of Na<sup>+</sup> in bulk material and number of electrons in the same values with Equation (2-1),  $F$  is the Faraday constant (96500 C mol<sup>-1</sup>) and  $\sigma$  is the Warburg coefficient. In **Table 2-2**, the fitted  $R_f$ ,  $R_{ct}$  and calculated  $D_{Na^+}$  values are listed. The film resistance ( $R_f$ ) of NVP/ONC, NVP/6.7NC and NVP/10.8NC electrodes are 4.8  $\Omega$ , 2.6  $\Omega$  and 5.9  $\Omega$ , respectively, and shows a slight increase to 9.9  $\Omega$ , 5.9  $\Omega$  and 8.0  $\Omega$ . Moreover, with increasing N-doped carbon coating content, the charge-transfer resistances ( $R_{ct}$ ) is reduced to 12.0  $\Omega$  and 11.1  $\Omega$  for NVP/6.7NC and NVP/10.8NC electrodes and lower than that of NVP/ONC (22.4  $\Omega$ ). After 35<sup>th</sup> cycles, the  $R_{ct}$  of the NVP/ONC electrode dramatically increases to 49.3  $\Omega$ , while the NVP/6.7NC and NVP/10.8NC electrodes exhibit only slight increases to 16.1  $\Omega$  and 11.2  $\Omega$ , respectively. This is demonstrating the facilitated interfacial charge-transfer and explains the enhanced cycling stability of the NVP materials with N-doped carbon coating. The Na-ion diffusion coefficients of the NVP composites calculated from EIS are one order of magnitude smaller compared to those obtained from CV which is due to the method used for the calculation of the diffusion coefficient.<sup>[84]</sup> Most importantly, both methods show the same trend, i.e., that the NVP/6.7NC electrode exhibits a slightly improved diffusion coefficient. Overall, the results demonstrate that an appropriate N-doped carbon coating can lead to improved interfacial stability and facilitated charge transfer, which is resulting in the superior electrochemical performance.

#### 2.1.4 Conclusions

The nitrogen-doped carbon coated Na<sub>3</sub>V<sub>2</sub>(PO<sub>4</sub>)<sub>3</sub> composites have been synthesized by simple solid-state method and investigated as cathodes in sodium ion batteries. The results demonstrate that the N content plays a significant role on both the structure of carbon layer and electrochemical performance of Na<sub>3</sub>V<sub>2</sub>(PO<sub>4</sub>)<sub>3</sub>/C electrodes. It is confirmed that the N-doping in the carbon later of NVP/C composite can improve the cycling stability in sodium ion batteries,

due to the facilitated interfacial charge transfer. By tuning the amount of N doped into the carbon lattice, various extrinsic defects are created. With appropriate amount of N-doping, a superior electrochemical behavior is obtained as evident from the decreased voltage hysteresis, higher capacity and better cycling stability. However, it should be noted that high contents of N doped into the carbon lead to reduced reversible capacities. Summarizing, we believe that N-doped carbon coatings are a promising strategy to increase the conductivity of, e.g., NVP electrode materials and, thus, also important for the application of sodium ion batteries.

## 2.2 Effect of Nitrogen-doped Carbon Matrix Dimensions on the Electrochemical Properties of $\text{Na}_3\text{V}_2(\text{PO}_4)_3$ Cathode

### 2.2.1 Introduction

Owing to the fast  $\text{Na}^+$  mobility in 3D framework,  $\text{Na}_3\text{V}_2(\text{PO}_4)_3$  (NVP) has achieved ubiquitous attention as promising cathode for SIBs.<sup>[85-87]</sup> However, as any NASICON compound, NVP suffers from poor electronic conductivity, leading to low rate capability and reduced cyclability.<sup>[49, 88]</sup> Carbon coating, considered as the most efficient way to improve the materials electric conductivity, is frequently applied to NVP materials. Additionally, the carbon framework, as conductive template, may reduce active material particle growth leading to shortened ion pathway and thus facilitated  $\text{Na}^+$  ion diffusion. For example, NVP in porous carbon matrix, generally prepared by the solution-based method, exhibits superior rate capability, resulting from the high  $\text{Na}^+$  accessibility in the conductive carbon skeleton.<sup>[79, 89]</sup> Besides, the use of hard carbon templates also turned to be an efficient approach to constructing 3D open structure as well as improving the conductivity. Jung et al. utilized graphene as conductive support to fabricate NVP/graphene composite, which delivers outstanding rate capability.<sup>[90]</sup> Furthermore, a conventional freeze-drying strategy was developed by Yu et al. to prepare a novel 3D NVP/C/rGO composite architecture, enabling an ultralong cycle-life even at an extremely high rate of 100 C.<sup>[91]</sup> Reviewing more recent achievements in this respect, both amorphous carbon from pyrolysis of organic precursors and hierarchical carbon frameworks could sufficiently satisfy the stringent requirements of  $\text{Na}_3\text{V}_2(\text{PO}_4)_3$  electrode materials in the construction of high-power and long life sodium ion batteries for energy storage applications.<sup>[50, 61, 92, 93]</sup>

In the above part, we have already demonstrated that the nitrogen-doped carbon coating could efficiently improve the electrochemical performance of NVP cathode materials for sodium ion batteries. Moreover, Mai et al. employed various carbon matrices, *i.e.* acetylene carbon nanospheres, carbon nanotubes and graphite nanosheets, to investigate the influence of carbon dimension on the electrochemical performance, demonstrating that NVP dispersed in acetylene carbon nanospheres exhibits the best performance even in symmetric sodium-ion batteries.<sup>[85]</sup> Inspired by these, we propose an approach combining ball-milling and high temperature calcination for the synthesis of NVP in N-doped carbon matrices. Also reported is the systematic performance investigation of as-synthesized composite materials with various carbons, *i.e.* pyrolytic carbon (C), carbon nanotubes (CNT), reduced graphene oxide nanosheets (rGO), and

Ketjen black nanospheres (KB), as cathodes for sodium ion batteries. The final products are herein after denoted as NVP/N-C, NVP/N-CNT, NVP/N-rGO, and NVP/N-KB, respectively.

In this approach, melamine is introduced by simple ball milling process, as mentioned nitrogen-rich source among the precursors, which does not leave any additional carbon after pyrolysis. Upon moderate calcination, the nitrogen originating from the decomposition of melamine dopes the carbon (C, CNT, GO and KB) with surface defects, and reducing  $V^{4+}$  to  $V^{3+}$  to form the well-crystallized  $Na_3V_2(PO_4)_3$ . With the N-doping, the  $Na_3V_2(PO_4)_3/C$  composites exhibit superior rate capability and cycling performance. In particular, NVP/N-CNT showed the best electrode performance even in symmetric sodium-ion cells.

## 2.2.2 Experimental Methods

### 2.2.2.1 Materials synthesis

$Na_3V_2(PO_4)_3/N-X$  (with  $X = C, CNT, rGO, KB$ ) composites were prepared by one-step solid state reaction of the precursors under inert atmosphere. The latter ones were obtained by ball-milling the appropriate stoichiometric amount of raw materials in acetone for 8h, followed by a drying and grinding step at room temperature. Sodium acetate trihydrate ( $CH_3COONa \cdot 3H_2O$ , VWR,  $\geq 99\%$ ), vanadyl acetylacetonate ( $VO(C_5H_7O_2)_2$ , Acros Organics,  $\geq 99\%$ ), ammonium dihydrogen phosphate ( $NH_4H_2PO_4$ , Alfa Aesar,  $\geq 99\%$ ), citric acid monohydrate ( $C_6H_8O_7 \cdot H_2O$ , Alfa Aesar,  $\geq 99\%$ ), carbon nanotube (Sigma Aldrich, multi-walled, carbon  $> 95\%$ ), graphene oxide monolayer powders (Nanoinnova Technologies), Ketjen black (AkzoNobel, EC-600JD) and melamine ( $C_3H_6N_6$ , Sigma Aldrich,  $\geq 99\%$ ) were used as received. The carbon nanotube and Ketjen black were treated with concentrated  $HNO_3$  (Merck Millipore, 65%) at  $60^\circ C$  for functional modification. The obtained precursors were pre-heated at  $300^\circ C$  for 4 h and sintered at  $800^\circ C$  for 8 h in Ar atmosphere to yield NVP/N-C, NVP/N-CNT, NVP/N-rGO and NVP/N-KB samples.

### 2.2.2.2 Materials characterization

X-ray diffraction analysis was performed in Bragg-Brentano geometry using a Bruker D8 Advance diffractometer (Bruker, Germany). All diffractograms were recorded with  $CuK\alpha$  radiation ( $\lambda = 0.154$  nm) in the  $2\theta$  range of  $10^\circ - 70^\circ$  with a step size of  $0.01^\circ$ . Morphological characterization was conducted on ZEISS 1550VP Field Emission SEM (Carl Zeiss, Germany). Thermal analysis was determined by a thermogravimetric analyzer (TGA-209F, Netzsch, Germany). Raman spectra were collected using a Renishaw 2000 system (Renishaw, UK) with a He-Ne laser (633 nm) and charge-coupled device detector. Spectra were collected using the extended scanning mode from  $880$  to  $1964\text{ cm}^{-1}$  and 10 s accumulation time, a single scan over the desired range took 1 min to

collect. XPS measurements were performed using a PHI 5800 Multi Technique ESCA system (Physical Electronic, USA). The spectra were acquired using monochromatic Al K $\alpha$  (1486.6 eV) radiation, a take-off angle of 45°, and pass energies at the electron analyzer of 29.35 and 93.9 eV for detail and survey scans, respectively. The main C1s peak with a binding energy of 284.8 eV was used for calibration.

### 2.2.2.3 Electrochemical measurements

The electrochemical tests were performed using three electrode Swagelok-type cells assembled in an argon-filled glove box with H<sub>2</sub>O and O<sub>2</sub> contents lower than 1 ppm. Sodium half-cells were assembled by using glass fiber (Whatman) as separator and sodium metal (99.8%, Acros Organics) as counter and reference electrodes. 1M NaPF<sub>6</sub> (Alfa Aesar, 99%) in propylene carbonate (PC) with 2 wt.% fluoroethylene carbonate (FEC) (BASF, Battery Grade) was used as electrolyte. The working electrodes were prepared by doctor-blade casting a slurry (80 wt.% of active material, 10 wt.% of carbon black (Super C65, IMERYS) and 10 wt.% of polyvinylidene fluoride (6020 Solef, Solvay Group) in N-methyl-2-pyrrolidone (anhydrous, Sigma-Aldrich)) on Al foil as current collector. After drying, electrodes with a diameter of 12 mm were punched, pressed and dried at 120 °C under high vacuum. The mass loading of the final electrodes is about 2.5 mg cm<sup>-2</sup>. A Maccor 4000 Battery system (Maccor, USA) was used for the galvanostatic charge/discharge test at various C-rates. Cyclic voltammetry was performed on a multichannel potentiostat/galvanostat (VMP3, Biologic Science Instruments, France). All measurements were performed in climatic chambers at a temperature of 20 ± 1 °C.

## 2.2.3 Results and Discussion

Structure and morphology of the synthesized Na<sub>3</sub>V<sub>2</sub>(PO<sub>4</sub>)<sub>3</sub> materials (see **Figure 2-11**) were investigated by X-ray diffraction (XRD) and scanning electron microscopy (SEM). All the diffraction reflections of NVP/N-C, NVP/N-CNT, NVP/N-rGO, and NVP/N-KB composites (see **Figure 2-11a, d, g and j**, respectively) can be indexed to the well-defined NASICON structure, rhombohedral *R*-3*c* space group, consistent with the standard diffraction pattern of NVP (JCPDS card no. 53-0018).<sup>[78]</sup> Moreover, there is no obvious difference among the four XRD patterns, suggesting that the melamine precursor and the carbon matrix formation do not adversely affect the crystallization of NVP.

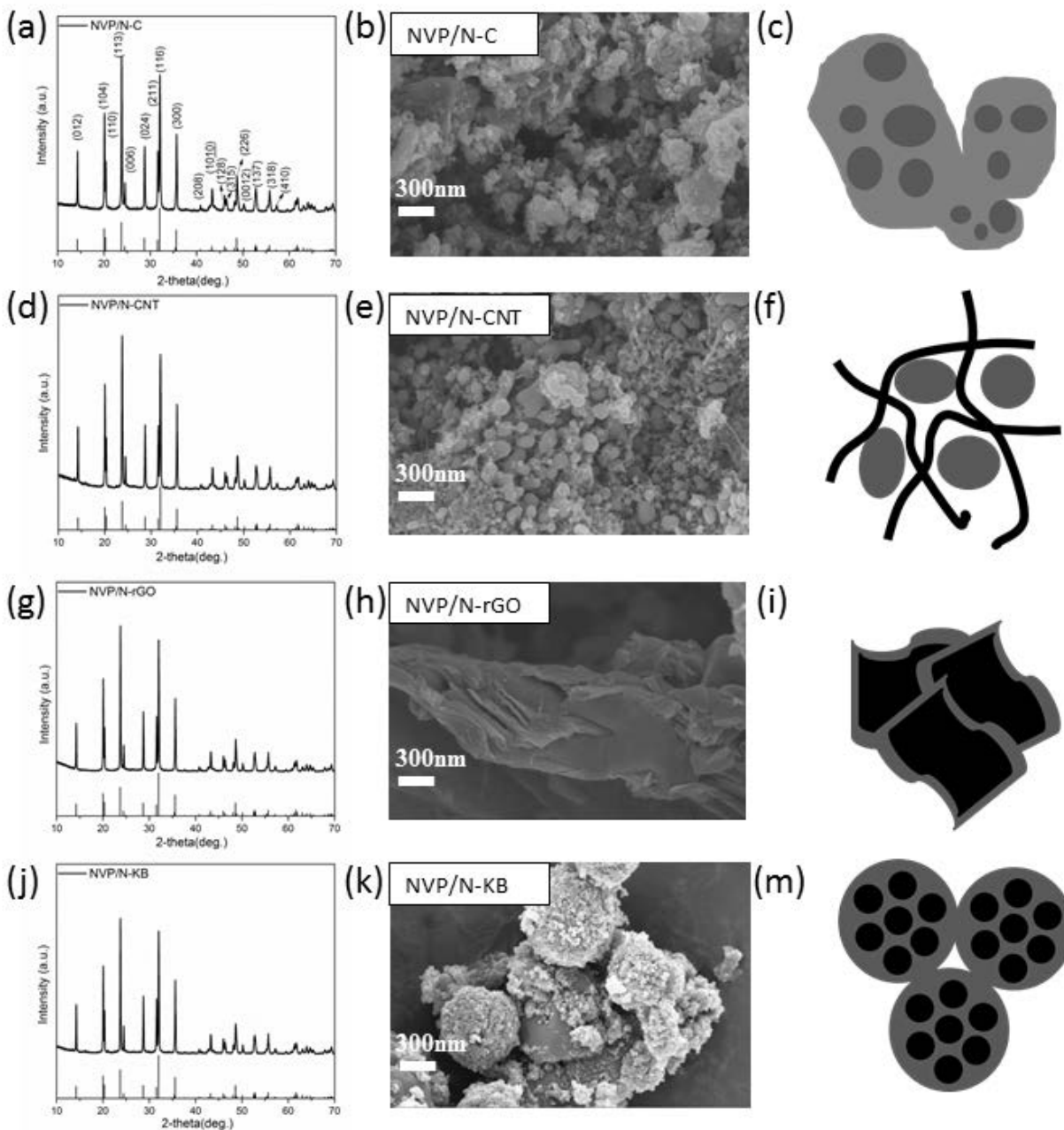


**Figure 2-11.** XRD patterns, SEM images and schematic illustrations of NVP/N-C (a, b, c), NVP/N-CNT (d, e, f), NVP/N-rGO (g, h, i), and NVP/N-KB (j, k, m) composites.

The morphology of the prepared NVP/N-C, NVP/N-CNT, NVP/N-rGO, and NVP/N-KB composites is shown in **Figure 2-11b, e, h and k**, respectively. It is noteworthy that the NVP/N-C material, obtained from the pyrolysis of citric acid, shows particles of irregular shape and uneven size distribution. On the other hand, the NVP/N-CNT material exhibits a more uniform particle size of about 200 nm and narrow size distribution. Regarding the NVP/N-rGO and

NVP/N-KB composites it can be seen that the NVP grows on the graphene nanosheets and Ketjen black nanoparticles, and aggregates into open networks which adopt the structural features of the carbon templates. The various morphologies are represented by the schematic illustrations in **Figure 2-11c, f, i and m**, respectively. The differences result from the carbon matrices introduced into the precursors acting as templates for the NVP nanograins growth, thus controlling the morphology. The intriguing morphology and conductivity of the carbon skeletons are expected to contribute to the electronic and ionic conductivities of the fabricated electrodes, which are critical for improving the electrochemical performance, especially, the rate capability and long-term cycling stability. The carbon amount in each composite material, as detected by thermogravimetric analysis is 3.4 wt.%, 4.8 wt.%, 2.0 wt.%, and 5.7 wt.%, respectively, for NVP/N-C, NVP/N-CNT, NVP/N-rGO, and NVP/N-KB composites.

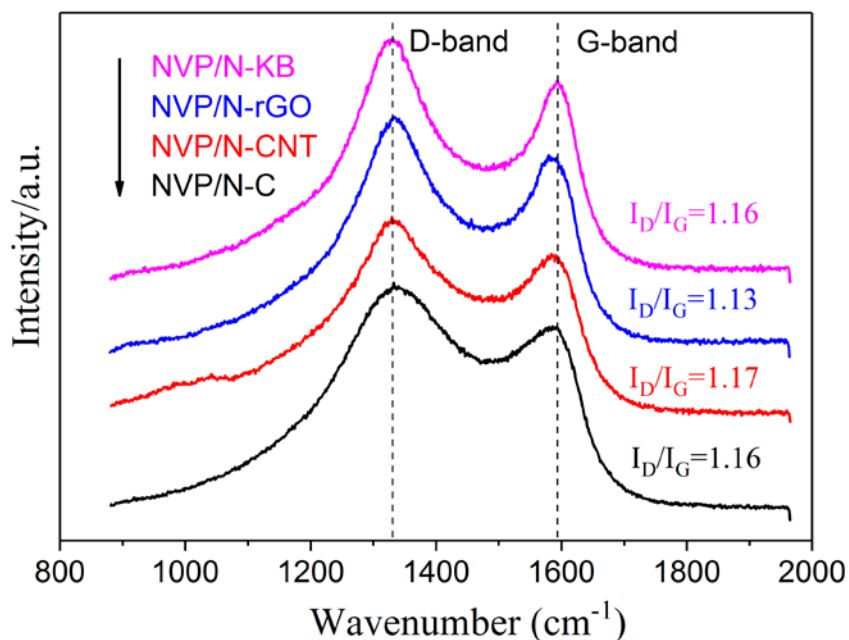


**Figure 2-12.** Raman spectra (a), schematic structure of possible binding conditions of N in a carbon lattice (b) and high-resolution XPS spectra of N1s (c–f) in NVP/N-C, NVP/N-CNT, NVP/N-rGO, and NVP/N-KB composites.

In order to confirm the effect of N heteroatoms on the carbon frameworks of the NVP composites, Raman spectra of all the samples were performed (**Figure 2-12**). In these spectra, broad D (1357  $\text{cm}^{-1}$ ) and G (1593  $\text{cm}^{-1}$ ) bands are observed, which are related to the defective and graphitic carbon, respectively.<sup>[72]</sup> The intensity ratio of the two bands ( $I_D/I_G$ ) is an efficient parameter to assess the structural disorder of carbon materials.<sup>[94-97]</sup> Specifically, the  $I_D/I_G$  values for NVP/N-C, NVP/N-CNT, NVP/N-rGO, and NVP/N-KB samples are 1.16, 1.17, 1.13, and 1.16, respectively. NVP/N-

CNT shows the largest value, indicating the highest number of defects caused by the introduction of N heteroatoms into the sp<sup>2</sup> carbon wall of CNT resulting in the structural disordering of the hybridized frameworks.<sup>[98]</sup> This is rather important, because, as reported in literature,<sup>[65, 67]</sup> the functionalization with N can significantly improve the electric conductivity and create extrinsic defects in the carbon layer, which, in turn, facilitate ions transfer across the interface between the electrode and electrolyte. Both actions are expected to be beneficial for the performance of the composite materials as electrodes.

**Table 2-3.** Contents of the N species and N/C atomic ratio in the N-doped carbon coated NVP composites as obtained by XPS analysis.

	NVP/N-C	NVP/N-CNT	NVP/N-rGO	NVP/N-KB
<b>Pyridinic N1</b>	62.1%	35.0%	39.9%	41.2%
<b>Pyrrolic N2</b>	27.9%	47.7%	42.8%	38.2%
<b>Quaternary N3</b>	3.8%	9.3%	8.1%	7.8%
<b>N-oxide</b>	6.2%	8.0%	9.2%	12.8%
<b>N/C atomic ratio</b>	10.8%	3.3%	6.3%	3.9%

To clarify the nature of the N sites formed in the hybridized carbon frameworks, X-ray photoelectron spectroscopy (XPS) measurements were also carried out on all samples. **Figure 2-13a-d** display the high-resolution N1s spectra of the NVP composites. As shown, the pyridinic (N1) nitrogen, which is formed by the substituting carbon atom on edges or defect sites in the plane, plays a dominant role in the NVP/N-C material. Rather, the NVP composites based on the hard carbon templates coating, namely the CNT, rGO, and KB, exhibit higher pyrrolic (N2) nitrogen content, which can be associated to exposed edges and/or planar defects. The specific N/C atomic ratios and the contents of various N species in NVP/N-C, NVP/N-CNT, NVP/N-rGO, and NVP/N-KB composites are listed in **Table 2-3**. The content of various N species in NVP/N-CNT is 35.0% (N1), 47.7% (N2) and 9.3% (N3), i.e., higher pyrrolic (N2) and quaternary (N3) nitrogen contents than all other samples. On the other hand, since it is easier to dope N into the carbon framework of NVP/N-C and NVP/N-rGO due to the *in-situ* formation progress of carbon from the pyrolysis of citric acid and the originally existing functional groups and defects in the structure of graphene oxide, the N/C ratio of NVP/N-C and NVP/N-rGO are substantially higher (10.8% and 6.3%). The various surface defects created by the N atom substitution in the carbon lattice could efficiently enhance the electronic conductivity of NVP/C composites and stabilize the electrode/electrolyte interface, which is highly desirable for electrodes with poor conductivity.<sup>[99, 100]</sup>



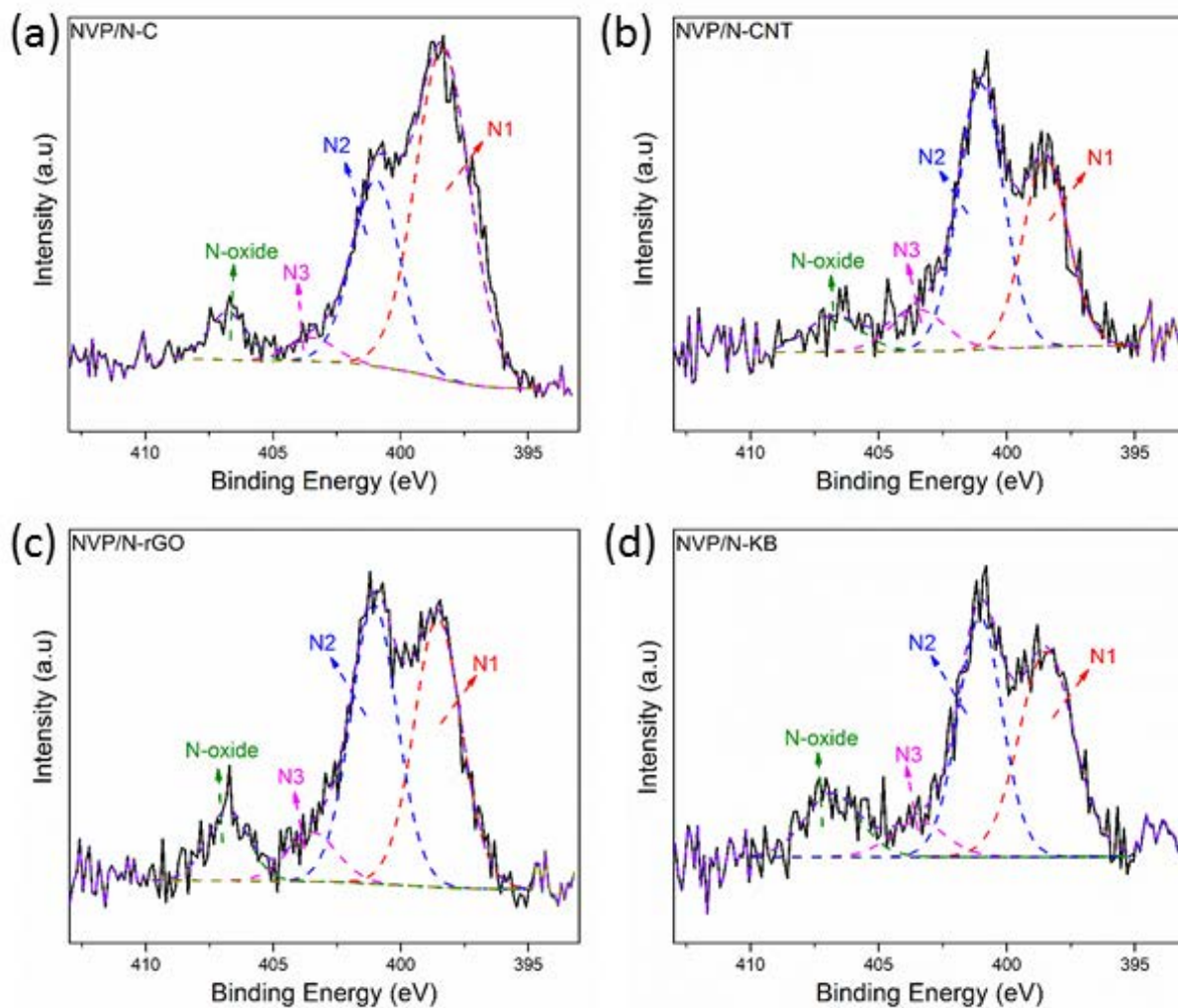


**Figure 2-13.** High-resolution XPS spectra of N1s of NVP/N-C, NVP/N-CNT, NVP/N-rGO, and NVP/N-KB composites.

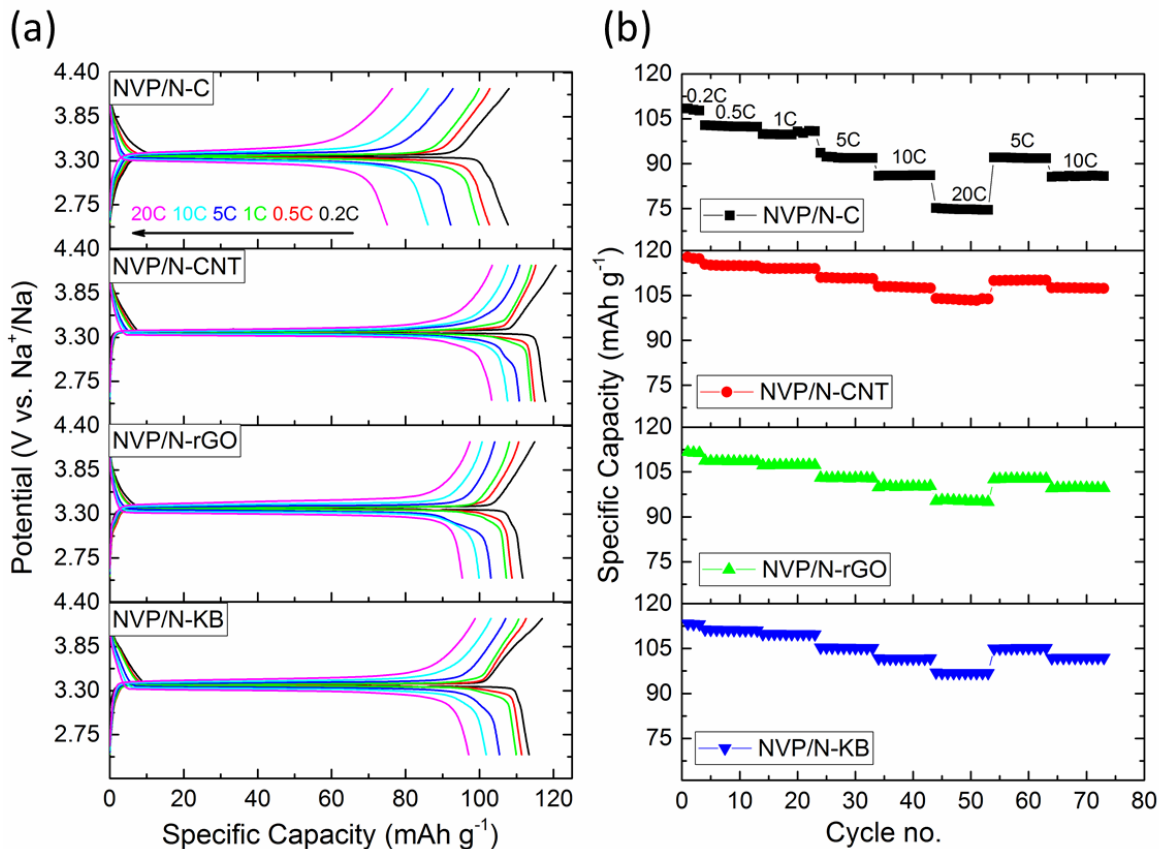


**Figure 2-14.** Electrochemical performances of NVP composite electrode materials: (a) charge-discharge profiles at 0.1 C, 0.5 C, 1.0 C, 5.0 C, 10.0 C, and 20.0 C, (b) C-rate stability test of NVP/N-C, NVP/N-CNT, NVP/N-rGO, and NVP/N-KB composites.

The electrochemical performance of all NVP electrodes was investigated in Swagelok-type cells, using sodium metal as counter and reference electrodes, in the potential range of 2.5–4.2 V vs. Na<sup>+</sup>/Na. **Figure 2-14a** shows the initial charge-discharge curves of all NVP composite materials at 0.1 C, 0.5 C, 1.0 C, 5.0 C, 10.0 C, and 20.0 C (1C=110 mA g<sup>-1</sup>). All curves exhibit flat plateaus at around 3.4 V, corresponding to the V<sup>3+</sup>/V<sup>4+</sup> redox couple. At low rate (0.1 C), the NVP/N-C, NVP/N-CNT, NVP/N-rGO, and NVP/N-KB cathodes deliver an initial discharge capacity of about 101 mAh g<sup>-1</sup>, 114 mAh g<sup>-1</sup>, 105 mAh g<sup>-1</sup>, and 108 mAh g<sup>-1</sup>, respectively. The 1<sup>st</sup> cycle coulombic efficiency for the four samples is 99.1%, 97.7%, 97.2%, and 97.0%, indicating that, despite the lower capacity delivered, NVP/N-C exhibits the highest reversibility of the process during the first cycle (at low current density). However, the initial coulombic efficiency of NVP/N-CNT cathode reaches 100% when cycled at the highest rate (20 C), *i.e.*, higher than all other samples, indicating a superior electrochemical reversibility and rate capability of the NVP/N-CNT electrode. This result can be attributed to the enhanced electronic conductivity of the composite with uniform

particle size resulting from the architecture of interconnected N-CNT networks, and improved electrode/electrolyte interface due to the introduction of defects into the carbon network. Moreover, the polarization is highly restrained after employing the N-doped carbon as matrix, in which the NVP/N-CNT exhibits the lowest polarization (0.08 V at 20 C versus 0.19 V for NVP/N-C, 0.16 V for NVP/N-rGO, and 0.14 V for NVP/N-KB). As generally known, the total polarization observed consists of different contributions such as the activation polarization related to the activation energy to be overcome during the electrochemical reaction, the ohmic polarization resulting from the resistance to the flow of ions and electrons in the electrolyte and the material, respectively, and the concentration polarization referred to the mass transport through the bulk of electrode.<sup>[101]</sup> In our case, the electrochemical behavior observed can be ascribed to the fact that the N-doped carbon frameworks enhance the bulk conductivities of the electrodes and the extrinsic defects created by the N-substitution provide more reaction sites for interfacial charge transfer. Therefore, we propose that the alleviated activation and ohmic polarizations are beneficial for the improvement of rate performance of the as-fabricated electrodes.<sup>[102]</sup> **Figure 2-14b** demonstrates the rate capability test for all electrodes. As the C-rate increases from 0.1 C to 20 C, the capacity decreases from 101 mAh g<sup>-1</sup> to 71 mAh g<sup>-1</sup> for NVP/N-C, 114 mAh g<sup>-1</sup> to 100 mAh g<sup>-1</sup> for NVP/N-CNT, 105 mAh g<sup>-1</sup> to 90 mAh g<sup>-1</sup> for NVP/N-rGO, and 108 mAh g<sup>-1</sup> to 93 mAh g<sup>-1</sup> for NVP/N-KB, corresponding to the capacity retention of 70%, 88%, 86%, and 85% with respect to 0.1 C, respectively. As expected, the NVP/N-CNT composite exhibits the best rate capability, which is well-recognized from the structural analysis with more uniform morphology and higher surface defects. When decreasing the C-rate back to 5 C, the specific capacity of all samples can recover to the previous values at 5 C, indicating the excellent reversibility of the NVP materials originating from the modification by N-doped carbon coating.

The long-term cycling performance of NVP materials dispersed in various N-doped carbon matrices at 20 C are depicted in **Figure 2-15**. After 3000 cycles, a specific capacity of about 98 mAh g<sup>-1</sup> was achieved for the NVP/N-CNT electrode, corresponding to 98% capacity retention, while the corresponding values for NVP/N-C, NVP/N-rGO and NVP/N-KB are 84%, 91% and 89%. Taken together, the NVP/N-rGO composite with only 2.0 wt.% graphene coating still demonstrates an outstanding rate and cycling performance, but, the NVP/N-CNT offers the best performance in terms of delivered capacity, low polarization and capacity retention upon cycling. The outstanding cycling performance for all the investigated materials fully confirms that embedding NVP in N-doped carbon matrices is a powerful strategy for the improvement of the cyclability and long-term stability as cathodes in sodium cells.

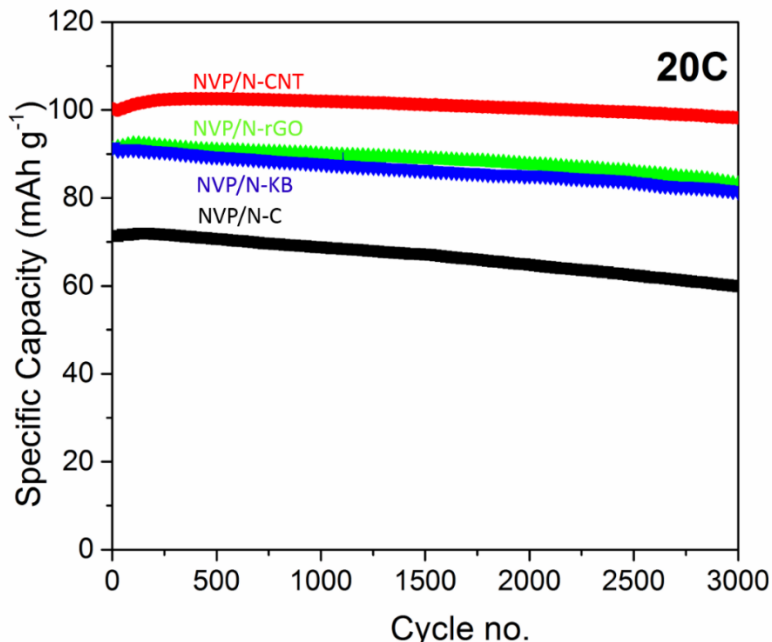


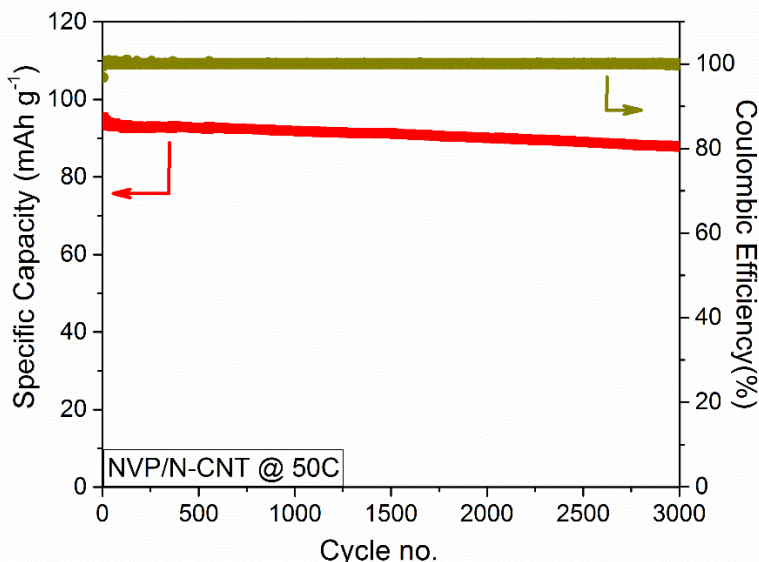
**Figure 2-15.** Long-term cycling performance at 20 C of NVP/N-C, NVP/N-CNT, NVP/N-rGO, and NVP/N-KB composites.

To further understand the electrochemical behavior of the various NVP particles embedded in N-doped carbon matrix, cyclic voltammetry in the potential range of 2.5-4.2 V (vs. Na<sup>+</sup>/Na) was performed (the profiles are displayed in **Appendix Figure S2-2**). All the voltammograms show a couple of symmetric redox peaks at around 3.4 V, well consistent with the plateaus observed in the charge-discharge profiles, associated with the redox activity of V<sup>3+/4+</sup>. At the scan rate of 0.1 mV s<sup>-1</sup>, the potential interval between the anodic and cathodic peaks of NVP/N-CNT electrode is ~100 mV, reflecting the highly enhanced redox kinetics resulting from the N-doped carbon nanotube matrix owing to improved conductivities and charge transfer.<sup>[79]</sup> The apparent Na<sup>+</sup> diffusion coefficients were calculated from the CV profiles at various scan rates (see **Appendix Figure S2-3**). It is found that the apparent  $D_{\text{Na}^+}$  values of NVP/N-C, NVP/N-CNT, NVP/N-rGO and NVP/N-KB are in the same order of magnitude, showing no obvious difference in the various carbon matrices in which the NVP particles are embedded. However, the values reported in this work are much larger than those of pristine NVP materials, indicating the N-doped carbon coated materials to feature significantly improved electrochemical performance due to the enhanced electronic conductivity and charge transfer in the electrode/electrolyte interface.<sup>[80, 103]</sup>

**Table 2-4.** Calculated diffusion coefficients of Na<sup>+</sup> ( $D_{\text{Na}^+}$ , cm<sup>2</sup> s<sup>-1</sup>) in various N-doped carbon coated NVP composites.

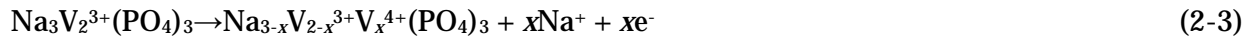
	NVP/N-C	NVP/N-CNT	NVP/N-rGO	NVP/N-KB
<b>Cathodic <math>D_{\text{Na}^+}</math></b>	$3.1 \times 10^{-12}$	$4.0 \times 10^{-12}$	$2.9 \times 10^{-12}$	$2.6 \times 10^{-12}$
<b>Anodic <math>D_{\text{Na}^+}</math></b>	$2.1 \times 10^{-12}$	$2.1 \times 10^{-12}$	$2.6 \times 10^{-12}$	$1.9 \times 10^{-12}$

In order to further investigate the superior rate performance of the NVP/N-CNT electrode, a galvanostatic cycling test at 50 C (5.5 A g<sup>-1</sup>) was performed, which results are reported in **Figure 2-16**. Even at such ultrahigh rate, the NVP/N-CNT electrode still delivers a reversible capacity of about 92 mAh g<sup>-1</sup> (80% of the capacity exhibited at 0.1 C) and presents an excellent capacity retention of 92% (84 mAh g<sup>-1</sup>) after 3000 cycles. The excellent rate and cycling performance is certainly ascribed to the surface modification by N-doping in the carbon layers, which result in a more efficient charge transfer process.<sup>[65]</sup>

**Figure 2-16.** Cycling performance of NVP/N-CNT at 50 C in sodium half-cell.

As reported, Na<sub>3</sub>V<sub>2</sub>(PO<sub>4</sub>)<sub>3</sub> exhibits electrochemical activity both at high and low potential values. Indeed, at a low potential values (around 1.6 V) the V<sup>3+/2+</sup> redox couple is active, while at high potential values (around 3.4 V) the V<sup>3+/4+</sup> redox couple is active. Accordingly, NVP can act as both positive and negative electrodes in sodium ion batteries.<sup>[49, 104]</sup> Therefore, the NVP/N-CNT-based sodium-ion cell in three-electrode configuration was investigated in the potential range of 1.4-3.6 V (vs. Na<sup>+</sup>/Na). The charge-discharge profiles of the 1<sup>st</sup> and 2<sup>nd</sup> cycles are shown in **Figure 2-17**.

The first charge capacity is about  $103 \text{ mAh g}^{-1}$ , attributable to a two-electron reaction (see reaction 2-3), while during the discharge process a specific capacity of  $179.0 \text{ mAh g}^{-1}$  is obtained when discharged to  $1.4 \text{ V}$  according to reaction (2-4) ( $0 \leq x \leq 2$ ,  $0 \leq y \leq 1$ ).



The NVP/N-CNT electrode delivers a capacity of  $179 \text{ mAh g}^{-1}$ ,  $159 \text{ mAh g}^{-1}$ ,  $154 \text{ mAh g}^{-1}$ ,  $142 \text{ mAh g}^{-1}$ ,  $135 \text{ mAh g}^{-1}$ ,  $123 \text{ mAh g}^{-1}$  at  $0.1 \text{ C}$ ,  $0.5 \text{ C}$ ,  $1 \text{ C}$ ,  $5 \text{ C}$ ,  $10 \text{ C}$ ,  $20 \text{ C}$ , respectively, and maintains a capacity of  $141 \text{ mAh g}^{-1}$  when turning the rate back to  $5 \text{ C}$ , demonstrating the excellent rate capability and reversibility of this material (**Figure 2-18a**) even in the very wide potential range. Moreover, the long-term cycling behavior reported in **Figure 2-18b** reveals the superior stability of the NVP/N-CNT material which exhibits a capacity retention of  $89\%$  after  $1000$  cycles at  $20 \text{ C}$  ( $2.2 \text{ A g}^{-1}$ ).

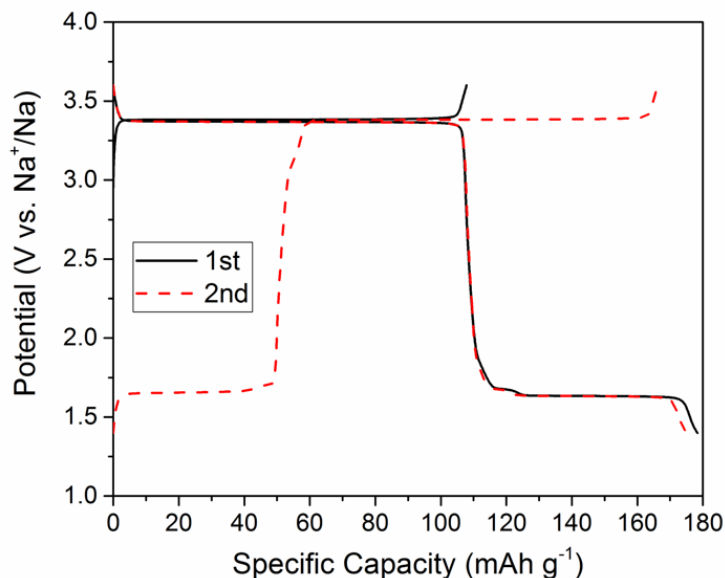


**Figure 2-17.** 1<sup>st</sup> and 2<sup>nd</sup> charge-discharge curves at  $0.1 \text{ C}$  of NVP/N-CNT in the potential range of  $1.4\text{-}3.6 \text{ V}$  (vs.  $\text{Na}^+/\text{Na}$ ).

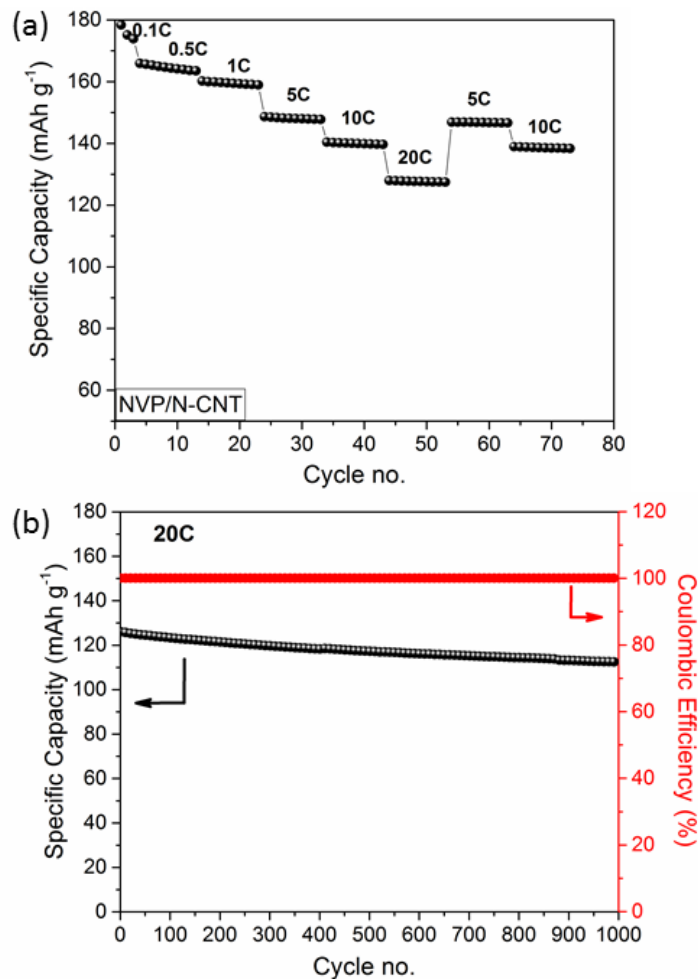


**Figure 2-18.** Rate capability test (a) and cycling performance at 20 C (b) of NVP/N-CNT composite in the potential range of 1.4V-3.6V (vs. Na<sup>+</sup>/Na).

To evaluate the anode performance of NVP composites, a symmetric two-electrode cell was fabricated (the cell is anode limited as resulting from the symmetric design). **Figure 2-19a** shows the charge-discharge curves of the symmetric cell at 0.1 C (11 mA g<sup>-1</sup>) within the 1.0-3.0 V voltage range. The NVP/N-CNT/ PC:FEC 98:2 %wt, 1M NaPF<sub>6</sub>/ NVP/N-CNT symmetric cell presents a flat plateau at 1.75 V, matching well with the potential difference between the two redox peaks at 3.40 V and 1.65 V. As anode, the NVP/N-CNT electrode delivers an initial discharge capacity of about 57 mA g<sup>-1</sup> at 0.1 C (a theoretical capacity of ~63 mAh g<sup>-1</sup> is calculated assuming the one-electron reaction). The stability test is performed by cycling the cell from 0.1 C to 20 C as shown in **Figure 2-19b**. At 20 C, the NVP/N-CNT anode maintains a capacity of 33 mAh g<sup>-1</sup>. These results suggest that the N-doped carbon coating enables the NVP materials as both high-performance positive and negative electrodes with superior rate capability and cycling stability.

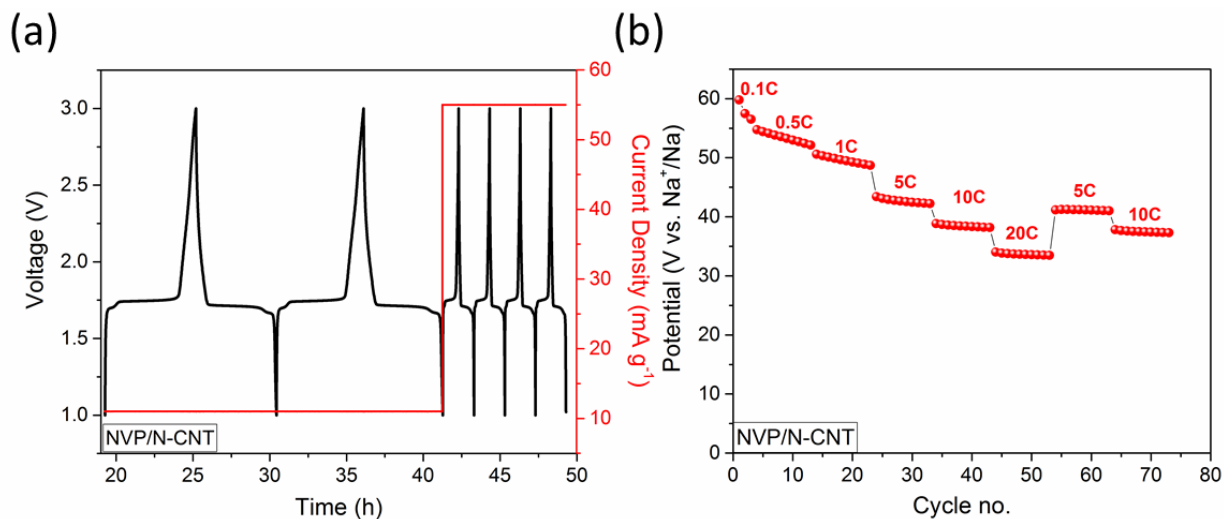


**Figure 2-19.** Charge-discharge curves (e) and rate capability test at various rates (f) of a NVP/N-CNT/ PC:FEC 98:2 wt.%, 1M NaPF<sub>6</sub>/NVP/N-CNT symmetric two-electrode sodium-ion cell in the 1.0-3.0 V voltage range.

#### 2.2.4 Conclusions

In summary, we have successfully developed a simple and low-cost method to synthesize well-crystallized NVP nanocomposites embedded in N-doped carbon matrix. Specifically, the pyrolytic carbon (C), carbon nanotubes (CNT), graphene oxide nanosheets (GO), and Ketjen black nanospheres (KB) were adopted as conductive templates to obtain NVP/N-C, NVP/N-CNT, NVP/N-rGO and NVP/N-KB composites with diverse architectural characters, and the electrochemical performance in half and full sodium-ion cells was systemically investigated. When used as cathodes in half-cell, these materials display outstanding rate capability and ultralong-term cyclability ( $\geq 80\%$  after 3000 cycles at 20 C). The results proved that the N-doped carbon modification could efficiently diminish the polarization of NVP materials due to enhanced conductivities and facilitated charge transfer in the electrode-electrolyte interface. Moreover, the NVP nanograins dispersed in N-doped carbon nanotube matrix exhibit the best rate and cycling performance (92 mAh g<sup>-1</sup> with a capacity retention of 92% after 3000 cycles at 50 C). Furthermore, a competitive performance was consistently observed in symmetric cells using NVP/N-CNT as both negative and positive electrodes, which reveals not only appropriate cathode performance but also superior anode performance. The achieved results suggest the practical utilization of nitrogen-doped carbon coated NVP materials as high performance electrode materials for sodium-ion batteries.



# Chapter 3

## High-voltage Cathodes with Phosphate Frameworks for Sodium-ion Batteries

The results in this chapter are partially published in the following publications:

1. **Zhang, H.**; Hasa, I.; Buchholz, D.; Qin, B.; Geiger, D.; Jeong, S.; Kaiser, U.; Passerini, S., Exploring the Ni Redox Activity in Polyanionic Compounds as Conceivable High Potential Cathodes for Na Rechargeable Batteries. *NPG Asia Materials* 2017, 9, e370.
2. **Zhang, H.**; Buchholz, D.; Passerini, S., Synthesis, Structure, and Sodium Mobility of Sodium Vanadium Nitridophosphate: A Zero-Strain and Safe High Voltage Cathode Material for Sodium-ion Batteries. *Energies* 2017, 10 (7), 889.

## 3.1 Mechanism Investigation of Ni Redox in Mixed-polyanionic Framework



### 3.1.1 Introduction

To date, the  $\text{LiFePO}_4$  olivine with  $(\text{PO}_4)^{3-}$  polyanionic framework, owing to its superior thermal stability and low cost, is considered as one of the best electrode material for LIBs mostly in view of its stable operating voltage and satisfactory specific capacity. However, the intrinsic tunability of the operating voltage of polyanionic compounds according to the presence of different transition metals such as Mn, Co, and Ni,<sup>[105-107]</sup> has triggered the interest in alternative frameworks exhibiting higher cell voltage. According to theoretical prediction, the lithium nickel phosphate has a remarkable high working potential ( $\sim 5.1$  V vs.  $\text{Li}^+/\text{Li}$ ) due to the  $\text{Ni}^{2+}/^{3+}$  redox activity.<sup>[47]</sup> Unfortunately, subsequent results have demonstrated that the implementation of this material is restricted by several drawbacks such as the intrinsic sluggish kinetics attributable to the low electronic conductivity, the poor lithium transport in commonly used electrolyte systems and the structural instability of the de-lithiated phases upon cycling, which require further studies for the obtainment of high performance Ni-based polyanionic phosphates as high voltage cathodes for battery application.<sup>[47, 108-115]</sup>

Averting the eyes to Na-based systems, considerable research has also been devoted to developing NASICON-type polyanionic materials such as  $\text{NaMPO}_4$ ,<sup>[43, 116]</sup>  $\text{Na}_2\text{MP}_2\text{O}_7$  (where M is a transition metal),<sup>[117, 118]</sup> and  $\text{Na}_3\text{V}_2(\text{PO}_4)_3$ <sup>[78, 119]</sup> as cathode materials for room temperature Na-ion batteries. However, the low energy densities resulting from the low theoretical capacity and generally low cell voltage, as well as the poor rate capability compared to their lithium have inhibited the widespread uptake of these materials.<sup>[13]</sup> Unlike  $\text{LiMPO}_4$ , the  $\text{NaMPO}_4$  thermodynamically stable phase obtained in conventional synthesis condition is the maricite phase, which is known to be electrochemically inactive respect to the olivine phase.<sup>[120, 121]</sup> Among the polyanionic frameworks, pyrophosphate compounds offer a stable three-dimensional  $(\text{P}_2\text{O}_7)^{4-}$  framework with multiple sites for sodium ions. It has been reported that Fe-based pyrophosphates exhibit enhanced rate capability performance most likely due to the presence of open diffusion pathways for sodium ions. Indeed, first principle calculations confirmed a relatively low migration barrier for the diffusion of the sodium ions.<sup>[117]</sup>

In this context, a new polyanionic compound of general formula  $\text{Na}_4\text{M}_3(\text{PO}_4)_2(\text{P}_2\text{O}_7)$  with  $\text{Fe}^{2+}/^{3+}$  redox couple has been proposed by Kang *et al.* as promising cathode in terms of its superior Na mobility and thermal stability.<sup>[45, 122]</sup> This material has a theoretical capacity of 129 mAh  $\text{g}^{-1}$  and

an operating potential of about 3.2 V vs. Na<sup>+</sup>/Na, which is higher than the one exhibited by NaFePO<sub>4</sub> and Na<sub>2</sub>FeP<sub>2</sub>O<sub>7</sub>.<sup>[44, 116]</sup> According to first principle calculation, the P<sub>2</sub>O<sub>7</sub> dimers can buffer the volume change during cycling (less than 4%) and offer Na diffusion pathways in the 3D open framework, which may ensure long-term cycling performance. Co-based polyanionic compounds show similar electrochemical properties with low conductivity and poor thermal stability as the Ni-based analogues in Li systems.<sup>[123, 124]</sup> However, the Na<sub>4</sub>Co<sub>3</sub>(PO<sub>4</sub>)<sub>2</sub>(P<sub>2</sub>O<sub>7</sub>) synthesized by a sol-gel method, shows an average working potential of ~4.4 V vs. Na<sup>+</sup>/Na and high rate capability for Na ions.<sup>[125]</sup> It is believed that a combination of different polyanionic groups could contribute to outstanding ion diffusion and voltage profile in Na ion batteries as well as structure stability during the Na (de-)insertion process. Interestingly, a theoretical prediction reported by Islam *et al.* has pointed out that doping the Na<sub>4</sub>Fe<sub>3</sub>(PO<sub>4</sub>)<sub>2</sub>(P<sub>2</sub>O<sub>7</sub>) with Ni can lead to a significant increase of the cell voltage.<sup>[126]</sup>

In light of such results, we report the synthesis and performance of a Ni-based polyanionic material for application as cathode for Na-ion batteries. In this work, the pristine and carbon coated materials, *i.e.* Na<sub>4</sub>Ni<sub>3</sub>(PO<sub>4</sub>)<sub>2</sub>(P<sub>2</sub>O<sub>7</sub>) and Na<sub>4</sub>Ni<sub>3</sub>(PO<sub>4</sub>)<sub>2</sub>(P<sub>2</sub>O<sub>7</sub>)/C, were stoichiometrically prepared by conventional solid-state method. This study represents an intriguing investigation both in terms of structural and electrochemical characterizations of Ni-based polyanions in Na battery. The high redox activity of the Ni<sup>2+/3+</sup> redox couple, predicted by previous theoretical calculations, is herein reported for the first time in sodium cells. The attractive possibility of using high operating voltage sodium-based cathode materials highlights the need of electrolyte media characterized by a wide electrochemical stability window thus a preliminary study using an ionic-liquid based electrolyte solution is also presented.

## 3.1.2 Experimental Methods

### 3.1.2.1 Materials synthesis

All chemicals were used as received without further purification. Syntheses were carried out by simple and time-efficient solid-state reaction. For the precursor preparation, sodium pyrophosphate decahydrate (Na<sub>4</sub>P<sub>2</sub>O<sub>7</sub>·10H<sub>2</sub>O, Alfa Aesar, ≥99%), nickel (II) acetate tetrahydrate (Ni(OCOCH<sub>3</sub>)<sub>2</sub>·4H<sub>2</sub>O (Alfa Aesar, ≥98%), and ammonium dihydrogen phosphate (NH<sub>4</sub>H<sub>2</sub>PO<sub>4</sub>), Merck Millipore, ≥99%) were mixed by ball-milling in acetone according to stoichiometric proportion. Citric acid monohydrate (C<sub>6</sub>H<sub>8</sub>O<sub>7</sub>·H<sub>2</sub>O, Alfa Aesar, ≥99%) was used as carbon source for the carbon coated sample. After intensive milling, the mixture was dried at room temperature and ground. The obtained precursor powder was preheated at 300 °C for 6h and then annealed at 500 °C (heating rate: 2 °C min<sup>-1</sup>) for 10h in an alumina crucible using a tubular furnace under

Ar flow. Cooling down to room temperature and grinding has followed. The carbon coated material was synthesized under the same condition using citric acid monohydrate as organic carbon source in the precursor preparation.

### 3.1.2.2 Materials characterization

X-ray diffraction analysis was performed in Bragg-Brentano geometry using a Bruker D8 Advance diffractometer (Bruker, Germany). All diffractograms were recorded with  $\text{CuK}_\alpha$  radiation ( $\lambda = 0.154 \text{ nm}$ ) in the  $2\theta$  range of  $10^\circ - 90^\circ$  with a step size of  $0.01^\circ$ . The structures were refined using the Rietveld method with the DIFFRAC PLUS TOPAS 4.2 software (Bruker, Germany). Morphological and structural characterizations were conducted *via* ZEISS 1550VP Field Emission SEM (Carl Zeiss, Germany) and Cs-corrected FEI Titan 80-300 kV High-resolution Transmission Electron Microscopy operated at an acceleration voltage of 80kV and 300kV (FEI, Netherlands). Thermal gravimetric analysis (TGA) was performed using a thermogravimetric analyzer (TGA-209F, Netzsch, Germany) under  $\text{O}_2$  flow of  $20 \text{ ml min}^{-1}$  within the temperature range of 30- 600 °C temperature range at  $5 \text{ }^\circ\text{C min}^{-1}$  scan rate.

### 3.1.2.3 Electrochemical characterization

The electrochemical tests were performed using three electrode Swagelok-type cells assembled in an argon-filled glove box. Sodium half-cells were assembled by using glass fiber (Whatman) as separators soaked in various electrolyte solutions and sodium metal as counter and reference electrodes. 1M  $\text{NaPF}_6$  (Alfa Aesar, 99%) in ethylene carbonate (EC) : diethyl carbonate (DEC) (1:1 w/w) (BASF, Battery Grade) and ionic liquid solutions were used as electrolytes. The ionic liquid-based electrolyte was prepared by dissolving 10 mol% NaTFSI (sodium bis(trifluoromethanesulfonyl)imide, SOLVIONIC, 99.5%) in  $\text{Py}_{13}\text{FSI}$  (N-propyl-N-methylpyrrolidinium bis(fluorosulfonyl)imide). Sodium metal was cut from sodium pieces (99.8%, Acros Organics), roll pressed and punched on the current collector. The electrodes were prepared by doctor-blade casting a slurry prepared by dispersing 80 wt% of active material, 10 wt% of carbon black as conductive agent (Super C65, IMERYS) and 10 wt% of polyvinylidene fluoride (PVDF 6020 Solef, Solvay Group) binder in N-methyl-2-pyrrolidone (NMP, anhydrous, 99.5%, Sigma-Aldrich) on Al foil as current collector. After drying, electrodes with a 12 mm diameter were punched, pressed and dried again. The mass loading is approximately  $\sim 2.8 \text{ mg cm}^{-2}$ . The cells were assembled in an argon-filled glove box with  $\text{H}_2\text{O}$  and  $\text{O}_2$  contents lower than 1 ppm. A Maccor 4000 Battery system (Maccor, USA) was used for the galvanostatic charge/discharge test between 3.0-4.9 V vs.  $\text{Na}^+/\text{Na}$  in organic electrolyte and 3.0-5.1 V vs.  $\text{Na}^+/\text{Na}$  in ionic liquid electrolyte at a current density of  $10 \text{ mA g}^{-1}$ . Cyclic voltammetry was performed on a multichannel

potentiostat/galvanostat (VMP3, Biologic Science Instruments, France) using a scan rate of 0.01 mV s<sup>-1</sup>, 0.05 mV s<sup>-1</sup>, 0.1 mV s<sup>-1</sup>, and 0.5 mV s<sup>-1</sup> in a voltage range of 3.0-5.0 V vs. Na<sup>+</sup>/Na (organic electrolyte) and 3.0-5.2 V vs. Na<sup>+</sup>/Na (ionic liquid electrolyte). All the potential values in the manuscript are referred to the Na<sup>+</sup>/Na reference electrode. All measurements were performed in climatic chambers at a temperature of 20 ± 1 °C.

### 3.1.3 Results and Discussion

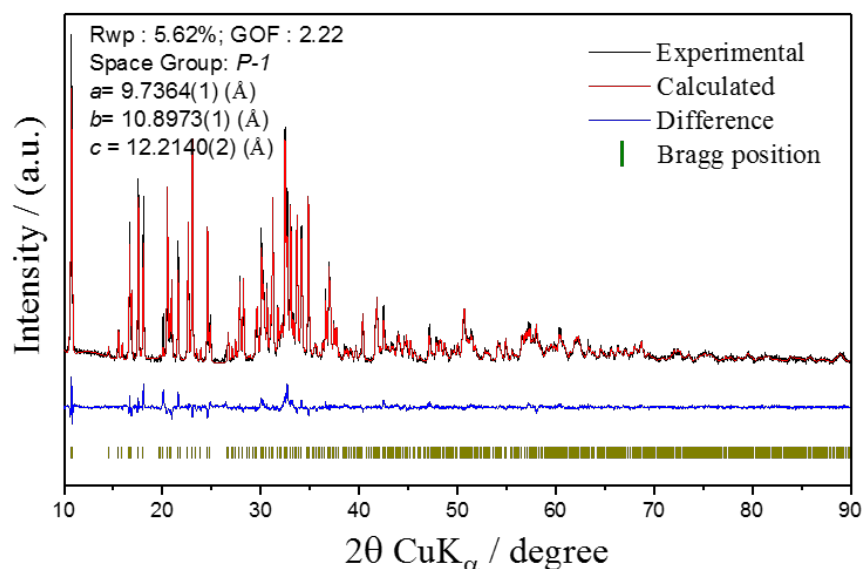


**Figure 3-1.** Rietveld refinement of powder XRD for Na<sub>2</sub>NiP<sub>2</sub>O<sub>7</sub>.

Firstly, NaNiPO<sub>4</sub> and Na<sub>2</sub>NiP<sub>2</sub>O<sub>7</sub> polyanions, which are expected to have higher working potential due to the Ni redox couple, were synthesized via solid state method. As the Co-based compound, the stoichiometric Na<sub>2</sub>NiP<sub>2</sub>O<sub>7</sub> crystallizes in the triclinic *P*-1 space group. The obtained XRD pattern is shown in **Figure 3-1**. However, as shown in **Figure 3-2**, this material shows no electrochemical activity in Na cell. NaNiPO<sub>4</sub> has been also synthesized, however orthorhombic Na<sub>4</sub>Ni<sub>3</sub>(PO<sub>4</sub>)<sub>2</sub>(P<sub>2</sub>O<sub>7</sub>) was obtained instead of maricite NaNiPO<sub>4</sub>, reflecting the preferably thermodynamical stability of Na<sub>4</sub>Ni<sub>3</sub>(PO<sub>4</sub>)<sub>2</sub>(P<sub>2</sub>O<sub>7</sub>). The obtained XRD pattern is presented in **Figure 3-3**.

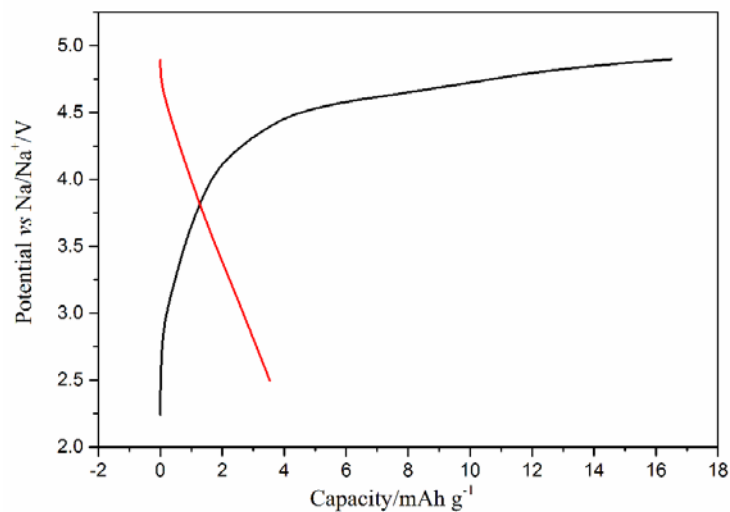


**Figure 3-2.** The 1<sup>st</sup> galvanostatic charge-discharge curves of  $\text{Na}_2\text{NiP}_2\text{O}_7$  at  $10 \text{ mA g}^{-1}$  in the potential range of 2.5-4.9 V.

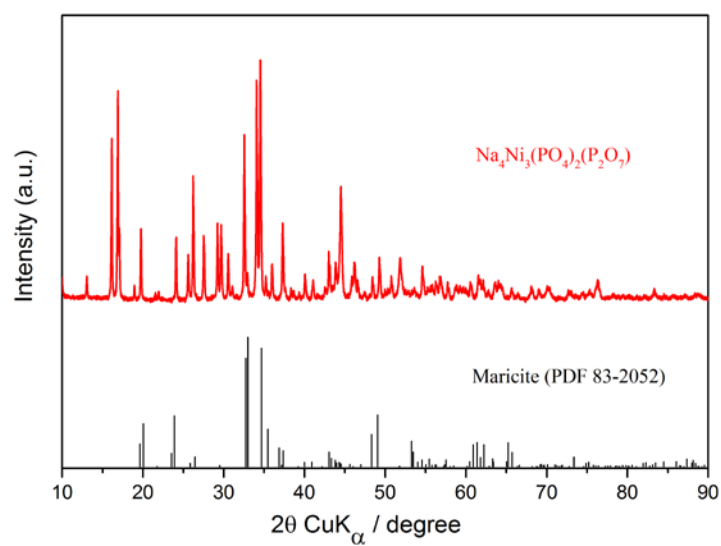


**Figure 3-3.** XRD pattern of the product from  $\text{NaNiPO}_4$  synthesis.

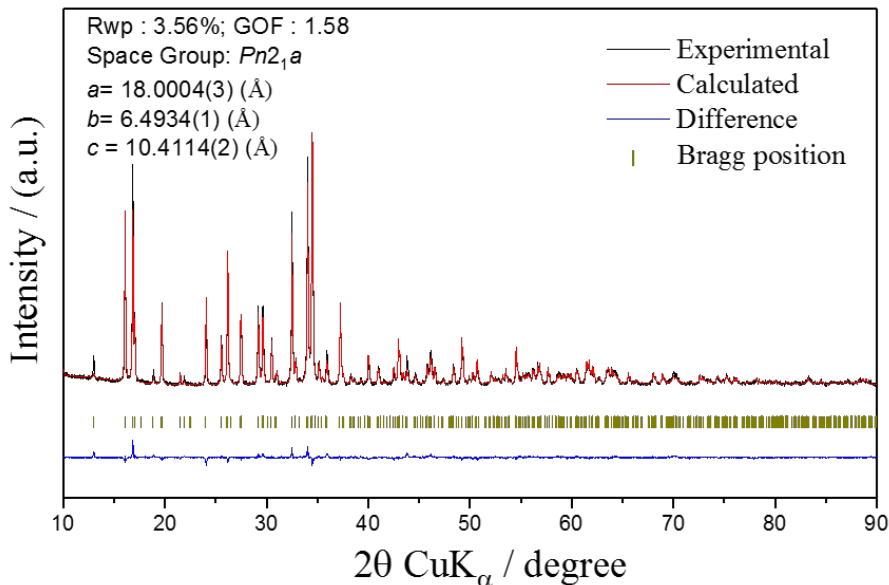


**Figure 3-4.** Rietveld refinement of powder XRD for  $\text{Na}_4\text{Ni}_3(\text{PO}_4)_2(\text{P}_2\text{O}_7)$ .

The  $\text{Na}_4\text{Ni}_3(\text{PO}_4)_2(\text{P}_2\text{O}_7)$  was synthesized via solid-state method. And the crystal structure has been confirmed by X-ray diffraction analysis. **Figure 3-4** shows the Rietveld refinement for  $\text{Na}_4\text{Ni}_3(\text{PO}_4)_2(\text{P}_2\text{O}_7)$ . Structure parameters were refined based on X-ray diffraction data. This confirms that the  $\text{Na}_4\text{Ni}_3(\text{PO}_4)_2(\text{P}_2\text{O}_7)$  compound is isostructural to  $\text{Na}_4\text{Fe}_3(\text{PO}_4)_2(\text{P}_2\text{O}_7)$  (ICSD: 236316) and crystallizes in the orthorhombic  $Pn2_1a$  space group with  $a = 18.000(4)$  Å,  $b = 6.493(4)$  Å and  $c = 10.411(4)$  Å. The refinement has been performed with a satisfactory agreement factor ( $R_{\text{wp}} = 3.56\%$ ,  $R_{\text{p}} = 2.67\%$ , Goodness of fit (GOF) = 1.58). The refined cell parameters and atomic occupancy values are summarized and presented respectively in **Table S3-1** and **Table S3-2** in **Appendix**. The crystallographic density of pristine  $\text{Na}_4\text{Ni}_3(\text{PO}_4)_2(\text{P}_2\text{O}_7)$  is  $3.45 \text{ g cm}^{-3}$ . The XRD pattern for  $(\text{Na}_4\text{Ni}_3(\text{PO}_4)_2(\text{P}_2\text{O}_7)/\text{C})$  is shown in **Figure 3-5**. It is shown that the carbon coating process has no effect on the structural characteristics of the material, which crystallizes in the same space group with comparable cell parameters.

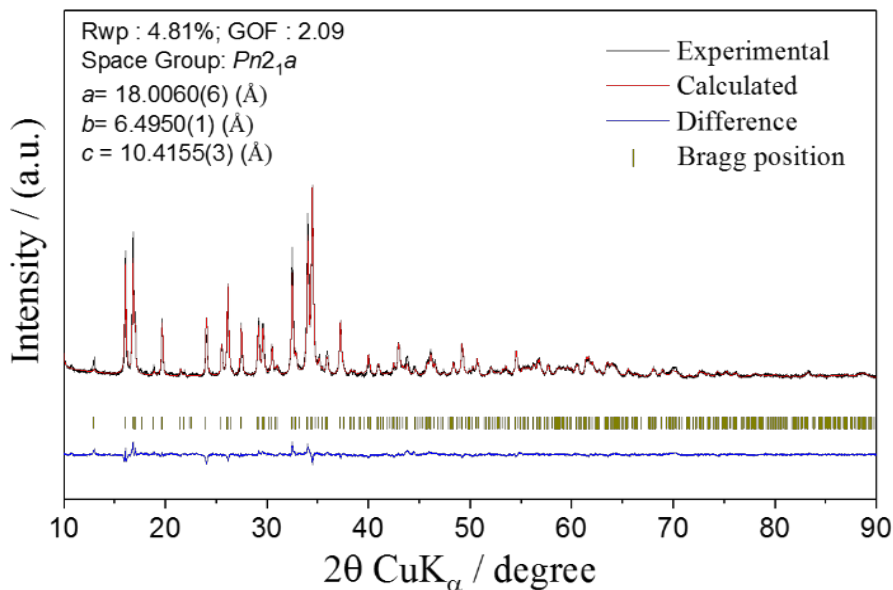


**Figure 3-5.** Rietveld refinement of XRD for  $\text{Na}_4\text{Ni}_3(\text{PO}_4)_2(\text{P}_2\text{O}_7)/\text{C}$  composite.

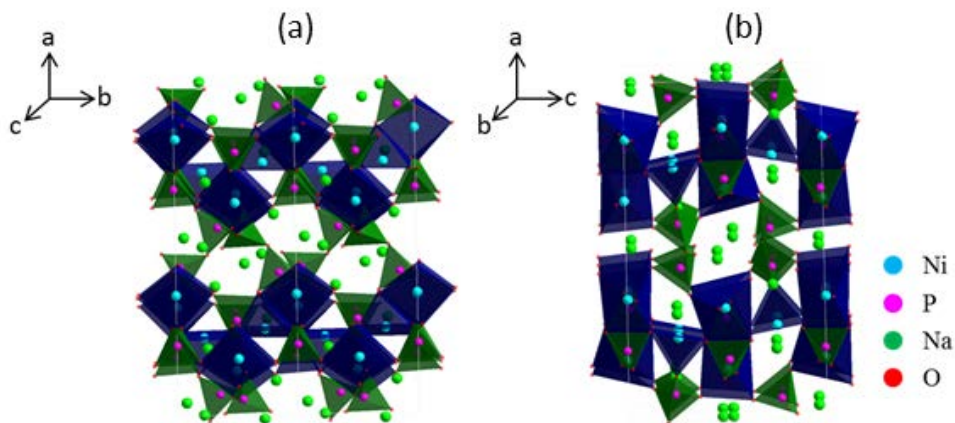


**Figure 3-6.** Schematic representation of  $\text{Na}_4\text{Ni}_3(\text{PO}_4)_2(\text{P}_2\text{O}_7)$  crystal structure viewed along the [001] and [010] directions.

The crystal structures of  $\text{Na}_4\text{Ni}_3(\text{PO}_4)_2(\text{P}_2\text{O}_7)$  viewed along the [001] and [010] directions are displayed in **Figure 3-6** (a) and (b). As the isostructural  $\text{Na}_4\text{Co}_3(\text{PO}_4)_2(\text{P}_2\text{O}_7)$  and  $\text{Na}_4\text{Fe}_3(\text{PO}_4)_2(\text{P}_2\text{O}_7)$ , the crystal structure of  $\text{Na}_4\text{Ni}_3(\text{PO}_4)_2(\text{P}_2\text{O}_7)$  is composed of 3D network layers of  $[\text{Ni}_3\text{P}_2\text{O}_{13}]_\infty$  jointly composed by  $\text{NiO}_6$  octahedra and  $(\text{PO}_4)^{3-}$  tetrahedra in the  $bc$  plane, which are bridged by the  $(\text{P}_2\text{O}_7)^{4-}$  dimers generating large channels along the  $b$ -axis with low activation barrier energy for  $\text{Na}^+$  ion diffusion.<sup>[45, 127]</sup> The Na ions occupy four distinguishable sites among which two (Na1 and Na4) are located in the large channels parallel to the  $b$ -axis. The Ni-based polyanions have been so far considered as electrochemically inactive cathode materials in both Li



and Na systems due to the low electronic conductivity resulting in the poor alkali ion diffusion activity.<sup>[115]</sup> However, in this study, the structure deriving from the mixed polyanionic  $\text{Na}_4\text{Ni}_3(\text{PO}_4)_2(\text{P}_2\text{O}_7)$  may stabilize the charged Ni analogue and open pathways for the improved and reversible  $\text{Na}^+$  diffusion.

Scanning electron microscopy (SEM) and high-resolution transmission electron microscopy (HRTEM) analysis were conducted to assess the morphological and structural aspects of the synthesized powders. **Figure 3-7a**, and **b** present the SEM images of  $\text{Na}_4\text{Ni}_3(\text{PO}_4)_2(\text{P}_2\text{O}_7)$  and  $\text{Na}_4\text{Ni}_3(\text{PO}_4)_2(\text{P}_2\text{O}_7)/\text{C}$ . The pristine  $\text{Na}_4\text{Ni}_3(\text{PO}_4)_2(\text{P}_2\text{O}_7)$  aggregates in shapeless micrometric particles, (*i.e.* polymorphic morphology). After the carbon coating treatment, the particle size of the powder is favorably reduced with well-defined edges. The transition electron microscopy (TEM) analysis of  $\text{Na}_4\text{Ni}_3(\text{PO}_4)_2(\text{P}_2\text{O}_7)/\text{C}$ , reported in **Figure 3-7c**, confirms the shapeless character of the particles which shows a sub-micrometric dimension with an average diameter of about 500 nm. Additionally, the HR-TEM image in **Figure 3-7d** shows clearly a lattice fringe of  $d=0.680$  nm, corresponding to the (201) plane diffraction of  $\text{Na}_4\text{Ni}_3(\text{PO}_4)_2(\text{P}_2\text{O}_7)/\text{C}$ .

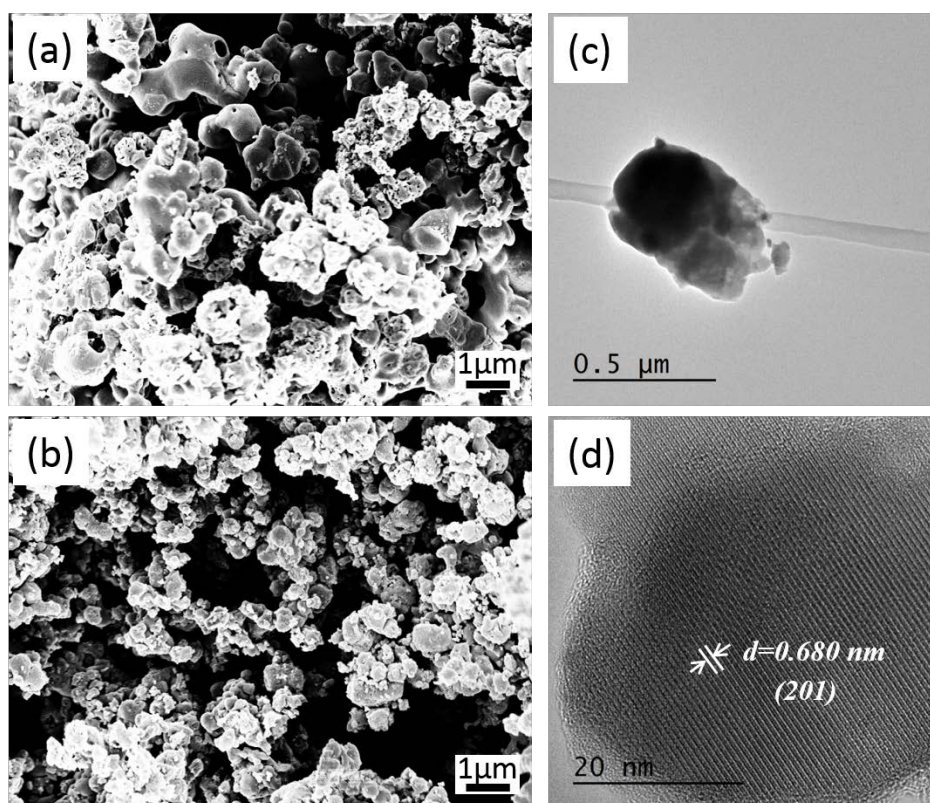


**Figure 3-7.** SEM images of (a)  $\text{Na}_4\text{Ni}_3(\text{PO}_4)_2(\text{P}_2\text{O}_7)$  and (b)  $\text{Na}_4\text{Ni}_3(\text{PO}_4)_2(\text{P}_2\text{O}_7)/\text{C}$  powders. (c, d) TEM images of  $\text{Na}_4\text{Ni}_3(\text{PO}_4)_2(\text{P}_2\text{O}_7)/\text{C}$ .

Thermal gravimetric analysis (TGA) was performed to investigate the thermal stability and carbon content of the prepared materials and results are presented in **Figure 3-8**. The thermogram of pristine  $\text{Na}_4\text{Ni}_3(\text{PO}_4)_2(\text{P}_2\text{O}_7)$  shows a slight weight loss before 100 °C attributable most likely to water desorption. The weight loss detected from 300 °C is related to the oxidation of residual carbon belonging to the organic salt precursor. Meanwhile, there is no weight loss observed after 500 °C even exposed in  $\text{O}_2$ , reflecting a considerable high thermal stability. The content of absorbed water in the carbon coated material is higher than in the pristine one, suggesting a higher sensitivity to moisture, most likely due to a higher surface area. The carbon content is calculated to be about 6.3% which corresponds to the weight detected within the 100-450 °C temperature range.

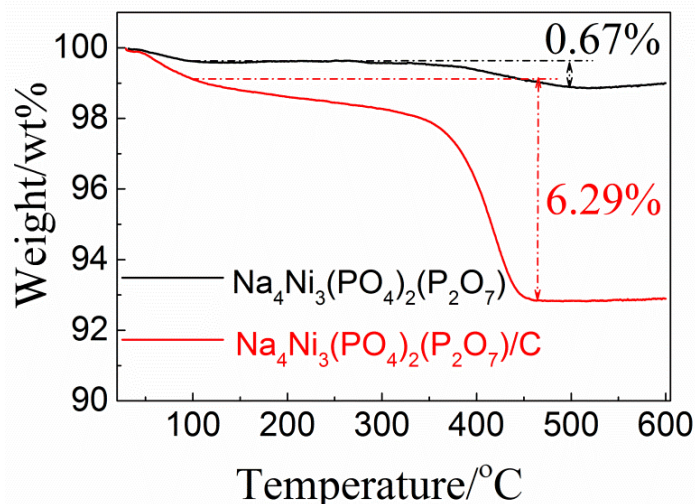


**Figure 3-8.** TG curves of  $\text{Na}_4\text{Ni}_3(\text{PO}_4)_2(\text{P}_2\text{O}_7)$  and  $\text{Na}_4\text{Ni}_3(\text{PO}_4)_2(\text{P}_2\text{O}_7)/\text{C}$  under  $\text{O}_2$  flow.

The electrochemical properties of the prepared materials were investigated in three electrode Swagelok-type sodium cells. Considering the low conductivity of Ni-based polyanions, we adopt  $\text{Na}_4\text{Ni}_3(\text{PO}_4)_2(\text{P}_2\text{O}_7)/\text{C}$  for the investigation. **Figure 3-9a** displays the CV curve of a three electrode cell cycled within the 5.0-3.0 V potential range using 1M  $\text{NaPF}_6$  in EC:DEC (1:1 w/w) electrolyte. The CV curve exhibits three anodic peaks at 4.58 V, 4.64 V, 4.96 V and only two cathodic peaks at 4.61 V and 4.90 V. To further investigate the redox activity at higher voltage values, an ionic liquid-based electrolyte with a wider electrochemical stability window and a satisfactory ionic conductivity was employed.<sup>[128-132]</sup> The CV curve in the potential range of 3.0-5.2V (vs.  $\text{Na}^+/\text{Na}$ ) using NaTFSI in  $\text{Py}_{13}\text{FSI}$  (with a mole ratio of 1:9) was performed as shown in **Figure 3-9b**. As the carbonate-based electrolyte, three anodic peaks at 4.61 V, 4.67 V, 5.01 V and only two cathodic peaks at 4.58 V and 4.92 V are observed employing the ionic liquid-based electrolyte. Above 5.1V, a significant oxidation of electrolyte was observed.

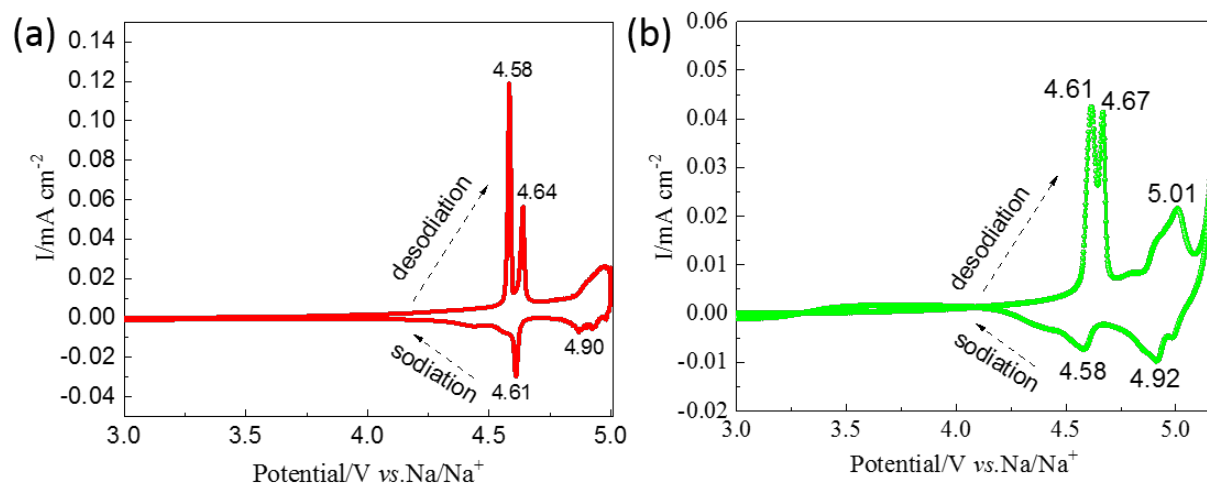


**Figure 3-9.** CV curves of  $\text{Na}_4\text{Ni}_3(\text{PO}_4)_2(\text{P}_2\text{O}_7)/\text{C}$  at a scan rate of  $0.01 \text{ mV s}^{-1}$  (a) in potential range of 3.0-5.0 V using 1M  $\text{NaPF}_6$  in EC:DEC (1:1 w/w) electrolyte and (b) in the potential range of 3.0-5.2 V using NaTFSI :  $\text{Py}_{13}\text{FSI}$  (1:9 mole ratio) electrolyte.

**Figure 3-10** shows the galvanostatic charge/discharge profiles of  $\text{Na}_4\text{Ni}_3(\text{PO}_4)_2(\text{P}_2\text{O}_7)/\text{C}$  in 1M  $\text{NaPF}_6$  in EC : DEC (1:1 w/w) and NaTFSI :  $\text{Py}_{13}\text{FSI}$  (1:9 mole ratio) electrolytes at the constant current density of  $10 \text{ mA g}^{-1}$ . During the first de-sodiation process (charge) up to 4.9V in the carbonate electrolyte, about 2.3 equivalent of Na are extracted from the electrode material, contributing to a specific capacity of about  $97 \text{ mAh g}^{-1}$ . However, in the following discharge step only 0.9 equivalent of sodium are re-inserted reversibly into the host structure with a total coulombic efficiency of the first (de-)sodiation process of about 40%. The voltage profile clearly suggests the redox activity of nickel at voltage values higher than 4.5 V, which is in good agreement with the CV profile.

In the ionic liquid electrolyte, the profile reveals the de-insertion of 2.7 equivalents Na following an insertion of 1.3 equivalents Na corresponding to a discharge capacity of  $63 \text{ mAh g}^{-1}$ , which is a remarkably higher value than the one obtained in the EC:DEC based electrolyte. Cycling performance demonstrates that the  $\text{Na}_4\text{Ni}_3(\text{PO}_4)_2(\text{P}_2\text{O}_7)/\text{C}$  delivers a discharge capacity of  $63 \text{ mAh g}^{-1}$  and a capacity of  $48 \text{ mAh g}^{-1}$  is maintained with retention of about 71 % after 10 cycles, suggesting a reversible redox process occurring at such high working potential, as shown in **Figure 3-11**.

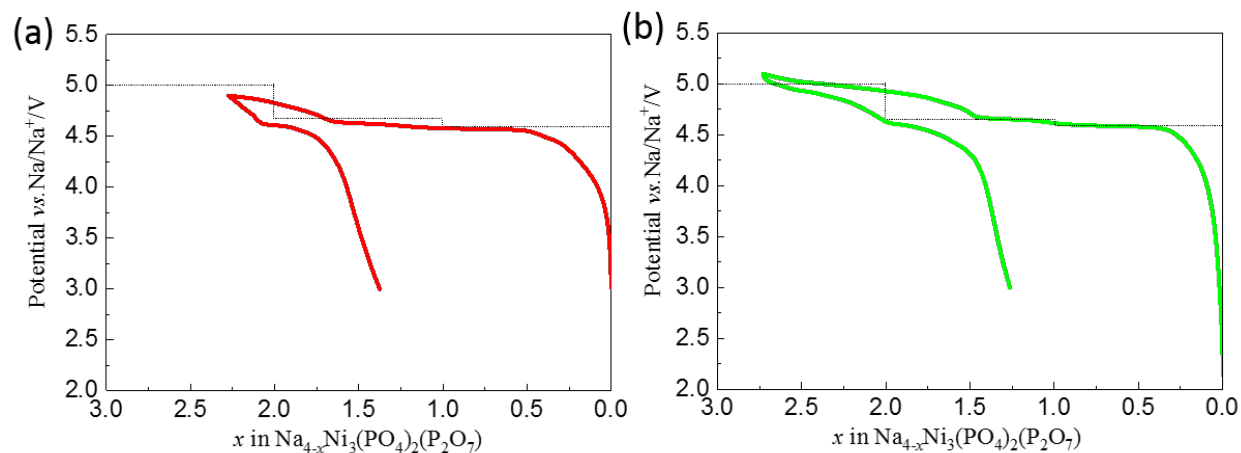


**Figure 3-10.** The 1<sup>st</sup> galvanostatic charge/discharge profiles of  $\text{Na}_4\text{Ni}_3(\text{PO}_4)_2(\text{P}_2\text{O}_7)/\text{C}$  in 1M  $\text{NaPF}_6$  in EC : DEC (1:1 w/w) (a) and  $\text{NaTFSI} : \text{Py}_{13}\text{FSI}$  (1:9 mole ratio) (b) electrolytes at the constant current density of  $10 \text{ mA g}^{-1}$ .

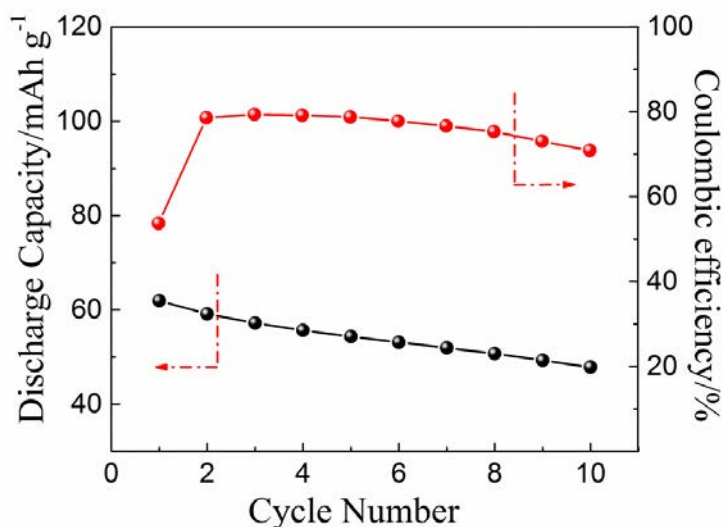


**Figure 3-11.** Cycling performance of  $\text{Na}_4\text{Ni}_3(\text{PO}_4)_2(\text{P}_2\text{O}_7)/\text{C}$  in  $\text{NaTFSI} : \text{Py}_{13}\text{FSI}$  (1:9 mole ratio) electrolyte between 3.0-5.1 V (vs.  $\text{Na}^+/\text{Na}$ ) at  $10 \text{ mA g}^{-1}$ .

The investigation of wider potential window shows clearly that there is no further redox process at potential values higher than 5.0 V and that the higher charge capacity observed may be ascribed also to electrolyte decomposition. In addition, aluminum current collector corrosion and possible oxidation of the carbon deriving from the carbon coating process, which may also affect the cycling performance, cannot be excluded at such high potential values vs.  $\text{Na}^+/\text{Na}$ .<sup>[133-136]</sup> However, the

used ionic liquid based electrolyte enables the achievement of a higher discharge capacity. Regardless of its high working potential, the material exhibits relatively low coulombic efficiency and poor cycling stability compared to the reported polyanionic compounds in both organic and ionic liquid electrolytes. To better understand the factors affecting the electrochemical performance exhibited, further structural investigation has been performed. It has been proposed that structural reorganization upon cycling could affect the reversibility of the sodium (de-)insertion. Indeed, the structural changes during Na (de-)insertion may derive from the instability of the de-sodiated electrode, most likely due to the distortion of  $P_2O_7$  dimers and changes of the unit cell volume.<sup>[45, 47]</sup>

The investigation of the Na (de-)insertion mechanism in  $Na_4Ni_3(PO_4)_2(P_2O_7)/C$  electrode was carried out by *ex situ* XRD measurements at different state of charge. **Figure 3-12a** displays the typical charge/discharge profile of a  $Na//Na_4Ni_3(PO_4)_2(P_2O_7)/C$  cell with points and letters indicating the potential values at which X-ray diffraction analysis has been performed. When charging the electrode to 5.0 V in EC:DEC based-electrolyte, the initial charge capacity is higher than the theoretical capacity, which can be attributed due to the cathode-electrolyte interphase (CEI) film formation on the surface of Ni-based electrode materials at such high working potential. [137, 138] The patterns collected in the  $10-60^\circ$   $2\theta$  range are displayed in **Figure 3-12b**. As shown the main reflections of the mixed polyanionic phase are maintained upon charge and discharge, while moderate peak shifting and intensity changes occur, suggesting no phase transition occurring during sodium (de-)insertion. The amplified XRD patterns in the  $2\theta$  range of  $10-25^\circ$  and  $25-35^\circ$  in **Figure 3-12c, d** clearly show the peak shifts during the electrochemical reaction. Interestingly, although the (200) peak at about  $10^\circ$  is moving to higher  $2\theta$  direction, other major peaks such as (011), (111), (220) and (022) show a slight shift to lower  $2\theta$  when the Na is extracted from the host material. During the discharge process, the peaks gradually move back to the original positions, suggesting the reversibility of the structural modifications associated to the volume change during the Na (de-)insertion.

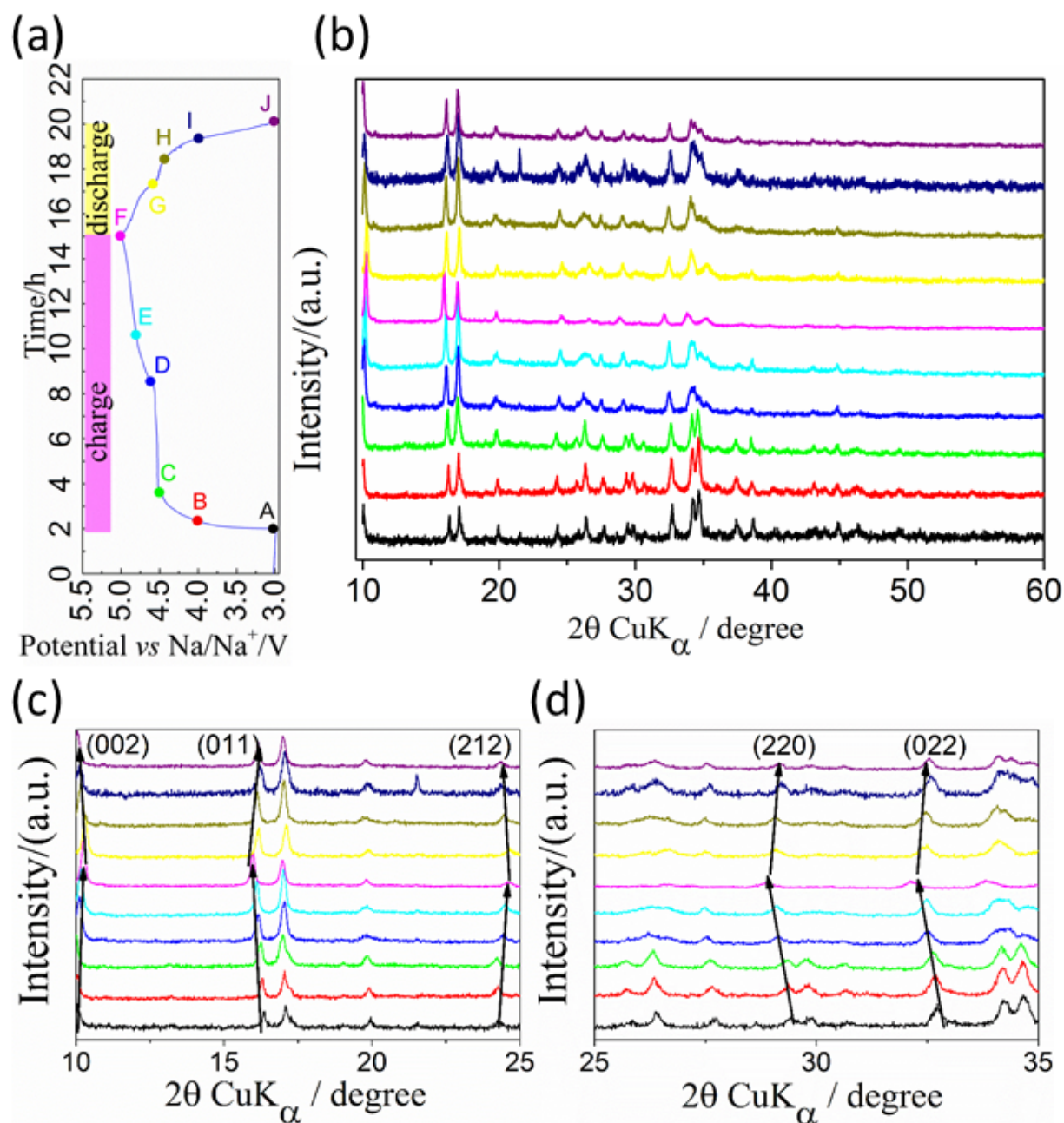


**Figure 3-12.** (a) Typical charge/discharge profile of  $\text{Na}_4\text{Ni}_3(\text{PO}_4)_2(\text{P}_2\text{O}_7)/\text{C}$  electrode. (b) *Ex-situ* XRD pattern of  $\text{Na}_4\text{Ni}_3(\text{PO}_4)_2(\text{P}_2\text{O}_7)/\text{C}$  electrode at various charge and discharge states. (c, d) Amplified XRD patterns in the  $2\theta$  range of 10-25°, 25-35°, respectively.

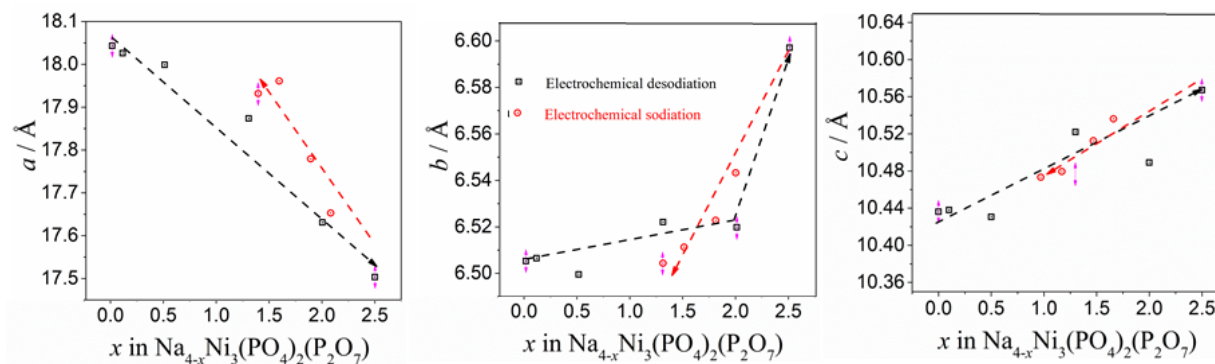


**Figure 3-13.** Lattice parameters ( $a, b, c$ ) changes of  $\text{Na}_{4-x}\text{Ni}_3(\text{PO}_4)_2(\text{P}_2\text{O}_7)/\text{C}$  during electrochemical charge/discharge process.

To investigate the mechanism of sodium (de-)insertion of the four different kinds of Na ions hosted in the structure, Rietveld refinement of the *ex-situ* XRD patterns has been performed. The evolution of the refined lattice parameters ( $a, b, c$ ) is shown in **Figure 3-13**. The  $a$  lattice parameter value decreases instantaneously when the Na ions are electrochemically removed from the crystal structure while  $b$  and  $c$  show an almost unchanged value until a potential value of 5.0 V is reached. The results herein reported slightly differ from those already reported for the Fe-based analogue system, suggesting different structural changes in the potential range investigated.<sup>[45, 122]</sup>

The Na occupancy values, reported in **Table 3-1**, indicate that Na1 and Na4, located in the large channels constructed by the  $\text{P}_2\text{O}_7$  dimers can be firstly electrochemically removed at relatively low voltage values resulting in the decrease of  $a$  lattice parameter and leading to a volume change of 3%. When charging up to 5.0 V, the other two Na ions, i.e. Na2 and Na3, are extracted subsequently, leading to the drastic increase of the  $b$  and  $c$  parameters. It should be noted that, when discharged back to 3.0 V, the lattice parameter values observed are slightly different from those of the pristine sample, suggesting a not fully reversible electrochemical process, as well indicated by the electrochemical characterization above. The low reversibility may be ascribed to the collapse of  $[\text{Ni}_3\text{P}_2\text{O}_{13}]_\infty$  layers along  $a$  axis to a certain extent blocking the Na diffusion channels, which confirms the instability of the de-sodiated electrode and reflects the low coulombic efficiency of the charge-discharge process. Further experimental analysis and theoretical studies should be devoted to this aspect. However, the superior thermal stability and small volume changes during cycling of the material demonstrate the advantages of using mixed polyanionic structures to construct large diffusion channel for Na ions proving this strategy as an efficient way to develop Ni-based polyanions for practical application as cathodes in Na-ion batteries.

**Table 3-1** Na occupancy during the charge/discharge process and expected values from the Rietveld refinement.

	<b>Na1 occ</b>	<b>Na2 occ</b>	<b>Na3 occ</b>	<b>Na4 occ</b>	<b>R<sub>wp</sub>/%</b>	<b>GOF</b>
<b>OCV</b>	1	1	1	1	10.89	1.14
<b>1<sup>st</sup> charge: 4.0 V</b>	0.9485	0.9999	1	1	9.43	1.21
<b>1<sup>st</sup> charge: 4.5 V</b>	0.5580	0.9999	1	0.9462	9.67	1.44
<b>1<sup>st</sup> charge: 4.6 V</b>	0.0986	0.9999	1	0.7204	12.56	2.10
<b>1<sup>st</sup> charge: 4.8 V</b>	0	0.916	1	0	12.79	2.38
<b>1<sup>st</sup> charge: 5.0 V</b>	0	0.7512	0.7201	0	12.78	2.48
<b>1<sup>st</sup> discharge: 4.6 V</b>	0	0.9996	0.9996	0	11.23	1.57
<b>1<sup>st</sup> discharge: 4.5 V</b>	0.1347	1	1	0.3632	10.68	1.75
<b>1<sup>st</sup> discharge: 4.0 V</b>	0.1278	1	1	0.4935	11.52	1.29
<b>1<sup>st</sup> discharge: 3.0 V</b>	0.4068	1	1	0.5598	9.12	1.51

### 3.1.4 Conclusions

In summary, we have synthesized the  $\text{Na}_4\text{Ni}_3(\text{PO}_4)_2(\text{P}_2\text{O}_7)$  polyanions via conventional solid state method and investigated such a material as cathode in Na-ion batteries. The carbon coating process allows the obtainment of a cathode material able to deliver a capacity of  $\sim 63 \text{ mAh g}^{-1}$  at an average potential of  $\sim 4.8\text{V}$  vs  $\text{Na}^+/\text{Na}$  when using ionic liquid-based electrolyte. In spite of the specific capacity delivered by the materials, we believe that further improvement of the electrochemical performance in terms of delivered capacity, open promises for the obtainment of high energy density Na-ion batteries due to the redox activity of nickel at high working potential. The mixed polyanionic structure, combining phosphate and pyrophosphate frameworks allows, thanks to the  $\text{P}_2\text{O}_7$  dimers, the construction of large Na diffusion channels and small volume changes during cycling, which represent a step forward the overcoming the drawbacks of Ni-analogues with low ionic/electronic conductivity and poor structural stability. The work herein presented, shows, for the first time, the realization of Ni-based mixed polyanionic compounds for application in sodium-ion battery with satisfactory performance and paves way for the discovery of new Na-based high potential cathode materials.



## 3.2 Nitridophosphate $\text{Na}_3\text{V}(\text{PO}_3)_3\text{N}$ as a Zero-strain and Safe High Voltage Cathode Material

### 3.2.1 Introduction

Since the energy of a battery is largely dependent on the gravimetric and volumetric capacities and operating voltages of the electrode materials, exploration on suitable active materials is highly-targeted. In this pursuit, there have been intensive efforts on expanding the range of available structural families. One strategy is to develop Na-containing host materials from lithium analogues. Such efforts have resulted in tremendous successes in realizing some known polyanionic frameworks, such as phosphate  $\text{NaMPO}_4/\text{Na}_3\text{M}_2(\text{PO}_4)_3$ ,<sup>[78, 120]</sup> pyrophosphate  $\text{Na}_2\text{MP}_2\text{O}_7$ ,<sup>[117]</sup> fluorophosphate  $\text{NaMPO}_4\text{F}/\text{Na}_3\text{M}_2(\text{PO}_4)_2\text{F}_3$ ,<sup>[139, 140]</sup> sulfate  $\text{Na}_x\text{M}(\text{SO}_4)_2$ ,<sup>[141]</sup> fluorosulphate  $\text{NaMSO}_4\text{F}$ ,<sup>[142]</sup> silicate  $\text{Na}_2\text{M}(\text{SiO}_4)$ ,<sup>[143]</sup> and mixed polyanionic  $\text{Na}_4\text{M}_3(\text{PO}_4)_2(\text{P}_2\text{O}_7)$ <sup>[126, 144]</sup> compounds. Basically, the electrochemical properties of anticipated polyanion electrode materials, including the operating potential and specific capacity, rely on the  $\text{M}^{n+}/\text{M}^{(n+x)+}$  redox process and the natures of polyanionic frameworks, *i.e.* electronegativity, and molecular weight.<sup>[145]</sup> Among these reported polyanion cathodes, the NASICON-type  $\text{Na}_3\text{V}_2(\text{PO}_4)_3$  in a rhombohedral structure with the space group *R-3c* attracts particular interests due to the vanadium redox couple, enabling a relatively high working voltage of  $\sim 3.4$  V (*vs.*  $\text{Na}^+/\text{Na}$ ), and the framework of  $\text{PO}_4$ , enabling superior thermal stability.<sup>[70, 78]</sup> During the course of the investigation of the vanadium-based phosphate family, it was found that doping with the more electronegative fluoride can enhance the operating potential of electroactive materials. For example, the  $\text{Na}_3\text{V}_2(\text{PO}_4)_2\text{F}_3$  compound shows promising potential improvement due to the high electronegativity of F ions.<sup>[146, 147]</sup>

Of particular interest are the members of a new compounds class with general formula  $\text{A}^{12}\text{M}^{\text{II}}_2(\text{PO}_3)_3\text{N}$ , where A = Na or Li, M = Mg, Fe, Mn and Co, which are addressed as potential electrode materials for lithium ion batteries. In fact, the polyanionic structure with  $\text{N}^{3-}$ , arising from three  $\text{PO}_3\text{N}$  tetrahedra sharing one  $\text{N}^{3-}$ , can provide intriguing voltage as cathodes. The divalent nitridophosphate analogue was firstly investigated as cathode for lithium ion batteries, with the  $\text{Fe}^{2+}/\text{Fe}^{3+}$  redox couple.<sup>[148]</sup> Due to the strong inductive effect of  $\text{PO}_3\text{N}$  groups,  $\text{Li}_2\text{Fe}_2(\text{PO}_3)_3\text{N}$  delivers a high potential, as high as 3.5 V (*vs.*  $\text{Li}^+/\text{Li}$ ), which is 0.1 V higher than the olivine  $\text{LiFePO}_4$ , and a high theoretical capacity of 142  $\text{mAh g}^{-1}$ , demonstrating the possibility to design high potential cathode materials for Li-ion batteries. On the Na-ion battery side, cubic  $\text{Na}_3\text{Ti}(\text{PO}_3)_3\text{N}$  exhibits good reversibility for sodium ions (de-)insertion with extremely small

volume changes during the sodiation and desodiation process.<sup>[149]</sup> However, this material only exhibits average working potential of 2.7 V vs. Na<sup>+</sup>/Na originating from the Ti<sup>3+</sup>/Ti<sup>4+</sup> redox couple, and theoretical capacity of 74 mAh g<sup>-1</sup>. To maximize the energy density of these kind materials, the most significant improvement lies in the flexibility to increase the open-circuit voltage by manipulation of the 3d-metal M<sup>n+</sup>/M<sup>(n+1)+</sup> redox couple in the polyanionic framework.

Herein, we report for the first time, the electrochemical properties of cubic Na<sub>3</sub>V(PO<sub>3</sub>)<sub>3</sub>N as cathodes for NIBs, with V<sup>3+/4+</sup> redox activities. The nitridophosphate was synthesized by conventional solid state method. As cathode in non-aqueous NIBs, this material exhibits an average operating potential around 4.0 V vs. Na<sup>+</sup>/Na, while 0.74 Na<sup>+</sup> can be extracted from the host structure.

### 3.2.2 Experimental Methods

#### 3.2.2.1 Materials synthesis

The Na<sub>3</sub>V(PO<sub>3</sub>)<sub>3</sub>N powder was synthesized via a conventional one-step solid state method. Typically, sodium polyphosphate ((NaPO<sub>3</sub>)<sub>n</sub>, pure, Acros Organics) and vanadium oxide (V<sub>2</sub>O<sub>5</sub>, ≥99.6%, ~10 mesh, Alfa Aesar) in a molar ratio of 6:1 were ground in a mortar. Then the yellow powders were placed in an alumina crucible with excessive melamine (5 molar equivalents, C<sub>3</sub>H<sub>6</sub>N<sub>6</sub>, Sigma Aldrich, ≥99%) as nitrogen sources, followed by a pre-heating treatment at 200 °C for 3 h and final calcination at 700 °C for 10 h under extremely slow Ar flow (heating rate: 5 °C min<sup>-1</sup>).

#### 3.2.2.2 Materials characterization

X-ray diffraction analysis was performed in Bragg-Brentano geometry using a Bruker D8 Advance diffractometer (Bruker, Germany). All diffractograms were recorded with CuKα radiation (λ = 0.154 nm) in the 2θ range of 10° - 90° with a step size of 0.01°. The structures were refined using the Rietveld method with DIFFRAC PLUS TOPAS 4.2 software (Bruker, Germany). Morphological characterization was conducted on ZEISS 1550VP Field Emission SEM (Carl Zeiss, Germany). Thermal stability was determined by a thermogravimetric analyzer (TGA-209F, Netzsch, Germany) from room temperature to 800 °C (heating rate = 5 °C min<sup>-1</sup>) under steady N<sub>2</sub> and O<sub>2</sub> flows (20 ml min<sup>-1</sup>), respectively. *In-situ* XRD analyses coupled with galvanostatic electrochemical sodiation and desodiation were performed.

#### 3.2.2.3 Electrochemical characterization

The electrochemical tests were performed using three electrode Swagelok-type cells assembled in an argon-filled glove box with H<sub>2</sub>O and O<sub>2</sub> contents lower than 1 ppm. Sodium half-cells were assembled by using glass fiber (Whatman) as separator and sodium metal (99.8%, Acros Organics) as counter and reference electrodes. 1M NaPF<sub>6</sub> (99%, Alfa Aesar) in propylene carbonate (PC) with 2 wt.% fluoroethylene carbonate (FEC) (Battery Grade, BASF) was used as electrolyte. The working electrodes were prepared by doctor-blade casting a slurry of 80 wt.% of active material, 10 wt.% of carbon black (Super C65, IMERYS) and 10 wt.% of polyvinylidene fluoride (6020 Solef, Solvay Group) in N-methyl-2-pyrrolidone (anhydrous, Sigma-Aldrich) on Al foil as current collector. After drying, electrodes with a diameter of 12 mm were punched, pressed and dried at 120 °C under high vacuum. The mass loading of the final electrodes is about 3.5 mg cm<sup>-2</sup>. A Maccor 4000 Battery system (Maccor, USA) was used for the galvanostatic charge/discharge test at 10 mA g<sup>-1</sup> and 20 mA g<sup>-1</sup>. Cyclic voltammetry was performed on a multichannel potentiostat/galvanostat (VMP3, Biologic Science Instruments, France). All measurements were performed in climatic chambers at a temperature of 20 ± 1 °C.

### 3.2.3 Results and Discussion

Pristine Na<sub>3</sub>V(PO<sub>3</sub>)<sub>3</sub>N powders were synthesized by conventional solid state method, but different from other reports on the nitridophosphate analogues synthesis, without flowing ammonia gas.<sup>[148-150]</sup> The crystal structure of Na<sub>3</sub>V(PO<sub>3</sub>)<sub>3</sub>N was determined by X-ray diffraction (XRD, **Figure 3-14**), including Rietveld refinement of the obtained XRD pattern. The results confirm that Na<sub>3</sub>V(PO<sub>3</sub>)<sub>3</sub>N adopts a cubic structure ( $a = 9.440(1) \text{ \AA}$ ) with a space group of  $P2_13$  and, thus, is isostructural to Na<sub>3</sub>Ti(PO<sub>3</sub>)<sub>3</sub>N (ICSD: 172056).<sup>[149]</sup> The refinement shows satisfactory agreement factors ( $R_{wp}=8.7\%$ ,  $GOF=1.41$ ). The diffractogram in Figure 1 does not depict crystalline impurity phases, suggesting that the simplified synthesis method herein used is successful to obtain pure cubic Na<sub>3</sub>M(PO<sub>3</sub>)<sub>3</sub>N phase. The refined cell parameters and atomic occupancy values are summarized in **Appendix Tables S3-3 and S3-4**, respectively. The SEM image (inset in **Figure 3-14**) shows that the synthesized powder is composed of irregular-shaped microscale particles.

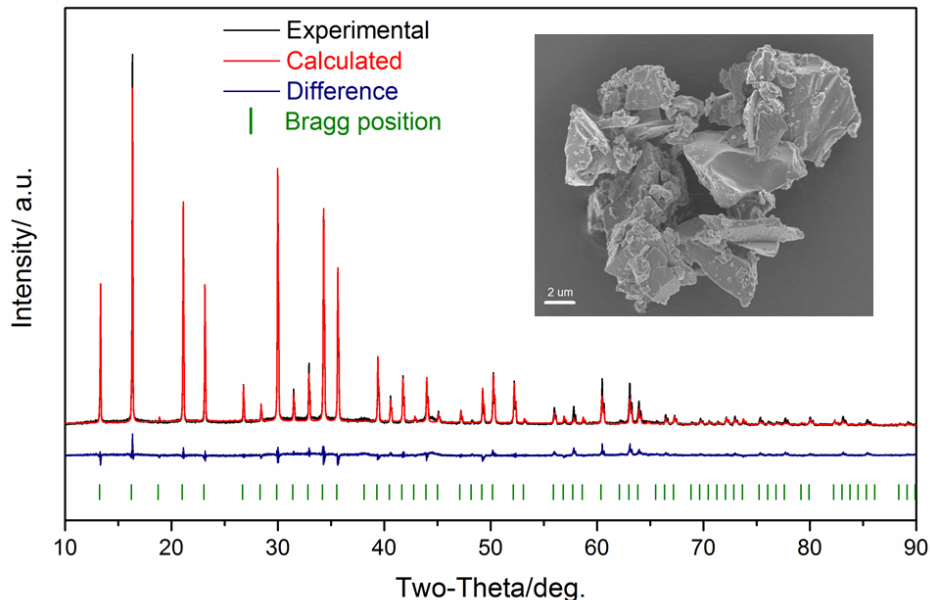


**Figure 3-14.** Rietveld refinement and powder X-ray diffraction (XRD) pattern for  $\text{Na}_3\text{V}(\text{PO}_3)_3\text{N}$  powders. The inset figure displays the SEM images.

The refined crystal structure and the connectivity of trimers of  $\text{PO}_3\text{N}$  tetrahedra with the local environments of Na and V atoms are shown in **Figure 3-15**. The structure of this compound is composed of  $\text{VO}_6$  octahedra and  $\text{PO}_3\text{N}$  tetrahedra. Three  $\text{PO}_3\text{N}$  tetrahedra build up a nitridotriphosphate group,  $(\text{PO}_3)_3\text{N}$  sharing a common  $\text{N}^{3-}$  anion. As shown in **Figure 3-15b**,  $\text{Na}^+$  ions occupy three distinct sites. One  $\text{Na}^+$  ion is coordinated by six O atoms and one N atom (Na1), while the other two  $\text{Na}^+$  cations are surrounded by six (Na2) and nine O anions (Na3: six more long-distanced O atoms are not shown in the structure), respectively.<sup>[151]</sup> Based on the calculation results on the  $\text{Na}_3\text{Ti}(\text{PO}_3)_3\text{N}$  system, Na1 and Na3 sites show high mobility for Na migration, while Na2 site is inaccessible due to the high energy barrier. And this cubic structure, bridged by trimers of  $\text{PO}_3\text{N}$  tetrahedra, offers a three-dimensional framework for Na-ion migration and contributes to the structural stability.<sup>[151]</sup>

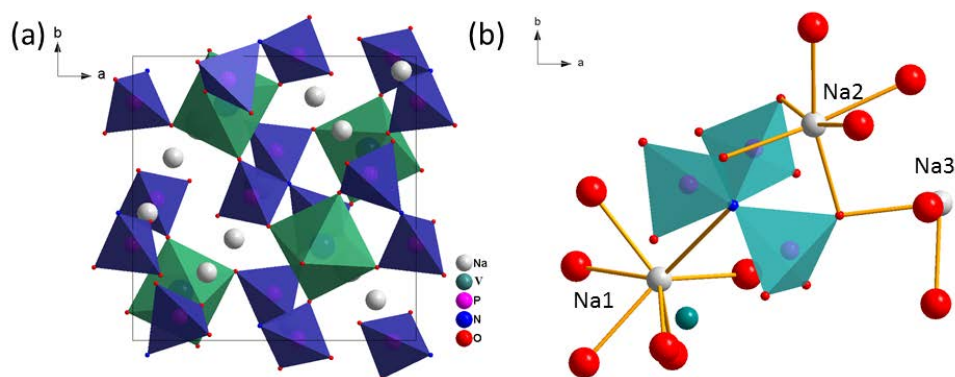


**Figure 3-15.** (a) Refined crystal structure of  $\text{Na}_3\text{V}(\text{PO}_3)_3\text{N}$  and (b) the connectivity of trimers of  $\text{PO}_3\text{N}$  tetrahedra with the local environments of Na, V atoms.

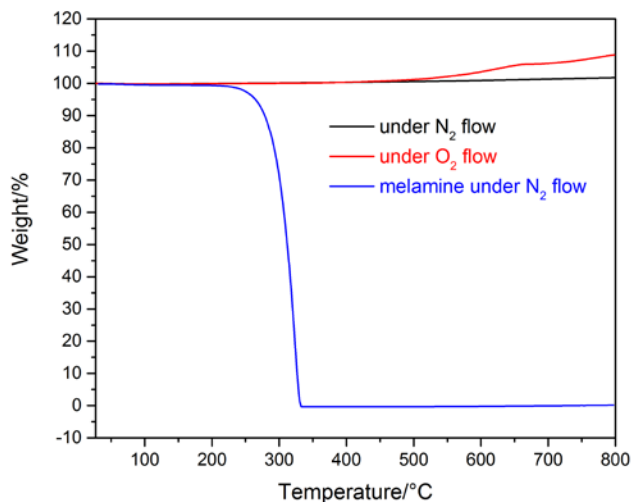


**Figure 3-16.** TG curves of  $\text{Na}_3\text{V}(\text{PO}_3)_3\text{N}$  under  $\text{N}_2$  and  $\text{O}_2$  flows and melamine under  $\text{N}_2$  flow within the temperature range of 30 - 800 °C at 5 °C  $\text{min}^{-1}$  heating rate.

Thermal gravimetric analysis (TGA) was used to assess the thermal stability of the material under both inert ( $\text{N}_2$ ) and oxygen ( $\text{O}_2$ ) atmospheres. The TGA curves in the temperature range of room-temperature-800 °C are displayed in **Figure 3-16**. It should be noted that there is no weight decrease under  $\text{N}_2$  flow up to 800 °C, indicating the superior thermal stability of the material. However, when exposed to  $\text{O}_2$ , a weight increase starting from 400 °C is observed, resulting from the oxidation of  $\text{V}^{3+}$  to  $\text{V}^{5+}$  and  $\text{V}^{4+}$ , which was also observed in  $\text{Na}_3\text{V}_2(\text{PO}_4)_3$  system. Apart from this oxidization process, it should be highlighted that no thermal decomposition is evident during heating, illustrating the excellent thermal stability, which is why  $\text{Na}_3\text{V}(\text{PO}_3)_3\text{N}$  can be regarded as safe electrode materials in batteries. It should be noted that the melamine will completely

decompose between 250–350 °C and does not introduce any additional carbon or impurities into the material, as indicated by the thermogravimetric analysis of pristine melamine in N<sub>2</sub> atmosphere.

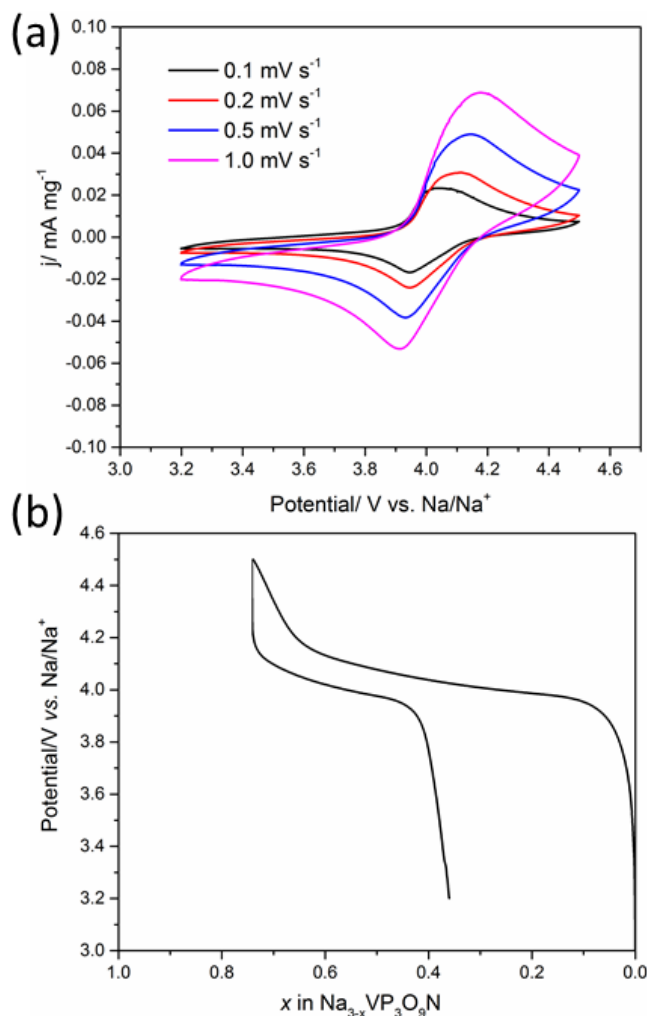


**Figure 3-17.** (a) Cyclic voltammograms in the potential range of 3.2–4.5 V at various scan rates and (b) first cycle galvanostatic discharge/charge profile between 3.2 and 4.5 V at a current of 10 mA g<sup>-1</sup> of Na<sub>3</sub>V(PO<sub>3</sub>)<sub>3</sub>N.

The electrochemical performance of pristine Na<sub>3</sub>V(PO<sub>3</sub>)<sub>3</sub>N electrode was investigated in T-type cells with Na-metal as counter and reference electrode. Cyclic voltammograms at various scan rates between 3.2 V– 4.5 V vs. Na/Na<sup>+</sup> are presented in **Figure 3-17a**. The CV sweeps reveal that the Na<sub>3</sub>V(PO<sub>3</sub>)<sub>3</sub>N electrode shows electrochemical activity centered at 4.0 V with only one pair of redox peaks associated to the V<sup>3+/4+</sup> redox couple. Despite the slight cell polarization, the reversibility of the sodium insertion is maintained at higher scan rate.

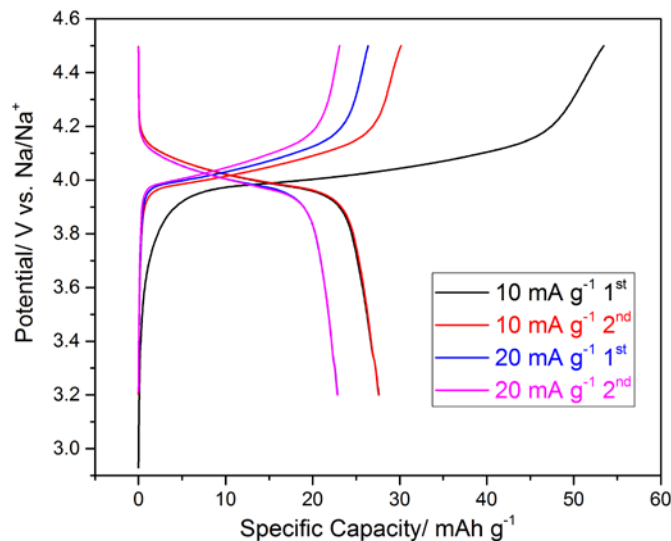


**Figure 3-18.** Galvanostatic charge–discharge profiles of  $\text{Na}_3\text{V}(\text{PO}_3)_3\text{N}$  at current density of  $10 \text{ mA g}^{-1}$  for the 1<sup>st</sup> and 10<sup>th</sup> cycles and  $20 \text{ mA g}^{-1}$  for 11<sup>th</sup> and 20<sup>th</sup> cycles.

**Figure 3-17b** shows the first galvanostatic charge and discharge (GCD) curve of the cell between 3.2 and 4.5 V at a current of  $10 \text{ mA g}^{-1}$ . The electrode exhibits a single plateau around 4.0 V in both charge and discharge. During the first charge to 4.5 V, 0.74 eq. of Na ( $55 \text{ mAh g}^{-1}$ ) are extracted from the host structure. However, only half (0.38 eq.) of the Na ions were re-inserted, leading to a high irreversible capacity for the first cycle. The theoretical capacity for the reversible shuttling of 1.0 eq.  $\text{Na}^+$  per each formula unit of  $\text{Na}_3\text{V}(\text{PO}_3)_3\text{N}$  is  $72 \text{ mAh g}^{-1}$ . The lower charge capacity in the first cycle, hence, indicates that not all  $\text{Na}^+$  can be extracted from the host structure. Increasing the current density to  $20 \text{ mA g}^{-1}$ , this material delivers a discharge capacity of  $24 \text{ mAh g}^{-1}$  (**Figure 3-18**). It is worth mentioning that, although the capacity is low, the measured discharge capacities are stable over 10 cycles, suggesting that such electrode could after optimization work with high cycling stability after the initial capacity loss. For instance, nano-sizing, carbon coating and doping are promising strategies to shorten ion diffusion length and enhance the electronic/ionic conductivities, thus improve the rate capabilities.

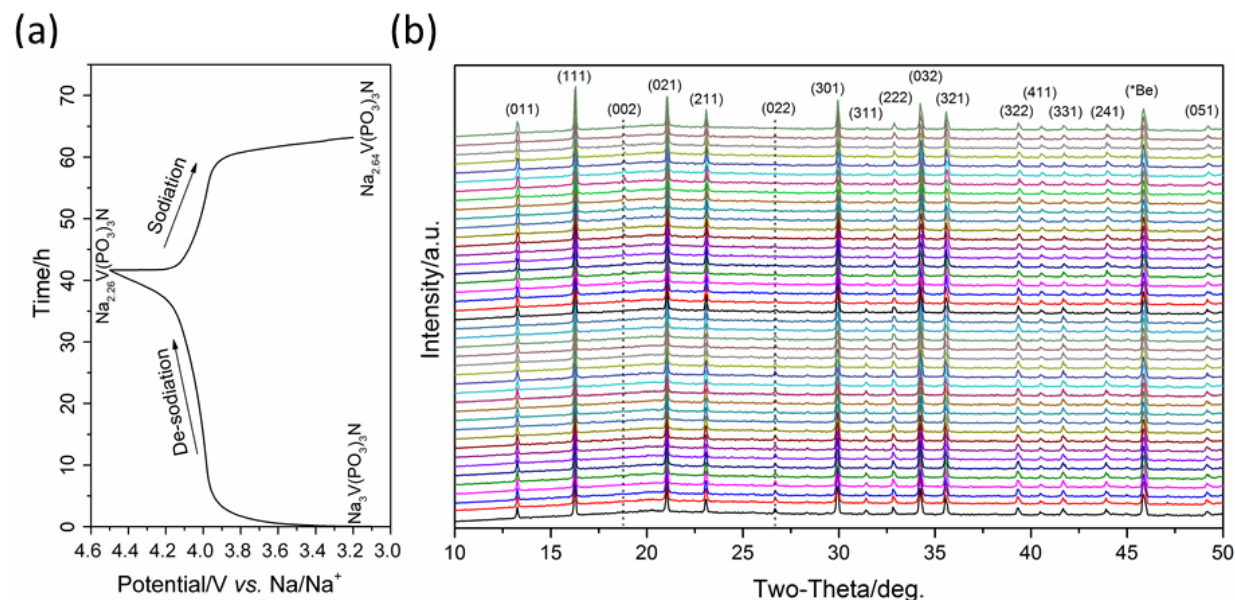


**Figure 3-19.** (a) Typical charge/discharge profile and (b) *in-situ* X-ray diffraction patterns of Na<sub>3</sub>V(PO<sub>3</sub>)<sub>3</sub>N electrode during the first cycle.

*In situ* XRD measurement was conducted to understand the structural changes during the initial sodiation and desodiation processes. The XRD patterns (**Figure 3-19b**) were collected during the first cycle, each after extraction or insertion of 0.025 eq. Na<sup>+</sup> (in total: 44 diffraction patterns). The voltage profile resulting from the galvanostatic steps during the *in situ* characterization is presented in **Figure 3-19a**. From **Figure 3-19b**, only imperceptible changes of the intensity and position of the reflections are observed. This suggests only small structural and volume changes to occur upon (de-)sodiation and supports a stable two-phase reaction (Na-poor and Na-rich), as also indicated by the flat charge-discharge potential profiles.<sup>[152]</sup>

**Table 3-2.** Refined Na occupancies, lattice parameter, and cell volume extracted from the Rietveld refinement of diffraction patterns from 10-45°2θ of Na<sub>3</sub>V(PO<sub>3</sub>)<sub>3</sub>N electrodes at OCV, fully charged and fully discharged state in the first cycle.

State	Na1 occ	Na2 occ	Na3 occ	a (Å)	V (Å <sup>3</sup> )	R <sub>wp</sub> /%	GOF
OCV	1.05(3)	1.00(2)	0.91(3)	9.445(1)	842.7(2)	3.38	1.14
1 <sup>st</sup> charge: 4.5 V	0.58(4)	0.97(2)	0.76(3)	9.438(1)	840.8(3)	3.43	1.16
1 <sup>st</sup> discharge: 3.2V	0.85(3)	1.01(2)	0.80(3)	9.440(1)	841.4(2)	3.27	1.10



To further investigate the desodiated and sodiated phases, Rietveld refinements of the XRD patterns of electrodes in fully charged (4.5 V) and discharged (3.2 V) state were performed. The according Na occupancies and lattice parameter are listed in **Table 3-2**. All diffractograms could satisfactorily be refined with the space group  $P2_13$ , i.e. cubic lattice parameters. The results demonstrate that  $\text{Na}^+$  ions at Na1 and Na3 sites are firstly extracted when charged to 4.5 V, resulting in a total amount of about 0.7 eq.  $\text{Na}^+$ . Na cations at these two sites are, therefore, more mobile. During the discharge process, 0.3 eq. of  $\text{Na}^+$  cannot be electrochemically re-inserted into the host structure, in agreement with the irreversible capacity in the first cycle as shown in **Figure 3-17b**. This preliminary result indicates that less capacity contribution is from Na3 site resulting from the higher diffusion barrier for Na3 than Na1, and there is almost no Na migration occurring at the Na2 site, in accordance with the previous study on  $\text{Na}_3\text{Ti}(\text{PO}_3)_3\text{N}$ .<sup>[149]</sup> However, the Na ion mobility at Na1 sites is very reversible. This insight may provide a strategy to improve the Na-migration by tuning the structural properties via selective doping, for example. Moreover, the volume change ( $\Delta V/V$ ), obtained from the calculated cell volume difference before (OCV) and after (4.5 V) Na removal by the Rietveld refinement, that occurs on Na-ion removal is approximately 0.2 %, a remarkably small volume shrinkage given the large ionic radius of Na ions. This is contributed by the framework constructed of  $\text{PO}_3\text{N}$  tetrahedra trimers.

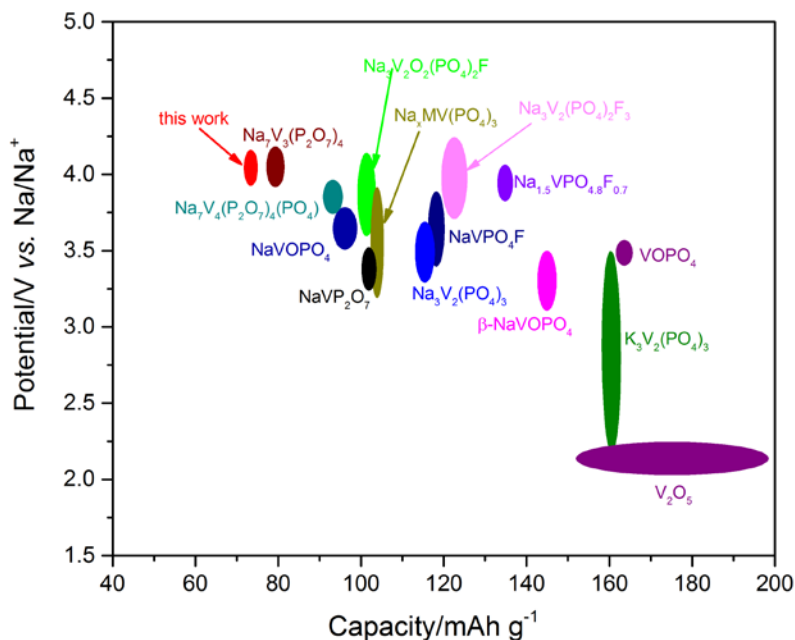


**Figure 3-20.** Average working potential versus gravimetric capacity for various vanadium-based positive electrode materials for sodium-ion batteries. Here only one electron reaction of  $\text{V}^{3+/4+}$  redox reaction is considered.

Overall, the nitridophosphate  $\text{Na}_3\text{V}(\text{PO}_3)_3\text{N}$  is showing favorable working potential. **Figure 3-20** illustrates the potential-capacity comparison of various vanadium-based cathode materials in sodium-ion batteries. Although the capacity is lower, the material still could reach comparable energy density to other V-based compounds.

### 3.2.4 Conclusions

Summarizing, the nitridophosphate  $\text{Na}_3\text{V}(\text{PO}_3)_3\text{N}$  with a cubic structure ( $a = 9.440(1) \text{ \AA}$ ,  $P2_13$  space group) can be successfully synthesized *via* a conventional solid state method without flowing ammonia gas as nitrogen source. This compound shows a high operating potential of 4.0 V vs.  $\text{Na}/\text{Na}^+$  due to  $\text{V}^{3+/4+}$  redox reactions. In the first charge, 0.74 eq.  $\text{Na}^+$  can be extracted but only 0.38 eq.  $\text{Na}^+$  (i.e. 28 mAh  $\text{g}^{-1}$ ) can be re-inserted into the framework and reversibly shuttled. It should be noted that the potential of  $\text{V}^{3+/4+}$  in most polyanionic cathodes is lower than 4.0 V vs.  $\text{Na}/\text{Na}^+$ , including  $\text{Na}_3\text{V}_2(\text{PO}_4)_3$ , which is considered as one of the most promising cathode materials for practical applications. The nitridophosphate  $\text{Na}_3\text{V}(\text{PO}_3)_3\text{N}$  exhibits a  $\text{V}^{3+/4+}$  redox reaction at 4.0 V, higher than that of  $\text{Na}_3\text{V}_2(\text{PO}_4)_3$  (3.4 V vs.  $\text{Na}/\text{Na}^+$ ). Although this kind of compound offers a limited reversible capacity, room to improve the performance and narrow the gap between the practical and theoretical capacities is existing. The most obvious is to improve the conductivity and optimize the particle size with morphology control via, e.g. nano-sizing and carbon-coating. However, the excellent thermal stability and very small volume changes during (de)sodiation, i.e. “zero strain”, with high operating voltage, make this kind of compounds a potentially interesting safe high-voltage cathode material for sodium-ion batteries.

# Chapter 4

## Polyanionic Electrode Based Nonaqueous and Aqueous Sodium-ion Batteries

The results in this chapter are partially published in the following publications:

1. **Zhang, H.**; Jeong, S.; Qin, B.; Carvalho, D. V.; Buchholz, D.; Passerini, S., Towards High-Performance Aqueous Sodium-ion Batteries: Stabilizing the Solid/Liquid Interface for NASICON-type  $\text{Na}_2\text{VTi}(\text{PO}_4)_3$  using Concentrated Electrolytes. *ChemSusChem* 2018, 11 (8), 1382-1389.
2. **Zhang, H.**; Qin, B.; Han, J.; Passerini, S., Aqueous/Nonaqueous Hybrid Electrolyte for Sodium-ion Batteries. *ACS Energy Letters* 2018, 3 (7), 1769-1770.
3. **Zhang, H.**; Qin, B.; Buchholz, D.; Passerini, S., High-Efficiency Sodium-ion Battery Based on NASICON Electrodes with High Power and Long Lifespan. *ACS Applied Energy Materials* 2018, 1 (11), 6425-6432.

## 4.1 Symmetric Sodium-ion Battery: $\text{Na}_2\text{VTi}(\text{PO}_4)_3//\text{Na}_2\text{VTi}(\text{PO}_4)_3$

### 4.1.1 Introduction

Sodium (Na)-ion batteries hold the great promise of enabling cost-effective grid energy storage owing to their cost advantages and good energy density.<sup>[14, 153]</sup> Indeed, the typical Na-ion battery, operating at ambient temperature with two host materials (e.g. hard carbon anode, layered transition metal oxide cathode) in an organic solution electrolyte, already delivers high energy density and good cycling stability.<sup>[154]</sup> Nevertheless, non-aqueous Na-ion batteries suffer from the toxicity, flammability, low ionic conductivity and relatively high cost of the electrolytes.<sup>[155]</sup> An attractive approach to circumvent this problem is to use an aqueous electrolyte.<sup>[2, 156]</sup> The success of the low-cost lead-acid battery demonstrates the potential of aqueous Na-ion batteries, e.g., for load leveling and grid stabilization. Still, the low energy density needs to be enhanced to establish aqueous Na-ion batteries as an attractive technology for power-management operations and grid-scale energy storage. Despite the considerable progress in the development of electrode materials such as layered oxides, Prussian blue derivatives and polyanionic compounds, especially the cycling stability and energy density need to be enhanced further.<sup>[157-164]</sup>

Polyanionic compounds with NASICON (Na Super Ionic Conductor) structure have attracted intensive interest because of their high structural stability, large ionic channels, and good accessibility of the sodium sites.<sup>[165, 166]</sup> The  $\text{V}^{4+}/\text{V}^{3+}$  and  $\text{Ti}^{4+}/\text{Ti}^{3+}$  redox processes in vanadium- and titanium based insertion hosts with NASICON-structure occur within the electrochemical stability window of water.<sup>[167]</sup> Hence, NASICON-type  $\text{NaTi}_2(\text{PO}_4)_3$  and  $\text{Na}_3\text{V}_2(\text{PO}_4)_3$  have been investigated intensively as electrode materials for aqueous Na-ion batteries. Especially  $\text{NaTi}_2(\text{PO}_4)_3$  has been of high interest because it is redox active at low voltages but within the stability of the aqueous electrolyte, enabling enhanced energy density.<sup>[168, 169]</sup> However, pristine  $\text{Na}_3\text{V}_2(\text{PO}_4)_3$  suffers from the structural degradation in aqueous electrolytes within few cycles. A recent study showed that this issue can be fixed by substitution of vanadium.<sup>[170]</sup> In consequence, amphoteric insertions host that can be used as cathode and anode materials are being developed. This enables the fabrication of symmetric batteries at reduced manufacturing costs.<sup>[82, 171]</sup> Goodenough and coworkers developed a symmetric aqueous Na-ion battery using NASICON-structured  $\text{Na}_3\text{MnTi}(\text{PO}_4)_3$ , exhibiting  $\text{Ti}^{4+}/\text{Ti}^{3+}$  and  $\text{Mn}^{3+}/\text{Mn}^{2+}$  redox couples at low and high voltages, respectively.<sup>[172]</sup> The symmetric non-aqueous Na-ion battery with NASICON-type  $\text{Na}_2\text{VTi}(\text{PO}_4)_3$  (NVTP) delivered superior rate capability and cycling stability.<sup>[173]</sup> In addition, the NVTP electrode could also be used in an aqueous symmetric Na-ion battery with an output voltage of ~1.2 V in conventional 1M  $\text{Na}_2\text{SO}_4$  aqueous electrolyte.<sup>[174]</sup> However, the high rate capability

and cycling stability should be further improved to demonstrate the feasibility for commercial applications.<sup>[175]</sup>

So far, Na<sub>2</sub>SO<sub>4</sub>-H<sub>2</sub>O, NaNO<sub>3</sub>-H<sub>2</sub>O, NaTFSI-H<sub>2</sub>O, NaFSI-H<sub>2</sub>O and NaOTF-H<sub>2</sub>O have been reported as electrolyte salts, but Na<sub>2</sub>SO<sub>4</sub> is most commonly used due to its low cost and environmental friendliness. It has been shown that the use of highly concentrated and sulfonate-based (NaCF<sub>3</sub>SO<sub>3</sub>) electrolytes widens the electrochemical stability window of the electrolyte and enhances the stability of the electrode by water solvation and thick solid electrolyte interphase formation.<sup>[164, 176, 177]</sup> As a result, further studies investigated the effect of Na-salt concentration in aqueous electrolytes.<sup>[178, 179]</sup> However, not only the electrochemical stability window and ionic conductivity but also increased cost need to be considered for concentrated aqueous electrolytes. In this regard, NaClO<sub>4</sub> is a promising candidate because it is relatively cheap and already widely studied in non-aqueous Na-ion batteries.<sup>[179-181]</sup> Therefore, an aqueous Na-ion battery consisting of polyanionic host electrodes and low-cost aqueous Na-salt electrolyte could be promising for large-scale energy storage applications.

Herein, NASICON-type Na<sub>2</sub>VTi(PO<sub>4</sub>)<sub>3</sub>/C (NVTP/C) composite is synthesized by a simple sol-gel method and investigated in a symmetric nonaqueous or aqueous Na-ion cell. The effect of NaClO<sub>4</sub> concentration on the performance of NVTP/C is unraveled. In addition, the superior electrochemical performance in 9.2 m (molality) NaCF<sub>3</sub>SO<sub>3</sub> (NaOTF) “water-in-salt” electrolyte is demonstrated. It is shown that the solid electrolyte interphase plays a critical role for a stable electrochemical performance and high rate capability.

## 4.1.2 Experimental Methods

### 4.1.2.1 Materials synthesis

The NASICON-type Na<sub>2</sub>VTi(PO<sub>4</sub>)<sub>3</sub>/C composite was synthesized via a sol-gel method. [173] In a typical synthesis, 0.02 mol CH<sub>3</sub>COONa·3H<sub>2</sub>O (VWR, ≥99%), 0.01 mol NH<sub>4</sub>VO<sub>3</sub> (Sigma Aldrich, ≥99%), and 0.03 mol NH<sub>4</sub>H<sub>2</sub>PO<sub>4</sub> (Alfa Aesar, ≥99%) were dissolved in 50 ml 0.02 M aqueous citric acid monohydrate (C<sub>6</sub>H<sub>8</sub>O<sub>7</sub>·H<sub>2</sub>O) (Alfa Aesar, ≥99%) solution. Then, 10 ml 1.0 M Ti(CH<sub>3</sub>CH<sub>2</sub>CH<sub>2</sub>CH<sub>2</sub>O)<sub>4</sub> (Sigma Aldrich, ≥98%) solution in absolute ethanol (VWR, ≥99.9%) was poured into the above solution with vigorous stirring. The blue powder was collected as the gel precursor after heated to 80 °C to evaporate the solvents. The precursor was pretreated at 350 °C for 5 h, followed by sintering at 800 °C for 12 h under argon flow to obtain the Na<sub>2</sub>VTi(PO<sub>4</sub>)<sub>3</sub>/C composite. The aqueous electrolytes were prepared by dissolving different concentrations of NaClO<sub>4</sub>·H<sub>2</sub>O (VWR, ≥99%) and Na<sub>2</sub>SO<sub>4</sub> (Sigma Aldrich, ≥99%) in Milli-Q water, i.e. 1 M, 4 M, 8

M NaClO<sub>4</sub> and 1 M Na<sub>2</sub>SO<sub>4</sub> (mol-salt per liter solution). The “water-in-salt” electrolyte was prepared according to the literature, i.e. 9.2 m (mol-salt in kg-solvent) NaCF<sub>3</sub>SO<sub>3</sub> (Alfa Aesar, ≥98%) in Milli-Q water.<sup>[178]</sup> All the aqueous electrolytes were degassed with N<sub>2</sub> for 2 h to remove the dissolved O<sub>2</sub> before use.

#### *4.1.2.2 Materials characterization*

Powder X-ray diffraction analysis was performed in Bragg-Brentano geometry using a Bruker D8 Advance diffractometer. The pattern was recorded with CuKα radiation ( $\lambda = 0.154$  nm) in the  $2\theta$  range of 10° - 90° with a step size of 0.01°. Raman spectra were collected on a RAM II FT-Raman module of a Bruker Vertex70 FT-IR spectrometer with a laser wavelength of 1064 nm for 1000 scans with a resolution of 2 cm<sup>-1</sup>, and analyzed using PeakFit software (version 4.12, SeaSolve Software, Inc.). The samples were sealed in glass tubes with argon as protective gas. Morphological characterization was conducted on ZEISS 1550VP Field Emission SEM (Carl Zeiss, Germany).

#### *4.1.2.3 Electrochemical characterization*

Ionic conductivities of the aqueous electrolytes were measured in sealed glass conductivity cells (AMEL 192/K1) equipped with two porous platinum electrodes (cell constant of  $1.0 \pm 0.1$  cm) using an AMEL 160 conductivity meter. The electrodes were prepared by doctor-blade casting of slurries in N-methyl-2-pyrrolidone (anhydrous, Sigma-Aldrich) with 80 wt.% Na<sub>2</sub>VTi(PO<sub>4</sub>)<sub>3</sub>/C, 10 wt.% carbon black (Super C65, IMERYS) and 10 wt.% polyvinylidene fluoride (Solef 6020, Solvay Group) on stainless steel. After drying, electrodes with a diameter of 12 mm were punched and dried at 120 °C under high vacuum. The average active material mass loading was ~10 mg cm<sup>-2</sup>. The cells using organic electrolyte were assembled in an argon-filled glove box with H<sub>2</sub>O and O<sub>2</sub> contents lower than 1.0 ppm. Sodium half-cells were assembled using glass fiber discs (GF/D, Whatman) as separators, 1M NaPF<sub>6</sub> (Alfa Aesar, 99%) in propylene carbonate/ethylene carbonate (1:1, v/v) (BASF, Battery Grade) as electrolyte and sodium metal (99.8%, Acros Organics) as counter and reference electrodes. Symmetric Na-ion cells were assembled using Na<sub>2</sub>VTi(PO<sub>4</sub>)<sub>3</sub>/C electrodes as anode and cathode in a weight ratio of ~1. A Maccor 4000 Battery system (Maccor, USA) was used for the galvanostatic charge/discharge test at various C-rates. Cyclic voltammetry and electrochemical impedance spectroscopy tests were performed on a multichannel potentiostat/galvanostat (VMP3, Biologic Science Instruments, France). The impedance spectra were recorded from NVTP electrodes at OCV and discharged state (after a potentiostatic step at 0.5 V for 30 min) with amplitude of 10 mV over the frequency range from 100 kHz to 100 mHz. All measurements were performed in climatic chambers at  $20 \pm 1$  °C.

### 4.1.3 Results and Discussion

The powder X-ray diffraction pattern of synthesized  $\text{Na}_2\text{VTi}(\text{PO}_4)_3/\text{C}$  is presented in **Figure 4-1a**. NASICON-type  $\text{NaTi}_2(\text{PO}_4)_3$  and  $\text{Na}_3\text{V}_2(\text{PO}_4)_3$  can be indexed with a rhombohedral unit cell and  $R\bar{3}c$  space group.<sup>[157, 173-175, 182]</sup> The morphology was examined by SEM (**Figure 4-1b**). The obtained NVTP/C materials are composed of irregular-shaped microscale particles. The carbon content is estimated to be ~6 wt.% according to carbon-hydrogen-nitrogen (CHN) elemental analysis.

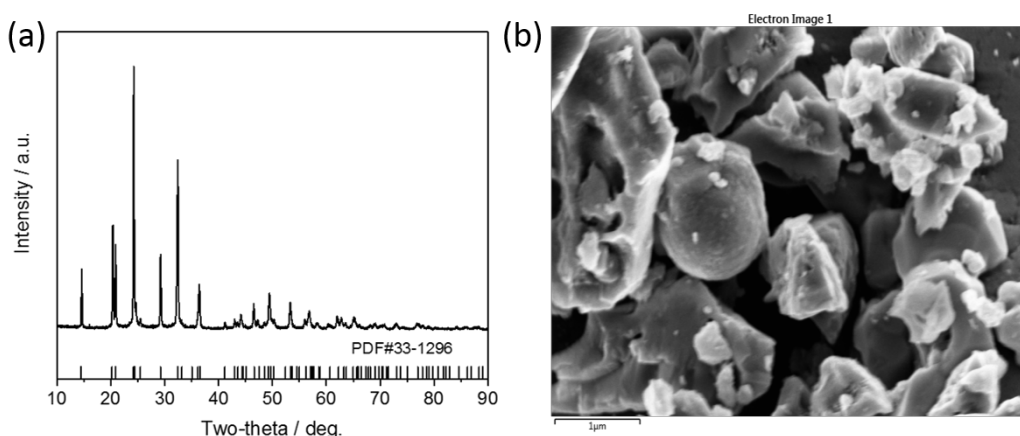


**Figure 4-1.** (a) XRD pattern and (b) SEM image of  $\text{Na}_2\text{VTi}(\text{PO}_4)_3/\text{C}$  composite.

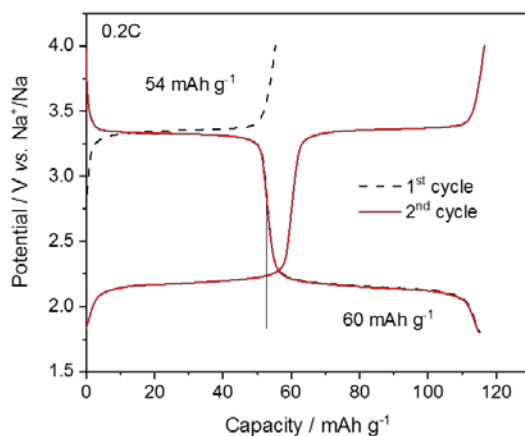


**Figure 4-2.** Initial and second galvanostatic charge-discharge profile of  $\text{Na}_2\text{VTi}(\text{PO}_4)_3/\text{C}$  between 1.5 and 4.0 V vs.  $\text{Na}^+/\text{Na}$  at 0.2 C (1C = 60  $\text{mA g}^{-1}$ ).

In the following, NVTP/C electrodes were investigated in three-electrode Swagelok half-cells with metallic sodium as counter and reference electrodes. **Figure 4-2** depicts the initial and second galvanostatic charge-discharge profiles in 1M  $\text{NaPF}_6$  in PC/EC (1:1 v/v) electrolyte between 1.5

and 4.0 V at 0.2 C (1 C = 60 mA g<sup>-1</sup>). In the initial charge process, the electrode exhibits the typical at ~3.4 V vs. Na<sup>+</sup>/Na, close to the potential of V<sup>3+</sup>/V<sup>4+</sup> redox process in Na<sub>3</sub>V<sub>2</sub>(PO<sub>4</sub>)<sub>3</sub>.<sup>[182]</sup> The first discharge potential profile features two plateaus at ~3.4 V and ~2.1 V vs. Na<sup>+</sup>/Na due to V<sup>4+</sup>/V<sup>3+</sup> and Ti<sup>4+</sup>/Ti<sup>3+</sup> redox couples, respectively. The initial charge capacity is 54 mAh g<sup>-1</sup>, while the discharge capacity is 114 mAh g<sup>-1</sup>. The second charge shows the same position and extent of the plateaus, demonstrating the highly reversible sodium storage in NVTP/C.

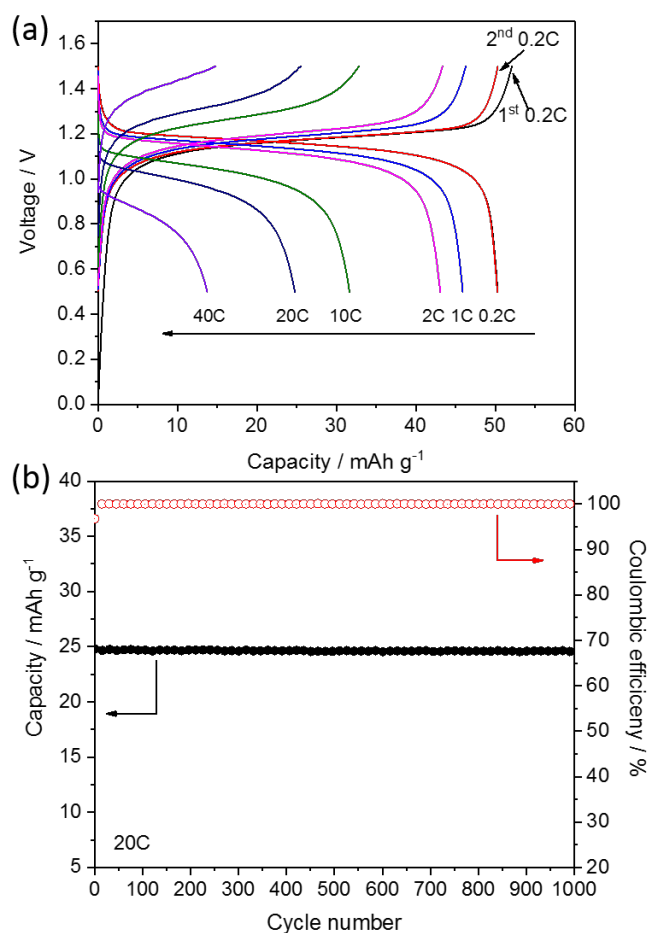


**Figure 4-3.** (a) Galvanostatic charge-discharge profiles of symmetric full cell between 0.5 and 1.5 V at different C-rates, and (b) long-term cycling stability test of the symmetric full cell at 20 C in 1M NaPF<sub>6</sub> PC/EC (1:1 v/v) organic electrolyte (1C = 60 mA g<sup>-1</sup>).

The galvanostatic charge-discharge profile of the symmetric Na-ion battery with organic electrolyte cycled in a coin cell between 0.5-1.5 V is displayed in **Figure 4-3a**. The full cell shows a stable plateau at ~1.2 V and delivers a reversible capacity of 51 mAh g<sup>-1</sup> at 0.2 C. The initial coulombic efficiency is about 96.6%. At increased current densities of 1 C, 2 C, 10 C, 20 C to 40 C, the reversible capacities reduce to 46, 43, 32, 24 and 14 mAh g<sup>-1</sup>, respectively. **Figure 4-3b**



displays the long-term cycling behavior of the symmetric full cell at 20 C. An extraordinary high capacity retention of ~99% is obtained after 1000 cycles with coulombic efficiency close 100%. This is demonstrating the excellent sodium storage and high rate capability of NVTP/C materials in the symmetric Na-ion cell.

Solvation structure and ion association of NaClO<sub>4</sub> aqueous solutions over a wide concentration range and 9.2 m NaOTF “water-in-salt” electrolyte were elucidated with Raman spectroscopy. As previously reported, the aggregation behavior of the salt and free water in electrolytes can be beneficial for interfacial stability of the electrode during electrochemical process.<sup>[178, 183]</sup> **Figure 4-4a** shows the ClO<sub>4</sub> stretching mode at room temperature in the range 890-970 cm<sup>-1</sup> to evaluate salt aggregation in NaClO<sub>4</sub> containing aqueous electrolytes. The peak position shifts to a higher wavenumber with increasing salt molarity. Via component band analysis, four Lorentz-Gaussian peaks at ~945.0, 935.0, 925.0 and 915.0 cm<sup>-1</sup> can be assigned to the contact ion pairs/aggregated cation-ion pairs, solvent-separated ion pairs, free solvated ClO<sub>4</sub><sup>-</sup>, and overtone  $\nu_2$ -ClO<sub>4</sub><sup>-</sup>, respectively.<sup>[184, 185]</sup> The curve fitting shows that the highest wavenumber peak of the contact ion pairs/ionic aggregates increases, whereas the solvent-separated ion pairs, free solvated ClO<sub>4</sub><sup>-</sup>, and overtone band  $\nu_2$ -ClO<sub>4</sub><sup>-</sup> decrease with increasing salt molarity. This shows that the solvent separated ion pairs between Na<sup>+</sup> and ClO<sub>4</sub><sup>-</sup> are dominant over the hydrogen bonds between water molecules. However, a significant degree of ion pairing and aggregation can be observed in all electrolytes.

The intensity of Raman OH bending and OH-stretching modes at ~1640 cm<sup>-1</sup> and ~3240 cm<sup>-1</sup>, respectively, can be used to determine hydrogen bond strength and identify the “free” water content in the aqueous solutions.<sup>[186]</sup> The Raman spectra of the OH bending and OH stretching regions of NaClO<sub>4</sub>-H<sub>2</sub>O and 9.2 m NaOTF “water-in-salt” electrolytes are shown in **Figure 4-4b** and c. The intensities of OH bending and stretching modes decrease with the increasing concentration, as the hydrogen bonds in water are broken in the highly concentrated solutions, consistent with the ion aggregation behavior. To confirm the salt aggregation behavior in the 9.2 m NaOTF “water-in-salt” electrolyte, the SO<sub>3</sub> stretching mode was examined (**Figure 4-4d**). The Lorentz-Gaussian deconvolution of the Raman spectrum reveals two major bands that can be associated to solvent-separated ion pairs and contact ion pairs/aggregated cation-anion pairs, which is in excellent agreement with a previous report.<sup>[178]</sup> Representative Na<sup>+</sup> cation solvate species (solvent-separated ion pairs, contact ion pairs and aggregated cation-anion pairs) in dilute and concentrated electrolytes can be seen in **Figure 4-5**.

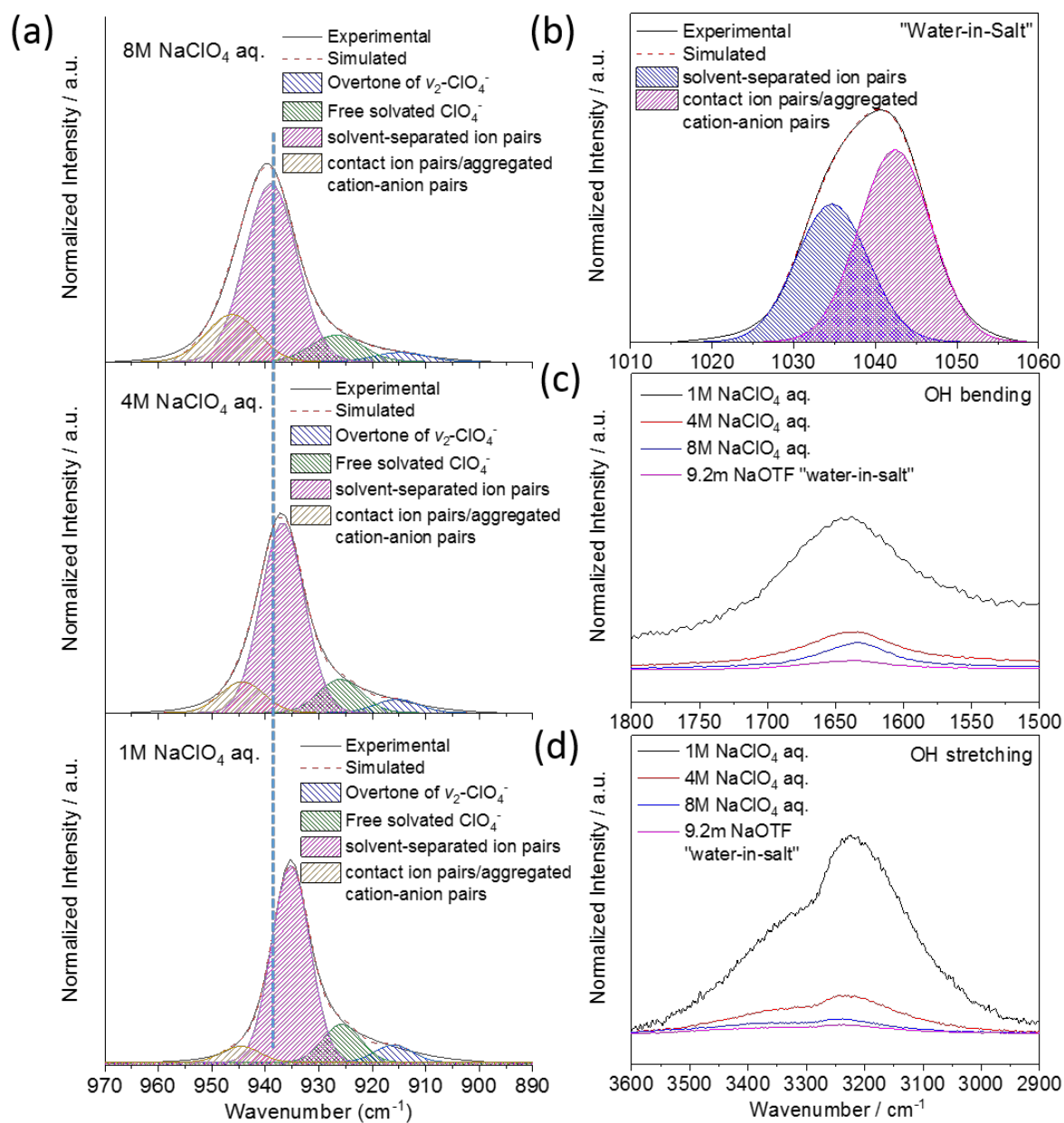


**Figure 4-4.** Raman spectra of the aqueous electrolytes. (a)  $\text{ClO}_4$  stretching mode in 1, 4 or 8 M  $\text{NaClO}_4$  aqueous electrolyte; (b) OH bending and (c) OH stretching bands in 1, 4 or 8 M  $\text{NaClO}_4$  and 9.2 m NaOTF “water-in-salt” electrolytes; (d)  $\text{SO}_3$  stretching mode in 9.2 m NaOTF “water-in-salt” electrolyte.

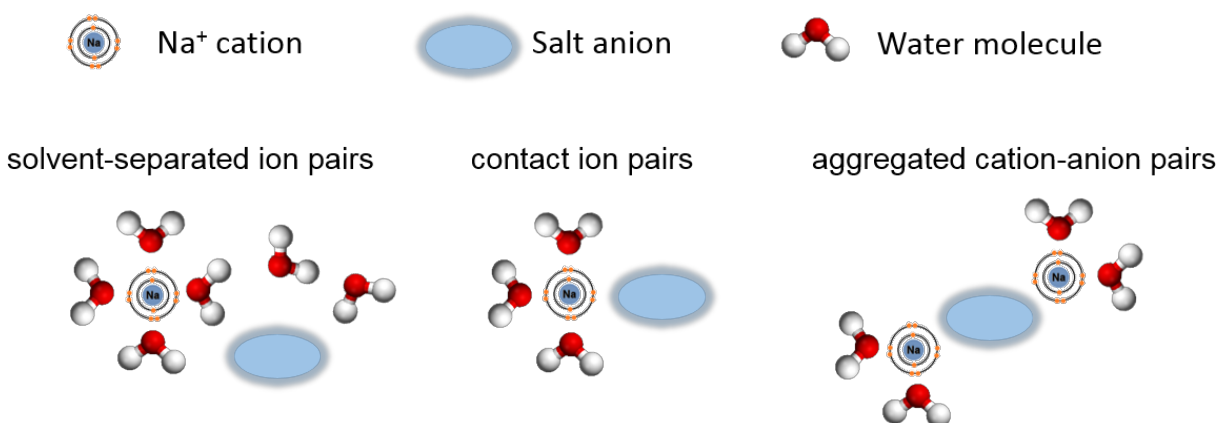


**Figure 4-5.** Representative  $\text{Na}^+$  cation solvate species (solvent-separated ion pairs, contact ion pairs and aggregated cation-anion pairs) in dilute and concentrated electrolytes.

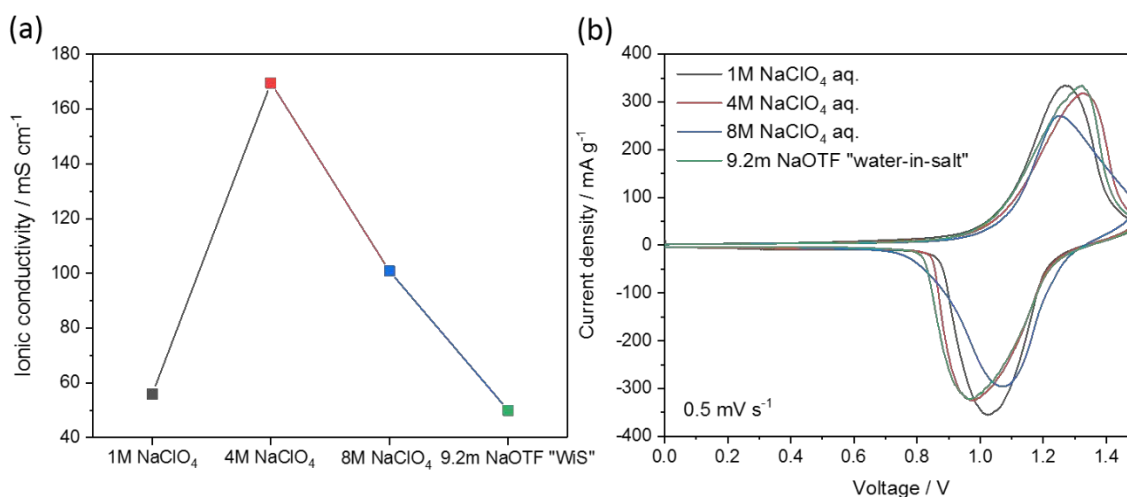


**Figure 4-6.** (a) Ionic conductivities of aqueous 1 M  $\text{NaClO}_4$ , 4 M  $\text{NaClO}_4$ , 8 M  $\text{NaClO}_4$ , and 9.2 m NaOTF “water-in-salt” electrolytes at 20 °C; (b) Cyclic voltammogram curves of the  $\text{Na}_2\text{VTi}(\text{PO}_4)_3/\text{C}$  symmetric full cells at a scan rate of  $0.5 \text{ mV s}^{-1}$  between 0 and 1.5V in various aqueous electrolytes.

The ionic conductivity of electrolytes with different concentrations at 20 °C is shown in **Figure 4-6a**. The 4 M  $\text{NaClO}_4$  aqueous solution shows the highest ionic conductivity.<sup>[160, 187]</sup> Higher  $\text{NaClO}_4$  concentrations lead to decreased ionic conductivities due to increased cation-anion aggregation and coulombic interactions. Although the increased ion aggregation leads to reduced ionic conductivity, it can facilitate the charge transfer and stabilize the interphase between water molecules and the reducing electrode surface.<sup>[178]</sup> Hence, the electrochemical behavior of symmetric cells with NVTP/C electrodes was evaluated via cyclic voltammetry (CV) in aqueous

electrolytes of different  $\text{NaClO}_4$  concentration and 9.2 m  $\text{NaOTF}$  “water-in-salt” electrolyte (**Figure 4-6b**). All cells exhibit a current peak at  $\sim 1.2$  V corresponding to the potential difference between  $\text{V}^{3+}/\text{V}^{4+}$  and  $\text{Ti}^{4+}/\text{Ti}^{3+}$  redox couples in NVTP/C. The peak intensities decrease with the increasing concentrations of  $\text{NaClO}_4$  salt, however, the voltage hysteresis is lowest in 8 M  $\text{NaClO}_4$  electrolyte.

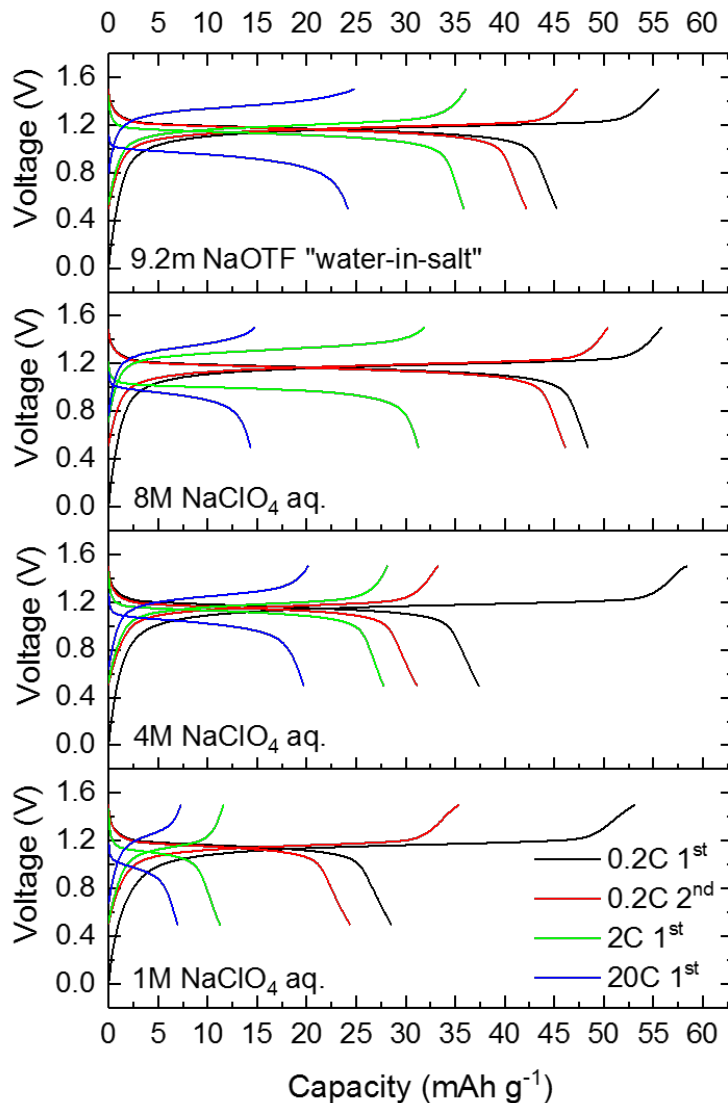


**Figure 4-7.** The galvanostatic charge-discharge profiles of  $\text{Na}_2\text{VTi}(\text{PO}_4)_3/\text{C}$  symmetric full cells at various C-rates using stainless steel foil as current collector in aqueous  $\text{NaClO}_4$  electrolytes (1 M, 4 M, 8 M) and 9.2 m  $\text{NaOTF}$  “water-in-salt” electrolyte.

The effect of electrolyte concentrations on the performance of NVTP/C symmetric cells was studied with galvanostatic cycling test (**Figure 4-7**). The initial charge capacities of all cells is

close to the theoretical values ( $62 \text{ mAh g}^{-1}$ ). However, an irreversible capacity is observed during discharge, leading to low initial coulombic efficiency, in accordance with other studies on aqueous Li- and Na-ion batteries.<sup>[157, 160, 188]</sup> Interestingly, the reversible capacities of NVTP/C electrodes increase with the salt concentrations at 0.2 C (i.e.,  $43.4 \text{ mAh g}^{-1}$  in 8 M  $\text{NaClO}_4$ ,  $37.4 \text{ mAh g}^{-1}$  in 4 M  $\text{NaClO}_4$  and only  $28.5 \text{ mAh g}^{-1}$  in 1 M  $\text{NaClO}_4$ ). However, at increased current densities of 20 C, the 4 M  $\text{NaClO}_4$  electrolyte delivers higher reversible capacities due to the higher ionic conductivity. Most importantly, when using the NVTP/C electrode in 9.2 m NaOTF “water-in-salt” electrolyte a superior electrochemical performance is observed. This is, e.g., evidenced by high reversible capacities of  $45.0 \text{ mAh g}^{-1}$  at 0.2 C and  $24.8 \text{ mAh g}^{-1}$  at 20 C. Thus, higher rate capability is obtained with respect to the other aqueous electrolytes despite the lower ionic conductivity.

**Figure 4-8a** shows the rate test from 0.2 C to 20 C of aqueous NVTP//NVTP symmetric cells. For 1 M, 4 M and 8 M  $\text{NaClO}_4$  aqueous electrolytes the performance at high rate of 10 C and 20 C is in accordance with observed ionic conductivity, i.e. the best rate performance being obtained in 4M electrolyte, followed by 8 M and 1 M. At low rate (from 0.2 C to 2 C), improved performance is obtained with increase of  $\text{NaClO}_4$  concentration. Again it needs to be highlighted that the NVTP/C electrode in concentrated 8 M  $\text{NaClO}_4$  electrolyte and 9.2 m NaOTF “water-in-salt” electrolyte exhibits an outstanding electrochemical performance at low but also high current rates in accordance with previous works. These results suggest that the interfacial stability and charge transfer at the electrode- electrolyte interface are different in the different electrolytes. Lower coulombic efficiencies (see **Figure 4-8b**) and higher capacity fading are observed in the more dilute electrolyte solutions. Electrical contact loss between electrode particles, hydrogen evolution and related material degradation are most probably the origin for these results and also explain the low electrochemical performance of NVTP/C between 0.2C and 2C in 1 M  $\text{NaClO}_4$  and 4 M  $\text{NaClO}_4$  electrolyte.<sup>[178, 187]</sup>

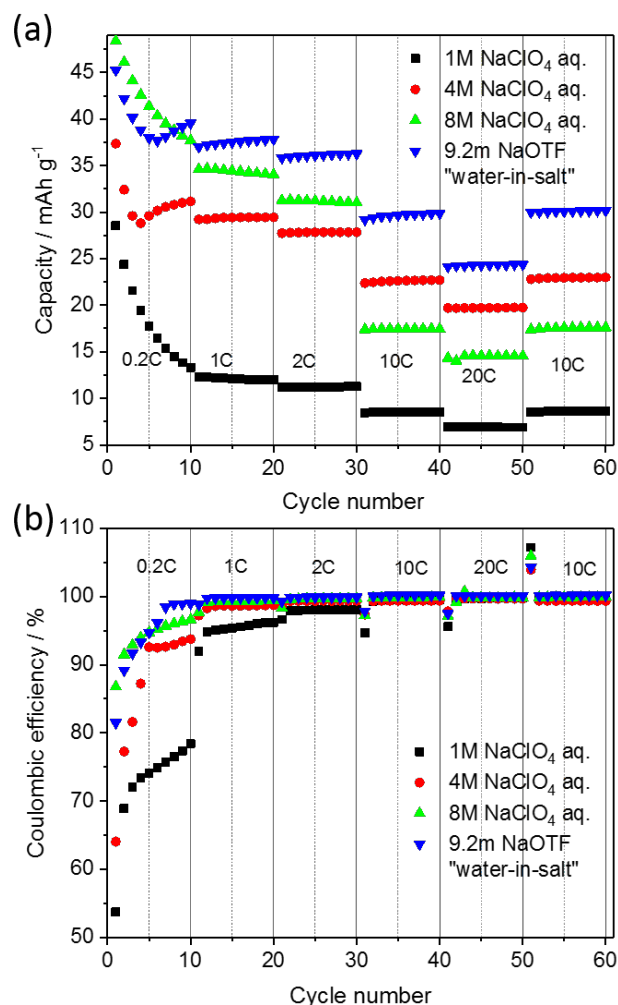


**Figure 4-8.** (a) Rate capability measurements, (b) corresponding coulombic efficiencies of  $\text{Na}_2\text{VTi}(\text{PO}_4)_3/\text{C}$  symmetric full cells in various aqueous electrolytes.

**Figure 4-9** shows the long-term cycling of NVTP/C symmetric full cells in various aqueous electrolytes at 20 C together with the capacity retention during cycling. All NVTP/C electrodes show extremely stable cycling behavior and no or negligible capacity fading for 1000 cycles. Therefore, superior performance is observed for NVTP/C cycling in 8 M  $\text{NaClO}_4$  and 9.2 m NaOTF “water-in-salt” electrolyte. The stable cycling performance is confirmed via the very good overlap of voltage profiles, recorded during 1<sup>st</sup>, 500<sup>th</sup> and 1000<sup>th</sup> cycle at 20 C, for the symmetric cells in 8 M  $\text{NaClO}_4$  and 9.2 m NaOTF “water-in-salt” electrolytes (**Figure 4-10**).

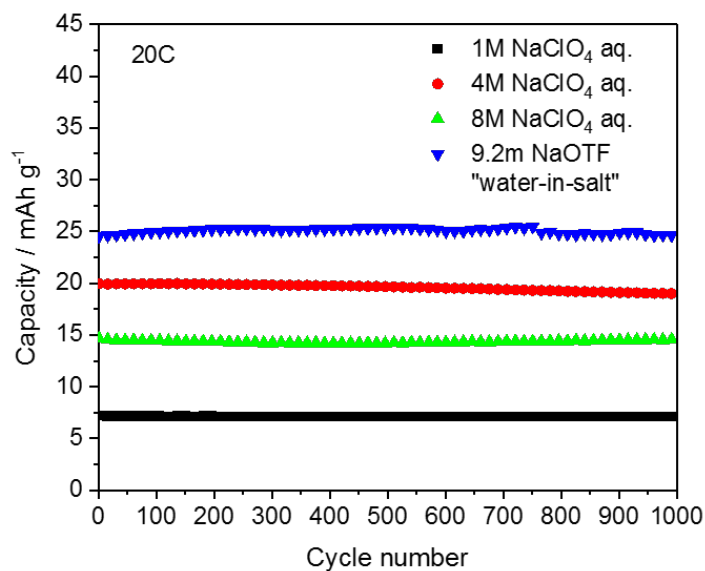


**Figure 4-9.** Cycling test at 20 C of  $\text{Na}_2\text{VTi}(\text{PO}_4)_3/\text{C}$  symmetric full cells in various aqueous electrolytes.

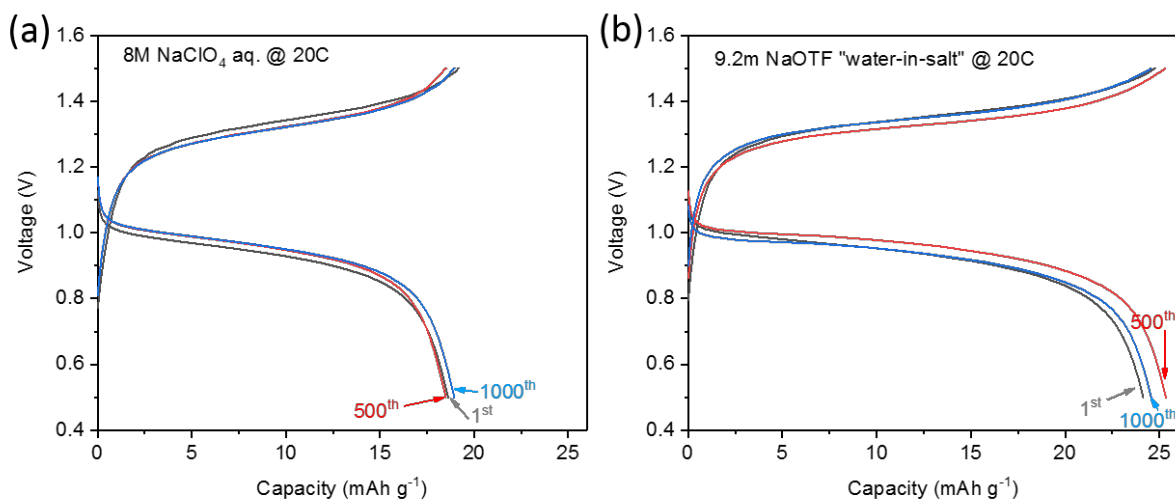


**Figure 4-10.** The galvanostatic charge-discharge profiles of  $\text{Na}_2\text{VTi}(\text{PO}_4)_3/\text{C}$  symmetric full cells at 20 C in 8 M  $\text{NaClO}_4$  aqueous electrolyte and 9.2 m  $\text{NaOTF}$  “water-in-salt” electrolyte (1<sup>st</sup>, 500<sup>th</sup> and 1000<sup>th</sup> cycles).

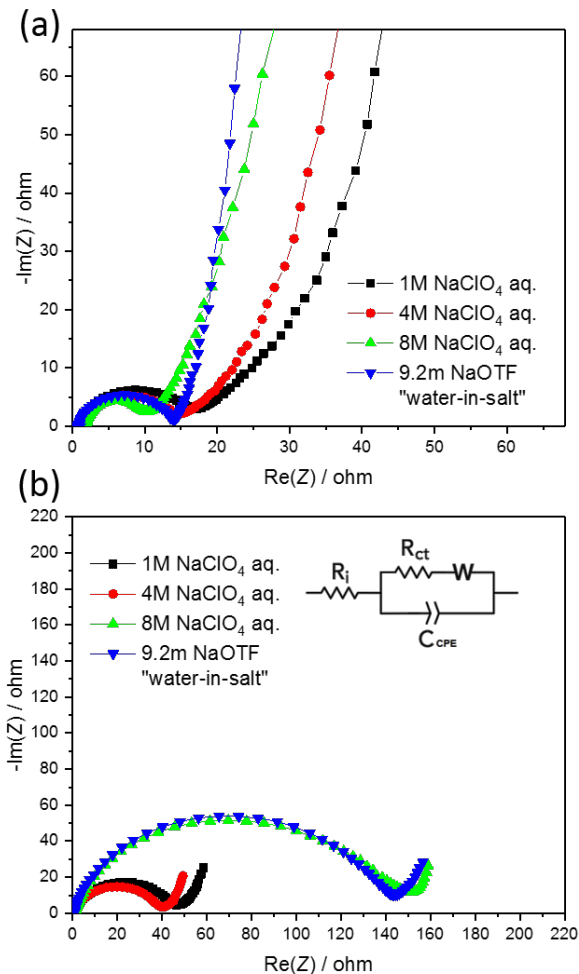


**Figure 4-11.** Nyquist and Bode plots of  $\text{Na}_2\text{VTi}(\text{PO}_4)_3/\text{C}$  symmetric full cells in various aqueous electrolytes. Impedance spectra were recorded (a) at open-circuit voltage and (b) after 50 cycles (fully discharged state).

Electrochemical impedance spectroscopy (EIS) was performed on NVTP/C electrodes in the different aqueous electrolytes because electrochemical performance tests strongly indicated the crucial impact of the charge transfer at the electrode-electrolyte interface. The EIS spectra are presented in **Figure 4-11**. The Nyquist plots consist of a semicircle referring to the electrolyte resistance (high-frequency intercept) and charge transfer resistance at the electrode/electrolyte interface, and a sloping line at low frequency related to the diffusion in the electrode. At OCV, the lower frequency intercept of the semicircle shifts to lower frequencies with higher salt concentration. After 50 cycles the lower frequency intercept increases for all the electrolytes. However, the largest increase of the frequency intercept, referring to a charge transfer resistance of 140-160  $\Omega$ , is observed for 8 M  $\text{NaClO}_4$  and 9.2 m NaOTF “water-in-salt” electrolyte. The minor



resistance increase for the more diluted aqueous electrolytes in the initial cycles is in accordance with available reports and indicates that a resistive but protective interphase is not formed on the NVTP electrode.

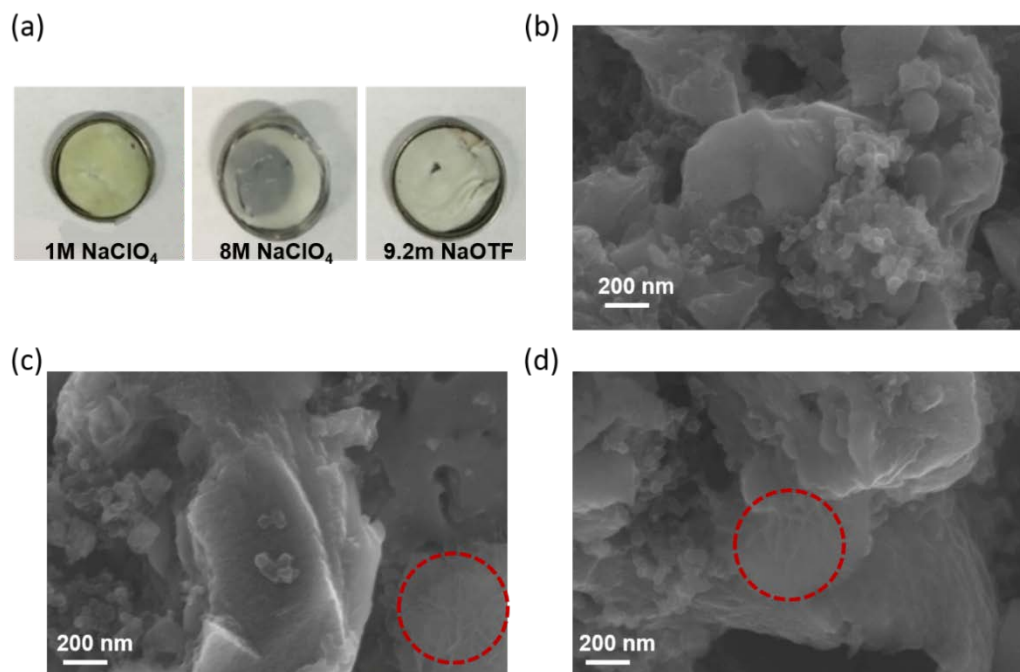


**Figure 4-12.** (a) Photographs of separators from the cells after 1000 cycles aiming to show the dissolution of  $V^{n+}$  species in aqueous solutions, and (b, c, d) SEM images of anodes in 1 M NaClO<sub>4</sub>, 8 M NaClO<sub>4</sub> aqueous electrolytes and 9.2 m NaOTF “water-in-salt”, respectively.

However, to provide further evidence, we performed post-mortem analysis of cells after 1000 cycles (**Figure 4-12**). In detail, separators from the cell with 1 M NaClO<sub>4</sub> electrolyte are yellowish due to the dissolution of vanadium species in the diluted aqueous solution over cycling. In contrast, separators from cells with 8 M NaClO<sub>4</sub> and 9.26 m NaOTF “water-in-salt” electrolyte remain white, indicating the efficient stabilization of electrodes. Indeed, SEM images reveal the formation of relatively dense and thick film on the active materials particles after cycling in these concentrated electrolytes (as cycled with red line in **Figure 4-12c** and d), while no film is present on the particle after cycling in 1M NaClO<sub>4</sub> electrolyte.

In non-aqueous lithium-ion batteries the increased resistance is commonly associated to the formation of solid-electrolyte interphase (SEI).<sup>[189]</sup> Therefore, these results indicate the formation of a resistive, but protective layer on the NVTP electrodes that, analogously to the SEI in Li-ion batteries, suppresses unwanted side reactions, such as H<sub>2</sub> evolution, at the electrode surface. This protective layer enables the improved electrochemical cycling performance in the highly

concentrated  $\text{NaClO}_4$  aqueous electrolytes and 9.2 m NaOTF “water-in-salt” electrolyte. Indeed, similar behavior, i.e. formation of a resistive SEI film, was also observed in other studies using “water-in-salt” sulfonate-based electrolytes.<sup>[177, 190]</sup>

#### 4.1.4 Conclusions

In this work, we successfully synthesized NASICON-type  $\text{Na}_2\text{VTi}(\text{PO}_4)_3/\text{C}$  composites and investigated their use as electrode material in symmetric  $\text{Na}_2\text{VTi}(\text{PO}_4)_3//\text{Na}_2\text{VTi}(\text{PO}_4)_3$  aqueous Na-ion batteries. The aqueous  $\text{NaClO}_4$  electrolytes with different concentration and a sulfonate-based “water-in-salt” electrolyte were used to study the impact of the electrolyte on the performance of the electrode materials. In detail, the salt concentration in the electrolyte significantly changes the charge transfer at the electrode-electrolyte interface. The symmetric aqueous Na-ion batteries with NASICON electrode materials were found to deliver very stable cycling performance and very good rate capability in the highly concentrated aqueous 8 M  $\text{NaClO}_4$  electrolyte and 9.2 m NaOTF “water in salt” electrolyte. At low current density, this can be attributed to the more pronounced ion aggregation and enhanced electrolyte stability. The formation of a resistive but protective interphase derived from concentrated electrolytes was found to be the origin for the superior performance at low and high rates. The “water-in-salt” sulfonate-containing electrolyte enabled extremely stable cycling at 20 C for 1000 cycles of the symmetric aqueous Na-ion battery without capacity fading. These results provide an important insight for the development of aqueous Na-ion batteries with stable long-term cycling performance for large-scale energy storage. Future work should be dedicated to the elucidation of the SEI forming mechanism in highly concentrated  $\text{NaClO}_4$  electrolyte and the electrical double layer in concentrated electrolytes.

## 4.2 Sodium-ion Battery: $\text{NaTi}_2(\text{PO}_4)_3//\text{Na}_3\text{V}_2(\text{PO}_4)_3$

### 4.2.1 Introduction

Polyanionic electrode materials are very interesting for battery applications requiring high safety and long lifespan, due to their negligible structure change during electrochemical reaction.<sup>[191]</sup> Among a number of electrode materials investigated for sodium-ion batteries, NASICON (Sodium Super Ionic Conductor)-structured materials show of great interest due to the open framework structures with fast ionic diffusion capability.<sup>[165, 192]</sup> In this respect, phosphate framework materials offer relatively high structural stability, facile producibility and rich structural diversity.<sup>[193]</sup> Polyanionic  $\text{Na}_3\text{V}_2(\text{PO}_4)_3$  compounds are considered as promising cathodes with a theoretical specific energy of  $400 \text{ W h kg}^{-1}$  ( $117.6 \text{ mAh g}^{-1}$  and  $3.4 \text{ V vs. Na/Na}^+$  with  $\text{V}^{3+}/\text{V}^{4+}$  redox couple) and high structural/thermal stabilities.<sup>[78, 194, 195]</sup> In a similar manner, the NASICON-structured  $\text{NaTi}_2(\text{PO}_4)_3$  has also been reported as excellent anode material in large-scale application on the basis of insertion mechanisms with  $\text{Ti}^{4+}/\text{Ti}^{3+}$  redox, benefiting from the open 3D framework with the large interstitial spaces, fast  $\text{Na}^+$  diffusion, and relatively high working potential, strongly reducing the risk of sodium metal plating.<sup>[196-198]</sup> However, the implementation of scaffolded functional carbon and nanostructured design should be applied to improve the electric conductivity and reduce the  $\text{Na}^+$  diffusion pathways, enabling satisfactory cycling stability and rate capability in SIBs. In Chapter 2, we have demonstrated the superior cycling and rate performance of  $\text{Na}_3\text{V}_2(\text{PO}_4)_3$  cathodes by functional carbon interpenetration together with simplified synthesis procedure.<sup>[182, 199]</sup> In this respect, the NASICON-type  $\text{Na}_3\text{V}_2(\text{PO}_4)_3$  cathode and  $\text{NaTi}_2(\text{PO}_4)_3$  anode could be coupled to build safer SIBs with high lifetime.<sup>[173, 200]</sup> But, few studies report on the development of scalable synthesis methods for the large-scale production of active materials, which can maintain the superior electrochemical performance realized in lab-scale fabrication.<sup>[201]</sup>

Moreover, rather than the energy density for portable electronics, cost and safety become more important for grid-energy storage.<sup>[202]</sup> Aqueous electrolytes promise increased operational safety and lower manufacturing cost. However, the narrow electrochemical window and poor materials stability limit the running of a successful device.<sup>[156, 203]</sup> Recently, a highly concentrated “water-in-salt” electrolyte (WiSE) was reported which can significantly reduce electrochemical activity of water and thus enable constructing high energy aqueous batteries.<sup>[161, 164, 204-206]</sup> On the other hand, NASICON-type  $\text{Na}_3\text{V}_2(\text{PO}_4)_3$  conceives to be a promising cathode for sodium-ion batteries, owing to its structural stability and comparable specific energy.<sup>[78]</sup> However, it suffers from the degradation in aqueous electrolytes during electrochemical reaction, resulting in the severe

energy-loss.<sup>[167, 169]</sup> Therefore, it is necessary to improve the stability of  $\text{Na}_3\text{V}_2(\text{PO}_4)_3$  electrode from both the materials optimization and electrolyte design.

First of all, we report the scalable synthesis of porous  $\text{Na}_3\text{V}_2(\text{PO}_4)_3$  and  $\text{NaTi}_2(\text{PO}_4)_3$  composites with excellent reversible capacities and rate capabilities. The realization and investigation of a full cell based on these two NASICON electrodes using a conventional carbonate electrolyte and copper or aluminum foil as negative current collector are also reported. Then, to further develop this combination in aqueous environment, we design an aqueous/nonaqueous hybrid electrolyte with an expanded electrochemical window up to 2.8 V and comparable conductivity ( $\sim 25 \text{ mS cm}^{-1}$  at 20 °C). The double-carbon confined  $\text{Na}_3\text{V}_2(\text{PO}_4)_3@\text{rGO}@C$  composite is synthesized. This study demonstrates the first use of centered hybrid aqueous/nonaqueous electrolyte in sodium-ion batteries that enables the stable operation of sodium ion battery with  $\text{Na}_3\text{V}_2(\text{PO}_4)_3/\text{NaTi}_2(\text{PO}_4)_3$  configuration in aqueous environment.

## 4.2.2 Experimental Methods

### 4.2.2.1 Materials synthesis

The NASICON-type  $\text{Na}_3\text{V}_2(\text{PO}_4)_3/\text{C}$  and  $\text{NaTi}_2(\text{PO}_4)_3/\text{C}$  composites were synthesized via a sol-gel method. Typically,  $\text{CH}_3\text{COONa}\cdot 3\text{H}_2\text{O}$  (VWR,  $\geq 99\%$ ),  $\text{NH}_4\text{VO}_3$  (Sigma Aldrich,  $\geq 99\%$ ),  $\text{NH}_4\text{H}_2\text{PO}_4$  (Alfa Aesar,  $\geq 99\%$ ), and citric acid monohydrate ( $\text{C}_6\text{H}_8\text{O}_7\cdot\text{H}_2\text{O}$ ) (Alfa Aesar,  $\geq 99\%$ ) were dissolved in deionized water and dried at 80 °C. The obtained precursor was ground and pre-treated at 350 °C for 6 h, followed by sintering at 800 °C for 12 h under argon flow to obtain the final  $\text{Na}_3\text{V}_2(\text{PO}_4)_3/\text{C}$  composite. Graphene oxide (Nanoinnova Technologies) was used to synthesize the  $\text{Na}_3\text{V}_2(\text{PO}_4)_3@\text{rGO}@C$  composite by following the same procedure as  $\text{Na}_3\text{V}_2(\text{PO}_4)_3/\text{C}$ . In the  $\text{NaTi}_2(\text{PO}_4)_3/\text{C}$  synthesis,  $\text{CH}_3\text{COONa}\cdot 3\text{H}_2\text{O}$  and  $\text{NH}_4\text{H}_2\text{PO}_4$  were firstly dissolved in deionized water. Then, polyvinyl pyrrolidone (PVP, K30, Sigma Aldrich) and  $\text{Ti}(\text{CH}_3\text{CH}_2\text{CH}_2\text{CH}_2\text{O})_4$  (Sigma Aldrich,  $\geq 98\%$ ) were dissolved in anhydrous ethanol (VWR,  $\geq 99.9\%$ ) and poured into the aqueous solution under vigorous stirring. The precursor collected after evaporating the solvents was sintered at 800 °C for 12 h under argon flow to obtain the  $\text{NaTi}_2(\text{PO}_4)_3/\text{C}$  composite.

The aqueous/nonaqueous hybrid electrolyte was prepared by mixing the same weights of 7 m (molality)  $\text{NaCF}_3\text{SO}_3$  (Alfa Aesar,  $\geq 98\%$ ) in Milli-Q water with 8 m  $\text{NaCF}_3\text{SO}_3$  (Solvionic, 99.5%) in propylene carbonate (BASF, Battery grade) under heating (35 °C). Low concentrated aqueous/nonaqueous hybrid electrolyte was prepared by dissolving 1 m  $\text{NaCF}_3\text{SO}_3$  in  $\text{H}_2\text{O}/\text{PC}$  solvents (v/v, 1:1). The “water-in-salt” electrolyte was prepared as used before, i.e. 9.26 m

NaCF<sub>3</sub>SO<sub>3</sub> (Solvionic, 99.5%) in Milli-Q water. All the aqueous electrolytes were degassed with N<sub>2</sub> for 2 h to remove the dissolved O<sub>2</sub> before use.

#### *4.2.2.2 Materials characterization*

Powder X-ray diffraction (XRD) analysis was performed in Bragg-Brentano geometry using a Bruker D8 Advance diffractometer. The pattern was recorded with CuK $\alpha$  radiation ( $\lambda = 0.154$  nm) in the  $2\theta$  range of  $10^\circ - 70^\circ$  with a step size of  $0.01^\circ$ . Morphological characterization was conducted on ZEISS 1550VP Field Emission SEM. Carbon, hydrogen, and nitrogen (CHN) elemental analyses were performed on a Perkin–Elmer EA 2400 instrument. The nitrogen adsorption and desorption isotherms were performed on Micromeritics ASAP 2020 surface area & porosity analyzer. The Brunauer–Emmett–Teller (BET) surface area and pore size distributions were obtained from BET plot and BJH (Barrett, Joyner, and Halenda) model. Liquid Raman spectra were collected on a RAM II FT-Raman module of a Bruker Vertex70 FT-IR spectrometer with a laser wavelength of 1064 nm for 1000 scans with a resolution of  $2\text{ cm}^{-1}$ . The samples were sealed in glass tubes with argon as protective gas.

#### *4.2.2.3 Electrochemical characterization*

The electrochemical performance was investigated in Swagelok-type cells. The electrodes were prepared by doctor-blade casting slurries with 90 wt.% active materials, 5 wt.% carbon black (Super C65, IMERYS) and 5 wt.% polyvinylidene fluoride (Solef 6020, Solvay Group) in N-methyl-2-pyrrolidone (anhydrous, Sigma-Aldrich) on aluminum foil for NVP/C, both copper and aluminum for NTP/C, respectively. After drying, electrodes with a diameter of 12 mm were punched and further dried at  $120^\circ\text{C}$  under high vacuum. The average active material mass loading was  $3.5\text{ mg cm}^{-2}$ . The electrolyte was prepared by dissolving 1 M NaPF<sub>6</sub> (Fluorochem) in propylene carbonate (PC, BASF) with 2 wt.% fluoroethylene carbonate (FEC, BASF) in an Ar-filled glovebox with H<sub>2</sub>O and O<sub>2</sub> contents less than 0.1 ppm. Glass fiber (GF/D, Whatman) disc was used as separator. The half-cells were assembled using sodium metal as counter and reference electrodes. NVP//NTP full cell was assembled in a cathode to anode weight ratio of 1–1.1.

The ionic conductivity of the hybrid electrolyte was measured in sealed glass conductivity cells (Materials Mates 192/K1) equipped with two porous platinum electrodes (cell constant of  $1.0 \pm 0.1$  cm) using a Bio-Logic conductivity meter. Coin cells are assembled as mentioned before, for the aqueous measurement. The electrodes were prepared by casting slurries of 80 wt.% active materials, 10 wt.% carbon black and 10 wt.% polyvinylidenedifluoride in N-methyl-2-pyrrolidone on stainless steel by a doctor blade equipment. After drying, electrodes with a diameter of 14 mm

were punched and further dried at 120 °C under high vacuum. The average active material mass loading was  $\sim 3 \text{ mg cm}^{-2}$ . NVP//NTP full cells were assembled in a cathode to anode weight ratio of 1-1.1.

A Maccor 4000 Battery system (Maccor, USA) was used for the galvanostatic charge-discharge test at various C-rates. Cyclic voltammetry and electrochemical impedance spectroscopy were performed with a multichannel potentiostat/galvanostat (VMP3, Biologic Science Instruments). The impedance spectra were recorded on the full cell at OCV and discharged state after cycling (after a potentiostatic step at 0.5 V for 30 min), with a signal amplitude of 10 mV over the frequency range from 100 kHz to 100 mHz. All measurements were carried out in climatic chambers at  $20 \pm 1 \text{ }^\circ\text{C}$ .

### 4.2.3 Results and Discussion

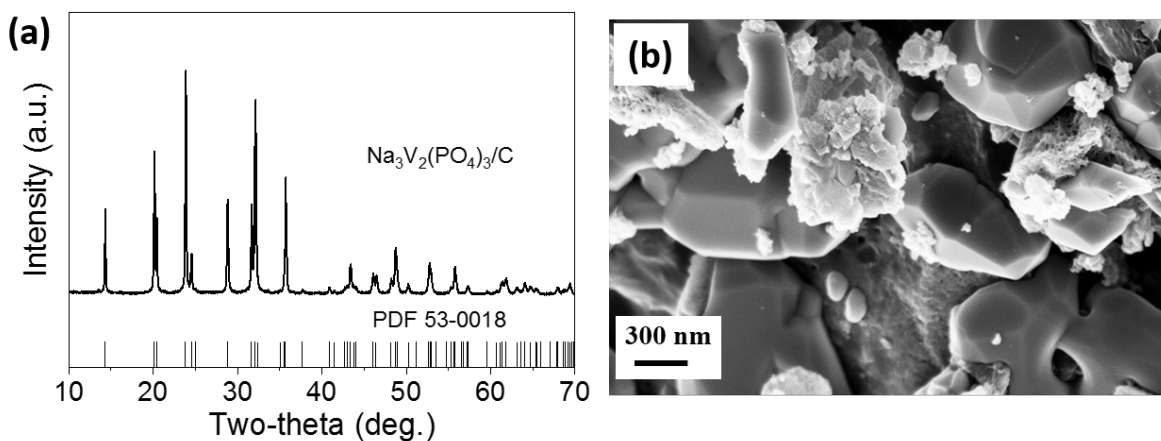


**Figure 4-13.** XRD pattern (a) and (b) SEM images of  $\text{Na}_3\text{V}_2(\text{PO}_4)_3/\text{C}$  composites.

The  $\text{Na}_3\text{V}_2(\text{PO}_4)_3/\text{C}$  (NVP/C) composites were synthesized via a simple sol-gel method followed by solid-state calcination. **Figure 4-13a** shows the XRD patterns of the synthesized NVP/C composites. The result confirms that the NVP/C crystallizes in rhombohedral NASICON structure with  $R3c$  space group. The diffractograms present no evidence of impurity phases, suggesting that the synthesis conditions adopted are suitable for targeted phase. The carbon amount in NVP/C, as determined by elemental analysis, is about 4.2%. The morphology of NVP/C composites is presented in **Figure 4-13b**. The SEM images show that NVP/C composite has a porous structure with some edge-sharp, crystalline NVP particles on the surface, resulting from the NVP melting induced from the high sintering temperature. According to the nitrogen adsorption-desorption test, the Brunauer-Emmett-Teller (BET) specific surface area of NVP/C is  $28 \text{ m}^2 \text{ g}^{-1}$ .

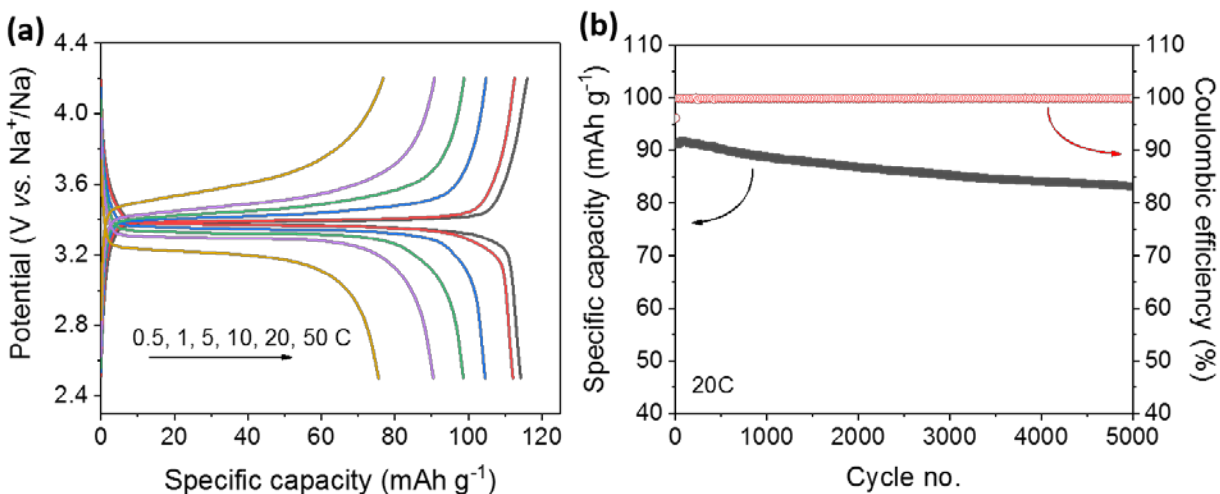


**Figure 4-14.** Electrochemical properties of NVP/C composite in half cells. (a) Selected charge-discharge profiles at various C-rates, and (b) long-term cycling performance at 20 C. (1C=120 mA g<sup>-1</sup>, 1M NaPF<sub>6</sub> in PC with 2%FEC as electrolyte)

The electrochemical properties of NVP/C as cathode were initially evaluated in Na half-cells. **Figure 4-14a** shows the typical charge-discharge profiles at different C-rates (1C = 120 mA g<sup>-1</sup>). As depicted, all the curves exhibit distinct charge-discharge voltage plateaus at around 3.4 V, in good agreement with the CV results. At 0.5 C, the NVP/C composite delivers a charge and capacity of 116 mAh g<sup>-1</sup> and 114 mAh g<sup>-1</sup>, respectively, leading to a high initial coulombic efficiency of 98.5%. At higher C-rates, the coulombic efficiency is always close to 100 %. To investigate the long-term cycling stability, the electrode was cycled at 20 C for 5000 cycles as shown in **Figure 4-14b**. It can be seen that the electrode can maintain 83 mAh g<sup>-1</sup> with capacity retention of 91.8% after long-term cycling. These results suggest that the NVP/C composite obtained via simple solution method can be used as high-power cathode materials in NIBs, because the porous materials structure enables the fast reaction kinetics.

The NaTi<sub>2</sub>(PO<sub>4</sub>)<sub>3</sub>/C (NTP/C) composites were confirmed by XRD test. As shown in **Figure 4-15a**, the XRD pattern of NTP/C composites can be indexed to a rhombohedral NASICON structure (PDF 33-1296) with space group of *R-3c*. No impurity peaks are observed. **Figure 4-15b** shows that NTP/C composites are composed of nanosized clusters with smaller nanoparticles aggregated by conductively porous carbon. The carbon amount in NTP/C, as determined by elemental analysis, is about 5.4%. The Brunauer–Emmett–Teller (BET) specific surface area of NTP/C is 73 m<sup>2</sup> g<sup>-1</sup>. Compared to the NVP/C composites, the morphological difference is attributed to the different carbon precursors and sintering procedures during the synthesis. And, the porous structure offers easy paths for electrolyte penetration.

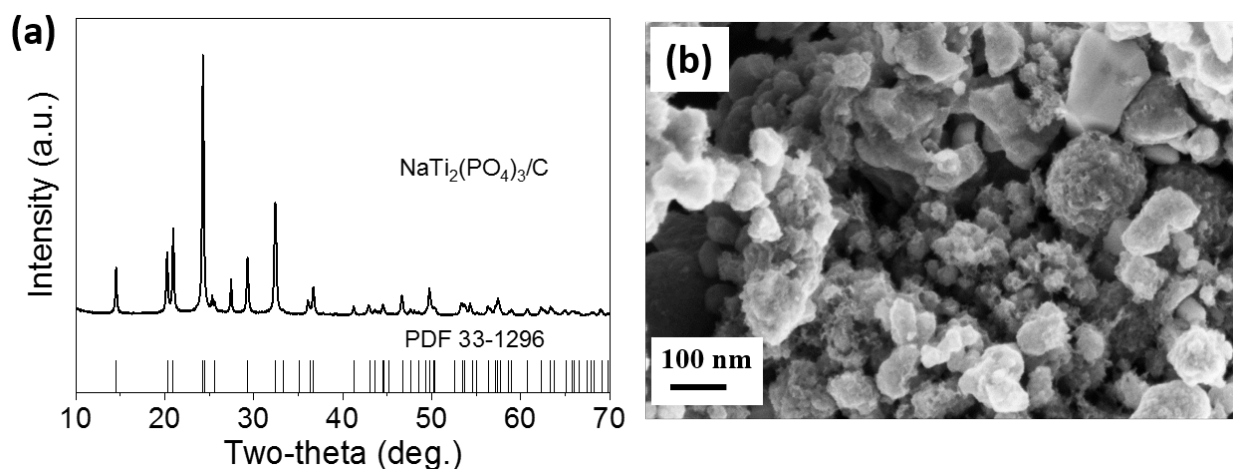


**Figure 4-15.** XRD pattern (a) and (b) SEM images of NaTi<sub>2</sub>(PO<sub>4</sub>)<sub>3</sub>/C composites.

The electrochemical performance of NTP/C composite as anode was evaluated in Na half-cell. The initial galvanostatic charge-discharge profiles of NTP/C electrode in a potential range of 1.4-3.0 V (vs. Na<sup>+</sup>/Na) at rates of 0.5, 1, 5, 10, 20, 50, 100 C (1C=120 mA g<sup>-1</sup>) are displayed in **Figure 4-16a**. The initial charge-discharge capacities are 100 and 102 mAh g<sup>-1</sup>, corresponding to a coulombic efficiency of about 98.3%. Such a high initial efficiency can be attributed to the insertion reaction of NASICON-structured materials and the improved reaction kinetics by structural confinements.<sup>[207, 208]</sup> The galvanostatic charge-discharge curves exhibit distinct charge and discharge potential plateaus, which still can be maintained at such high rate of 100 C, revealing the superior power capability and reversibility. The long-term cycling stability test at 50 C is depicted in **Figure 4-16b**. The electrode exhibits excellent capacity retention of 98% after 1000 cycles with coulombic efficiency close to 100%.



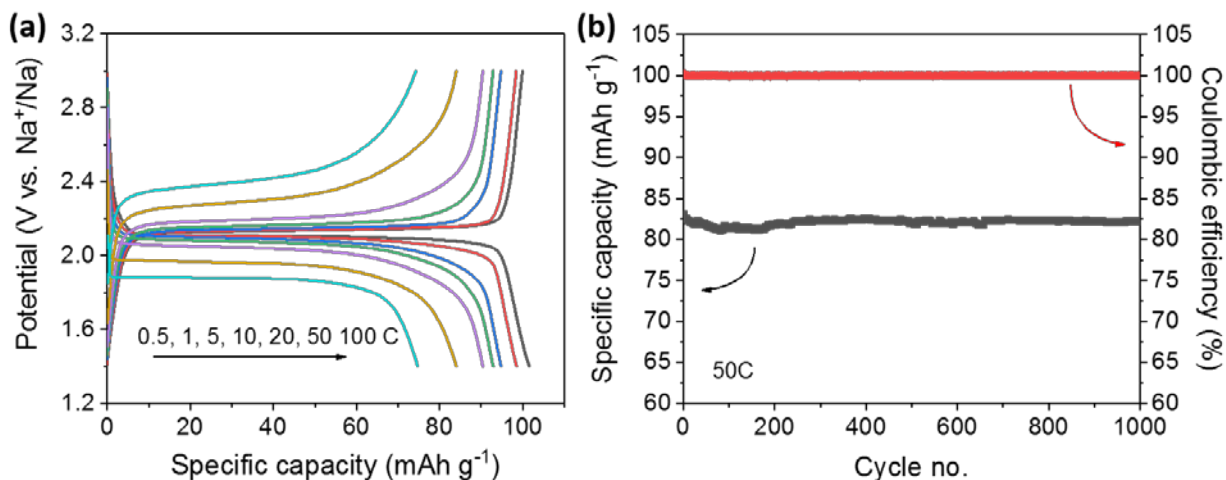


**Figure 4-16.** Electrochemical properties of NTP/C composite in half cells. (a) Galvanostatic charge-discharge profiles at various C-rates; and (b) cycling performance at 50 C. (1C=120 mA g<sup>-1</sup>, 1M NaPF<sub>6</sub> in PC with 2%FEC as electrolyte)

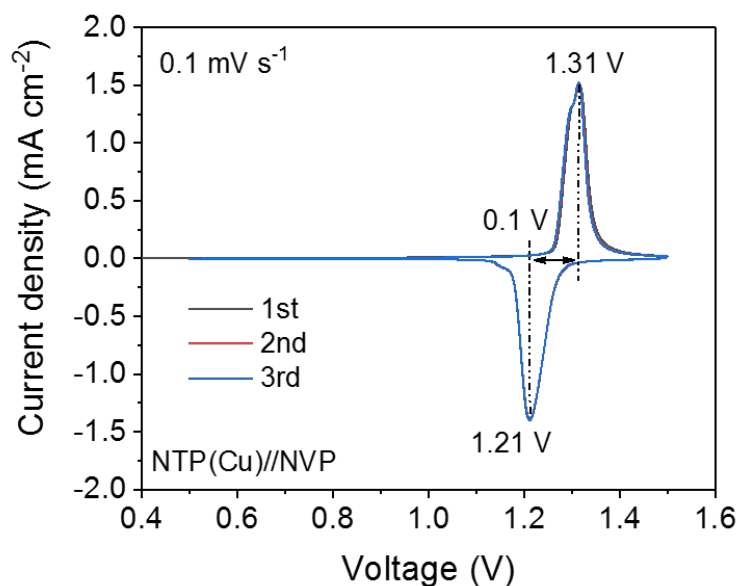


**Figure 4-17.** Typical cyclic voltammetry curves of initial three scans at 0.1 mV s<sup>-1</sup> of NTP//NVP full cell using copper as anode current collector in voltage range of 0.5-1.5 V. (1M NaPF<sub>6</sub> in PC with 2%FEC as electrolyte)

Encouraged by the very good electrochemical performance of both NVP/C and NTP/C materials in half cells, a sodium-ion full cell based on NVP/C cathode and NTP/C anode was constructed. Benefiting from the high coulombic efficiencies of both cathode and anode, a presodiation step, aggravating cell manufacturing, can be avoided.<sup>[209]</sup> **Figure 4-17** presents the CV curves of the

NTP(Cu)//NVP full cell at scan rate of  $0.1 \text{ mV s}^{-1}$  in the voltage range of 0.5-1.5 V. As shown, the cell exhibits a pair of redox peaks centered at around 1.25 V, in good agreement with the potential difference between NVP and NTP electrodes. At low scan rate the anodic and cathodic peak are only separated by 0.1 V, which can be attributed to the improved kinetics of the electrodes.

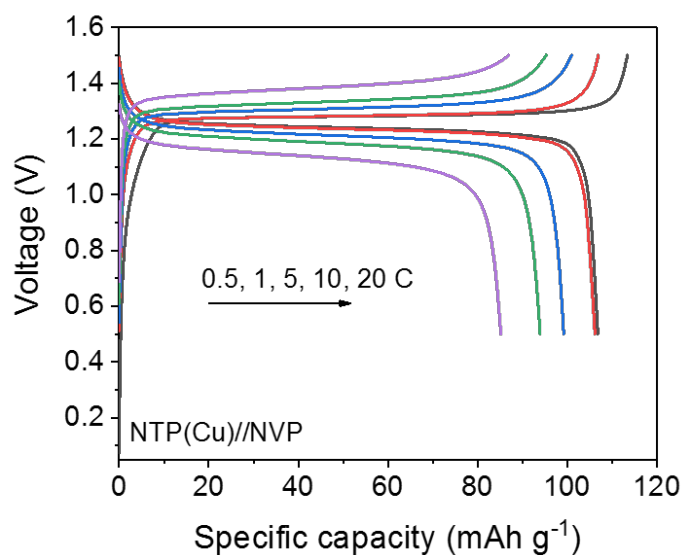


**Figure 4-18.** Initial galvanostatic charge-discharge profiles of NTP//NVP full cell using copper as anode current collector at various C-rates in voltage range of 0.5-1.5 V. (1C=120  $\text{mA g}^{-1}$ , 1M  $\text{NaPF}_6$  in PC with 2%FEC as electrolyte)

The initial galvanostatic charge-discharge curves at different C-rates (**Figure 4-18**) are in accordance with the CV results. At 0.5 C, the full cell can deliver a discharge capacity of  $107 \text{ mAh g}^{-1}$  (based on the weight of the cathode active material) with a high initial coulombic efficiency of 95%. Even at higher C-rates, the cell can still maintain stable charge-discharge plateaus with low voltage hysteresis, enabling high energy efficiency for applications requiring high power. The rate capability was tested as displayed in **Figure 4-19a**. Correspondingly, the cell delivers discharge capacity of  $107$  and  $85 \text{ mAh g}^{-1}$  at 0.5 and 20 C, respectively, and  $99 \text{ mAh g}^{-1}$  when the current density turns back to 5 C after the rate test, showing superior power capability and reversibility. **Figure 4-19b** displays the cycling performance of the full cell at high rate of 20 C. After 5000 cycles, reversible capacity of  $80 \text{ mAh g}^{-1}$  are achieved, corresponding to a capacity retention of 94%, indicating once again the very good high power performance and cycling stability of the full cell. Moreover, the coulombic efficiency of the full cell is always close to 100% during cycling. The outstanding power performance and long lifespan of the full cell reported here, makes it a very interesting candidate for large-scale energy storage.

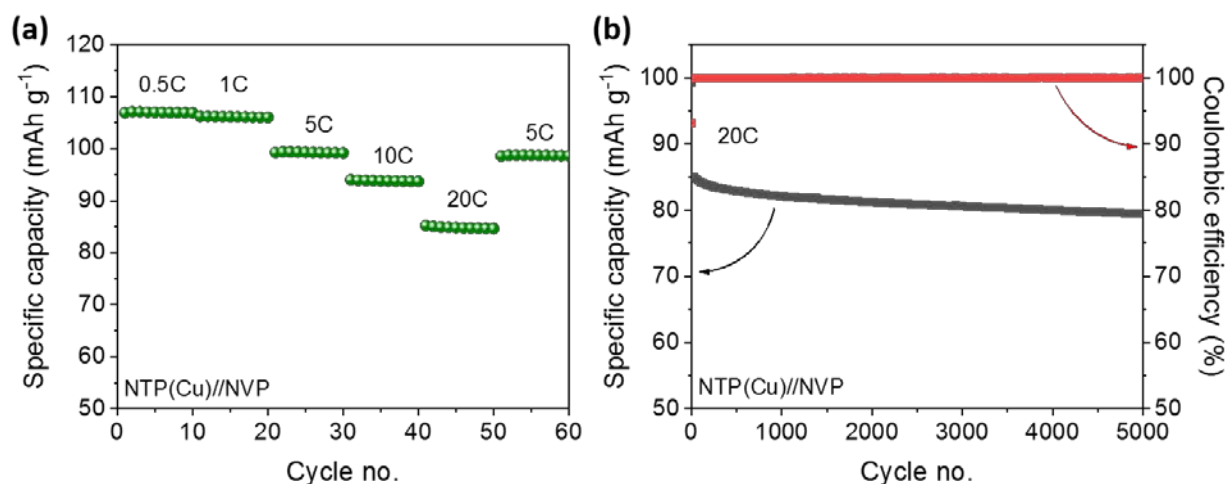


**Figure 4-19.** Rate capability test (a), and (b) cycling performance at 20 C of NTP//NVP full cell using copper as anode current collector. (1C=120 mA g<sup>-1</sup>, 1M NaPF<sub>6</sub> in PC with 2%FEC as electrolyte)

As aluminum is available as a current collector in sodium cells, the cost could be further reduced by replacing copper with aluminum as anode current collector. [14, 210] Therefore, NTP/C composite was also casted on aluminum current collector and the impact on the NTP(Al)//NVP full cell performance was investigated. **Figure 20a** displays the initial galvanostatic charge-discharge profiles at different C-rates. All curves exhibit similar plateaus of NTP(Cu)/NTP full cell, however, larger voltage hysteresis is observed at higher C-rate, which is in agreement with CV test. At low rate of 0.5 C, an initial coulombic efficiency of 94.6% and discharge capacity of 104 mAh g<sup>-1</sup> are obtained. At higher C-rates, the cell shows higher coulombic efficiency close to 100%. At higher C-rate of 20 C, only 53 mAh g<sup>-1</sup> is maintained, lower than the copper one. To understand the cycling stability of the cell, the long-term cycling performance at 5 C is depicted in **Figure 20b**. It can be seen that the NTP(Al)/NTP cell exhibits a high capacity retention of 94.3% after 1000 cycles with coulombic efficiency of ~100%. Thus, lower rate performance and cycling stability is obtained in comparison to the cell with copper anode current collector, which can be attributed to the poor stability and low electric conductivity of aluminum.

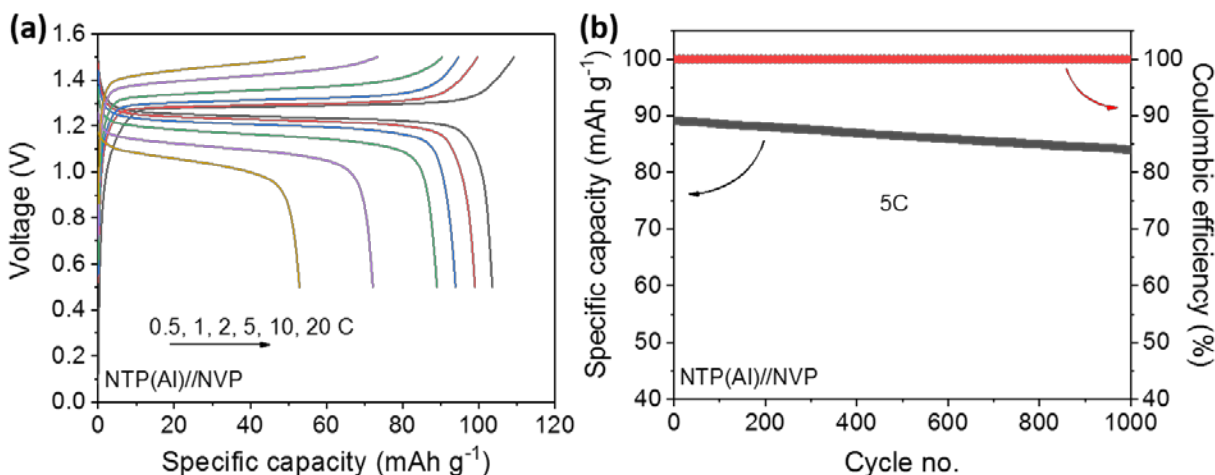


**Figure 4-20.** (a) Initial galvanostatic charge-discharge profiles and (b) cycling performance at 5 C of NTP//NVP full cell using aluminum as anode current collector at various C-rates in voltage range of 0.5-1.5 V. (1C=120 mA g<sup>-1</sup>, 1M NaPF<sub>6</sub> in PC with 2%FEC as electrolyte)

To further understand the impact of aluminum on the overall performance of full cell, the cyclic voltammetry was performed. The CV curves of NTP//NVP full cells using copper and aluminum are shown in **Figure 4-21**. As shown before, the NTP(Cu)//NVP full cell exhibits a voltage hysteresis of 0.1 V at 0.1 mV s<sup>-1</sup>. However, the NTP(AI)//NVP full cell exhibits a single pair of redox peaks (cathodic at 1.35 V and anodic at 1.18 V). The voltage hysteresis of 0.17 V is a bit larger than the one using copper as anode current collector (~0.1V). All peaks overlap during the initial three scan cycles, indicating the good reversibility of the full cell with aluminum anode current collector at low current density. However, at a faster scan rate of 1.0 mV s<sup>-1</sup>, the redox peaks shift asymmetrically, which it occurs at scan rate of 5.0 mV s<sup>-1</sup> of the copper one. These results show that the voltage hysteresis is much severer with aluminum than the copper at faster scan rate, which will result in poor energy efficiency at high power.

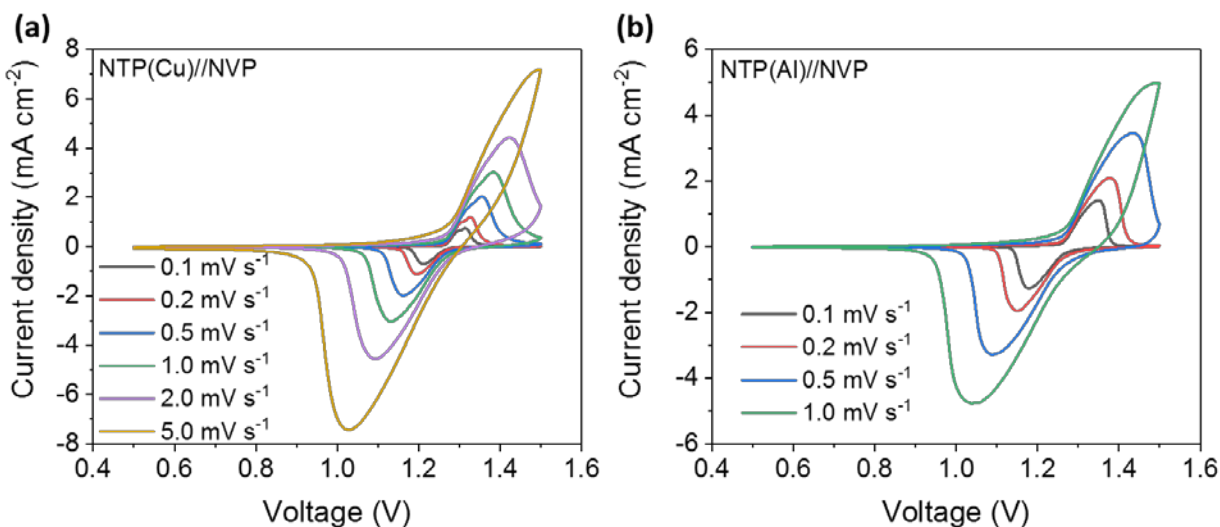


**Figure 4-21.** CV curves of NTP(Cu)//NVP (a) and NTP(Al)//NVP (b) full cells at various scan rates. ( $1C=120 \text{ mA g}^{-1}$ ,  $1M \text{ NaPF}_6$  in PC with 2%FEC as electrolyte)

Electrochemical impedance spectroscopy (EIS) was performed to understand the performance difference between aluminum anode current collector and copper. **Figure 22** displays the Nyquist plots collected on the full cells using copper and aluminum as anode current collectors at open-circuit voltage (OCV) state and discharged state (0.5 V) after 100 cycles at 10 C, respectively. The spectra consist of a semicircle associated to bulk resistance ( $R_i$ , high frequency intercept) and the charge transfer resistance ( $R_{CT}$ ). At lower frequencies, a sloping line is observed that is associated to  $\text{Na}^+$ -ion diffusion.<sup>[211, 212]</sup> The cell with copper anode current collector shows no increase on the charge-transfer resistance after 100 cycles at 10 C, while the one with aluminum exhibits an increase from  $5.0 \Omega$  to  $10.1 \Omega$ . This behavior is probably due to the uncompleted passivation of the aluminum electrode, which takes place at higher potentials via the generation of  $\text{F}^-$  from the  $\text{PF}_6^-$  decomposition in turns leading to the formation of the very stable aluminum oxyfluoride species. Such an incomplete passivation leads to the continuous increase of the electrode resistance upon long-term cycling, which limits the power capability and cycling stability of sodium-ion battery.

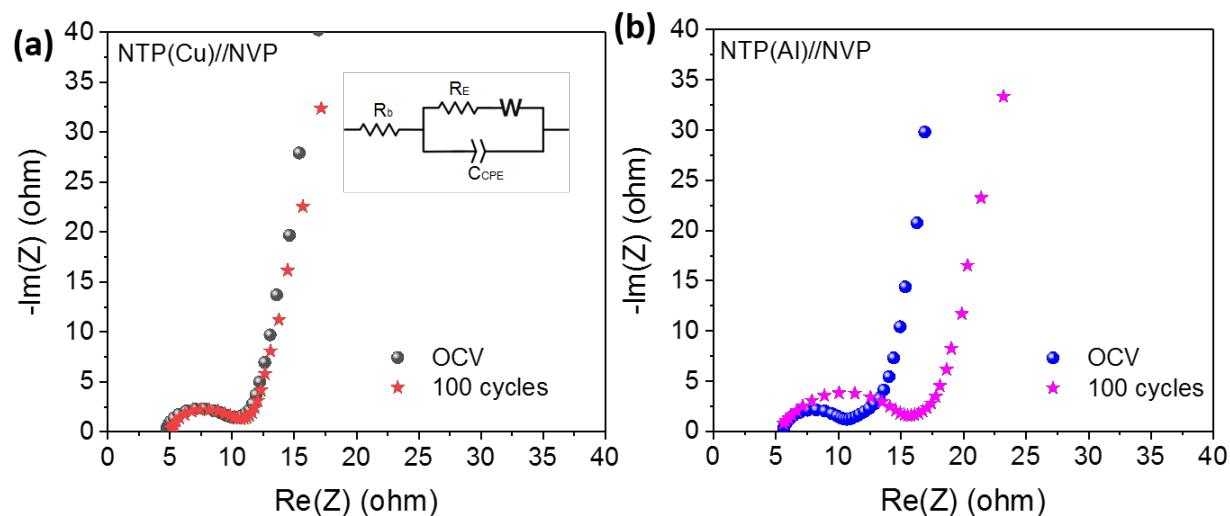


**Figure 4-22.** (a) Nyquist plots obtained in NTP(Cu)//NVP full cell at OCV and after 100 cycles at 10 C, and (b) Nyquist plots obtained in NTP(Al)//NVP full cell at OCV and after 100 cycles at 10 C. (1M NaPF<sub>6</sub> in PC with 2%FEC as electrolyte)

In a view of potential application for grid-scale energy storage, we evaluated the relations among energy density, power density and energy efficiency of the full cells with copper or aluminum as anode current collector. The Ragone plot (**Figure 4-23a**) was drawn considering the total weight of NVP and NTP active materials. The specific energy of the NTP(Cu)//NVP cell is 67.1 Wh kg<sup>-1</sup> and 47.5 Wh kg<sup>-1</sup> at specific power of 37.0 W kg<sup>-1</sup> and 1342.2 W kg<sup>-1</sup>, respectively. The NTP(Al)//NVP cell delivers comparable 63.5 Wh kg<sup>-1</sup> at low specific power of 36.6 W kg<sup>-1</sup> but only 27.0 Wh kg<sup>-1</sup> at 1227.3 W kg<sup>-1</sup>. The relation between specific power and energy efficiency is shown in **Figure 4-23b**. The cell with copper anode current collector exhibits higher energy efficiency than the aluminum one at both low and high power conditions. Specifically, at low specific power of 37 W kg<sup>-1</sup> and 74 W kg<sup>-1</sup>, the energy efficiencies of NTP(Cu)//NVP cell are 95.8% and 94.9%. The cell still can maintain a high energy efficiency of 80% even at 1342.1 W kg<sup>-1</sup>. In comparison, only 69% of the energy efficiency is achieved with NTP(Al)//NVP cell at high specific power.

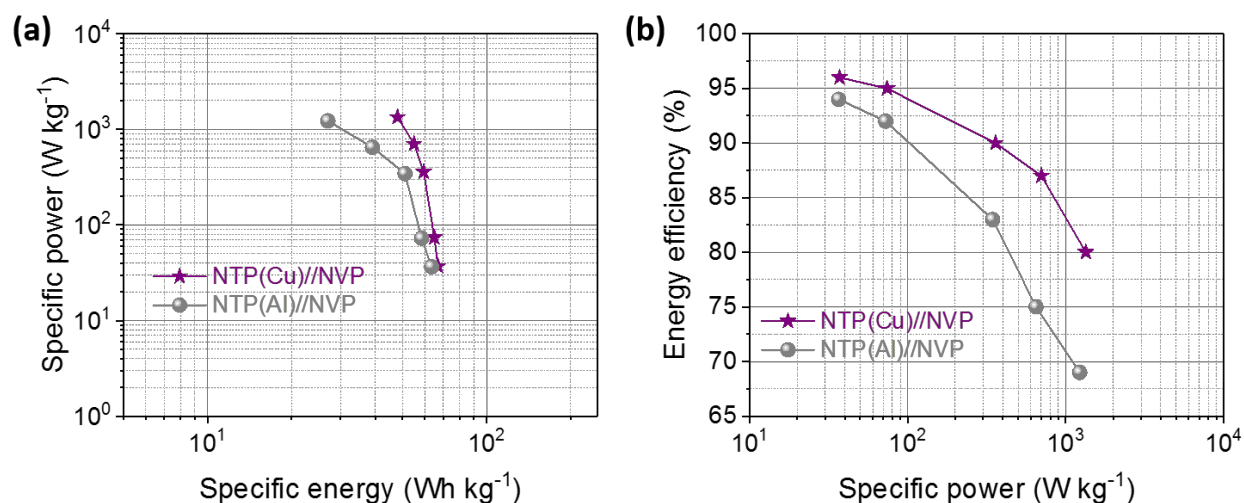


**Figure 4-23.** (a) Ragone plot, and (b) comparison of energy efficiency and power density for NTP(Cu)//NVP and NTP(Al)//NVP full cells. (1M NaPF<sub>6</sub> in PC with 2%FEC as electrolyte)

To investigate the availability of this NTP//NVP combination in aqueous environment, we test the NTP//NVP cell in the 9.26m NaOTf aqueous “water-in-salt” electrolyte (WiSE), where the stainless steel is used as current collector for both cathode and anode. As shown in **Figure 4-24**, we can clearly see the cell can be charged to 105 mAh g<sup>-1</sup> with a flat plateau at around 1.2 V, however, only capacity of 22 mAh g<sup>-1</sup> can be achieved over discharge. The cell only exhibits an initial coulombic efficiency of 21% in WiSE. This can be attributed to the dissolution of V-based materials over electrochemical reaction in aqueous electrolyte. Therefore, the materials strategies of double-carbon coating and electrolyte design have been adopted.

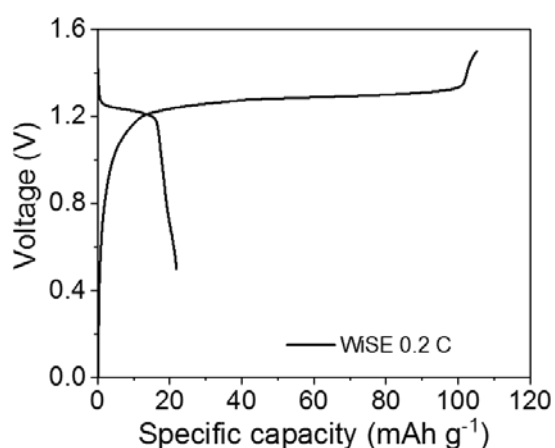


**Figure 4-24.** Initial galvanostatic charge-discharge profiles of NTP//NVP full cell in 9.26m NaOTf aqueous “water-in-salt” electrolyte (WiSE) in 0.5-1.5 V at 0.2 C. (1 C=120 mA g<sup>-1</sup>)

The double-carbon confined  $\text{Na}_3\text{V}_2(\text{PO}_4)_3@\text{rGO}@\text{C}$  composites were synthesized via sol-gel method and solid state reaction. The XRD pattern is shown in **Figure 4-25a**. As seen, the synthesized  $\text{Na}_3\text{V}_2(\text{PO}_4)_3@\text{rGO}@\text{C}$  composites are crystallized in well-defined rhombohedral NASICON structure with  $R3c$  space group (PDF 01-078-7289). The morphology of these composites is presented in **Figure 4-25b**. From the SEM image, we can see that the composites are in irregular shape, and the large piece of reduced graphene oxide (rGO) sheets cover on the surface of NVP particles. The formed double-carbon confined structure would be beneficial for the active materials stability in the presence of water electrolyte. The carbon content in  $\text{Na}_3\text{V}_2(\text{PO}_4)_3@\text{rGO}@\text{C}$  composites is about 9 wt% with ~5 wt% of rGO.

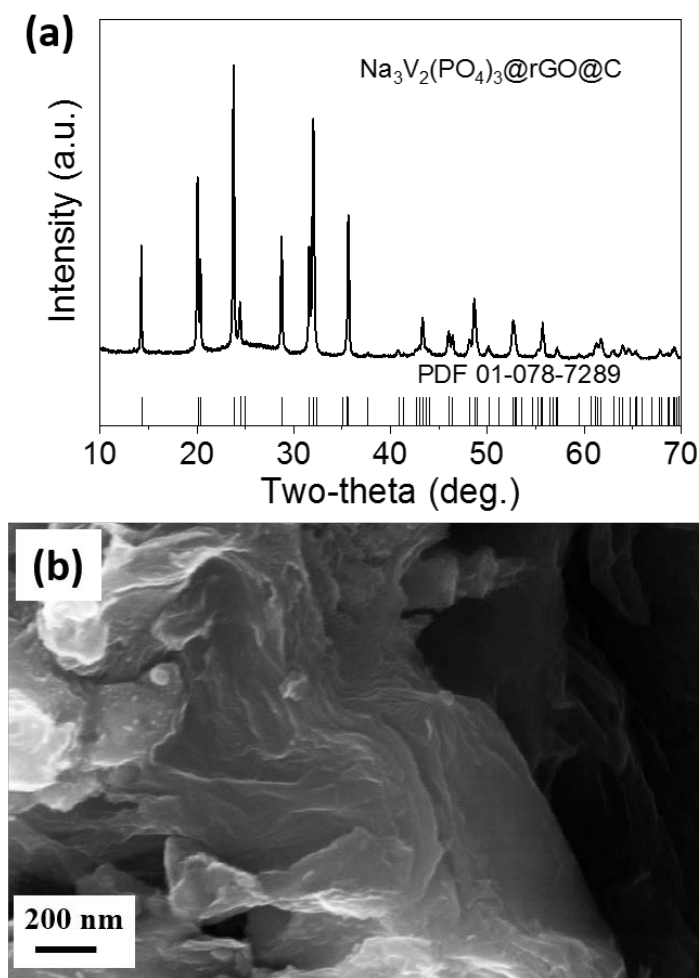


**Figure 4-25.** Powder XRD pattern (a) and (b) SEM images of  $\text{Na}_3\text{V}_2(\text{PO}_4)_3@\text{rGO}@\text{C}$  composites.

To enable the stable operation of NTP//NVP prototype in aqueous environment, the hybrid electrolyte was prepared by mixing the same weights of 7 m (molality) NaOTf in water with 8 m NaOTf in PC. This hybrid electrolyte delivers a wide electrochemical stability window up to 2.8



V, from  $-1.25$  to  $1.55$  V vs. Ag/AgCl<sub>KCl</sub> at  $20$  °C on stainless steel (**Figure 4-26**). A higher concentration is required to widen the electrochemical window of sodium solution due to the lower charge density of  $\text{Na}^+$  inducing the weaker interaction with solvent. Compared to the reported  $9.26$  m NaOTf WiSE,<sup>[178]</sup> the electrochemical stability is a bit more improved, which can be preliminarily attributed to the mixing of PC organic solvent. Moreover, the typical cyclic voltammograms of NTP and NVP electrodes on stainless steel are presented within the electrochemical window, showing a  $\sim 1.2$  V output.<sup>[167]</sup>

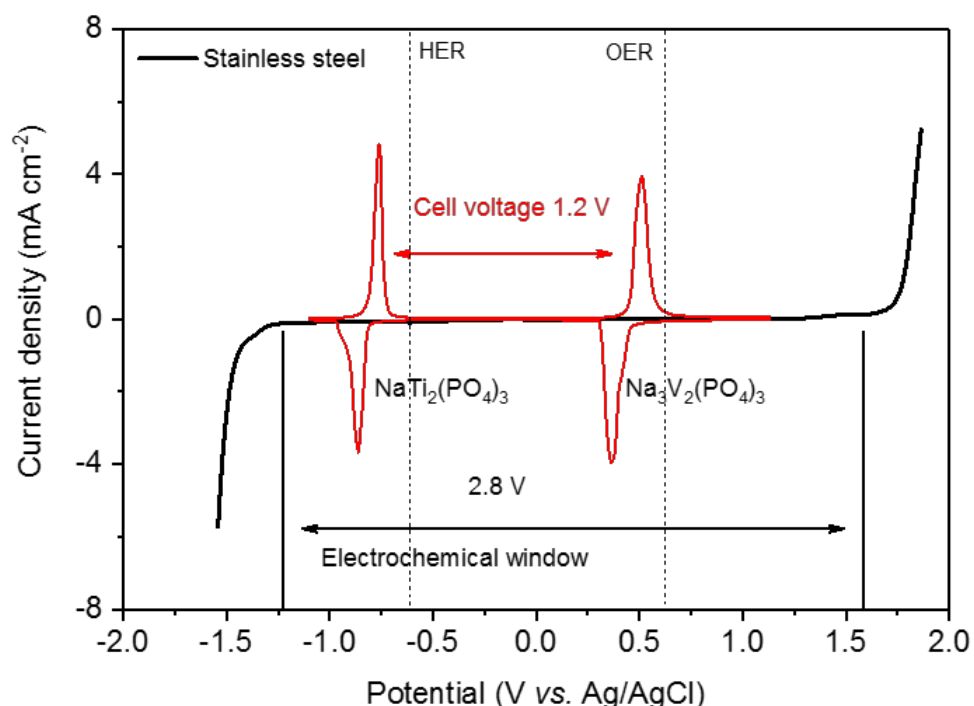


**Figure 4-26.** Electrochemical stability of aqueous/nonaqueous hybrid electrolyte based on NaOTf on stainless steel evaluated using linear sweep voltammetry at a scan rate of  $10$   $\text{mV s}^{-1}$ . Typical cyclic voltammograms of NTP and NVP electrodes are presented within the electrochemical window.

**Figure 4-27a** displays the temperature-dependent conductivity of aqueous/nonaqueous hybrid electrolyte. The conductivity strongly depends on the operating temperature, which decreases from  $\sim 60$  at  $55$  °C to  $\sim 25$   $\text{mS cm}^{-1}$  at  $20$  °C. Moreover, this electrolyte still remains a conductivity of  $\sim 5.0$   $\text{mS cm}^{-1}$  at such low temperature of  $-15$  °C, comparable to that of nonaqueous electrolyte ( $4.0$   $\text{mS cm}^{-1}$ ). To probe the solution structure, Raman spectroscopy was performed as shown in **Figure 4-27b**. The change of  $\text{SO}_3$  stretching band ( $1010$ - $1060$   $\text{cm}^{-1}$ ) was used to evaluate the salt aggregation behavior of NaOTf.<sup>[178]</sup> In concentrated aqueous/nonaqueous hybrid electrolyte, the

largest blueshift demonstrates the increased contact ion pairs/aggregated cation–anion pairs compared to low concentrated solution and WiSE. This intensified cation-anion association is beneficial for the formation of an interphase that stabilizes water molecules against the reducing surfaces of the electrode materials.<sup>[178, 211]</sup>

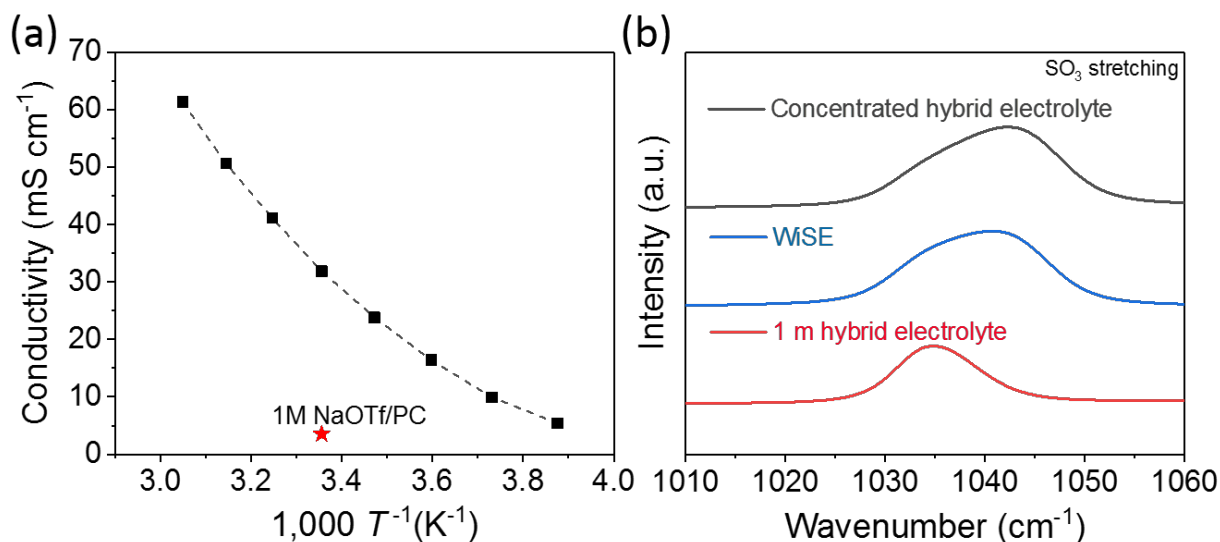


**Figure 4-27.** (a) Temperature-dependent conductivities, and (b) Raman spectra in the wavenumber region corresponding to the SO<sub>3</sub> stretching modes of aqueous/nonaqueous hybrid electrolyte.

A full sodium-ion cell using a Na<sub>3</sub>V<sub>2</sub>(PO<sub>4</sub>)<sub>3</sub>@rGO@C cathode and a NaTi<sub>2</sub>(PO<sub>4</sub>)<sub>3</sub>/C anode was assembled to evaluate the viability of aqueous/nonaqueous hybrid NaOTf electrolyte. The cyclic voltammogram of NTP//NVP cell at 0.1 mV s<sup>-1</sup> in **Figure 4-28a** exhibits anodic and cathodic peaks at 1.4 V and 1.1 V with a voltage hysteresis of 0.3 V. During 2<sup>nd</sup> scan, there is no increased polarization observed. The galvanostatic charge/discharge profiles at different rates are presented in **Figure 4-28b**. The initial charge and discharge capacities are 115 and 91 mAh g<sup>-1</sup>, with an initial coulombic efficiency of 79%. An energy density of 45 Wh kg<sup>-1</sup> was thus delivered based on the total electrode mass. However, the cell only exhibits an initial coulombic efficiency of 21% in WiSE.

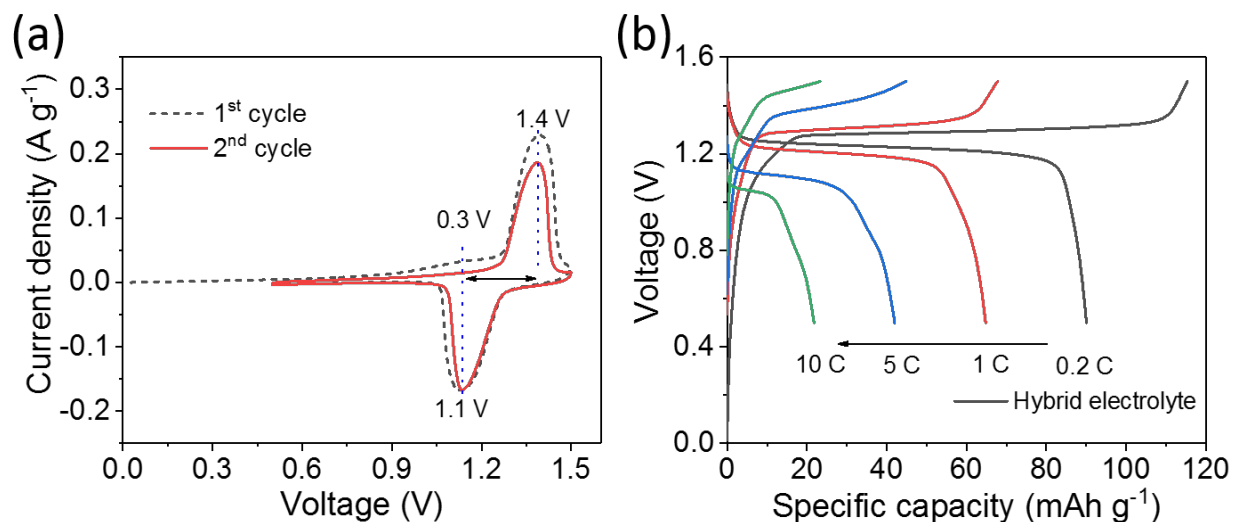


**Figure 4-28.** CV curves (a) and galvanostatic charge-discharge profiles (b) at various C-rates of NTP//NVP full cell in aqueous/nonaqueous hybrid electrolyte. (scan rate:  $0.1 \text{ mV s}^{-1}$ , voltage range:  $0.5\text{-}1.5 \text{ V}$ )

**Figure 4-29** depicts the C-rate and cycling performance of the full cell, where the capacity drops from  $65$  to  $22 \text{ mAh g}^{-1}$ , when increasing from  $1 \text{ C}$  to  $10 \text{ C}$ , but in the subsequent cycles the coulombic efficiency reaches to  $99.8\%$ . The initial irreversible processes apparently diminish and eventually disappear, which is a typical behavior of SEI formation and subsequently stabilization.<sup>[177]</sup> Moreover, the cell underwent 100 cycles at  $10 \text{ C}$  ( $1.2 \text{ A g}^{-1}$ ) without any capacity decay, indicating the superior reversibility of NVP and favorable suppression of electrolyte decomposition on the anode surface.

The electrochemical impedance spectra were performed at OCV and 30 cycles (**Figure 4-30**). The Nyquist plots show an increased charge transfer resistance after cycling, suggesting a passivation layer is formed in this aqueous electrolyte which could be highly intriguing for the stable operation of aqueous batteries.<sup>[211]</sup>

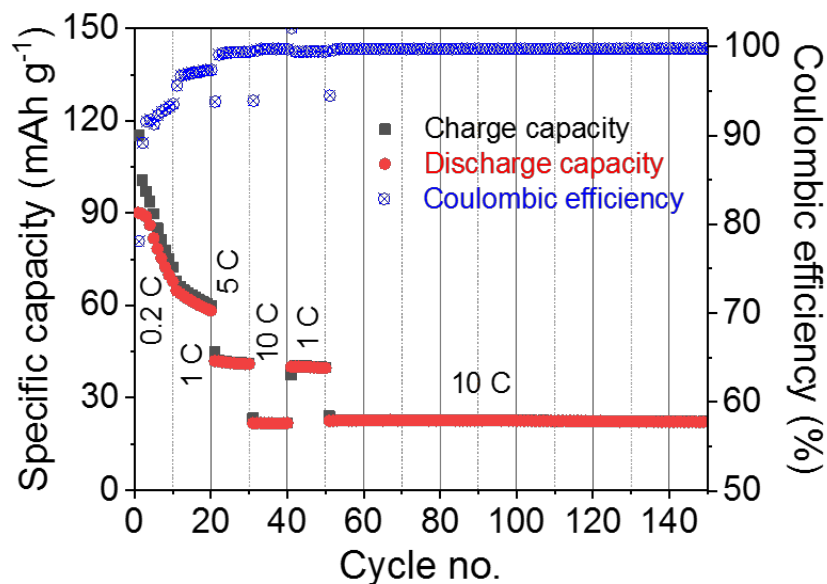


**Figure 4-29.** Rate capability test and long cycling stability test of NTP//NVP full cell in aqueous/nonaqueous hybrid electrolyte. (1C=120 mA g<sup>-1</sup>, voltage range: 0.5-1.5 V)

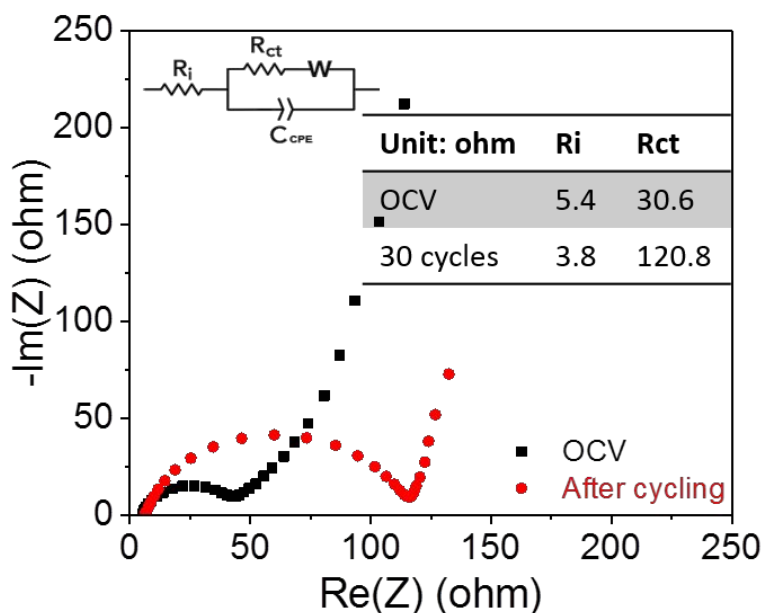


**Figure 4-30.** Nyquist plots of NTP//NVP full cell in the aqueous/nonaqueous hybrid electrolyte at open-circuit voltage and after 30 cycles.

#### 4.2.4 Conclusions

In summary, we synthesized the carbon coated Na<sub>3</sub>V<sub>2</sub>(PO<sub>4</sub>)<sub>3</sub> (NVP) and NaTi<sub>2</sub>(PO<sub>4</sub>)<sub>3</sub> (NTP) composites with porous structure via a scalable sol-gel method. The synthesis process is simple

and feasible for large-scale production for both cathode and anode materials. With low carbon contents in both the composites and electrode fabrication, the as-prepared NVP/C and NTP/C materials exhibit excellent electrochemical performance with high power capability and cycling stability. The NTP//NVP full cell using organic electrolyte constructed by the obtained materials exhibits not only high power performance (85 mAh g<sup>-1</sup> at 2.4 A g<sup>-1</sup> based on cathode), ultralong cycle life (94 % over 5000 cycles), and high energy efficiency (80%), but also simple manufacturability and intriguing safety due to the high thermal stability of the phosphate-based cathode and anode materials. These results demonstrate that the NTP//NVP configuration could be used as high efficiency battery for grid-scale energy storage, as it offers both high power and long lifetime. In addition, the cell still exhibits good performance if the copper anode current collector is replaced with aluminum, although use of the latter leads to reduced power capability and energy efficiency. To enable the high safety and low cost for large-scale energy storage, aqueous sodium ion battery in the same configuration was investigated. We have demonstrated the first use of an aqueous/nonaqueous hybrid electrolyte that provides a potential window up to 2.8 V. Meanwhile, a composite of double-carbon confined Na<sub>3</sub>V<sub>2</sub>(PO<sub>4</sub>)<sub>3</sub>@rGO@C was synthesized. It enables the stable and reversible operation of a sodium-ion battery using Na<sub>3</sub>V<sub>2</sub>(PO<sub>4</sub>)<sub>3</sub> cathode and NaTi<sub>2</sub>(PO<sub>4</sub>)<sub>3</sub> anode. The widened stability window ensures further improved cell voltage and consequently the energy density by using higher voltage cathode materials. This electrolyte expands an avenue for exploration of sodium-ion battery with high safety and electrochemical stability.



# Chapter 5

## Summary and Outlook

The target of this thesis is the investigation and exploration of polyanionic cathode materials for application in sodium-ion batteries (SIBs), enabling the realization of low cost, safe, long lasting and high energy density lab scale battery prototypes for large-scale stationary energy storage application.

In this thesis, both novel materials development and optimization of already proposed promising materials have been conducted. In the latter case, attention has been focused toward a better understanding of the structure-function correlation linked with the sodium ions diffusion in  $\text{Na}_3\text{V}_2(\text{PO}_4)_3$ . Aiming at the improvement of the electrochemical performance, mainly in terms of rate capability, a strategy combining the implementation of carbon composite materials with nitrogen doped carbon coating has been developed. The nitrogen-doping induced defects improve the sodium ions diffusion, while the morphology of carbon matrices strongly affects the sodium storage capability. The resultant materials exhibit highly improved rate capability and cycling stability, due to the enhanced electronic conductivity and facilitated charge transfer. However, further progresses on the materials should be attempted to improve the energy density, such as increasing the specific capacity and working voltage.

In an attempt to improve the energy density of cathode materials, an explorative research of novel high voltage polyanionic materials has been undertaken. New mixed polyanionic compounds, such as  $\text{Na}_4\text{Ni}_3(\text{PO}_4)_2(\text{P}_2\text{O}_7)$ , and innovative polyanionic frameworks, such as  $\text{Na}_3\text{V}(\text{PO}_3)_3\text{N}$ , were successfully synthesized in pure crystalline phases. The feasibility of the sodium storage mechanism in the new materials has been proven for the first time. The work represents a promising step forward the design of new cathode materials characterized by high operating voltage enabled by a rational tuning of the transition metals and polyanionic groups. Despite the promising results, it is worth mentioning that the reversible capacity and cycling stability still need to be improved to fill the gap between theoretical and practical capacities.

In line with the low cost and environmental friendly philosophy of SIBs, efforts were devoted to the design of full cell prototypes. Two sodium-ion cell prototypes, i.e.  $\text{Na}_2\text{VTi}(\text{PO}_4)_3//\text{Na}_2\text{VTi}(\text{PO}_4)_3$  and  $\text{NaTi}_2(\text{PO}_4)_3//\text{Na}_3\text{V}_2(\text{PO}_4)_3$ , have been designed and employed in both conventional organic and aqueous electrolytes. By using organic electrolyte, the sodium-ion cells delivered superior cycling stability and energy efficiency, which are very interesting properties in

view of their implementation in stationary energy storage systems. In addition, the aqueous sodium-ion cells employing polyanionic electrodes were successfully fabricated and the use of highly concentrated electrolytes enabled a relatively stable cycling performance. However, further improvements in power and energy density are still required. In this regard, the main challenges reside in the increase of the electrochemical stability window of aqueous electrolytes and degradation resistant cathode materials.

The work in this thesis demonstrates that the sodium-ion technology has the potential to fulfill the requirements needed by stationary energy storage applications. SIBs represent the next-generation power sources of choice and in agreement with the market diversification, they might be considered as a complimentary to and competing technology to LIBs. The conducted research represents a step forward in the development of low cost and environmentally friendly materials as well as high performance cathode materials characterized by high operating voltage and improved rate capability. Further studies and research are required for the development of the sodium-based technology. However, taking into account the increased interest on low cost and environmentally friendly energy storage systems, it is believed that great advancement in the near future years will lead to a fast commercialization of sodium cell prototypes.



## 6 Appendix

### 6.1 Abbreviations

BET	Brunauer–Emmett–Teller
CV	Cyclic voltammetry
CNT	Carbon nanotube
CHN	Carbon, hydrogen, nitrogen
DEC	Diethyl carbonate
DOD	Depth of discharge
EV	Electric vehicle
EMF	Electromotive force
EDX	Energy-dispersive X-ray spectroscopy
EIS	Electrochemical Impedance Spectroscopy
EC	Ethylene carbonate
FEC	Fluoroethylene carbonate
GOF	Goodness of fit
GCD	Galvanostatic charge-discharge
HOMO	Highest occupied molecular orbital
KB	Ketjen black
LUMO	Lowest unoccupied molecular orbital
LIB	Lithium-ion battery
NASICON	Sodium super ionic conductor
NaFSI	Sodium bis(fluorosulfonyl)imide
NaTFSI	Sodium bis(trifluoromethanesulfonyl)imide
NC	Nitrogen-doped carbon
NMP	N-Methyl-2-pyrrolidone
NVP	Sodium vanadium phosphate
NVTP	Sodium vanadium titanium phosphate
NaOTf	Sodium trifluoromethanesulfonate
NTP	Sodium titanium phosphate
OCV	Open-circuit voltage
PB	Prussian blue
PC	Propylene carbonate
Py13FSI	N-propyl-N-methylpyrrolidinium bis(fluorosulfonyl)imide
PVDF	Polyvinylidene fluoride
rGO	Reduced graphene oxide
SEI	Solid-electrolyte interphase
SEM	Scanning electron microscopy
SHE	Standard hydrogen electrode
TEM	Transmission electron microscopy
TGA	Thermogravimetric analysis
XPS	X-ray photoelectron spectroscopy
XRD	X-ray powder diffraction
WiSE	Water-in-salt electrolyte

## 6.2 List of Figures

<b>Figure 1-1.</b> Schematics of “rocking-chair” mechanism and sodium-ion batteries. Adapted from reference <sup>[13]</sup> . .....	2
<b>Figure 1-2.</b> The illustration of electrode and electrolyte materials in sodium-ion battery system. Adapted from reference <sup>[14]</sup> . .....	4
<b>Figure 1-3.</b> Schematic energy level diagram for a sodium-ion battery, illustrating the origin of the EMF (electromotive force). The Fermi level of the Na metal anode is reported above the LUMO of the electrolyte indicating reduction of the electrolyte and SEI formation. During de-intercalation of sodium at the cathode, the Fermi level will shift down as indicated by the grey arrow. Adapted from reference <sup>[5]</sup> . .....	6
<b>Figure 1-4.</b> A schematic illustration of the crystal structures for layered Na-containing oxides ( $\text{Na}_x\text{MO}_2$ ) for a) P2-type, b) O2-type, c) O3-type, and d) P3-type stacking. The blue and yellow balls represent the transition metal and $\text{Na}^+$ ions in the O-type frameworks, respectively. Adapted from reference <sup>[26]</sup> . .....	8
<b>Figure 1-5.</b> The schematic crystal structures of Prussian blue frameworks: a) an intact $\text{Na}_2\text{M}_{\text{II}}[\text{Fe}_{\text{II}}(\text{CN})_6]$ framework, b) a defective $\text{NaM}_{\text{II}}[\text{Fe}_{\text{II}}(\text{CN})_6]_{0.75}\square_{0.25}$ framework with 25% $\text{Fe}(\text{CN})_6$ vacancies existing in each unit cell. Adapted from reference <sup>[38]</sup> . .....	9
<b>Figure 1-6.</b> Crystal structure of (a) $\text{NaFePO}_4$ and (b) $\text{Na}_2\text{FeP}_2\text{O}_7$ , c) $\text{Na}_4\text{Fe}_3(\text{PO}_4)_2(\text{P}_2\text{O}_7)$ . Adapted from references <sup>[43-45]</sup> . .....	11
<b>Figure 1-7.</b> General strategies for performance enhancement and their rationale. Adapted from reference <sup>[46]</sup> . .....	13
<b>Figure 1-8.</b> Calculated Na voltage vs. Li voltage for different structures. Adapted from reference <sup>[47]</sup> . .....	14
<b>Figure 1-9.</b> (a) Coin cell structures and (b) T-cell structures. ....	18
<b>Figure 2-1.</b> XRD patterns of (a) NVP/ONC, NVP/6.7NC and NVP/10.8NC composites and (b) NVP/NC composite (with an exceed melamine in weight ratio of melamine to citric acid 3:3)..	25
<b>Figure 2-2.</b> SEM images of (a) NVP/ONC, (b) NVP/6.7NC and (c) NVP/10.8NC.....	26
<b>Figure 2-3.</b> TGA curves of NVP/NC composite.....	27
<b>Figure 2-4.</b> Raman spectra (a), normalized XPS C1s spectra (b) and high-resolution N1s spectra (c, d) for various NVP composites. ....	27
<b>Figure 2-5.</b> Normalized XPS C1s spectra (b) and high-resolution N1s spectra (c, d) for various NVP composites.....	28
<b>Figure 2-6.</b> Initial charge/discharge curves of (a) NVP/ONC, (b) NVP/6.7NC and (c) NVP/10.8NC electrodes in the potential range of 2.5-4.2 V (vs. $\text{Na}^+/\text{Na}$ ) recorded during a C-rate capability tests. (d) Specific discharge capacity vs. cycle number for the cycling at various current rates.....	30
<b>Figure 2-7.</b> (a) Long-term cycling performance and (b) capacity retention vs. cycling number of NVP/ONC, NVP/6.7NC and NVP/10.8NC at 20 C. ....	31
<b>Figure 2-8.</b> Voltage hysteresis at 50% depth-of-discharge (DOD) from the charge-discharge profiles of NVP/ONC, NVP/6.7NC and NVP/10.8NC at various C-rates. ....	32

<b>Figure 2-9.</b> (a) CV curves at 0.5 mV s <sup>-1</sup> in three-electrode half-cell and (b) Impedance spectra obtained in symmetric cells of NVP/0NC, NVP/6.7NC and NVP/10.8NC electrodes at fully discharged state (1.0 V) in the 5th and 35th cycle (inset: magnified high frequency region and equivalent circuit).....	33
<b>Figure 2-10.</b> (a) Typical charge-discharge profiles of NVP symmetric cell at 0.1 C (11 mA g <sup>-1</sup> ) in the 1.0-3.0 V voltage range. (b) Discharge curves at 0.1 C (11 mA g <sup>-1</sup> ) of NVP electrode in 1.4-3.6 V (vs. Na <sup>+</sup> /Na) potential range.....	34
<b>Figure 2-11.</b> XRD patterns, SEM images and schematic illustrations of NVP/N-C (a, b, c), NVP/N-CNT (d, e, f), NVP/N-rGO (g, h, i), and NVP/N-KB (j, k, m) composites.....	40
<b>Figure 2-12.</b> Raman spectra (a), schematic structure of possible binding conditions of N in a carbon lattice (b) and high-resolution XPS spectra of N1s (c–f) in NVP/N-C, NVP/N-CNT, NVP/N-rGO, and NVP/N-KB composites.....	41
<b>Figure 2-13.</b> High-resolution XPS spectra of N1s of NVP/N-C, NVP/N-CNT, NVP/N-rGO, and NVP/N-KB composites. ....	43
<b>Figure 2-14.</b> Electrochemical performances of NVP composite electrode materials: (a) charge-discharge profiles at 0.1 C, 0.5 C, 1.0 C, 5.0 C, 10.0 C, and 20.0 C, (b) C-rate stability test of NVP/N-C, NVP/N-CNT, NVP/N-rGO, and NVP/N-KB composites. ....	44
<b>Figure 2-15.</b> Long-term cycling performance at 20 C of NVP/N-C, NVP/N-CNT, NVP/N-rGO, and NVP/N-KB composites. ....	46
<b>Figure 2-16.</b> Cycling performance of NVP/N-CNT at 50 C in sodium half-cell.....	47
<b>Figure 2-17.</b> 1 <sup>st</sup> and 2 <sup>nd</sup> charge-discharge curves at 0.1 C of NVP/N-CNT in the potential range of 1.4-3.6 V (vs. Na <sup>+</sup> /Na).....	48
<b>Figure 2-18.</b> Rate capability test (a) and cycling performance at 20 C (b) of NVP/N-CNT composite in the potential range of 1.4V-3.6V (vs. Na <sup>+</sup> /Na).....	49
<b>Figure 2-19.</b> Charge-discharge curves (e) and rate capability test at various rates (f) of a NVP/N-CNT/ PC:FEC 98:2 wt.%,1M NaPF <sub>6</sub> /NVP/N-CNT symmetric two-electrode sodium-ion cell in the 1.0-3.0 V voltage range. ....	50
<b>Figure 3-1.</b> Rietveld refinement of powder XRD for Na <sub>2</sub> NiP <sub>2</sub> O <sub>7</sub> . ....	55
<b>Figure 3-2.</b> The 1 <sup>st</sup> galvanostatic charge-discharge curves of Na <sub>2</sub> NiP <sub>2</sub> O <sub>7</sub> at 10 mA g <sup>-1</sup> in the potential range of 2.5-4.9 V. ....	56
<b>Figure 3-3.</b> XRD pattern of the product from NaNiPO <sub>4</sub> synthesis.....	56
<b>Figure 3-4.</b> Rietveld refinement of powder XRD for Na <sub>4</sub> Ni <sub>3</sub> (PO <sub>4</sub> ) <sub>2</sub> (P <sub>2</sub> O <sub>7</sub> ). ....	57
<b>Figure 3-5.</b> Rietveld refinement of XRD for Na <sub>4</sub> Ni <sub>3</sub> (PO <sub>4</sub> ) <sub>2</sub> (P <sub>2</sub> O <sub>7</sub> )/C composite.....	58
<b>Figure 3-6.</b> Schematic representation of Na <sub>4</sub> Ni <sub>3</sub> (PO <sub>4</sub> ) <sub>2</sub> (P <sub>2</sub> O <sub>7</sub> ) crystal structure viewed along the [001] and [010] directions.....	58
<b>Figure 3-7.</b> SEM images of (a) Na <sub>4</sub> Ni <sub>3</sub> (PO <sub>4</sub> ) <sub>2</sub> (P <sub>2</sub> O <sub>7</sub> ) and (b) Na <sub>4</sub> Ni <sub>3</sub> (PO <sub>4</sub> ) <sub>2</sub> (P <sub>2</sub> O <sub>7</sub> )/C powders. (c, d) TEM images of Na <sub>4</sub> Ni <sub>3</sub> (PO <sub>4</sub> ) <sub>2</sub> (P <sub>2</sub> O <sub>7</sub> )/C.....	59
<b>Figure 3-8.</b> TG curves of Na <sub>4</sub> Ni <sub>3</sub> (PO <sub>4</sub> ) <sub>2</sub> (P <sub>2</sub> O <sub>7</sub> ) and Na <sub>4</sub> Ni <sub>3</sub> (PO <sub>4</sub> ) <sub>2</sub> (P <sub>2</sub> O <sub>7</sub> )/C under O <sub>2</sub> flow. ....	60
<b>Figure 3-9.</b> CV curves of Na <sub>4</sub> Ni <sub>3</sub> (PO <sub>4</sub> ) <sub>2</sub> (P <sub>2</sub> O <sub>7</sub> )/C at a scan rate of 0.01 mV s <sup>-1</sup> (a) in potential range of 3.0-5.0 V using 1M NaPF <sub>6</sub> in EC:DEC (1:1 w/w) electrolyte and (b) in the potential range of 3.0-5.2 V using NaTFSI : Py <sub>13</sub> FSI (1:9 mole ratio) electrolyte. ....	61

- Figure 3-10.** The 1<sup>st</sup> galvanostatic charge/discharge profiles of Na<sub>4</sub>Ni<sub>3</sub>(PO<sub>4</sub>)<sub>2</sub>(P<sub>2</sub>O<sub>7</sub>)/C in 1M NaPF<sub>6</sub> in EC : DEC (1:1 w/w) (a) and NaTFSI : Py<sub>13</sub>FSI (1:9 mole ratio) (b) electrolytes at the constant current density of 10 mA g<sup>-1</sup>. ..... 62
- Figure 3-11.** Cycling performance of Na<sub>4</sub>Ni<sub>3</sub>(PO<sub>4</sub>)<sub>2</sub>(P<sub>2</sub>O<sub>7</sub>)/C in NaTFSI : Py<sub>13</sub>FSI (1:9 mole ratio) electrolyte between 3.0-5.1 V (vs. Na<sup>+</sup>/Na) at 10 mA g<sup>-1</sup>. ..... 62
- Figure 3-12.** (a) Typical charge/discharge profile of Na<sub>4</sub>Ni<sub>3</sub>(PO<sub>4</sub>)<sub>2</sub>(P<sub>2</sub>O<sub>7</sub>)/C electrode. (b) *Ex-situ* XRD pattern of Na<sub>4</sub>Ni<sub>3</sub>(PO<sub>4</sub>)<sub>2</sub>(P<sub>2</sub>O<sub>7</sub>)/C electrode at various charge and discharge states. (c, d) Amplified XRD patterns in the 2θ range of 10-25°, 25-35°, respectively. .... 64
- Figure 3-13.** Lattice parameters (*a, b, c*) changes of Na<sub>4</sub>Ni<sub>3</sub>(PO<sub>4</sub>)<sub>2</sub>(P<sub>2</sub>O<sub>7</sub>)/C during electrochemical charge/discharge process. .... 65
- Figure 3-14.** Rietveld refinement and powder X-ray diffraction (XRD) pattern for Na<sub>3</sub>V(PO<sub>3</sub>)<sub>3</sub>N powders. The inset figure displays the SEM images. .... 70
- Figure 3-15.** (a) Refined crystal structure of Na<sub>3</sub>V(PO<sub>3</sub>)<sub>3</sub>N and (b) the connectivity of trimers of PO<sub>3</sub>N tetrahedra with the local environments of Na, V atoms. .... 71
- Figure 3-16.** TG curves of Na<sub>3</sub>V(PO<sub>3</sub>)<sub>3</sub>N under N<sub>2</sub> and O<sub>2</sub> flows and melamine under N<sub>2</sub> flow within the temperature range of 30 - 800 °C at 5 °C min<sup>-1</sup> heating rate. .... 71
- Figure 3-17.** (a) Cyclic voltammograms in the potential range of 3.2–4.5 V at various scan rates and (b) first cycle galvanostatic discharge/charge profile between 3.2 and 4.5 V at a current of 10 mA g<sup>-1</sup> of Na<sub>3</sub>V(PO<sub>3</sub>)<sub>3</sub>N. .... 72
- Figure 3-18.** Galvanostatic charge–discharge profiles of Na<sub>3</sub>V(PO<sub>3</sub>)<sub>3</sub>N at current density of 10 mA g<sup>-1</sup> for the 1<sup>st</sup> and 10<sup>th</sup> cycles and 20 mA g<sup>-1</sup> for 11<sup>th</sup> and 20<sup>th</sup> cycles. .... 73
- Figure 3-19.** (a) Typical charge/discharge profile and (b) *in-situ* X-ray diffraction patterns of Na<sub>3</sub>V(PO<sub>3</sub>)<sub>3</sub>N electrode during the first cycle. .... 74
- Figure 3-20.** Average working potential versus gravimetric capacity for various vanadium-based positive electrode materials for sodium-ion batteries. Here only one electron reaction of V<sup>3+/4+</sup> redox reaction is considered. .... 75
- Figure 4-1.** (a) XRD pattern and (b) SEM image of Na<sub>2</sub>VTi(PO<sub>4</sub>)<sub>3</sub>/C composite. .... 81
- Figure 4-2.** Initial and second galvanostatic charge-discharge profile of Na<sub>2</sub>VTi(PO<sub>4</sub>)<sub>3</sub>/C between 1.5 and 4.0 V vs. Na<sup>+</sup>/Na at 0.2 C (1C = 60 mA g<sup>-1</sup>). .... 81
- Figure 4-3.** (a) Galvanostatic charge-discharge profiles of symmetric full cell between 0.5 and 1.5 V at different C-rates, and (b) long-term cycling stability test of the symmetric full cell at 20 C in 1M NaPF<sub>6</sub> PC/EC (1:1 v/v) organic electrolyte (1C = 60 mA g<sup>-1</sup>). .... 82
- Figure 4-4.** Raman spectra of the aqueous electrolytes. (a) ClO<sub>4</sub> stretching mode in 1, 4 or 8 M NaClO<sub>4</sub> aqueous electrolyte; (b) OH bending and (c) OH stretching bands in 1, 4 or 8 M NaClO<sub>4</sub> and 9.2 m NaOTF “water-in-salt” electrolytes; (d) SO<sub>3</sub> stretching mode in 9.2 m NaOTF “water-in-salt” electrolyte. .... 84
- Figure 4-5.** Representative Na<sup>+</sup> cation solvate species (solvent-separated ion pairs, contact ion pairs and aggregated cation-anion pairs) in dilute and concentrated electrolytes. .... 85
- Figure 4-6.** (a) Ionic conductivities of aqueous 1 M NaClO<sub>4</sub>, 4 M NaClO<sub>4</sub>, 8 M NaClO<sub>4</sub>, and 9.2 m NaOTF “water-in-salt” electrolytes at 20 °C; (b) Cyclic voltammogram curves of the Na<sub>2</sub>VTi(PO<sub>4</sub>)<sub>3</sub>/C symmetric full cells at a scan rate of 0.5 mV s<sup>-1</sup> between 0 and 1.5V in various aqueous electrolytes. .... 85

- Figure 4-7.** The galvanostatic charge-discharge profiles of  $\text{Na}_2\text{VTi}(\text{PO}_4)_3/\text{C}$  symmetric full cells at various C-rates using stainless steel foil as current collector in aqueous  $\text{NaClO}_4$  electrolytes (1 M, 4 M, 8 M) and 9.2 m NaOTF “water-in-salt” electrolyte..... 86
- Figure 4-8.** (a) Rate capability measurements, (b) corresponding coulombic efficiencies of  $\text{Na}_2\text{VTi}(\text{PO}_4)_3/\text{C}$  symmetric full cells in various aqueous electrolytes. .... 88
- Figure 4-9.** Cycling test at 20 C of  $\text{Na}_2\text{VTi}(\text{PO}_4)_3/\text{C}$  symmetric full cells in various aqueous electrolytes..... 89
- Figure 4-10.** The galvanostatic charge-discharge profiles of  $\text{Na}_2\text{VTi}(\text{PO}_4)_3/\text{C}$  symmetric full cells at 20 C in 8 M  $\text{NaClO}_4$  aqueous electrolyte and 9.2 m NaOTF “water-in-salt” electrolyte (1<sup>st</sup>, 500<sup>th</sup> and 1000<sup>th</sup> cycles). .... 89
- Figure 4-11.** Nyquist and Bode plots of  $\text{Na}_2\text{VTi}(\text{PO}_4)_3/\text{C}$  symmetric full cells in various aqueous electrolytes. Impedance spectra were recorded (a) at open-circuit voltage and (b) after 50 cycles (fully discharged state). .... 90
- Figure 4-12.** (a) Photographs of separators from the cells after 1000 cycles aiming to show the dissolution of  $\text{V}^{n+}$  species in aqueous solutions, and (b, c, d) SEM images of anodes in 1 M  $\text{NaClO}_4$ , 8 M  $\text{NaClO}_4$  aqueous electrolytes and 9.2 m NaOTF “water-in-salt”, respectively..... 91
- Figure 4-13.** XRD pattern (a) and (b) SEM images of  $\text{Na}_3\text{V}_2(\text{PO}_4)_3/\text{C}$  composites. .... 96
- Figure 4-14.** Electrochemical properties of NVP/C composite in half cells. (a) Selected charge-discharge profiles at various C-rates, and (b) long-term cycling performance at 20 C. (1C=120 mA  $\text{g}^{-1}$ , 1M  $\text{NaPF}_6$  in PC with 2%FEC as electrolyte)..... 97
- Figure 4-15.** XRD pattern (a) and (b) SEM images of  $\text{NaTi}_2(\text{PO}_4)_3/\text{C}$  composites..... 98
- Figure 4-16.** Electrochemical properties of NTP/C composite in half cells. (a) Galvanostatic charge-discharge profiles at various C-rates; and (b) cycling performance at 50 C. (1C=120 mA  $\text{g}^{-1}$ , 1M  $\text{NaPF}_6$  in PC with 2%FEC as electrolyte) ..... 99
- Figure 4-17.** Typical cyclic voltammetry curves of initial three scans at 0.1  $\text{mV s}^{-1}$  of NTP//NVP full cell using copper as anode current collector in voltage range of 0.5-1.5 V. (1M  $\text{NaPF}_6$  in PC with 2%FEC as electrolyte) ..... 99
- Figure 4-18.** Initial galvanostatic charge-discharge profiles of NTP//NVP full cell using copper as anode current collector at various C-rates in voltage range of 0.5-1.5 V. (1C=120 mA  $\text{g}^{-1}$ , 1M  $\text{NaPF}_6$  in PC with 2%FEC as electrolyte) ..... 100
- Figure 4-19.** Rate capability test (a), and (b) cycling performance at 20 C of NTP//NVP full cell using copper as anode current collector. (1C=120 mA  $\text{g}^{-1}$ , 1M  $\text{NaPF}_6$  in PC with 2%FEC as electrolyte) ..... 101
- Figure 4-20.** (a) Initial galvanostatic charge-discharge profiles and (b) cycling performance at 5 C of NTP//NVP full cell using aluminum as anode current collector at various C-rates in voltage range of 0.5-1.5 V. (1C=120 mA  $\text{g}^{-1}$ , 1M  $\text{NaPF}_6$  in PC with 2%FEC as electrolyte) ..... 102
- Figure 4-21.** CV curves of NTP(Cu)//NVP (a) and NTP(Al)//NVP (b) full cells at various scan rates. (1C=120 mA  $\text{g}^{-1}$ , 1M  $\text{NaPF}_6$  in PC with 2%FEC as electrolyte).....103
- Figure 4-22.** (a) Nyquist plots obtained in NTP(Cu)//NVP full cell at OCV and after 100 cycles at 10 C, and (b) Nyquist plots obtained in NTP(Al)//NVP full cell at OCV and after 100 cycles at 10 C. (1M  $\text{NaPF}_6$  in PC with 2%FEC as electrolyte) ..... 104

- Figure 4-23.** (a) Ragone plot, and (b) comparison of energy efficiency and power density for NTP(Cu)//NVP and NTP(Al)//NVP full cells. (1M NaPF<sub>6</sub> in PC with 2%FEC as electrolyte) ....105
- Figure 4-24.** Initial galvanostatic charge-discharge profiles of NTP//NVP full cell in 9.26m NaOTf aqueous “water-in-salt” electrolyte (WiSE) in 0.5-1.5 V at 0.2 C. (1 C=120 mA g<sup>-1</sup>) .....105
- Figure 4-25.** XRD pattern (a) and (b) SEM images of Na<sub>3</sub>V<sub>2</sub>(PO<sub>4</sub>)<sub>3</sub>@rGO@C composites. .... 106
- Figure 4-26.** Electrochemical stability of aqueous/nonaqueous hybrid electrolyte based on NaOTf on stainless steel evaluated using linear sweep voltammetry at a scan rate of 10 mV s<sup>-1</sup>. Typical cyclic voltammograms of NTP and NVP electrodes are presented within the electrochemical window. ....107
- Figure 4-27.** (a) Temperature-dependent conductivities, and (b) Raman spectra in the wavenumber region corresponding to the SO<sub>3</sub> stretching modes of aqueous/nonaqueous hybrid electrolyte..... 108
- Figure 4-28.** CV curves (a) and galvanostatic charge-discharge profiles (b) at various C-rates of NTP//NVP full cell in aqueous/nonaqueous hybrid electrolyte. (scan rate: 0.1 mV s<sup>-1</sup>, voltage range: 0.5-1.5 V)..... 109
- Figure 4-29.** Rate capability test and long cycling stability test of NTP//NVP full cell in aqueous/nonaqueous hybrid electrolyte. (1C=120 mA g<sup>-1</sup>, voltage range: 0.5-1.5 V) ..... 110
- Figure 4-30.** Nyquist plots of NTP//NVP full cell in the aqueous/nonaqueous hybrid electrolyte at open-circuit voltage and after 30 cycles. .... 110

### 6.3 List of Tables

<b>Table 2-1.</b> Content of different N species in N-doped carbon coated NVP/6.7NC and NVP/10.8NC composites. ....	29
<b>Table 2-2.</b> Diffusion coefficients of Na <sup>+</sup> ( $D_{cvNa+}$ , cm <sup>2</sup> s <sup>-1</sup> ) calculated from CV curves, and R <sub>f</sub> (Ω), R <sub>ct</sub> (Ω), Na <sup>+</sup> diffusion coefficients ( $D_{EISNa+}$ , cm <sup>2</sup> s <sup>-1</sup> ) in symmetric cells calculated from EIS measurements.....	34
<b>Table 2-3.</b> Contents of the N species and N/C atomic ratio in the N-doped carbon coated NVP composites as obtained by XPS analysis. ....	42
<b>Table 2-4.</b> Calculated diffusion coefficients of Na <sup>+</sup> ( $D_{Na+}$ , cm <sup>2</sup> s <sup>-1</sup> ) in various N-doped carbon coated NVP composites. ....	47
<b>Table 3-1</b> Na occupancy during the charge/discharge process and expected values from the Rietveld refinement. ....	66
<b>Table 3-2.</b> Refined Na occupancies, lattice parameter, and cell volume extracted from the Rietveld refinement of diffraction patterns from 10-45° 2θ of Na <sub>3</sub> V(PO <sub>3</sub> ) <sub>3</sub> N electrodes at OCV, fully charged and fully discharged state in the first cycle. ....	74

## 6.4 Appendix 1 contains the supporting information for Chapter 2.

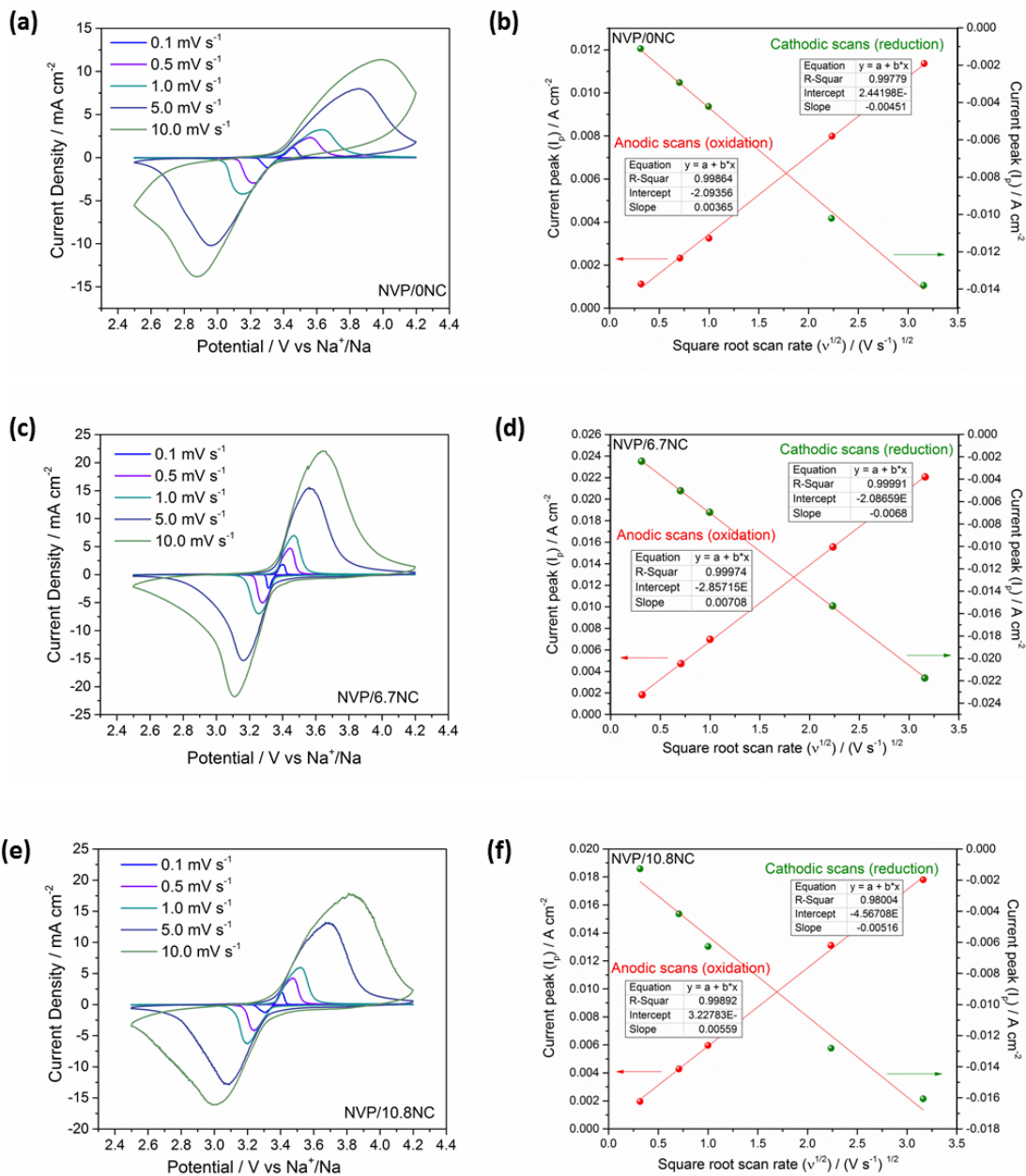


**Figure S2-1.** (a, c, e) CV curves of NVP/0NC, NVP/6.7NC and NVP/10.8NC at various scan rates; (b, d, f) peak current ( $I_p$ , A cm<sup>-2</sup>) vs. square root of scan rate ( $v^{1/2}$ , V<sup>1/2</sup> s<sup>-1/2</sup>) and related linear fit corresponding to the V<sup>3+/4+</sup> redox processes.



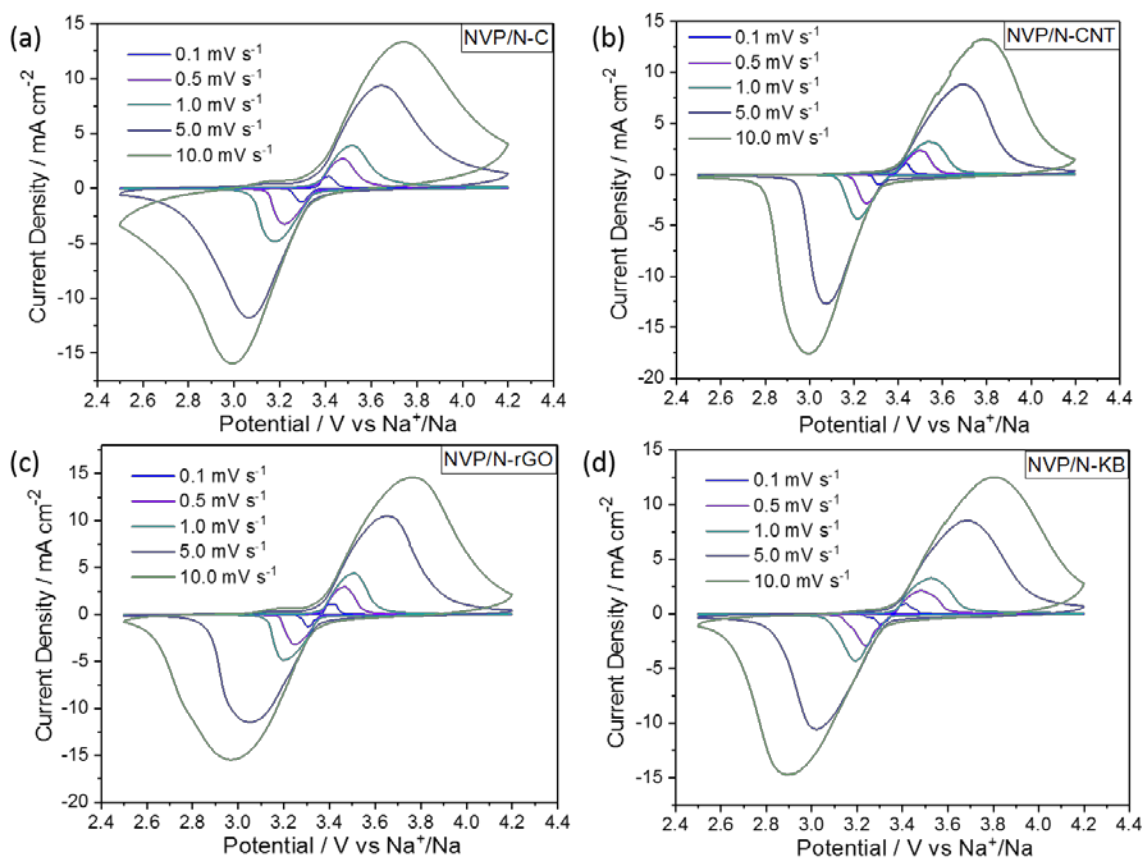


**Figure S2-2.** Cyclic voltammograms at various scan rates of NVP/N-C, NVP/N-CNT, NVP/N-rGO, and NVP/N-KB composites.

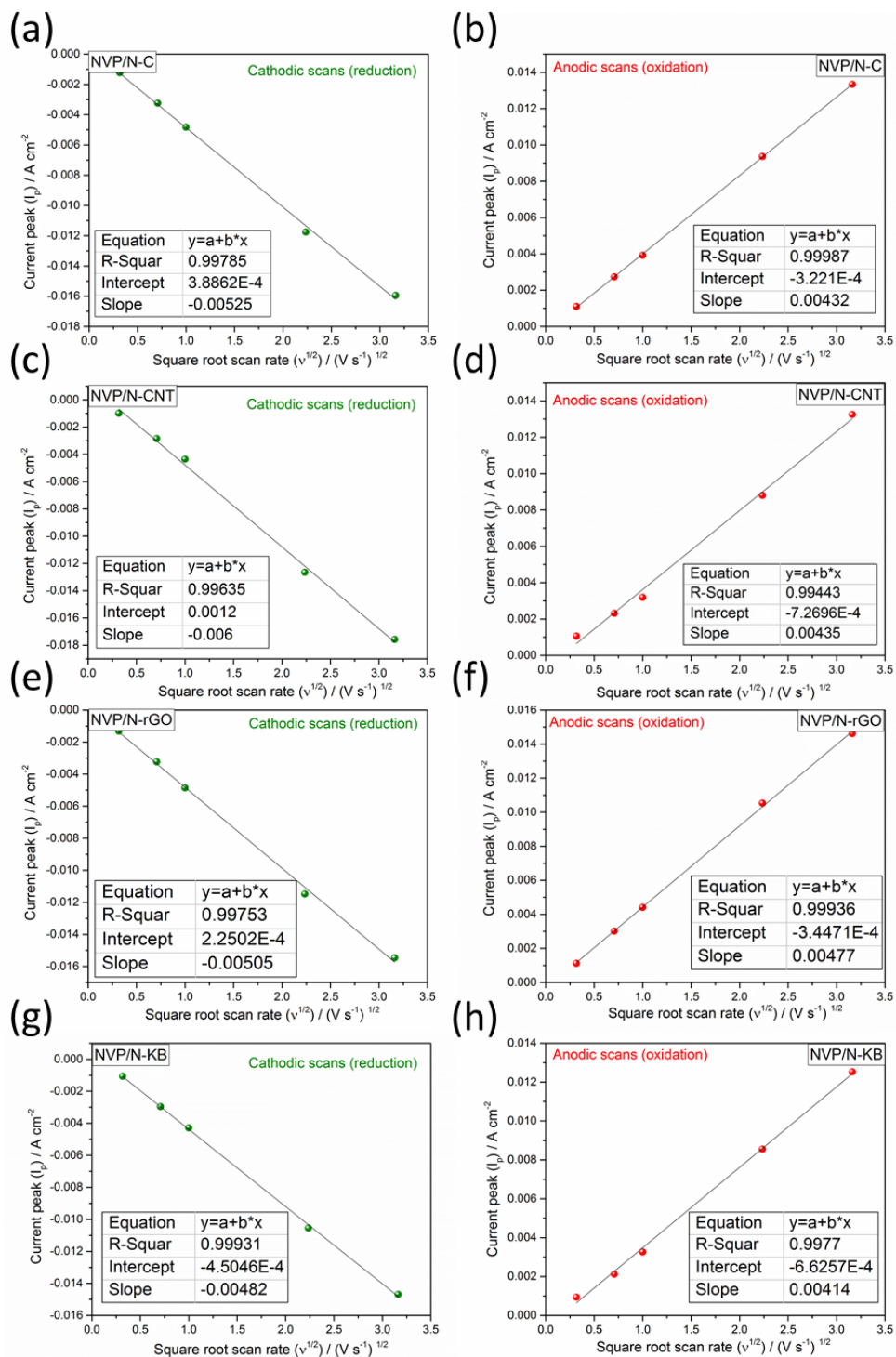


**Figure S2-3.** Peak current ( $I_p$ ,  $A\ cm^{-2}$ ) vs. square root of scan rate ( $v^{1/2}$ ,  $V^{1/2}\ s^{-1/2}$ ) and related linear fit corresponding to the  $V^{3+/4+}$  redox processes.

## 6.5 Appendix 2 contains the supporting information for Chapter 3.

**Table S3-1.** Crystallographic data of  $\text{Na}_4\text{Ni}_3(\text{PO}_4)_2\text{P}_2\text{O}_7$ .

	<b>Value</b>
<b>Chemical formula</b>	$\text{Na}_4\text{Ni}_3(\text{PO}_4)_2\text{P}_2\text{O}_7$
<b>Crystal System, space group</b>	Orthorhombic, $Pn2_1a$
<b>R-Bragg</b>	5.44%
<b>Cell Mass</b>	2527.6
<b>Cell Volume (<math>\text{\AA}^3</math>)</b>	1216.92(3)
<b>Crystal Density (<math>\text{g cm}^{-3}</math>)</b>	3.4490(1)
<b>Temperature</b>	~298 K (ambient)
<b>Lattice parameters</b>	
<b><i>a</i>, <i>b</i>, <i>c</i> (<math>\text{\AA}</math>)</b>	$a = 18.0004(3)$ , $b = 6.4934(1)$ , $c = 10.4114(2)$
<b><math>R_{\text{wp}}</math></b>	3.56%
<b><math>R_{\text{p}}</math></b>	2.67%
<b>GOF</b>	1.58
<b>Radiation type</b>	Cu $K_{\alpha}$ , $\lambda = 1.541(8) \text{\AA}$

**Table S3-2.** Atomic parameters for  $\text{Na}_4\text{Ni}_3(\text{PO}_4)_2\text{P}_2\text{O}_7$ .

<b>Site</b>	<b><math>x^*</math></b>	<b><math>y^*</math></b>	<b><math>z^*</math></b>	<b>Atom</b>	<b>Occ*</b>	<b><math>B_{\text{eq}}^*</math></b>
<b>Ni1</b>	0.3377	0.138	0.5042	$\text{Ni}^{2+}$	1	0.03
<b>Ni2</b>	0.1402	0.624	0.4886	$\text{Ni}^{2+}$	1	0.03
<b>Ni3</b>	0.244	0.358	0.7469	$\text{Ni}^{2+}$	1	0.03
<b>P1</b>	0.295	0.618	0.502	$\text{P}^{5+}$	1	0.13
<b>P2</b>	0.1772	0.123	0.4918	$\text{P}^{5+}$	1	0.13
<b>P3</b>	0.563	0.488	0.7382	$\text{P}^{5+}$	1	0.13
<b>P4</b>	0.4446	0.173	0.7323	$\text{P}^{5+}$	1	0.13
<b>Na1</b>	0.4923	0.822	0.984	$\text{Na}^+$	1	1.1
<b>Na2</b>	0.2941	0.868	0.75	$\text{Na}^+$	1	1.1
<b>Na3</b>	0.3949	0.459	0.2686	$\text{Na}^+$	1	1.1
<b>Na4</b>	0.4681	0.695	0.5473	$\text{Na}^+$	1	1.1
<b>O1</b>	0.2417	0.59	0.6136	$\text{O}^{2-}$	1	0.29
<b>O2</b>	0.3563	0.439	0.4731	$\text{O}^{2-}$	1	0.29

<b>O3</b>	0.3335	0.814	0.5351	O <sup>2-</sup>	1	0.29
<b>O4</b>	0.2414	0.649	0.3874	O <sup>2-</sup>	1	0.29
<b>O5</b>	0.2355	0.138	0.6097	O <sup>2-</sup>	1	0.29
<b>O6</b>	0.1258	-0.071	0.5074	O <sup>2-</sup>	1	0.29
<b>O7</b>	0.2299	0.086	0.3848	O <sup>2-</sup>	1	0.29
<b>O8</b>	0.1352	0.302	0.4674	O <sup>2-</sup>	1	0.29
<b>O9</b>	0.4819	0.401	0.7019	O <sup>2-</sup>	1	0.29
<b>O10</b>	0.551	0.595	0.876	O <sup>2-</sup>	1	0.29
<b>O11</b>	0.6225	0.326	0.7502	O <sup>2-</sup>	1	0.29
<b>O12</b>	0.5816	0.634	0.6339	O <sup>2-</sup>	1	0.29
<b>O13</b>	0.4558	0.123	0.8585	O <sup>2-</sup>	1	0.29
<b>O14</b>	0.3709	0.191	0.6882	O <sup>2-</sup>	1	0.29
<b>O15</b>	0.4915	0.026	0.6515	O <sup>2-</sup>	1	0.29

\* These parameters are fixed from the isostructural Na<sub>3</sub>Fe<sub>2</sub>(PO<sub>4</sub>)<sub>2</sub>(P<sub>2</sub>O<sub>7</sub>) with the replacement of Fe by Ni atom.

**Table S3-3.** Crystallographic data of Na<sub>3</sub>V(PO<sub>3</sub>)<sub>3</sub>N.

	<b>Value</b>
<b>Chemical formula</b>	Na <sub>3</sub> V(PO <sub>3</sub> ) <sub>3</sub> N
<b>Crystal System, space group</b>	Cubic, <i>P</i> 2 <sub>1</sub> 3
<b>R-Bragg</b>	9.7%
<b>Cell Mass</b>	1483.3
<b>Cell Volume (Å<sup>3</sup>)</b>	841.3(9)
<b>Crystal Density (g cm<sup>-3</sup>)</b>	2.9307(3)
<b>Temperature</b>	~298 K (ambient)
<b>Lattice parameters</b>	
<b><i>a</i> (Å)</b>	9.440(1)
<b>R<sub>wp</sub></b>	8.7%
<b>R<sub>p</sub></b>	6.7%
<b>GOF</b>	1.41
<b>Radiation type</b>	Cu K <sub>α</sub> , λ = 1.541(8) Å

**Table S3-4.** Atomic parameters for Na<sub>3</sub>V(PO<sub>3</sub>)<sub>3</sub>N.

<b>Site</b>	<b>x*</b>	<b>y*</b>	<b>z*</b>		<b>Occ*</b>	<b>B<sub>eq</sub>*</b>
<b>Na1</b>	-0.26140	0.73860	0.73860	Na <sup>+</sup>	1	0.0255
<b>Na2</b>	0.14230	0.64230	0.85770	Na <sup>+</sup>	1	0.0181
<b>Na3</b>	-0.05180	0.94820	0.94820	Na <sup>+</sup>	1	0.029
<b>V1</b>	0.33070	0.83070	0.66930	V <sup>3+</sup>	1	0.0109
<b>P1</b>	0.00415	0.83568	0.58270	P <sup>5+</sup>	1	0.0092
<b>N1</b>	0.05150	0.94850	0.44850	N <sup>3-</sup>	1	0.0087
<b>O1</b>	-0.09860	0.72930	0.52000	O <sup>2-</sup>	1	0.0154
<b>O2</b>	0.13720	0.75680	0.62370	O <sup>2-</sup>	1	0.0124
<b>O3</b>	-0.06150	0.91810	0.70020	O <sup>2-</sup>	1	0.017

\* These parameters are fixed from the isostructural Na<sub>3</sub>Ti(PO<sub>3</sub>)<sub>3</sub>N with the replacement of Ti by V atom.



## Bibliography

- [1] M. Hightower, S.A. Pierce, *Nature* 452 (2008) 285-286.
- [2] B. Dunn, H. Kamath, J.-M. Tarascon, *Science* 334 (2011) 928-935.
- [3] B. Scrosati, J. Garche, *J. Power Sources* 195 (2010) 2419-2430.
- [4] J.B. Goodenough, K.-S. Park, *J. Am. Chem. Soc.* 135 (2013) 1167-1176.
- [5] H. Zhang, I. Hasa, S. Passerini, *Adv. Energy Mater.* 8 (2018) 1702582.
- [6] M.S. Whittingham, *Science* 192 (1976) 1126-1127.
- [7] C. Delmas, J.-J. Braconnier, C. Fouassier, P. Hagenmuller, *Solid State Ionics* 3 (1981) 165-169.
- [8] V. Palomares, P. Serras, I. Villaluenga, K.B. Hueso, J. Carretero-Gonzalez, T. Rojo, *Energy Environ. Sci.* 5 (2012) 5884-5901.
- [9] M.D. Slater, D. Kim, E. Lee, C.S. Johnson, *Adv. Funct. Mater.* 23 (2013) 947-958.
- [10] D. Kundu, E. Talaie, V. Duffort, L.F. Nazar, *Angew. Chem., Int. Ed.* 54 (2015) 3431-3448.
- [11] K. Kubota, S. Komaba, *J. Electrochem. Soc.* 162 (2015) A2538-A2550.
- [12] S.Y. Hong, Y. Kim, Y. Park, A. Choi, N.-S. Choi, K.T. Lee, *Energy Environ. Sci.* 6 (2013) 2067-2081.
- [13] N. Yabuuchi, K. Kubota, M. Dahbi, S. Komaba, *Chem. Rev.* 114 (2014) 11636-11682.
- [14] J.-Y. Hwang, S.-T. Myung, Y.-K. Sun, *Chem. Soc. Rev.* 46 (2017) 3529-3614.
- [15] J.B. Goodenough, Y. Kim, *Chem. Mater.* 22 (2010) 587-603.
- [16] M. Gauthier, T.J. Carney, A. Grimaud, L. Giordano, N. Pour, H.-H. Chang, D.P. Fenning, S.F. Lux, O. Paschos, C. Bauer, F. Maglia, S. Lupart, P. Lamp, Y. Shao-Horn, *J. Phys. Chem. Lett.* 6 (2015) 4653-4672.
- [17] C. Liu, Z.G. Neale, G. Cao, *Mater. Today* 19 (2016) 109-123.
- [18] J.W. Choi, D. Aurbach, *Nat. Rev. Mater.* 1 (2016) 16013.
- [19] Y. Kim, K.-H. Ha, S.M. Oh, K.T. Lee, *Chem. - Eur. J.* 20 (2014) 11980-11992.
- [20] H. Hou, X. Qiu, W. Wei, Y. Zhang, X. Ji, *Adv. Energy Mater.* 7 (2017) 1602898.
- [21] S. Guo, J. Yi, Y. Sun, H. Zhou, *Energy Environ. Sci.* 9 (2016) 2978-3006.
- [22] M. Lao, Y. Zhang, W. Luo, Q. Yan, W. Sun, S.X. Dou, *Adv. Mater.* 29 (2017) 1700622.
- [23] F. Klein, B. Jache, A. Bhide, P. Adelhelm, *Phys. Chem. Chem. Phys.* 15 (2013) 15876-15887.
- [24] X. Zheng, C. Bommier, W. Luo, L. Jiang, Y. Hao, Y. Huang, *Energy Storage Mater.* 16 (2019) 6-23.
- [25] B.L. Ellis, L.F. Nazar, *Curr. Opin. Solid State Mater. Sci.* 16 (2012) 168-177.
- [26] P.-F. Wang, Y. You, Y.-X. Yin, Y.-G. Guo, *Adv. Energy Mater.* 8 (2017) 1701912.
- [27] I. Hasa, D. Buchholz, S. Passerini, J. Hassoun, *ACS Appl. Mater. Interfaces* 7 (2015) 5206-5212.

- [28] D. Hamani, M. Ati, J.-M. Tarascon, P. Rozier, *Electrochem. Commun.* 13 (2011) 938-941.
- [29] S. Komaba, C. Takei, T. Nakayama, A. Ogata, N. Yabuuchi, *Electrochem. Commun.* 12 (2010) 355-358.
- [30] N. Yabuuchi, M. Kajiyama, J. Iwatate, H. Nishikawa, S. Hitomi, R. Okuyama, R. Usui, Y. Yamada, S. Komaba, *Nat. Mater.* 11 (2012) 512-517.
- [31] D. Buchholz, A. Moretti, R. Kloepsch, S. Nowak, V. Siozios, M. Winter, S. Passerini, *Chem. Mater.* 25 (2013) 142-148.
- [32] I. Hasa, D. Buchholz, S. Passerini, B. Scrosati, J. Hassoun, *Adv. Energy Mater.* 4 (2014) 1400083.
- [33] M. Sathiya, K. Hemalatha, K. Ramesha, J.M. Tarascon, A.S. Prakash, *Chem. Mater.* 24 (2012) 1846-1853.
- [34] H. Wang, X.-Z. Liao, Y. Yang, X. Yan, Y.-S. He, Z.-F. Ma, *J. Electrochem. Soc.* 163 (2016) A565-A570.
- [35] J.S. Thorne, R.A. Dunlap, M.N. Obrovac, *J. Electrochem. Soc.* 161 (2014) A2232-A2236.
- [36] S. Kalluri, K.H. Seng, W.K. Pang, Z. Guo, Z. Chen, H.-K. Liu, S.X. Dou, *ACS Appl. Mater. Interfaces* 6 (2014) 8953-8958.
- [37] I. Hasa, S. Passerini, J. Hassoun, *J. Mater. Chem. A* 5 (2017) 4467-4477.
- [38] J. Qian, C. Wu, Y. Cao, Z. Ma, Y. Huang, X. Ai, H. Yang, *Adv. Energy Mater.* 8 (2018) 1702619.
- [39] Z. Gong, Y. Yang, *Energy Environ. Sci.* 4 (2011) 3223-3242.
- [40] C. Masquelier, L. Croguennec, *Chem. Rev.* 113 (2013) 6552-6591.
- [41] A.K. Padhi, V. Manivannan, J.B. Goodenough, *J. Electrochem. Soc.* 145 (1998) 1518-1520.
- [42] G. Hautier, A. Jain, H. Chen, C. Moore, S.P. Ong, G. Ceder, *J. Mater. Chem.* 21 (2011) 17147-17153.
- [43] R. Tripathi, S.M. Wood, M.S. Islam, L.F. Nazar, *Energy Environ. Sci.* 6 (2013) 2257-2264.
- [44] P. Barpanda, G. Liu, C.D. Ling, M. Tamaru, M. Avdeev, S.-C. Chung, Y. Yamada, A. Yamada, *Chem. Mater.* 25 (2013) 3480-3487.
- [45] H. Kim, I. Park, D.-H. Seo, S. Lee, S.-W. Kim, W.J. Kwon, Y.-U. Park, C.S. Kim, S. Jeon, K. Kang, *J. Am. Chem. Soc.* 134 (2012) 10369-10372.
- [46] N. Nitta, F. Wu, J.T. Lee, G. Yushin, *Mater. Today* 18 (2015) 252-264.
- [47] S.P. Ong, V.L. Chevrier, G. Hautier, A. Jain, C. Moore, S. Kim, X. Ma, G. Ceder, *Energy Environ. Sci.* 4 (2011) 3680-3688.
- [48] J. Lu, T. Wu, K. Amine, *Nat. Energy* 2 (2017) 17011.
- [49] Z. Jian, L. Zhao, H. Pan, Y.-S. Hu, H. Li, W. Chen, L. Chen, *Electrochem. Commun.* 14 (2012) 86-89.



- [50] Y. Xu, Q. Wei, C. Xu, Q. Li, Q. An, P. Zhang, J. Sheng, L. Zhou, L. Mai, *Adv. Energy Mater.* 6 (2016) 1600389.
- [51] H. Li, X. Yu, Y. Bai, F. Wu, C. Wu, L.-Y. Liu, X.-Q. Yang, *J. Mater. Chem. A* 3 (2015) 9578-9586.
- [52] M.J. Aragón, P. Lavela, G.F. Ortiz, J.L. Tirado, *ChemElectroChem* 2 (2015) 995-1002.
- [53] R. Klee, P. Lavela, M.J. Aragón, R. Alcántara, J.L. Tirado, *J. Power Sources* 313 (2016) 73-80.
- [54] P. Hu, X. Wang, T. Wang, L. Chen, J. Ma, Q. Kong, S. Shi, G. Cui, *Adv. Sci.* 3 (2016) 1600112.
- [55] R. Dominko, M. Bele, M. Gaberscek, M. Remskar, D. Hanzel, S. Pejovnik, J. Jamnik, *J. Electrochem. Soc.* 152 (2005) A607-A610.
- [56] M. Yoshio, H. Wang, K. Fukuda, Y. Hara, Y. Adachi, *J. Electrochem. Soc.* 147 (2000) 1245-1250.
- [57] H. Li, H. Zhou, *Chem. Commun.* 48 (2012) 1201-1217.
- [58] Y. Zhou, X. Rui, W. Sun, Z. Xu, Y. Zhou, W.J. Ng, Q. Yan, E. Fong, *ACS Nano* 9 (2015) 4628-4635.
- [59] Y. Luo, X. Xu, Y. Zhang, Y. Pi, Y. Zhao, X. Tian, Q. An, Q. Wei, L. Mai, *Adv. Energy Mater.* 4 (2014) 1400107.
- [60] H. Li, C. Wu, Y. Bai, F. Wu, M. Wang, *J. Power Sources* 326 (2016) 14-22.
- [61] Q. Zhang, W. Wang, Y. Wang, P. Feng, K. Wang, S. Cheng, K. Jiang, *Nano Energy* 20 (2016) 11-19.
- [62] F. Su, C.K. Poh, J.S. Chen, G. Xu, D. Wang, Q. Li, J. Lin, X.W. Lou, *Energy Environ. Sci.* 4 (2011) 717-724.
- [63] B. Liu, H. Shioyama, H. Jiang, X. Zhang, Q. Xu, *Carbon* 48 (2010) 456-463.
- [64] D. Guo, R. Shibuya, C. Akiba, S. Saji, T. Kondo, J. Nakamura, *Science* 351 (2016) 361-365.
- [65] L. Zhao, Y.-S. Hu, H. Li, Z. Wang, L. Chen, *Adv. Mater.* 23 (2011) 1385-1388.
- [66] Z. Ding, L. Zhao, L. Suo, Y. Jiao, S. Meng, Y.-S. Hu, Z. Wang, L. Chen, *Phys. Chem. Chem. Phys.* 13 (2011) 15127-15133.
- [67] W. Shen, C. Wang, Q. Xu, H. Liu, Y. Wang, *Adv. Energy Mater.* 5 (2015) 1400982.
- [68] J.-Z. Guo, X.-L. Wu, F. Wan, J. Wang, X.-H. Zhang, R.-S. Wang, *Chem. - Eur. J.* 21 (2015) 17371-17378.
- [69] P. Nie, Y. Zhu, L. Shen, G. Pang, G. Xu, S. Dong, H. Dou, X. Zhang, *J. Mater. Chem. A* 2 (2014) 18606-18612.
- [70] I. Zatorovsky, *Acta Crystallogr., Sect. E* 66 (2010) i12.
- [71] A.C. Ferrari, J. Robertson, *Phys. Rev. B* 61 (2000) 14095-14107.

- [72] J. Hou, C. Cao, F. Idrees, X. Ma, *ACS Nano* 9 (2015) 2556-2564.
- [73] C. Chen, J. Zhang, B. Zhang, C. Yu, F. Peng, D. Su, *Chem. Commun.* 49 (2013) 8151-8153.
- [74] P. Ge, M. Fouletier, *Solid State Ionics* 28 (1988) 1172-1175.
- [75] H. Kim, J. Hong, G. Yoon, H. Kim, K.-Y. Park, M.-S. Park, W.-S. Yoon, K. Kang, *Energy Environ. Sci.* 8 (2015) 2963-2969.
- [76] X.-Y. Shan, Y. Wang, D.-W. Wang, F. Li, H.-M. Cheng, *Adv. Energy Mater.* 6 (2016) 1502064.
- [77] Z. Jian, W. Han, X. Lu, H. Yang, Y.-S. Hu, J. Zhou, Z. Zhou, J. Li, W. Chen, D. Chen, L. Chen, *Adv. Energy Mater.* 3 (2013) 156-160.
- [78] K. Saravanan, C.W. Mason, A. Rudola, K.H. Wong, P. Balaya, *Adv. Energy Mater.* 3 (2013) 444-450.
- [79] Y. Jiang, Z. Yang, W. Li, L. Zeng, F. Pan, M. Wang, X. Wei, G. Hu, L. Gu, Y. Yu, *Adv. Energy Mater.* 5 (2015) 1402104.
- [80] N. Böckenfeld, A. Balducci, *J. Solid State Electrochem.* 18 (2014) 959-964.
- [81] J. Illig, M. Ender, T. Chrobak, J.P. Schmidt, D. Klotz, E. Ivers-Tiffée, *J. Electrochem. Soc.* 159 (2012) A952-A960.
- [82] L.S. Plashnitsa, E. Kobayashi, Y. Noguchi, S. Okada, J.-i. Yamaki, *J. Electrochem. Soc.* 157 (2010) A536-A543.
- [83] Y.C. Chang, J.H. Jong, G.T.K. Fey, *J. Electrochem. Soc.* 147 (2000) 2033-2038.
- [84] K. Tang, X. Yu, J. Sun, H. Li, X. Huang, *Electrochim. Acta* 56 (2011) 4869-4875.
- [85] S. Li, Y. Dong, L. Xu, X. Xu, L. He, L. Mai, *Adv. Mater.* 26 (2014) 3545-3553.
- [86] C. Zhu, K. Song, P.A. van Aken, J. Maier, Y. Yu, *Nano Lett.* 14 (2014) 2175-2180.
- [87] G. Li, Z. Yang, Y. Jiang, C. Jin, W. Huang, X. Ding, Y. Huang, *Nano Energy* 25 (2016) 211-217.
- [88] H. Huang, S.C. Yin, T. Kerr, N. Taylor, L.F. Nazar, *Adv. Mater.* 14 (2002) 1525-1528.
- [89] W. Shen, C. Wang, H. Liu, W. Yang, *Chem. - Eur. J.* 19 (2013) 14712-14718.
- [90] Y.H. Jung, C.H. Lim, D.K. Kim, *J. Mater. Chem. A* 1 (2013) 11350-11354.
- [91] X. Rui, W. Sun, C. Wu, Y. Yu, Q. Yan, *Adv. Mater.* 27 (2015) 6670-6676.
- [92] R. Rajagopalan, L. Zhang, S.X. Dou, H.K. Liu, *Adv. Mater. Interfaces* 3 (2016) 1600007.
- [93] S. Tao, P. Cui, W. Huang, Z. Yu, X. Wang, S. Wei, D. Liu, L. Song, W. Chu, *Carbon* 96 (2016) 1028-1033.
- [94] J.-S. Lee, G.S. Park, S.T. Kim, M. Liu, J. Cho, *Angew. Chem., Int. Ed.* 52 (2013) 1026-1030.
- [95] L.G. Bulusheva, A.V. Okotrub, A.G. Kurennya, H. Zhang, H. Zhang, X. Chen, H. Song, *Carbon* 49 (2011) 4013-4023.
- [96] B. Guo, Q. Liu, E. Chen, H. Zhu, L. Fang, J.R. Gong, *Nano Lett.* 10 (2010) 4975-4980.

- [97] Z. Chen, D. Higgins, H. Tao, R.S. Hsu, Z. Chen, *J. Phys. Chem. C* 113 (2009) 21008-21013.
- [98] M.S. Dresselhaus, A. Jorio, M. Hofmann, G. Dresselhaus, R. Saito, *Nano Lett.* 10 (2010) 751-758.
- [99] D.H. Youn, A. Heller, C.B. Mullins, *Chem. Mater.* 28 (2016) 1343-1347.
- [100] T. Lin, I.-W. Chen, F. Liu, C. Yang, H. Bi, F. Xu, F. Huang, *Science* 350 (2015) 1508-1513.
- [101] S.H. Chan, K.A. Khor, Z.T. Xia, *J. Power Sources* 93 (2001) 130-140.
- [102] Z. Shao, S.M. Haile, *Nature* 431 (2004) 170-173.
- [103] W. Shen, H. Li, Z. Guo, C. Wang, Z. Li, Q. Xu, H. Liu, Y. Wang, Y. Xia, *ACS Appl. Mater. Interfaces* 8 (2016) 15341-15351.
- [104] Z. Jian, Y. Sun, X. Ji, *Chem. Commun.* 51 (2015) 6381-6383.
- [105] C.A.J. Fisher, V.M. Hart Prieto, M.S. Islam, *Chem. Mater.* 20 (2008) 5907-5915.
- [106] A.K. Padhi, K.S. Nanjundaswamy, J.B. Goodenough, *J. Electrochem. Soc.* 144 (1997) 1188-1194.
- [107] H. Wang, Y. Yang, Y. Liang, L.-F. Cui, H. Sanchez Casalongue, Y. Li, G. Hong, Y. Cui, H. Dai, *Angew. Chem.* 123 (2011) 7502-7506.
- [108] B. Ellis, P. Subramanya Herle, Y.H. Rho, L.F. Nazar, R. Dunlap, L.K. Perry, D.H. Ryan, *Faraday Discuss.* 134 (2007) 119-141.
- [109] Y. Feng, H. Zhang, L. Fang, Y. Ouyang, Y. Wang, *J. Mater. Chem. A* 3 (2015) 15969-15976.
- [110] J. Wolfenstine, J. Allen, *J. Power Sources* 136 (2004) 150-153.
- [111] N.N. Bramnik, K. Nikolowski, D.M. Trots, H. Ehrenberg, *Electrochem. Solid-State Lett.* 11 (2008) A89-A93.
- [112] S.P. Ong, A. Jain, G. Hautier, B. Kang, G. Ceder, *Electrochem. Commun.* 12 (2010) 427-430.
- [113] G. Chen, T.J. Richardson, *J. Power Sources* 195 (2010) 1221-1224.
- [114] S.-W. Kim, J. Kim, H. Gwon, K. Kang, *J. Electrochem. Soc.* 156 (2009) A635-A638.
- [115] F. Sanz, C. Parada, J.M. Rojo, C. Ruíz-Valero, *Chem. Mater.* 13 (2001) 1334-1340.
- [116] S.-M. Oh, S.-T. Myung, J. Hassoun, B. Scrosati, Y.-K. Sun, *Electrochem. Commun.* 22 (2012) 149-152.
- [117] H. Kim, R.A. Shakoor, C. Park, S.Y. Lim, J.-S. Kim, Y.N. Jo, W. Cho, K. Miyasaka, R. Kahraman, Y. Jung, J.W. Choi, *Adv. Funct. Mater.* 23 (2013) 1147-1155.
- [118] P. Barpanda, T. Ye, M. Avdeev, S.-C. Chung, A. Yamada, *J. Mater. Chem. A* 1 (2013) 4194-4197.
- [119] N. Sharma, P. Serras, V. Palomares, H.E.A. Brand, J. Alonso, P. Kubiak, M.L. Fdez-Gubieda, T. Rojo, *Chem. Mater.* 26 (2014) 3391-3402.
- [120] K.T. Lee, T.N. Ramesh, F. Nan, G. Botton, L.F. Nazar, *Chem. Mater.* 23 (2011) 3593-3600.

- [121] M. Avdeev, Z. Mohamed, C.D. Ling, J. Lu, M. Tamaru, A. Yamada, P. Barpanda, *Inorg. Chem.* 52 (2013) 8685-8693.
- [122] H. Kim, I. Park, S. Lee, H. Kim, K.-Y. Park, Y.-U. Park, H. Kim, J. Kim, H.-D. Lim, W.-S. Yoon, K. Kang, *Chem. Mater.* 25 (2013) 3614-3622.
- [123] G. Hautier, A. Jain, S.P. Ong, B. Kang, C. Moore, R. Doe, G. Ceder, *Chem. Mater.* 23 (2011) 3495-3508.
- [124] P.S. Herle, B. Ellis, N. Coombs, L.F. Nazar, *Nat. Mater.* 3 (2004) 147-152.
- [125] M. Nose, H. Nakayama, K. Nobuhara, H. Yamaguchi, S. Nakanishi, H. Iba, *J. Power Sources* 234 (2013) 175-179.
- [126] S.M. Wood, C. Eames, E. Kendrick, M.S. Islam, *J. Phys. Chem. C* 119 (2015) 15935-15941.
- [127] F. Sanz, C. Parada, U. Amador, M.A. Monge, C.R. Valero, *J. Solid State Chem.* 123 (1996) 129-139.
- [128] J.-H. Shin, W.A. Henderson, S. Passerini, *Electrochem. Commun.* 5 (2003) 1016-1020.
- [129] Q. Zhou, W.A. Henderson, G.B. Appetecchi, M. Montanino, S. Passerini, *J. Phys. Chem. B* 112 (2008) 13577-13580.
- [130] R.D. Rogers, K.R. Seddon, *Science* 302 (2003) 792-793.
- [131] M. Galiński, A. Lewandowski, I. Stępnia, *Electrochim. Acta* 51 (2006) 5567-5580.
- [132] F. Wu, N. Zhu, Y. Bai, L. Liu, H. Zhou, C. Wu, *ACS Appl. Mater. Interfaces* 8 (2016) 21381-21386.
- [133] O. Yamamoto, Z. Ogumi, M. Morita, L.J. Krause, W. Lamanna, J. Summerfield, M. Engle, G. Korba, R. Loch, R. Atanasoski, *J. Power Sources* 68 (1997) 320-325.
- [134] J. Vetter, P. Novák, M.R. Wagner, C. Veit, K.C. Möller, J.O. Besenhard, M. Winter, M. Wohlfahrt-Mehrens, C. Vogler, A. Hammouche, *J. Power Sources* 147 (2005) 269-281.
- [135] X. Zhang, B. Winget, M. Doeff, J.W. Evans, T.M. Devine, *J. Electrochem. Soc.* 152 (2005) B448-B454.
- [136] F. La Mantia, R.A. Huggins, Y. Cui, *J. Appl. Electrochem.* 43 (2013) 1-7.
- [137] A. Jarry, S. Gottis, Y.-S. Yu, J. Roque-Rosell, C. Kim, J. Cabana, J. Kerr, R. Kostecki, *J. Am. Chem. Soc.* 137 (2015) 3533-3539.
- [138] J.-H. Kim, N.P.W. Pieczonka, P. Lu, Z. Liu, R. Qiao, W. Yang, M.M. Tessema, Y.-K. Sun, B.R. Powell, *Adv. Mater. Interfaces* 2 (2015) 1500109.
- [139] B.L. Ellis, W.R.M. Makahnouk, W.N. Rowan-Weetaluktuk, D.H. Ryan, L.F. Nazar, *Chem. Mater.* 22 (2010) 1059-1070.
- [140] K. Chihara, A. Kitajou, I.D. Gocheva, S. Okada, J.-i. Yamaki, *J. Power Sources* 227 (2013) 80-85.

- [141] P. Singh, K. Shiva, H. Celio, J.B. Goodenough, *Energy Environ. Sci.* 8 (2015) 3000-3005.
- [142] P. Barpanda, J.-N. Chotard, N. Recham, C. Delacourt, M. Ati, L. Dupont, M. Armand, J.-M. Tarascon, *Inorg. Chem.* 49 (2010) 7401-7413.
- [143] S. Li, J. Guo, Z. Ye, X. Zhao, S. Wu, J.-X. Mi, C.-Z. Wang, Z. Gong, M.J. McDonald, Z. Zhu, K.-M. Ho, Y. Yang, *ACS Appl. Mater. Interfaces* 8(2016)17233–17238.
- [144] H. Zhang, I. Hasa, D. Buchholz, B. Qin, D. Geiger, S. Jeong, U. Kaiser, S. Passerini, *NPG Asia Mater.* 9 (2017) e370.
- [145] P. Barpanda, M. Ati, B.C. Melot, G. Rousse, J.N. Chotard, M.L. Doublet, M.T. Sougrati, S.A. Corr, J.C. Jumas, J.M. Tarascon, *Nat. Mater.* 10 (2011) 772-779.
- [146] R.K.B. Gover, A. Bryan, P. Burns, J. Barker, *Solid State Ionics* 177 (2006) 1495-1500.
- [147] Z. Liu, Y.-Y. Hu, M.T. Dunstan, H. Huo, X. Hao, H. Zou, G. Zhong, Y. Yang, C.P. Grey, *Chem. Mater.* 26 (2014) 2513-2521.
- [148] J. Liu, X. Yu, E. Hu, K.-W. Nam, X.-Q. Yang, P.G. Khalifah, *Chem. Mater.* 25 (2013) 3929-3931.
- [149] J. Liu, D. Chang, P. Whitfield, Y. Janssen, X. Yu, Y. Zhou, J. Bai, J. Ko, K.-W. Nam, L. Wu, Y. Zhu, M. Feygenson, G. Amatucci, A. Van der Ven, X.-Q. Yang, P. Khalifah, *Chem. Mater.* 26 (2014) 3295-3305.
- [150] D. Massiot, R. Conanec, W. Feldmann, R. Marchand, Y. Laurent, *Inorg. Chem.* 35 (1996) 4957-4960.
- [151] M. Kim, S.-J. Kim, *Acta Crystallogr., Sect. E* 69 (2013) i34.
- [152] N. Recham, J.N. Chotard, L. Dupont, C. Delacourt, W. Walker, M. Armand, J.M. Tarascon, *Nat. Mater.* 9 (2010) 68-74.
- [153] Y. Li, Y. Lu, C. Zhao, Y.-S. Hu, M.-M. Titirici, H. Li, X. Huang, L. Chen, *Energy Storage Mater.* 7 (2017) 130-151.
- [154] M. Keller, C. Vaalma, D. Buchholz, S. Passerini, *ChemElectroChem* 3 (2016) 1124-1132.
- [155] D. Larcher, J.M. Tarascon, *Nat. Chem.* 7 (2015) 19-29.
- [156] H. Kim, J. Hong, K.-Y. Park, H. Kim, S.-W. Kim, K. Kang, *Chem. Rev.* 114 (2014) 11788-11827.
- [157] Z. Li, D. Young, K. Xiang, W.C. Carter, Y.-M. Chiang, *Adv. Energy Mater.* 3 (2013) 290-294.
- [158] X.-y. Wu, M.-y. Sun, Y.-f. Shen, J.-f. Qian, Y.-l. Cao, X.-p. Ai, H.-x. Yang, *ChemSusChem* 7 (2014) 407-411.
- [159] Z. Hou, X. Li, J. Liang, Y. Zhu, Y. Qian, *J. Mater. Chem. A* 3 (2015) 1400-1404.
- [160] K. Nakamoto, Y. Kano, A. Kitajou, S. Okada, *J. Power Sources* 327 (2016) 327-332.
- [161] R.-S. Kühnel, D. Reber, C. Battaglia, *ACS Energy Lett.* 2 (2017) 2005-2006.

- [162] J. Yu, C. Mu, X. Qin, C. Shen, B. Yan, H. Xue, H. Pang, *Adv. Mater. Interfaces* 4 (2017) 1700279.
- [163] J.O.G. Posada, A.J.R. Rennie, S.P. Villar, V.L. Martins, J. Marinaccio, A. Barnes, C.F. Glover, D.A. Worsley, P.J. Hall, *Renewable Sustainable Energy Rev.* 68, Part 2 (2017) 1174-1182.
- [164] L. Suo, O. Borodin, T. Gao, M. Olguin, J. Ho, X. Fan, C. Luo, C. Wang, K. Xu, *Science* 350 (2015) 938-943.
- [165] S. Chen, C. Wu, L. Shen, C. Zhu, Y. Huang, K. Xi, J. Maier, Y. Yu, *Adv. Mater.* 29 (2017) 1700431.
- [166] Q. Ni, Y. Bai, F. Wu, C. Wu, *Adv. Sci.* 4 (2017) 1600275.
- [167] Q. Zhang, C. Liao, T. Zhai, H. Li, *Electrochim. Acta* 196 (2016) 470-478.
- [168] L. Chen, J. Liu, Z. Guo, Y. Wang, C. Wang, Y. Xia, *J. Electrochem. Soc.* 163 (2016) A904-A910.
- [169] W. Song, X. Ji, Y. Zhu, H. Zhu, F. Li, J. Chen, F. Lu, Y. Yao, C.E. Banks, *ChemElectroChem* 1 (2014) 821-821.
- [170] C.W. Mason, F. Lange, *ECS Electrochem. Lett.* 4 (2015) A79-A82.
- [171] S. Guo, H. Yu, P. Liu, Y. Ren, T. Zhang, M. Chen, M. Ishida, H. Zhou, *Energy Environ. Sci.* 8 (2015) 1237-1244.
- [172] H. Gao, J.B. Goodenough, *Angew. Chem., Int. Ed.* 55 (2016) 12768-12772.
- [173] D. Wang, X. Bie, Q. Fu, D. Dixon, N. Bramnik, Y.-S. Hu, F. Fauth, Y. Wei, H. Ehrenberg, G. Chen, F. Du, *Nat. Commun.* 8 (2017) 15888.
- [174] H. Wang, T. Zhang, C. Chen, M. Ling, Z. Lin, S. Zhang, F. Pan, C. Liang, *Nano Res.* 11 (2018) 490-498.
- [175] J. Dong, G. Zhang, X. Wang, S. Zhang, C. Deng, *J. Mater. Chem. A* 5 (2017) 18725-18736.
- [176] K. Miyazaki, T. Shimada, S. Ito, Y. Yokoyama, T. Fukutsuka, T. Abe, *Chem. Commun.* 52 (2016) 4979-4982.
- [177] L. Suo, D. Oh, Y. Lin, Z. Zhuo, O. Borodin, T. Gao, F. Wang, A. Kushima, Z. Wang, H.-C. Kim, Y. Qi, W. Yang, F. Pan, J. Li, K. Xu, C. Wang, *J. Am. Chem. Soc.* 139 (2017) 18670-18680.
- [178] L. Suo, O. Borodin, Y. Wang, X. Rong, W. Sun, X. Fan, S. Xu, M.A. Schroeder, A.V. Cresce, F. Wang, C. Yang, Y.-S. Hu, K. Xu, C. Wang, *Adv. Energy Mater.* 7 (2017) 1701189.
- [179] K. Nakamoto, R. Sakamoto, M. Ito, A. Kitajou, S. Okada, *Electrochem.* 85 (2017) 179-185.
- [180] P.R. Kumar, Y.H. Jung, B. Moorthy, D.K. Kim, *J. Electrochem. Soc.* 163 (2016) A1484-A1492.
- [181] H. Tomiyasu, H. Shikata, K. Takao, N. Asanuma, S. Taruta, Y.-Y. Park, *Sci. Rep.* 7 (2017) 45048.

- [182] H. Zhang, I. Hasa, B. Qin, T. Diemant, D. Buchholz, R.J. Behm, S. Passerini, *ChemElectroChem* 4 (2017) 1256-1263.
- [183] J. Zheng, J.A. Lochala, A. Kwok, Z.D. Deng, J. Xiao, *Adv. Sci.* 4 (2017) 1700032.
- [184] X. Guo, J.-j. Shou, Y.-h. Zhang, J.P. Reid, *Analyst* 135 (2010) 495-502.
- [185] Y. Terashima, K. Takeda, M. Honda, *Chem. Phys.* 430 (2014) 23-28.
- [186] D.M. Carey, G.M. Korenowski, *J. Phys. Chem.* 108 (1998) 2669-2675.
- [187] W. Wu, S. Shabhag, J. Chang, A. Rutt, J.F. Whitacre, *J. Electrochem. Soc.* 162 (2015) A803-A808.
- [188] J.Y. Luo, Y.Y. Xia, *Adv. Funct. Mater.* 17 (2007) 3877-3884.
- [189] M.D. Levi, D. Aurbach, *J. Phys. Chem. B* 101 (1997) 4630-4640.
- [190] X. Zhan, M. Shirpour, *Chem. Commun.* 53 (2017) 204-207.
- [191] Y. Zhu, T. Gao, X. Fan, F. Han, C. Wang, *Acc. Chem. Res.* 50 (2017) 1022-1031.
- [192] Z. Jian, Y.-S. Hu, X. Ji, W. Chen, *Adv. Mater.* 29 (2017) 1601925.
- [193] Y. Fang, J. Zhang, L. Xiao, X. Ai, Y. Cao, H. Yang, *Adv. Sci.* 4 (2017) 1600392.
- [194] W. Song, X. Ji, Z. Wu, Y. Zhu, Y. Yang, J. Chen, M. Jing, F. Li, C.E. Banks, *J. Mater. Chem. A* 2 (2014) 5358-5362.
- [195] W. Ren, X. Yao, C. Niu, Z. Zheng, K. Zhao, Q. An, Q. Wei, M. Yan, L. Zhang, L. Mai, *Nano Energy* 28 (2016) 216-223.
- [196] D. Wang, Q. Liu, C. Chen, M. Li, X. Meng, X. Bie, Y. Wei, Y. Huang, F. Du, C. Wang, G. Chen, *ACS Appl. Mater. Interfaces* 8 (2016) 2238-2246.
- [197] Y. Fang, L. Xiao, J. Qian, Y. Cao, X. Ai, Y. Huang, H. Yang, *Adv. Energy Mater.* 6 (2016) 1502197.
- [198] Q. Hu, M. Yu, J. Liao, Z. Wen, C. Chen, *J. Mater. Chem. A* 6 (2018) 2365-2370.
- [199] H. Zhang, I. Hasa, D. Buchholz, B. Qin, S. Passerini, *Carbon* 124 (2017) 334-341.
- [200] X. Jiang, Z. Zeng, L. Xiao, X. Ai, H. Yang, Y. Cao, *ACS Appl. Mater. Interfaces* 9 (2017) 43733-43738.
- [201] J. Mao, C. Luo, T. Gao, X. Fan, C. Wang, *J. Mater. Chem. A* 3 (2015) 10378-10385.
- [202] A. Manthiram, *ACS Cent. Sci.* 3 (2017) 1063-1069.
- [203] Z. Guo, Y. Zhao, Y. Ding, X. Dong, L. Chen, J. Cao, C. Wang, Y. Xia, H. Peng, Y. Wang, *Chem* 3 (2017) 348-362.
- [204] C. Yang, J. Chen, T. Qing, X. Fan, W. Sun, A. von Cresce, M.S. Ding, O. Borodin, J. Vatamanu, M.A. Schroeder, N. Eidson, C. Wang, K. Xu, *Joule* 1 (2017) 122-132.
- [205] D.P. Leonard, Z. Wei, G. Chen, F. Du, X. Ji, *ACS Energy Lett.* 3 (2018) 373-374.

- [206] F. Wang, O. Borodin, M.S. Ding, M. Gobet, J. Vatamanu, X. Fan, T. Gao, N. Edison, Y. Liang, W. Sun, S. Greenbaum, K. Xu, C. Wang, *Joule* 2 (2018) 927-937.
- [207] G. Yang, H. Song, M. Wu, C. Wang, *J. Mater. Chem. A* 3 (2015) 18718-18726.
- [208] H.-K. Roh, H.-K. Kim, M.-S. Kim, D.-H. Kim, K.Y. Chung, K.C. Roh, K.-B. Kim, *Nano Res.* 9 (2016) 1844-1855.
- [209] J. Deng, W. Luo, S. Chou, H. Liu, S. Dou, *Adv. Energy Mater.* 8 (2018) 1701428.
- [210] C. Vaalma, D. Buchholz, M. Weil, S. Passerini, *Nat. Rev. Mater.* 3 (2018) 18013.
- [211] H. Zhang, S. Jeong, B. Qin, D.V. Carvalho, D. Buchholz, S. Passerini, *ChemSusChem* 11 (2018) 1382-1389.
- [212] K. Du, H. Guo, G. Hu, Z. Peng, Y. Cao, *J. Power Sources* 223 (2013) 284-288.



---

## List of Publications

### Peer-reviewed Publications:

1. Liu, X.; **Zhang, H.**; Han, J.; Varzi, A.; Moretti, A.; Passerini, S., Calcium Vanadate Sub-microfibers as Highly Reversible Host Cathode Materials for Aqueous Zinc-ion Batteries. *Chemical Communications* (doi: 10.1039/C8CC07243D)
2. Qin, B.; **Zhang, H.**; Diemant, T.; Dou, X.; Geiger, D.; Behm, R. J.; Kaiser, U.; Varzi, A.; Passerini, S., Exploring High Concentration Nitrogen-doped-carbon Interpenetrated SnS Nanoparticles as Anodes for Sodium Batteries. *Electrochimica Acta* 2019, 296, 806-813.
3. **Zhang, H.**; Qin, B.; Buchholz, D.; Passerini, S.\*, High-Efficiency Sodium-Ion Battery Based on NASICON Electrodes with High Power and Long Lifespan. *ACS Applied Energy Materials* 2018, 1 (11), 6425-6432.
4. Qin, B.; Jeong, S.; **Zhang, H.**; Ulissi, U.; Carvalho, D. V.; Varzi, A.; Passerini, S., Enabling Reversible (De-)Lithiation of Aluminum via Bis(fluorosulfonyl)imide-based Electrolytes. *ChemSusChem* (doi: 10.1002/cssc.201801806)
5. Han, J.; **Zhang, H.**; Varzi, A.; Passerini, S., Fluorine-free Water-in-Salt Electrolyte for Green and Low-cost Aqueous Sodium-ion Batteries. *ChemSusChem* 2018, 11 (21), 3704-3707.
6. Geng, C.; Buchholz, D.; Kim, G-T.; Carvalho, D. V.; **Zhang, H.**; Chagas, L. G.; Passerini, S., Influence of Salt Concentration on the Properties of Sodium-based Electrolytes. *Small Method* (doi:10.1002/smt.d.201800208)
7. **Zhang, H.**; Qin, B.; Han, J.; Passerini, S.\*, Aqueous/Nonaqueous Hybrid Electrolyte for Sodium-ion Batteries. *ACS Energy Letters* 2018, 3, 1769-1770.
8. Li, K.; Zhang, Y.; Sun, Y.; Xu, Y.\*; **Zhang, H.\***; Ye, P.; Zheng, M.; Zhou, N.; Wang, D., Template-Free Synthesis of Biomass-Derived Carbon Coated  $\text{Li}_4\text{Ti}_5\text{O}_{12}$  Microspheres as High Performance Anodes for Lithium-Ion Batteries. *Applied Surface Science* 2018, 459, 572-582.
9. **Zhang, H.**; Jeong, S.; Qin, B.; Carvalho, D. V.; Buchholz, D.; Passerini, S.\*, Towards High-Performance Aqueous Sodium-Ion Batteries: Stabilizing the Solid/Liquid Interface for NASICON-Type  $\text{Na}_2\text{VTi}(\text{PO}_4)_3$  using Concentrated Electrolytes. *ChemSusChem* 2018, 11 (8), 1382-1389.
10. **Zhang, H.**; Hasa, I.\*; Passerini, S.\*, Beyond Insertion for Na-Ion Batteries: Nanostructured Alloying and Conversion Anode Materials. *Advanced Energy Materials* 2018, 8 (17), 1702582.
11. Ma, Y.; Ma, Y.; Geiger, D.; Kaiser, U.; **Zhang, H.**; Kim, G.-T.; Diemant, T.; Behm, R. J.; Varzi, A.; Passerini, S., ZnO/ZnFe<sub>2</sub>O<sub>4</sub>/N-doped C Micro-polyhedrons with Hierarchical Hollow Structure as High-performance Anodes for Lithium-ion Batteries. *Nano Energy* 2017, 42,

341-352.

12. **Zhang, H.**; Hasa, I.; Qin, B.; Diemant, T.; Buchholz, D.; Behm, R. J.; Passerini, S.\*, Excellent Cycling Stability and Superior Rate Capability of  $\text{Na}_3\text{V}_2(\text{PO}_4)_3$  Cathodes Enabled by Nitrogen-Doped Carbon Interpenetration for Sodium-Ion Batteries. *ChemElectroChem* 2017, 4 (5), 1256-1263.
13. **Zhang, H.**; Hasa, I.; Buchholz, D.; Qin, B.; Passerini, S.\*, Effects of Nitrogen Doping on the Structure and Performance of Carbon Coated  $\text{Na}_3\text{V}_2(\text{PO}_4)_3$  Cathodes for Sodium-ion Batteries. *Carbon* 2017, 124, 334-341.
14. **Zhang, H.**; Hasa, I.; Buchholz, D.; Qin, B.; Geiger, D.; Jeong, S.; Kaiser, U.; Passerini, S.\*, Exploring the Ni Redox Activity in Polyanionic Compounds as Conceivable High Potential Cathodes for Na Rechargeable Batteries. *NPG Asia Materials* 2017, 9, e370.
15. Qin, B.; **Zhang, H.**; Diemant, T.; Geiger, D.; Raccichini, R.; Behm, R. J.; Kaiser, U.; Varzi, A.; Passerini, S., Ultrafast Ionic Liquid-Assisted Microwave Synthesis of SnO Microflowers and Their Superior Sodium-Ion Storage Performance. *ACS Applied Materials & Interfaces* 2017, 9 (32), 26797-26804.
16. **Zhang, H.**; Buchholz, D.\*; Passerini, S.\*, Synthesis, Structure, and Sodium Mobility of Sodium Vanadium Nitridophosphate: A Zero-Strain and Safe High Voltage Cathode Material for Sodium-Ion Batteries. *Energies* 2017, 10 (7), 889.
17. Zhao, C.\*; Wang, Q.; **Zhang, H.\***; Passerini, S.; Qian, X., Two-Dimensional Titanium Carbide/RGO Composite for High-Performance Supercapacitors. *ACS Applied Materials & Interfaces* 2016, 8 (24), 15661-15667.
18. Wang, Q.; Zhang, Y.; **Zhang, H.**; Xu, Y.; Dong, H.; Zhao, C., Structure and Electrochemical Performance of Cobalt Oxide Layer Coated on  $\text{LiNi}_{0.03}\text{Mn}_{1.97}\text{O}_4$  Cathode Materials. *Journal of Alloys and Compounds* 2017, 693, 474-481.
19. Zhang, Y.; Dong, H.; **Zhang, H.**; Liu, Y.; Ji, M.; Xu, Y.; Wang, Q.; Luo, L.,  $\text{Li}_4\text{Ti}_5\text{O}_{12}$ /Ketjen Black with Open Conductive Frameworks for High-performance Lithium-ion Batteries. *Electrochimica Acta* 2016, 201, 179-186.
20. Luo, L.; Xu, Y.\*; **Zhang, H.\***; Han, X.; Dong, H.; Xu, X.; Chen, C.; Zhang, Y.; Lin, J., Comprehensive Understanding of High Polar Polyacrylonitrile as an Effective Binder for Li-Ion Battery Nano-Si Anodes. *ACS Applied Materials & Interfaces* 2016, 8 (12), 8154-8161.

#### **Congress Contribution:**

1. **Zhang, H.**; Passerini, S., "Exploring the Ni Redox Activity in Polyanionic Compounds as Conceivable High Potential Cathodes for Na Rechargeable Batteries" Oral Presentation, EUROMAT 2017 Congress, Thessaloniki, Greece, 17-22 September 2017.